Structural Modification of Electrochromic Thin Films towards Optimized Mixed Ionic and Electronic Conduction

Dissertation

Zur Erlangung des Doktorgrades

der Naturwissenschaften

(Dr. rer. nat.)

von

Thi Hai Quyen Nguyen

vorgelegt dem Fachbereich 07

der Justus-Liebig-Universität Gießen

Juni 2022

1. Reviewer / Gutachter: Prof. Dr. Derck Schlettwein

2. Reviewer / Gutachter: Prof. Dr. Bernd M. Smarsly

Eigenständigkeitserklärung

Ich erkläre: Ich habe die vorgelegte Dissertation selbstständig und ohne unerlaubte fremde Hilfe und nur mit den Hilfen angefertigt, die ich in der Dissertation angegeben habe. Alle Textstellen, die wörtlich oder sinngemäß aus veröffentlichten Schriften entnommen sind, und alle Angaben, die auf mündlichen Auskünften beruhen, sind als solche kenntlich gemacht. Ich stimme einer evtl. Überprüfung meiner Dissertation durch eine Antiplagiat-Software zu. Bei den von mir durchgeführten und in der Dissertation erwähnten Untersuchungen habe ich die Grundsätze guter wissenschaftlicher Praxis, wie sie in der „Satzung der Justus-Liebig-Universität Gießen zur Sicherung guter wissenschaftlicher Praxis" niedergelegt sind, eingehalten.

_____   _____

  Ort, Datum   Unterschrift

Kurzfassung

Smart Windows bieten mithilfe von elektrochromen Materialien eine einstellbare Verdunklung der Fenstergläser an. Dadurch kann der Energieverbrauch, der zum Heizen oder Kühlen eines Gebäudes genutzt wird, reduziert werden und zusätzlich der Komfort innerhalb des Gebäudes verbessert werden. Die zum jetzigen Zeitpunkt kommerziell verfügbaren Smart Windows benötigen bis zu einigen Minuten, um von einem optischen Zustand zum anderen zu schalten. Aus diesem Grund soll ein besonderes Augenmerk auf die Schaltgeschwindigkeiten von elektrochromen Materialien für den optimalen Einsatz in Smart Windows gelegt werden. Die Schaltgeschwindigkeiten hängen stark vom Elektronentransfer und der Diffusion der ladungsausgleichenden Ionen im elektrochromen Material ab und damit auch von der Anwesenheit von geeigneten Transportwegen für die Elektronen und Ionen in elektrochromen Dünnfilmen. Ein Teil dieser Arbeit fokussierte sich auf Wolframoxid als wohlbekanntes elektrochromes Material. Dünne Wolframoxid-Schichten wurden mittels Spin-Coating hergestellt. Optional wurden verschiedene Polymere als strukturdirigierende Agenzien zugegeben, um die Porosität und innere Struktur der Schichten zu modifizieren. Wolframoxid-Dünnfilme, die mit einer optimalen Zugabe von Polymeren präpariert wurden, lieferten zugängliche poröse Netzwerke. Diese erleichterten die Diffusion der interkalierten Ionen durch den Film, wodurch die Rate und der Hub des Schaltvorgangs zwischen zwei Transmissionszuständen der Filme verbessert werden konnten. Ein anderer Teil der Arbeit widmete sich neuartig substituierte Phthalocyaninen als alternative elektrochrome Materialien. Dünne Schichten bestehend aus verschiedenen fluorierten Phthalocyaninen wurden mithilfe physikalischer Gasphasenabscheidung hergestellt. Die intermolekulare Kopplung der Moleküle in den Schichten wird durch den Grad der Fluorierung beeinflusst. Die gewünschte moderat starke intermolekulare Kopplung, welche zu einem gleich schnellen Transport von Elektronen und Ionen führen sollte, konnte sowohl für Filme bestehend aus einer gezielt substituierten Phthalocyanin-Molekülart als auch für Filme bestehend aus einer geschickten Mischung von zwei etablierten Phthalocyanin-Molekülen erzielt werden. Die Rate für den Transport von Elektronen und/oder Ionen konnte mithilfe von unterschiedlichen Ansätzen durch solche Modifikationen der

Filmeigenschaften von Wolframoxid- sowie Phthalocyanin-Dünnfilmen erhöht werden, was in schnellen und stabilen elektrochromen Schaltvorgängen resultierte.

Abstract

Smart windows based on electrochromic materials offer adjustable shading which can reduce the energy consumption required to cool or heat a building and increase the indoor occupant comfort. Commercial smart windows currently available on the market, however, may require up to several minutes to switch from one optical state to another. Therefore, special attention must be given to the enhancement of the switching kinetics of the electrochromic materials for the optimal use in smart windows. The switching kinetics are strongly dependent on the transfer of electrons and the diffusion of charge-balancing ions in the electrochromic material and, hence, on the presence of suitable pathways for the transport of electrons and ions in the electrochromic thin films. One part of this work focused on tungsten oxide as a well-known electrochromic material. Thin films of tungsten oxide were prepared by spin-coating with optional addition of different polymers as structure-directing agents to allow for fine-tuning of the porosity and the internal structure of the films. Tungsten oxide thin films prepared with optimum compositions of the polymers provided accessible porous networks which enabled facilitated diffusion of the intercalating ions through the film and, thus, improvement in the rate and modulation of the switching between two transmittance states of the films. Another part of this work dealt with new substituted phthalocyanines as an alternative group of electrochromic materials. Thin films composed of different fluorinated phthalocyanines were fabricated via physical vapor deposition. The intermolecular coupling of the molecules in the solid state is influenced by the degree of fluorination. The aimed moderate degree of intermolecular coupling that allowed a well-balanced, equally fast transport of electrons and ions could be obtained for films consisting of either one type of specifically substituted phthalocyanine molecules or an appropriate mixture of two well-established phthalocyanine molecules. The rate of the electron and/or ion transport could be enhanced by versatile approaches that allowed proper modifications of the film properties of thin films of tungsten oxide as well as of phthalocyanines leading to fast and stable electrochromic switching.

Table of Contents

1 Introduction

Windows are a key element in nearly every building worldwide. To date, buildings constructed with traditional windows, however, account for around 40 % of the total global energy consumption, e.g. for heating and cooling in buildings [1]. As the building sector is continuously growing, promising strategies are urgently needed for achieving energy conservation and sustainable energy management in buildings [1,2]. One of these strategies may involve the development and application of switchable windows, also known as smart windows [2,3]. These windows with tunable shading allow for reduction of the energy consumption, especially during summer and winter, by regulation of light and heat entering the building [4–7]. As claimed by the commercial provider SageGlass up to around 45 % of the energy consumption in buildings could be reduced with the help of smart windows compared to single-pane windows [8,9]. An additional benefit of smart windows is that disturbing shadows being cast on occupants or objects, as when using curtains or blinds, and, presumably, extended use of shading, can be avoided, thus, contributing to improvement of the comfort of occupants [3,10].

The term 'smart window' was introduced in 1984 by Svensson and Granqvist [11,12] to describe the usage of electrochromic materials in fenestration of buildings [12,13]. The optical properties of electrochromic materials can be changed by applying an appropriate potential [14,15]. Tungsten oxide (WO_3) as a promising electrochromic material exhibits the ability to conduct electrons as well as ions and, hence, belongs to the group of mixed ionic electronic conductors (MIECs) [16,17]. WO_3 offers a high transparency and reversible switching between the bleached and blue-colored states under an applied potential in the presence of an electrolyte consisting of small charge-balancing ions [18,19]. Nowadays, smart windows with thin films of WO_3 are already installed in public buildings [20,21]. Further commercially available applications of electrochromic materials include displays [22], anti-glare rear-view mirrors for vehicles [22–24] and aircraft windows [15,24]. All these electrochromic applications can maintain their optical state with only a small or even no extra power input [14,17].

However, commercial smart windows based on WO_3 still exhibit rather long response times of up to a few minutes to switch from one optical state to another [25]. To allow a

fast adjustment of brightness and heat input in the room, short response times are desirable [26,27]. For films of WO_3, the transport of electrons is fast [28,29] whereas the diffusion of ions is typically the rate-limiting step in the electrochromic switching process [30–32]. Hence, the electrochromic performance of WO_3 including the response time is dictated by the transport of ions which in turn is highly influenced by the structure (amorphous or crystalline nature) and the porosity of the WO_3 thin films [33,34]. Porous and amorphous thin films of WO_3 can provide improved electrochromic switching characteristics owing to the facile transport of ions compared to compact and crystalline WO_3 films [33–35]. Thus, a facile accessibility of the WO_3 thin films with short diffusion pathways is crucial for a high diffusion rate of ions through the film network resulting in short response times [33,34,36].

Several different approaches exist towards preparation of WO_3 thin films [37]. In industry, coatings of WO_3 are typically prepared by sputter deposition [37–39]. However, such deposition is expensive [37], so that alternative fabrication techniques providing WO_3 thin films with short response times are sought. A simple and low-cost method for the fabrication of thin films of WO_3 is the solution-based processing [37,40] by spin-coating [41], dip-coating [42] or electrodeposition [43]. The addition of numerous different structure-directing agents such as polymers or surfactants into the precursor solution enables facile preparation of WO_3 thin films with modified porosity and internal film structure, beneficial for enhancing the electrochromic switching of WO_3 [34,44].

Besides WO_3 as well-established inorganic material with electrochromic properties, electrochromism can be found in other inorganic materials [18,45] and also in many organic materials [14,15,46]. Anti-glare rear-view mirrors produced by Gentex, e.g., are based on viologens as organic electrochromic material [22,24]. Compared to inorganic electrochromic materials, organic materials show various color changes as well as higher molar extinction coefficients so that thinner films can be used in electrochromic devices resulting in shorter pathways of ion and electron transport leading to faster electrochromic switching [24,46,47]. An attractive alternative group of materials for the use in electrochromic devices are phthalocyanines [46,48,49]. Phthalocyanines exhibit more narrow absorption bands than WO_3 but offer various selection of different colorations [50,51], interesting for information displays [51] and aesthetic aspects of smart windows for modern buildings. The electrochromic switching characteristics of phthalocyanines as MIECs can be tuned by the central metal ion and/or substituents on the aromatic ring system which both influence the redox characteristics as well as the intermolecular coupling of the molecules in the solid state and, thus, the transfer of electrons and

diffusion of ions in the films [51–56]. Thin films consisting of phthalocyanine molecules with a strong intermolecular coupling in the solid state allowed a fast transfer of electrons [54–56] but hampered ion diffusion [54]. For thin films composed of weakly interacting phthalocyanine molecules, the diffusion of ions was faster than the electron transfer [54]. To ensure fast electrochromic switching, phthalocyanine thin films have to provide an optimized balance of both, electron and ion transport [54].

The goal of this work is the optimization of the electrochromic switching kinetics of thin films consisting of these two prototypes of electrochromic materials by modification of their film properties. On the one hand, WO_3 thin films are prepared by spin-coating using different structure-directing agents to tune the porosity and internal film structure. On the other hand, thin films of phthalocyanines showing a moderate degree of intermolecular coupling in the solid state are studied. The common goal of both approaches consists in providing electrochromic thin films that exhibit fast electrochromic switching due to fast transport of electrons and ions through the film network, desirable for the application in electrochromic devices.

2 Fundamentals

2.1 Electrochromism

Electrochromism can be found in different classes of chemical compounds such as transition metal oxides or organic molecules [13,46,49]. The optical properties of an electrochromic material can be reversibly changed by its electrochemical reduction or oxidation induced by an applied electric potential [14,18,48].

2.2 Types of Electrochromic Devices

Electrochromic devices can be divided into three different types [14,57]. Type I includes electrochromic species that are dissolved in solution in the reduced as well as in the oxidized state as observed for methyl viologen in aqueous solution [14,57,58]. The change of color occurs by the transfer of electrons between the species in solution and a solid electrode [14,57,58]. If the electrochromic species are soluble in the neutral state but create a solid film on the electrode after the electron-transfer process, the resulting devices such as those based on heptyl viologen belong to type II [14,57–59]. Many electrochromic devices can be classified into type III, e.g. those based on tungsten oxide, phthalocyanines or Prussian blue [14,49,57]. Thin solid films of these materials deposited on an electrode remain in their solid state upon reduction and oxidation [14,49,57]. In contact with an electrolyte consisting of small ions their redox processes are accompanied by intercalation and deintercalation of charge-balancing ions into the thin films [14,15,57].

2.3 Construction of an Electrochromic Device

A typical construction of a type III electrochromic device [14,15,18], is shown in Figure 2.1. The outer layers are both composed of transparent substrates such as glass or polymer foil on which a transparent conductor (TC) is deposited, acting as an electron

conductive layer [15,18]. Indium doped tin oxide (ITO) or fluorine doped tin oxide (FTO) are widely used as transparent conductors due to their high electrical conductivity, chemical stability and superior optical transparency [13,15,60,61], with FTO often preferred over ITO because of its lower cost and higher thermal stability [60,62,63]. One of the electron conductive layers is covered with an electrochromic layer such as WO_3 that allows a transport of both electrons and ions along with changing its transmittance [15,18]. The electrolyte serves as ionic conductor and separates the electrochromic layer from an ionic storage layer which is deposited on the other transparent conducting layer [15,18]. The ionic storage layer can be composed of an optically passive material [15,18], e.g. cerium oxide (CeO_2) [64,65] or of a second electrochromic material which changes its optical properties complementary to the first electrochromic layer [15,18]. The application of an appropriate potential between the transparent conductors leads to a change in optical transmittance of the electrochromic films by reduction or oxidation of the material [14,15,18]. A decrease of the transmittance during reduction and intercalation of cations can be found for cathodic electrochromic materials including WO_3 [15,18] while a decrease of the transmittance during oxidation and deintercalation of cations is known for anodic electrochromic materials such as nickel oxide (NiO) [15,18]. For this reason, NiO often serves as a complementary layer to a WO_3 layer in electrochromic devices [66,67].
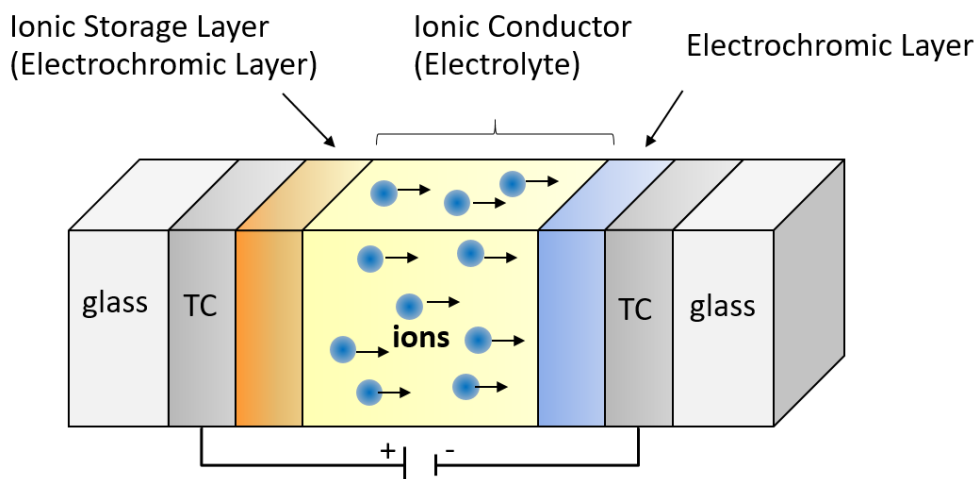

Figure 2.1: Typical construction of an electrochromic device. Adapted from [18].

In order to transport small ions, e.g. H^+ or Li^+, different types of electrolytes can be utilized [13,15]. Lithium perchlorate ($LiClO_4$) in propylene carbonate (PC) is commonly used as transparent liquid electrolyte [15] whereas tantalum pentoxide (Ta_2O_5) is a well-known solid electrolyte [68,69]. By gelifying liquid electrolytes with a polymer host such as poly(methyl methacrylate) (PMMA), polymer electrolytes can be obtained [70,71].

The switching characteristics of the electrochromic film between a colored and a bleached state, or in general between a reduced and an oxidized state, can be described and evaluated by different parameters [14,15]. One of the most important parameters is the transmittance modulation $\Delta T(\lambda) = |T_2 - T_1|$, hence, the difference of transmittance between the reduced T_1 and the oxidized state T_2 at a given wavelength λ [15]. A conscientious choice of the materials serving as the two electrochromic layers in smart windows enables a high transmittance modulation along with color neutrality in the bleached state [15,18]. Another relevant parameter consists in the response or switching time, the time required to achieve the optical transmittance of the reduced or oxidized state of the electrochromic material after applying a defined potential [14,15]. By convention, the time needed to obtain 90 % of the maximum transmittance modulation is chosen [15,72,73]. Another important parameter is the coloration efficiency CE at a given wavelength (Equation 2.1) defined as the logarithm of the ratio of T_2 and T_1 per inserted or extracted charge Q of a film with the active surface area A [15,18]. Thus, if a small charge suffices to generate a large change in transmittance, a high coloration efficiency can be obtained for the electrochromic film [15,18].

$$CE(\lambda) = \frac{\log\left(\frac{T_2}{T_1}\right) \cdot A}{Q} \tag{2.1}$$

To ensure a high lifetime of electrochromic devices, a high chemical reversibility R_{EC} of the electrochromic switching processes is needed [14,15]. Therefore, the long-term stability of the electrochromic material under operational use should be considered, e.g. by switching over multiple cycles between the reduced and oxidized states [14,15]. Many reports focused on the electrochemical and spectroelectrochemical analyses of a single electrochromic thin film in contact with an electrolyte in order to directly resolve the switching characteristics of the electrochromic material of interest [14,15].

2.4 Inorganic and Organic Electrochromic Materials

2.4.1 Tungsten Oxide

WO_3 belongs to the most commonly investigated cathodic electrochromic materials [19,74,75]. Its electrochromic properties were already discussed in the 1960s by Deb [19,76]. WO_3 is a wide band gap semiconductor with a band gap of around 2.6 eV depending on its crystal structure and crystallinity [77–80]. The valence band of WO_3 comprises occupied oxygen 2p states and is separated by the band gap from the conduction band which consists of unoccupied tungsten 5d states [17,18,81,82]. Insertion of electrons together with charge-balancing ions into WO_3 results in a partially filled d-band leading to optical absorption, thus, coloration of WO_3 [17,18,82].
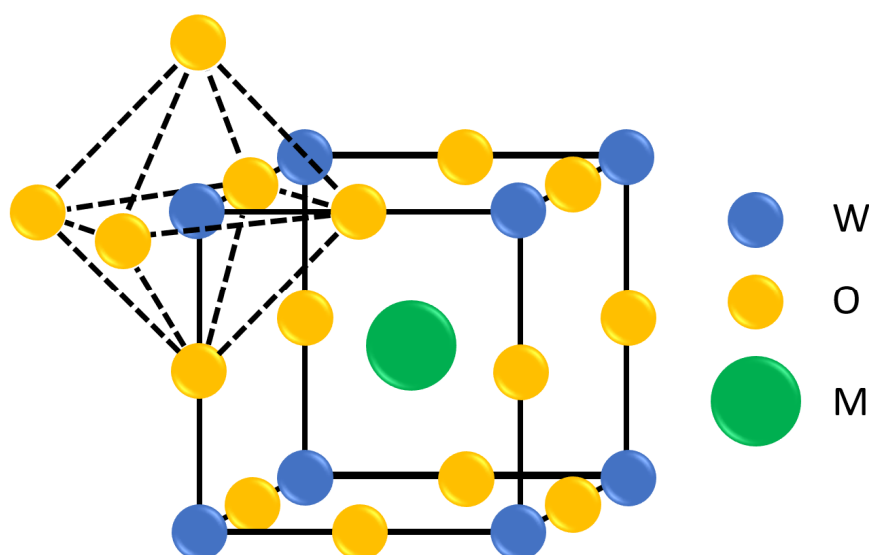

Figure 2.2: Crystal structure of MWO_3 where M represents an intercalated ion. Adapted from [82].

WO_3 ideally exhibits a defective perovskite structure that can be well derived from the perovskite structure as also found for MWO_3 with M representing an intercalated ion as shown in Figure 2.2 [18,82,83]. In each cubic unit cell, the W^{6+} ions are located at the corners and the oxygen ions (O^{2-}) are placed at the centers of the edges whereas the center of the cube remains unoccupied similar to the rhenium oxide (ReO_3) structure [18,82–87]. Such a structure can be described, in the case of WO_3, as a three-dimensional network of WO_6 octahedra in which each W^{6+} ion is surrounded by six oxygen ions (Figure 2.2) [18,83–86].

In crystalline and stoichiometric WO_3, each octahedron shares corners with the adjacent octahedra [17,84–86]. The existence of cubic WO_3 could be observed in a few studies [88–90]. However, WO_3 may commonly deviate from the ideal cubic phase due to different arrangement of corner-sharing octahedra depending on the temperature which leads to different crystal phases [18,83]. At room temperature, WO_3 is most stable in the monoclinic phase [82,91]. Other stable phases of WO_3 which can be observed at room temperature are the triclinic and hexagonal structures [80,92–98]. Going to temperatures between $330 - 740\,°C$, the orthorhombic phase is dominating while at temperatures higher than $740\,°C$ WO_3 appears in the tetragonal phase [94,99,100]. Sub-stoichiometric WO_3 may contain not only corner-sharing but also edge-sharing octahedra due to distortion of the octahedra caused by oxygen deficiencies [18,101]. These sub-stoichiometric WO_3 phases are also known as Magnéli phases [18]. For amorphous WO_3, a short-range ordering of the network consisting of WO_6 octahedra is assumed [77].

The octahedral coordination plays a crucial role for the electrochromic properties of tungsten oxide [17,18]. Adequately large empty spaces between the octahedra allow for intercalation of small ions [17,18,84]. Depending on the arrangement of the octahedra, the size of these empty spaces can be varied providing pathways for the transport of ions through the network [17,18]. When the intercalated ions are placed into the empty spaces, the crystal structure of WO_3 resembles a perovskite structure (Figure 2.2) in which the center of the cubic unit cell is filled with the intercalated ion [18,82].

The coloration of WO_3 can be described by Equation 2.2 leading to the formation of colored tungsten bronze (M_xWO_3) [74,102,103]:

$$WO_3 \text{ (transparent)} + x M^+ + x e^- \leftrightarrow M_xWO_3 \text{ (colored)} \qquad (2.2)$$
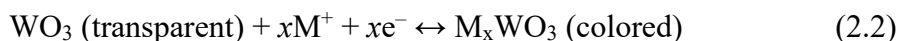
with $M = H^+$, Li^+, Na^+, K^+ etc. and the number of inserted electrons and ions x [74,102,103].

The coloration of the reduced WO_3 is independent of the nature of the cations inserted into the films [14,104,105]. Electrochromic switching with a high R_{EC} of WO_3 is observed for $x \leq 0.7$ whereas higher x-values lead to light-brownish thin films showing optical irreversibility [106,107]. The detailed mechanism of electrochromism in WO_3 still is not fully understood. However, several models exist serving as good explanations of the possible mechanism of coloration and bleaching of WO_3 [18,84].

Among the different models, two of them, namely the small polaron absorption and the intervalence charge transfer (IVCT) transition, are widely accepted for the description of the electrochromic mechanism in amorphous tungsten oxide [84,102,108]. Based on the small polaron absorption, Schirmer et al. proposed that the insertion of electrons leads to reduction of W^{6+} to W^{5+} states and, hence, the electrons are localized at the W^{5+} states causing polarization of the surrounding lattice which results in the formation of small polarons [84,108,109]. The coloration of tungsten oxide occurs due to absorption of a photon of the energy hv caused by transitions of small polarons (Equation 2.3), also known as polaron hopping, between site A and site B [108,109].

$$hv + W^{5+}(A) + W^{6+}(B) \rightarrow W^{6+}(A) + W^{5+}(B) \tag{2.3}$$
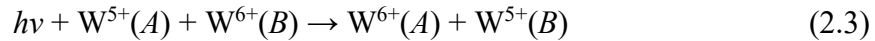
The model of IVCT transition suggested by Faughnan et al. shows similarities with the model based on small polarons [102,103,108]. The insertion of ions and electrons leads to reduction of some W^{6+} to W^{5+} states [84,102,103]. The optical absorption is induced by the IVCT which is the transfer of electrons between the W^{5+} states and the neighboring W^{6+} states [84,102,103].

However, both models are not suitable for the explanation of transparent as-prepared tungsten oxide films with oxygen deficiency [109,110]. A modified model [109,110] suggested the presence of mainly W^{6+} and W^{4+} states in the as-prepared films. These films remain transparent as long as no polarons are present [110]. Small polaron transitions or IVCT transitions between the W^{5+} and W^{4+} states as well as between the W^{5+} and W^{6+} states are possible (Equations 2.3 and 2.4) resulting in coloration of tungsten oxide [109–111].

$$hv + W^{4+}(A) + W^{5+}(B) \rightarrow W^{5+}(A) + W^{4+}(B) \tag{2.4}$$
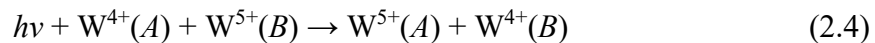
Berggren et al. found out that for an amount of intercalated ions up to $x \approx 0.5$ in Li_xWO_3 IVCT transitions occur mainly between the W^{6+} and W^{5+} states providing a high optical absorption [106,107]. For values $x > 0.6$, the strength of the optical absorption decreases due to a decline of transitions between the W^{6+} and W^{5+} states and an increase of transitions between the W^{5+} and W^{4+} states as well as between W^{6+} and W^{4+} states leading to higher transmittance of the films [106,107].

Another model describing the electrochromic mechanism of WO_3 was developed by Deb in which the coloration of WO_3 is attributed to the presence of oxygen vacancies [19]. Each neutral oxygen vacancy $V_O{}^0$ leads to generation of two adjacent W^{5+} ions [19]. After relaxation, the W^{5+} ions are transformed into one W^{4+} and one W^{6+} ion, respectively [19]. Defect levels caused by the oxygen vacancies are assumed to be inside or close to the valence band with each defect level filled with two electrons [19]. If one electron is extracted from the defect level, $V_O{}^0$ changes into a positively charged oxygen vacancy $V_O{}^+$, and thus, W^{4+} into W^{5+} [19]. The positively charged oxygen vacancy provokes a coulombic repulsion which leads to displacement of the adjacent W ions and shifting of the defect level into the band gap and, hence, formation of a color center [19,77]. The optical transition from $V_O{}^+$ to a double positively charged oxygen vacancy $V_O{}^{2+}$ or from W^{5+} to W^{6+} which is a state in the conduction band results in coloration of WO_3 [19]. This model correlates well with the modified model based on small polaron or IVCT transitions [19,109,110].

For crystalline tungsten oxide films, the coloration mechanism can be described with the Drude theory [112–114]. The injected electrons are delocalized rather than localized as in amorphous WO_3 and act as free electrons while the intercalated ions serve as scatterers for the electrons resulting in coloration of crystalline WO_3 [112–114].

2.4.2 Phthalocyanines

Organic materials such as phthalocyanines have gained interest as cost-effective alternatives in different fields of application including electrochromic devices [46,49,115]. The electrochromism of phthalocyanines has been studied since the 1970s [49]. Phthalocyanines are planar macrocyclic compounds and consist of an aromatic π-system [50,115] as shown in Figure 2.3. The molecule comprises four isoindole units connected by four nitrogen atoms [50,115]. Its systematic name is tetrabenzotetraazaporphyrin [115,116]. The center of the phthalocyanine molecule can contain either two protons, divalent metal ions or higher valent metal ions with additional axial ligands [50,115].

The optical properties of the phthalocyanines can be modified by variation of the central metal ion and the substituents on the phthalocyanine ring [50,115,116]. For zinc or copper phthalocyanines, electronic transitions occurring from the highest occupied molecular orbital (HOMO) to the lowest unoccupied molecular orbital (LUMO) of the

phthalocyanine ring lead to the characteristic Soret-band below 400 nm and the Q-band around 500 – 800 nm in the optical absorption spectra [47,116–118]. For phthalocyanine complexes with, e.g. iron or cobalt as central metal ion, the d orbitals of the central metal ion may also contribute to the electronic transitions providing an additional band in the absorption spectra [47,116–118]. The intensity and position of the Q-band can be influenced by the nature of the central metal ion and the substituents [115,116]. For instance, the presence of electron-donating substituents can lead to enlargement of the π-system that causes a shift of the Q-band to longer wavelengths [116,119].

Similar to WO_3, the electrochromic switching processes of thin films of phthalocyanines involve the transport of electrons and ions leading to spectral changes of the films [14,46]. The electrochemical reduction or oxidation of the phthalocyanine species can occur on the phthalocyanine ring or also include the central metal ion [48,120–122]. Substituting the aromatic hydrogen atoms on the phthalocyanine ring by electron-withdrawing substituents such as fluorine atoms or perfluoroalkyl groups provides electrochromic reduction and re-oxidation with a high R_{EC} [53,54,123]. In copper perfluoro phthalocyanine, $F_{16}PcCu$, all aromatic hydrogen atoms of a copper phthalocyanine molecule are substituted by fluorine atoms ($R_1 = R_2 = R_3 = F$ as shown in Figure 2.3) [54,55]. Substitution of the eight peripheral hydrogen atoms by perfluoroisopropyl groups ($R_2 = R_3 = C_3F_7$) and the other eight non-peripheral hydrogen atoms by fluorine atoms ($R_1 = F$) results in copper octakis-perfluoroisopropyl-perfluoro phthalocyanine, $F_{64}PcCu$ (Figure 2.3) [53,54,56]. In copper tetrakis-perfluoroisopropyl-perfluoro phthalocyanine, $F_{40}PcCu$ (Figure 2.3), 12 hydrogen atoms are substituted by fluorine atoms ($R_1 = R_2 = F$) and only four by perfluorisopropyl groups ($R_3 = C_3F_7$) [124]. The presence of fluorine atoms and/or perfluoroalkyl groups as substituents clearly influences the intermolecular interactions of the molecules in the solid state and, hence, the rate of the electron and ion transport in thin films [54,124].

Thin films of different fluorinated and/or perfluoroalkylated phthalocyanines have been investigated in aqueous electrolytes [53,54,123], promising for potential use in environmentally friendly devices. Although the solubility of phthalocyanines in organic solvents can be enhanced by substitution with perfluoroalkyl groups [125,126], a poor solubility is ensured in water due to the hydrophobic character of the perfluoroalkyl substituents [127,128]. However, a clear influence of the nature of the intercalating ion on the R_{EC} of the electrochromic switching has been found [54,123]. The electrochromic switching of the thin films of fluorinated phthalocyanines is observed to show a high R_{EC} when using K^+ as charge-balancing ions [54,123] whereas Li^+ ions presumably exhibit

stronger interactions with the reduced phthalocyanine species and, thus, suppress the re-oxidation process [123].
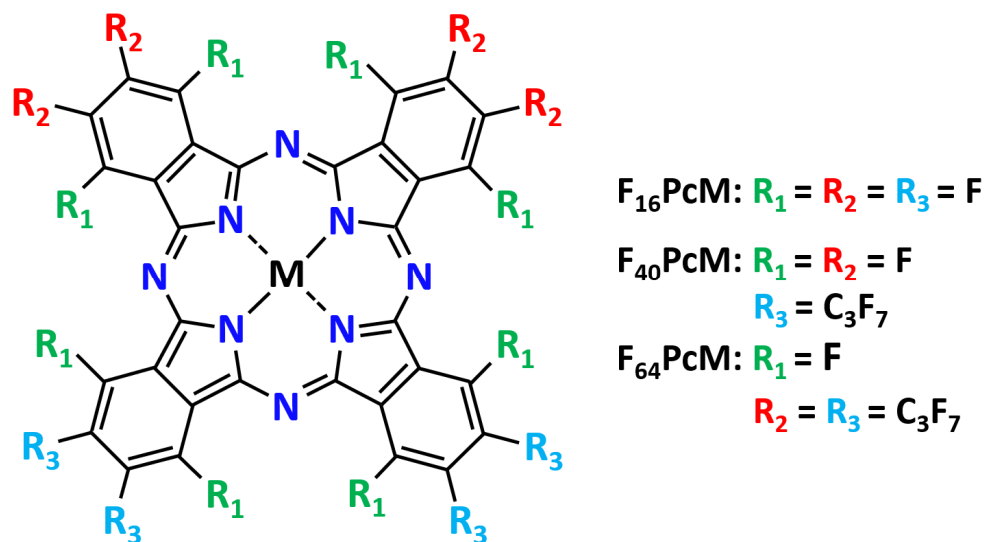

Figure 2.3: Structural formula of a phthalocyanine molecule. M is the central metal ion (with M = Cu or Zn in this work), R_1 represents the substituents in the non-peripheral positions and R_2 and R_3 stand for the substituents in the peripheral positions of the phthalocyanine ring.

2.5 Preparation of Thin Films

Typical thin films of phthalocyanines are prepared by vapor deposition technique [48,115]. For WO_3, the sol-gel processing is proven to be a versatile method for the fabrication of thin films with modified porosity and internal film structure [34,44]. In the following, both methods are described in more detail.

2.5.1 Sol-Gel Process

The sol-gel process is a versatile and low-cost method for the fabrication of various materials like oxide materials or hybrid organic-inorganic materials from molecular precursors [37,129]. A sol is described as a stable suspension containing nanoparticles or molecules which are dispersed in a solvent such as water or alcohol [129]. The transformation of the sol into a gel, also known as gelation, is triggered by interactions between the particles or molecules resulting in a three-dimensional network which is surrounded by the solvent [40,129]. By removal of the solvent through evaporation, a xerogel is formed [129]. If the solvent is replaced with a gas during the drying process then an aerogel is obtained [129]. The sol-gel processing allows for the synthesis of powders and the fabrication of thin films [37,129]. Thin films can be prepared, e.g. by spin-coating or dip-coating and using the sol as precursor solution [37,40,129]. One of the drawbacks of the sol-gel process is the possibility of shrinkage and cracking of the thin films during the drying process [37,129]. However, the benefits of the sol-gel process include the use of polymers or surfactants as structure-directing agents into the precursor solution providing a facile modification of the porosity and crystallinity of the obtained material [34,44,129]. Another advantage of the sol-gel process is the requirement of relatively low temperatures and low-cost equipment, only [37,129].

Spin-Coating

Spin-coating is a simple method to prepare homogeneous thin films with a defined thickness on flat substrates [130–133]. For this purpose, the substrate is mounted on a rotatable holder [130]. A precursor solution containing the material to be deposited is applied on the substrate with the help of a syringe or a pipette, either just before or during rotation of the substrate [131–133]. This results in an outward radial spread of the solution due to the centrifugal force allowing a uniform distribution of the solution on the surface

of the substrate and the evaporation of the solvent [130–133]. To ensure a full coverage of the surface with the solution, pretreatment of the substrate can be of help [133]. The modification of the hydrophilic or hydrophobic character of the surface may provide an optimal wetting of the surface with the precursor solution [133]. By UV-ozone treatment, for example, the surface of the substrate may become more hydrophilic which is optimal for water-based precursor solutions [133,134]. During the spinning process the solvents are removed by evaporation and a thin gel layer consisting of coating material remains on the surface of the substrate [130–133]. The sample may undergo a heat treatment to transform the coating material into the desired material [132,133]. The high loss of dispensed material during the spinning process and the challenge to deposit thin and uniform films on substrates with large areas belong to the disadvantages of the spin-coating technique [131]. Nevertheless, the advantages of this method are the possibility to quickly obtain thin films and the versatile adjustment of the film thickness by many factors, e.g. the spin speed, the viscosity of the solution, the evaporation rate and the surface tension [131–133]. When using the same precursor solution and substrate, a higher spin speed leads to formation of thinner films [130–133].

2.5.2 Thermal Evaporation

Thermal evaporation is a widely used method to prepare thin films and belongs to the physical vapor deposition (PVD) techniques [135,136]. Ceramic crucibles or metal boats containing the material to be deposited on a substrate can be used as evaporation source [135]. A current passes through the metal boat or in the case of the ceramic crucible through a heating coil in which the crucible is placed to heat up the desired material [135]. At a sufficient temperature the material starts to evaporate, moves through the chamber and then condenses on the substrate creating a thin film [135,136]. Since the deposition process takes place under vacuum condition, collisions of the evaporated particles with the gas molecules can be avoided by a long mean free path which allows the evaporated particles to straightly reach the substrate [135,136]. Thermal evaporation enables an optimal adjustment of the film thickness and the deposition rate which is monitored by a quartz crystal microbalance [137,138]. In addition, utilizing more than one evaporation source allows for convenient fabrication of mixed films or multilayer samples [139,140].

2.6 Spectroelectrochemistry

Spectroelectrochemistry is a powerful technique for probing electrochromic materials [14,141,142]. It combines electrochemical with optical analyses and allows the simultaneous study of the correlation between the redox processes and the changes in optical properties of the material of interest [141,142], while avoiding superposition of different contributions from other layers such as the ionic storage layer (Figure 2.1). A classical three-electrode setup combined with a UV-Vis spectrometer for performing spectroelectrochemical measurements is shown in Figure 2.4. The three-electrode setup consists of an electrochromic material as the working electrode, a platinum (Pt) electrode as the counter electrode and a silver/silver chloride (Ag/AgCl) electrode as the reference electrode in contact to an electrolyte while the UV-Vis spectrometer is equipped with a light source and a detector [14,141]. Typically, nitrogen (N_2) gas is flushed through the electrolyte for removing the dissolved oxygen from the solution before the measurement and afterwards, the N_2 tube is lifted and N_2 flows over the solution to keep out air [124,143].
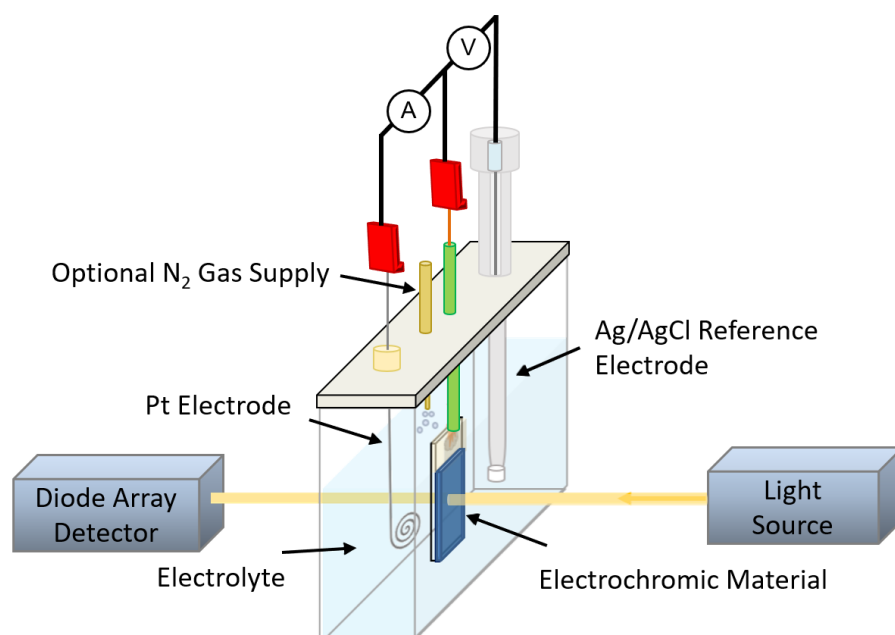

Figure 2.4: Setup for performing spectroelectrochemical measurements.

2.6.1 UV-Vis Spectroscopy

UV-Vis (ultraviolet-visible) spectroscopy is a suitable method to analyze the absorption of light at different wavelength by a material of interest due to excitation of an electron [144,145] from the valence band into the conduction band or from the HOMO into the LUMO, for inorganic or organic materials, respectively [145,146]. The sample is irradiated by light sources covering the UV and Vis range [144,145]. For UV radiation a deuterium lamp can be used as the light source whereas a halogen lamp can be utilized to generate Vis radiation [144,145]. Since the comparison of the transmittance and the reflectance of amorphous WO_3 thin films in the bleached and colored states revealed values of less than around 10 % for the reflectance in the Vis range [147,148] and the analysis of the transmittance, absorbance and reflectance of a CuPc thin film showed values of reflectance smaller than 0.3 % [149], the contributions of reflection and scattering are neglected for the present analysis. Therefore, the light intensity I at each wavelength after passing through the sample, which is recorded by, e.g. a diode array detector, can be expressed by the Lambert-Beer law (Equation 2.5) with the initial intensity of the incident light I_0, the wavelength-dependent absorption coefficient $\alpha(\lambda)$ and the thickness of the sample d [144,145,150]. The absorbance A_λ or the logarithm of the reciprocal of the transmittance T_λ can be obtained from the logarithm of I_0 divided by I (Equation 2.6) [144,145]. The values of A_λ or T_λ of the material is depicted in dependence of the wavelength in an absorption or transmittance spectrum [144–146].

$$I = I_0 \cdot \mathrm{e}^{-\alpha(\lambda)d} \tag{2.5}$$

$$A_\lambda = \log\left(\frac{1}{T_\lambda}\right) = \log\left(\frac{I_0}{I}\right) \tag{2.6}$$

UV-Vis spectroscopy can give insights into many aspects such as the coloration of materials and their electronic structures [144–146].

2.6.2 Cyclic Voltammetry

Cyclic voltammetry (CV) is one of the most widely practiced electrochemical techniques to analyze the electrochemical reduction and oxidation processes occurring at an electrode, namely the working electrode in contact with an electrolyte [14,141,143].

In order to close the electrical circuit a counter electrode is placed into the electrolyte [141,143]. Typically, an inert material such as platinum is chosen as the counter electrode to transfer charge, while avoiding interference with the electrochemical reaction [141,143]. In a three-electrode configuration, a reference electrode with a known electrode potential such as the widely used Ag/AgCl electrode serves to measure and control the applied potential of the working electrode [141,143]. The current flow should occur mainly between the working and the counter electrode and not through the reference electrode to ensure an unchanged potential of the reference electrode [14,141,143]. A potentiostat is used for measuring the current flow between the working and the counter electrode and controlling the potential difference between the working and the reference electrode [14,141,143]. The potential of the working electrode is swept with a constant scan rate v from potential E_1 to potential E_2 [141,143]. Afterwards, the potential sweep occurs in the reverse scan direction [141,143]. During the potential sweep, the cathodic and anodic current are measured resulting in a current-voltage curve, the cyclic voltammogram (Figure 2.5) [14,141,143].
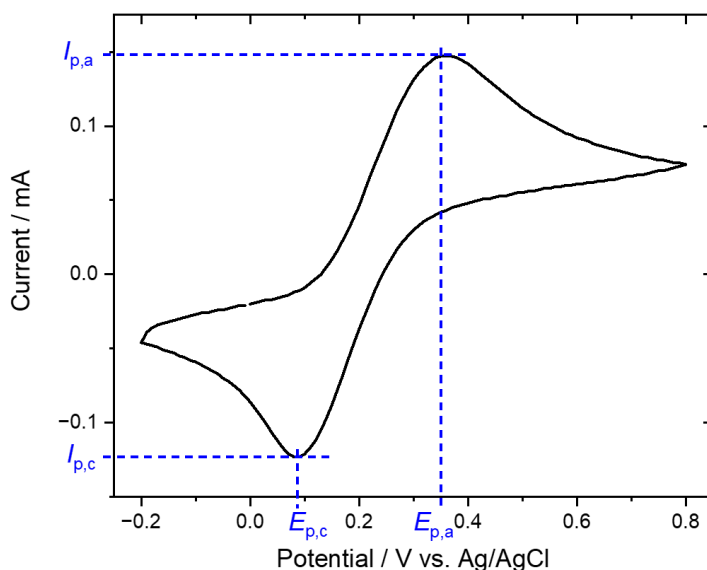

Figure 2.5: Cyclic voltammogram of ferrocene in propylene carbonate with the cathodic and anodic peak currents, $I_{p,c}$ and $I_{p,a}$, and the corresponding peak potentials $E_{p,c}$ and $E_{p,a}$.

The mass transport of the electroactive species is controlled by migration, convection and/or diffusion [141,143]. Migration describes the movement of the ions in the presence of an applied electric field [141,143]. A sufficiently high concentration of electroactive species in the electrolyte is needed and an excess of non-electroactive ions may be added into the solution to decrease its resistance and to minimize the contribution of migration

to the mass transport of the electroactive species [141,143]. Convection can be suppressed by avoiding mechanical perturbation of the electrolyte [141,143]. A concentration gradient of the electroactive species near the electrode caused by electrochemical reactions results in diffusion of the reactants/products to/from the electrode as the dominant contribution to mass transport [141,143]. Hence, the shape of the cyclic voltammogram is influenced by the diffusion of electroactive species at the electrode [141,143]. In the presence of electrochemical processes, characteristic peaks are observed in the cyclic voltammogram [141,143]. Scanning the potential from E_1 to E_2 results in a current and, thereby, in depletion of the reactants near the electrode [141,143]. The continuous expansion of the diffusion layer at the electrode surface containing the products slows down the diffusion of reactants from the bulk of the electrolyte to the electrode resulting in decrease of the current [141,143]. By scanning the potential from E_2 to E_1, these processes are reversed leading to the respective shape of the reversal current [141,143]. As exemplary depicted in Figure 2.5, the cathodic and anodic peak currents, $I_{p,c}$ and $I_{p,a}$, and the corresponding peak potentials, $E_{p,c}$ and $E_{p,a}$, are assigned to the reduction and oxidation processes, respectively [141,143].

Different transport processes governing the redox reaction exist that can be resolved by the dependence of the peak currents on the scan rate [141,151–153]. For reversible electrochemical processes involving fast electron transfer, the peak current under diffusion control is proportional to the square root of the scan rate (I_p vs. $v^{1/2}$), as described by the Randles-Ševčík equation with the active surface area A of the electrode, the concentration c of the electroactive species in the bulk of the electrolyte, the number of electrons n transferred in the electrochemical reaction and the diffusion coefficient D of the electroactive species (Equation 2.7) [141,143].

$$I_p = 2.69 \cdot 10^5 \cdot n^{3/2} A D^{1/2} c v^{1/2} \tag{2.7}$$

A peak-to-peak separation of $\Delta E_p = 59/n$ mV and half of the peak width at half maximum of $|E_p - E_{p/2}| = 57/n$ mV at room temperature are expected for diffusion-controlled reversible redox reactions with fast electron transfer [141,143]. For reversible redox processes without transport limitation, a linear dependence of $I_p \sim v$ is typically observed, as in the case of an ideal adsorbed monolayer [141]. A dependency of $I_p \sim v^{0.6}$ is characteristic for redox reactions showing limitation by electron hopping between the redox centers [151–153].

In order to limit the thickness of a diffusion layer in an electrolyte, a rotating disk electrode can be used providing a steady-state mass transport and a controlled convection [141,154]. The electrode is mounted on a vertical shaft of a motor and the rotation speed can be adjusted allowing the electrode to rotate with a constant angular velocity ω [141,155]. As a consequence, a continuous flow of electroactive species from the bulk of the electrolyte to the electrode is established in case of diffusion-limited currents [141,154,155]. The thickness of the diffusion layer decreases with faster angular velocity [141,154,155]. The limiting current I_L at a given potential in the diffusion-limited regime measured at different rotation speeds is proportional to the square root of the angular velocity $\omega^{1/2}$ as expressed by the Levich equation where F represents the Faraday constant, v_k is the kinematic viscosity of the electrolyte and ω is given in rad s^{-1} (Equation 2.8) [141,154,155].

$$I_L = 0.62 \cdot nFAcD^{2/3}v_k^{-1/6}\omega^{1/2} \tag{2.8}$$

Electrochemical reactions which are not only limited by diffusion but also exhibit kinetic limitations can be described with the Koutecký-Levich equation (Equation 2.9) with the measured current I_m, the kinetically-limited current I_k and the diffusion-limited current I_L [141]. For a thin film deposited on an electrode, I_L corresponds to the diffusion of the electroactive species in the bulk electrolyte and I_k can refer to the diffusion in the thin film [141,156].

$$\frac{1}{I_m} = \frac{1}{I_k} + \frac{1}{I_L} = \frac{1}{I_k} + \frac{1}{0.62 \cdot nFAcD^{2/3}v_k^{-1/6}\omega^{1/2}} \tag{2.9}$$

For electrochromic thin films as working electrodes which are in contact with an electrolyte consisting of small ions, cyclic voltammetry combined with UV-Vis spectroscopy can be of help to clarify the redox mechanism of the electrochromic films and to determine appropriate potentials for electrochromic switching between the reduced and oxidized states along with a high R_{EC} [14,15].

2.6.3   Chronoamperometry

Chronoamperometry is a powerful technique for investigating the kinetics of electrochemical processes [141]. Similarly, as described in chapter 2.6.2, a three-electrode configuration can be used for the chronoamperometric analysis [141]. A defined potential is applied for a given time to the working electrode which is in contact with a solution containing electroactive species to enable the reduction or oxidation process of these species [141]. Initially, the concentration of the electroactive species is typically set for a sufficiently high level, thus, a large current is measured [141]. During the analysis, depletion of the electroactive species near the electrode surface leads to a decay of the current [141]. Using double potential step chronoamperometry, the reduction as well as the oxidation process can be analyzed by applying two different potentials, one sufficiently negative and the other one sufficiently positive of the redox potential [141]. A dependence of the current I_c on the inverse square root of time $t^{-1/2}$ is characteristic for diffusion-controlled processes and can be described by the Cottrell equation (Equation 2.10) [141].

$$I_c = nFcAD^{1/2}\pi^{-1/2}t^{-1/2} \tag{2.10}$$

To investigate the electron and ion transport in an electrochromic thin film as working electrode, the application of an appropriate potential allows for reduction or oxidation of the electrochromic material along with intercalation or deintercalation of charge-balancing ions [14,15]. Electrochemical measurements mimic the switching processes of the electrochromic films in smart windows which can provide, in combination with *in situ* UV-Vis spectroscopy, insights into the long-term stability and response times of the studied thin films [14,15]. For electrochromic materials which conduct both electrons and ions, the Randles-Ševčík equation and the Cottrell equation (Equations 2.7 and 2.10), allow the determination of an effective diffusion coefficient that corresponds to the combined transport of electrons and ions in the films [157–159].

2.6.4   Electrochemical Impedance Spectroscopy

A widely used electrochemical technique for investigating different processes in an electrochemical system is the electrochemical impedance spectroscopy (EIS) [141]. During EIS analysis, an alternating voltage $U(\omega_f)$ of low magnitude is superimposed to

the electrode potential of interest applied to the system while the frequency ω_f of the alternating voltage is typically varied over a wide range from MHz to mHz [141]. The alternating current response $I(\omega_f)$ may be shifted from the signal of $U(\omega_f)$ by the phase angle Φ [141]. The ratio of $U(\omega_f)$ and $I(\omega_f)$ is equal to the frequency-dependent impedance $Z(\omega_f)$ as a complex number (Equation 2.11) [141]. Thus, $Z(\omega_f)$ can be described as the sum of a real part Z' and an imaginary part Z'' (Equation 2.11) [141].

$$Z(\omega_f) = \frac{U(\omega_f)}{I(\omega_f)} = |Z|e^{i\Phi} = Z' + iZ'' \tag{2.11}$$

Often, the measured data are presented in a Nyquist plot in which Z'' is plotted against Z' for different values of the frequency corresponding to the time scales of the occurring processes in the system [141]. By using a suitable equivalent circuit for the description of the studied electrochemical system, the measured data points can be fitted to elucidate diffusion-controlled processes in the electrodes and the electrolyte as well as charge transfer processes at the interface of the electrodes [141].

A typical Nyquist plot of an electrochromic film, in particular, WO_3 deposited on an electron conductive layer and in contact with an electrolyte [30,160] is illustrated in Figure 2.6 (a). This plot can be fitted with an equivalent circuit (Figure 2.6 (b)) which is also called the Randles equivalent circuit [30,160].
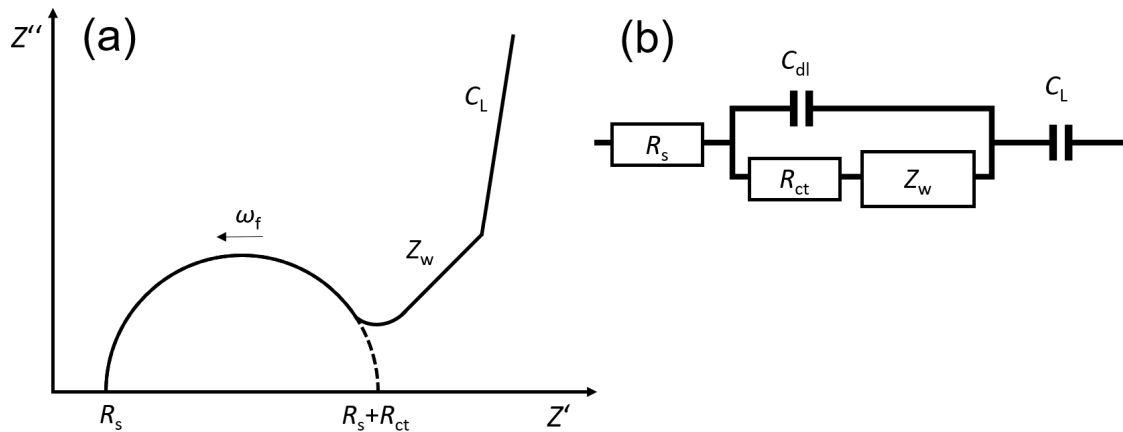

Figure 2.6: (a) Typical Nyquist plot of a thin film of WO_3 and (b) the Randles equivalent circuit. Adapted from [30,160].

R_s describes the series resistance caused by the electrolyte and the substrate [30,161–164]. The charge transfer process through the interface of the electrochromic film and the electrolyte can be described with a charge transfer resistance R_{ct} [30,160,162–165]. The capacitance C_{dl} is assigned to the electrochemical double layer which consists of ions on the electrolyte side and electrons at the electrode surface [30,141,160,162,163]. The capacitance is replaced by a constant phase element (CPE) [161,164,165] in the case of deviations from the ideal capacitor caused by, e.g. electrodes with a rough surface [166,167]. The impedance Z_{CPE} of the constant phase element is defined by the Equation 2.12 where Q is the CPE parameter and α corresponds to the CPE exponent [166,167]. When $\alpha = 1$, CPE is equivalent to a capacitor [166,167].

$$Z_{CPE} = \frac{1}{Q(i\omega_f)^\alpha} \tag{2.12}$$

The addition of an element for the diffusion impedance Z_w also known as Warburg impedance into the equivalent circuit (Figure 2.6 (b)) allows for describing diffusion-controlled processes in the system [141]. Z_w mainly contributes to the measured data at low frequencies, hence, a linear behavior of Z'' and Z' with a slope of 45° is typically observed in this frequency range (Figure 2.6 (a)) indicating the semi-infinite diffusion of intercalating ions into the electrochromic film [30,160,162,165]. For even lower frequencies, the data can be fitted with a limiting capacitance C_L (Figure 2.6 (a)) that considers the finite length of the electrochromic film and represents a diffusion that is limited by accumulation of charges in the film [30,160,161,168]. At higher frequencies, R_{ct} and C_{dl} become more important [141]. The diameter of the semicircle corresponds to R_{ct} and the shift of the semicircle at the Z' axis is assigned to R_s as shown in Figure 2.6 (a) [30,160]. The diffusion coefficient D_I of the intercalating ions can be determined from the Warburg coefficient A_w following the Equation 2.13 with the molar gas constant R_m and the temperature T [141,169].

$$D_I = \frac{R_m^2 T^2}{2A^2 n^4 F^4 c^2 A_w^2} \tag{2.13}$$

3 Spectroelectrochemical Performance of Different Porous WO$_3$ Films (Publication 1)

Background for Publication 1

Amorphous tungsten oxide films are preferred over crystalline ones as they enable a facile transport of ions through the film network leading to improvement of the electrochromic properties [41,147,170]. Thin films of amorphous WO$_3$ showing enhanced electrochromic properties could be fabricated by Zhao et al. [41] from a precursor solution based on peroxotungstic acid via spin-coating followed by heat treatment. Another important factor that influences the electrochromic performance is the porosity of the thin films [34,44]. Porous WO$_3$ thin films exhibit a high internal surface area that provides an increased contact interface with the electrolyte and a high amount of accessible reaction sites allowing for a fast diffusion of ions due to short transport distances within the films [34,44]. In many different studies [42,171–174], poly(ethylene glycol) (PEG) of different molecular weight served as structure-directing agent for the preparation of WO$_3$ thin films by solution-based processing. The addition of PEG resulted in higher accessibility leading to improved electrochromic performance of the WO$_3$ thin films compared to the films prepared without PEG [42,171–174]. Block copolymers such as Pluronic P123 [175] or polystyrene-*block*-poly(ethylene oxide) (PS-*b*-PEO) [176] creating micelles in the precursor solution have been proven to be excellent candidates for the fabrication of mesoporous thin films. Nevertheless, in several studies [177,178] regarding films with spherical mesopores the presence of widely isolated pores instead of interconnected pores led to attenuation of the diffusion of ions through the film. For this reason, the usage of block copolymers in combination with long-chained additives offered chances to obtain thin films consisting of mesopores which are interconnected by micropores. This approach was confirmed to be successful for the fabrication of titanium oxide (TiO$_2$) thin films with mesopores connected by worm-like pores by using polyisobutylene-*block*-poly(ethylene oxide) (PIB$_{50}$-*b*-PEO$_{45}$) as block copolymer and 1-hexadecyl-3-methylimidazolium chloride (C$_{16}$mimCl) as surfactant-like ionic liquid [178]. Using such strategy proved very useful also for the preparation of WO$_3$ as shown in Publication 1.

Context of Publication 1

Publication 1 focused on the study of the direct correlation between the internal film structure, porosity and electrochromic performance of thin films of WO$_3$.

Based on previous studies [41,42,174] first experiments to modify the porosity and structure of WO$_3$ thin films were performed in cooperation with Sophie Göbel and Lukas Gümbel by using PEG 400 and PEG 600 as structure-directing agents in the peroxotungstic acid precursor solution in different volume ratios. The addition of PEG in a volume ratio of 1.5:10 into the precursor solution led to thin films (WO$_{3|}\mu$p400 and WO$_{3|}\mu$p600) consisting of interconnected micropores that provided pathways allowing a high R_{EC} of the electrochromic switching with fast intercalation and deintercalation of the ions compared to compact and amorphous WO$_3$ thin films (WO$_{3|}$comp) obtained without additives. In collaboration with Marius Eckert, time-of-flight secondary ion mass spectrometry (ToF-SIMS) analysis was performed to provide insight into the distribution of the intercalated Li$^+$ ions within the films. While an accumulation of Li$^+$ ions was observed at the surface of the WO$_{3|}$comp thin films, no Li$^+$ accumulation was detected for the films of WO$_{3|}\mu$p400 and WO$_{3|}\mu$p600 confirming the facile intercalation of ions throughout the films containing interconnected micropores. The amorphous nature of the WO$_3$ thin films annealed up to 300 °C and the crystallinity of the films after heat treatment at temperatures higher than 400 °C were confirmed by grazing incidence X-ray diffraction (GIXRD). As expected, the spectroelectrochemical results showed that in any case amorphous WO$_3$ thin films led to better electrochromic characteristics than the crystalline films [41,147,170].

Since the presence of PEG in the peroxotungstic acid precursor solution led to WO$_3$ thin films with improved electrochromic performance, the question arose if thin films of WO$_3$ containing spherical mesopores could also provide enhanced electrochromic properties. Therefore, in cooperation with Pascal Cop, the block copolymer PIB$_{50}$-b-PEO$_{45}$, which had already been used to successfully prepare mesoporous titanium oxide [178,179], was added into the precursor solution as structure-directing agent. The amount of polymer was adapted from [179] to obtain a homogeneous distribution of mesopores within the films after heat treatment at 300 °C for 12 h. The analysis of the films by scanning electron microscopy (SEM) revealed the formation of mesoporous WO$_3$ films (WO$_{3|}$mp). However, these films showed a slightly brownish color indicative of some polymer still remaining within the films. The incomplete decomposition of PIB$_{50}$-b-PEO$_{45}$ was confirmed by thermogravimetry (TG) analysis of the corresponding precursor.

Mainly isolated spherical pores were observed for the films of WO$_3$|mp from the SEM cross-section analysis. The WO$_3$|mp films with isolated spherical mesopores and residual polymer fragments resulted in trapping of ions leading to electrochromic properties only similar to those obtained for the WO$_3$|comp thin films.

The presence of interconnected pores is crucial for a high accessibility of the films. Therefore, in cooperation with Florian Eberheim and Pascal Cop, PIB$_{50}$-*b*-PEO$_{45}$ and PEG 600 were used as additives in different ratios in the peroxotungstic acid precursor solution to achieve WO$_3$ thin films (WO$_3$|µmp) consisting of both, mesopores and interconnected micropores. Optimized electrochromic characteristics could be obtained for such thin films. Almost complete decomposition of the polymers was confirmed by TG analysis showing a high loss of mass of the precursor. Subsequent experiments performed in collaboration with Sophie Göbel showed that the addition of smaller amounts of PEG 600 resulted in WO$_3$ thin films which were similar to those prepared with a higher amount of PEG 600. SEM analysis of the WO$_3$|µmp films revealed the presence of interconnected mesopores, as desired. Furthermore, the specific surface area obtained from Kr physisorption analysis was found significantly higher for WO$_3$|µmp than for WO$_3$|µp600 or WO$_3$|mp. From the density of the films which was obtained via microwave plasma atomic emission spectroscopy (MP-AES) of the films dissolved in NH$_3$ solution, the porosity could be determined. The highest porosity was found for WO$_3$|µmp, followed by WO$_3$|mp, WO$_3$|µp600 and WO$_3$|µp400. A similar trend was revealed by ellipsometry analysis.

The high specific surface area and porosity of the WO$_3$|µmp films are well in line with the optimized electrochromic switching characteristics of these films including large transmittance modulations, high coloration efficiencies, and high effective diffusion coefficients. For the bleaching and the coloration processes of the WO$_3$|µmp thin films very short response times of around 2 s were determined. These values are further improved against those obtained for the thin films of WO$_3$|µp400 and WO$_3$|µp600 confirming the presence of facilitated pathways in the WO$_3$|µmp films with interconnected mesopores.

For all films, energy-dispersive X-ray spectroscopy (EDX) and X-ray photoelectron spectroscopy (XPS) showed the successful formation of WO$_3$. XPS carried out on the films after intercalation of Li$^+$ ions showed a significant increase in the concentration of W^{5+} assigned to the reduced states of WO$_3$ [180,181].

In cooperation with Florian Eberheim, thicker WO$_3$ films could be obtained that reached a nearly as deep blue coloration as a commercial WO$_3$ film (commWO$_3$) of similar thickness from EControl-Glas GmbH & Co. KG. The spectroelectrochemical analyses of such WO$_3$ films confirmed that the presence of a porous and accessible film structure led to improved electrochromic characteristics.

3.1 Publication 1: Enhancing the Spectroelectrochemical Performance of WO$_3$ Films by Use of Structure-Directing Agents during Film Growth

The experiments of this paper were mainly planned by me with some suggestions from the cooperation partners (Pascal Cop and Bernd M. Smarsly from the Institute of Physical Chemistry at the Justus-Liebig-University in Gießen). Florian Eberheim, Sophie Göbel, Marius Eckert, Tim P. Schneider and Lukas Gümbel assisted me with the preparation of the precursor solutions, the fabrication of the thin films and the spectroelectrochemical measurements under my supervision. Furthermore, Florian Eberheim assisted me with the Raman spectroscopy measurements and the preparation of the samples for TG and ellipsometry analyses. Marius Eckert helped me with the ToF-SIMS analysis. Sophie Göbel assisted me with the preparation of samples for Kr physisorption and MP-AES measurements. The profilometry measurements were carried out by Florian Eberheim, Sophie Göbel, Tim P. Schneider and me. Pascal Cop helped me with the *in situ* GIXRD measurement. Additional GIXRD measurements and all SEM and EDX analyses were performed by me at the Institute of Physical Chemistry at the Justus-Liebig-University in Gießen. The EIS measurements were carried out by me. Thin films for the XPS analyses were prepared by me and the interpretation of the data were carried out by me. Derck Schlettwein planned and supervised the project work. The draft of the manuscript was written by me, fine-tuned with Derck Schlettwein and discussed with all co-authors.

Article

Enhancing the Spectroelectrochemical Performance of WO$_3$ Films by Use of Structure-Directing Agents during Film Growth

Thi Hai Quyen Nguyen [1,2], Florian Eberheim [1,2], Sophie Göbel [1,2], Pascal Cop [2,3], Marius Eckert [1,2], Tim P. Schneider [1,2], Lukas Gümbel [1,2], Bernd M. Smarsly [2,3] and Derck Schlettwein [1,2,*]

[1] Institute of Applied Physics, Justus-Liebig-University Giessen, Heinrich-Buff-Ring 16, 35392 Giessen, Germany; thi.h.nguyen@ap.physik.uni-giessen.de (T.H.Q.N.); florian.eberheim@gmail.com (F.E.); sophie.goebel@materialwiss.uni-giessen.de (S.G.); marius.eckert@chemie.uni-giessen.de (M.E.); tim.p.schneider@physik.uni-giessen.de (T.P.S.); lukas.guembel@materialwiss.uni-giessen.de (L.G.)

[2] Center for Materials Research (ZfM), Justus-Liebig-University Giessen, Heinrich-Buff-Ring 16, 35392 Giessen, Germany; pascal.cop@gmx.de (P.C.); bernd.smarsly@phys.chemie.uni-giessen.de (B.M.S.)

[3] Institute of Physical Chemistry, Justus-Liebig-University Giessen, Heinrich-Buff-Ring 17, 35392 Giessen, Germany

[*] Correspondence: schlettwein@uni-giessen.de

Abstract: Thin, porous films of WO$_3$ were fabricated by solution-based synthesis via spin-coating using polyethylene glycol (PEG), a block copolymer (PIB$_{50}$-*b*-PEO$_{45}$), or a combination of PEG and PIB$_{50}$-*b*-PEO$_{45}$ as structure-directing agents. The influence of the polymers on the composition and porosity of WO$_3$ was investigated by microwave plasma atomic emission spectroscopy, energy-dispersive X-ray spectroscopy, scanning electron microscopy, X-ray diffraction, and gas sorption analysis. The electrochromic performance of the WO$_3$ thin films was characterized with LiClO$_4$ in propylene carbonate as electrolyte. To analyze the intercalation of the Li$^+$ ions, time-of-flight secondary ion mass spectrometry, and X-ray photoelectron spectroscopy were performed on films in a pristine or reduced state. The use of PEG led to networks of micropores allowing fast reversible electrochromic switching with a high modulation of the optical transmittance and a high coloration efficiency. The use of PIB$_{50}$-*b*-PEO$_{45}$ provided isolated spherical mesopores leading to an electrochromic performance similar to compact WO$_3$, only. Optimum characteristics were obtained in films which had been prepared in the presence of both, PEG and PIB$_{50}$-*b*-PEO$_{45}$, since WO$_3$ films with mesopores were obtained that were interconnected by a microporous network and showed a clear progress in electrochromic switching beyond compact or microporous WO$_3$.

Keywords: tungsten oxide; structure-directing agent; smart windows; electrochromism; porosity; spin-coating

1. Introduction

Windows are an essential component in almost every building. Switchable glass, also known as a smart window, provides tunable shading that can improve the indoor occupant comfort and reduce the energy consumption caused by heating and cooling of a building [1,2]. For smart windows, electrochromic materials are of high interest [3,4]. Along with an electrolyte containing small ions, electrochromic thin films can offer a reversible coloration under an applied voltage [1,5]. Tungsten oxide (WO$_3$) is a widely used electrochromic material [6,7] that can change color from colorless transparent to dark blue with good switching characteristics upon reduction and intercalation of small charge-balancing countercations such as H$^+$, Li$^+$, Na$^+$, or K$^+$ ions [7].

Thin films of WO$_3$ can be fabricated by various deposition techniques [8] such as sputtering [9,10], thermal vapor deposition [11,12], or sol–gel processing [13,14] from precursor solutions by spin-coating [14], dip-coating [15] or electrodeposition [16] which

provide good options of device production at low cost and low environmental footprint [8]. Precursor solutions based on tungsten hexachloride [17,18], peroxotungstic acid [14,19], sodium tungstate [16,20] or ammonium metatungstate [21] have been used successfully for the preparation of tungsten oxide thin films. Further, the internal structure of WO$_3$ can be tuned in a wide range using such solution-based approach [22,23].

The electrochromic properties of tungsten oxide and, in particular, the charge transport in the films are highly influenced by the structure (amorphous vs. crystalline) and the porosity of the films [2,15]. Compact WO$_3$ thin films with improved electrochromic characteristics could be obtained from a precursor solution containing peroxotungstic acid upon annealing of the samples at 250 °C, and it was observed that amorphous WO$_3$ thin films showed a larger change in coloration between the colored and bleached state, a faster diffusion of ions and a higher coloration efficiency compared to crystalline films [14].

The addition of polymers or surfactants as structure-directing agents into the precursor solution allows a facile modification of the porosity and atomic arrangement (amorphous vs. crystalline) of the WO$_3$ films [22,23]. Polyethylene glycol (PEG) of different molecular weight has been largely used in sol–gel processes to inhibit crystallization of WO$_3$ [22,24]. Djaoued et al. [25] and Cremonesi et al. [26] added PEG 600 to a tungsten hexachloride-based precursor solution and prepared WO$_3$ thin films by dip-coating followed by heat treatment at different temperatures. The films prepared in the presence of PEG 600 and annealed at 300 °C showed a higher coloration efficiency compared to the films prepared without PEG 600 [25,26]. Lu et al. [27] used PEG 400 as additive in a peroxotungstic acid-based precursor solution in a volume ratio of 1:10. Thin films were obtained by dip-coating and annealing at 300 °C. These films exhibited better electrochromic characteristics than the films prepared without polymers [27]. Hence, the addition of PEG 400 or PEG 600 consistently provided WO$_3$ films with a high active surface area leading to good electrochromic properties [25–27]. The proper amount of polymer in the precursor solution is crucial for adjusting the structure and porosity of the films [22]. WO$_3$ thin films which were electrodeposited by Deepa et al. [28] showed that the amount of PEG 400 in the peroxotungstic acid deposition solution significantly influenced the morphology of the films and, thus, their electrochromic characteristics. WO$_3$ thin films with improved electrochromic properties could also be obtained by addition of polyethylene glycol of a higher molecular weight such as PEG 2000 [29] or PEG 20,000 [30] with different precursor solutions. The improvement in electrochromic parameters such as the coloration efficiency by nanoscaled porosity is supposed to be attributable to enhanced diffusion of Li$^+$, which is a relevant issue in regard to the desired fast switching times [2]. Hence, further previous studies addressed the impact of different nanoscaled porosity on the electrochromic performance. Block copolymers such as polystyrene-*block*-polyethylene oxide (PS-*b*-PEO) [31] or Pluronic P123 [32] that are forming micelles allow the formation of mesoporous films with 4–30 nm large pores providing enhanced electrochromic characteristics such as short switching time, high coloration efficiency and large transmittance modulation [31,32]. Note that in diverse previous studies films with spherical mesopores were investigated which inherently suffer from restricted connection between the spherical pores, impeding Li$^+$ diffusion [33,34]. In view of such experience, a combination of block copolymers and long-chained additives might be promising to prepare WO$_3$ films with both, spherical mesopores as well as interconnected micropores. Such strategy already was successful in the preparation of titanium oxide thin films using polyisobutylene-*block*-polyethylene oxide (PIB$_{50}$-*b*-PEO$_{45}$) as block copolymer and 1-hexadecyl-3-methylimidazolium chloride (C$_{16}$mimCl) as surfactant-like ionic liquid in different ratios to tune the porosity and permeability of titanium oxide thin films by creating a film structure with mesopores (caused by PIB$_{50}$-*b*-PEO$_{45}$) connected by worm-like pores (caused by C$_{16}$mimCl) [35].

In the present work, thin films of WO$_3$ were prepared via spin-coating with similar polymers as structure-directing agents to influence the internal film structure and porosity and to improve the electrochromic switching characteristics. The precursor solution based on peroxotungstic acid showing a high stability can be easily and inexpensively

prepared by dissolution of tungsten in hydrogen peroxide with no need of anhydrous conditions [8,14,36]. It is desirable to use PEG of low molecular weight to create a network of interconnected micropores in the films since such PEG can be easily removed after annealing for a shorter time compared to PEG of high molecular weight [27,30]. Therefore, a peroxotungstic acid-based precursor solution was used with addition of PEG 400, PEG 600 (for a formation of micropores [37]) or the diblock copolymer PIB_{50}-*b*-PEO_{45} that had been successfully used for the preparation of mesoporous titanium oxide [35,38]. To obtain WO₃ thin films with interconnected mesopores, a mixture of PEG 600 and PIB_{50}-*b*-PEO_{45} was established. The structural, optical, electrochemical and spectroelectrochemical properties of the WO₃ thin films using these approaches were characterized and compared to compact films prepared without additives. The addition of PEG 400 or PEG 600 into the precursor solution created a network of interconnected micropores within the films. An enhancement of the electrochromic switching properties compared to compact WO₃ films was observed. The largest transmittance modulations, highest coloration efficiencies and fastest diffusion of ions along with highly reversible and stable switching processes could be obtained for WO₃ films prepared with PIB_{50}-*b*-PEO_{45} combined with PEG 600 as additives, leading to films with interconnected mesopores. The great potential of solution-based processing for WO₃ suitable for the application in smart windows is thereby demonstrated.

2. Experimental

2.1. Preparation of WO₃ Thin Films

Silicon (111) wafers (WACKER, Munich, Germany) or fluorine doped tin oxide (FTO) coated glass substrates (Kaivo, Zhuhai, China, <15 Ohm sq^{-1}, cut into 25 mm × 35 mm pieces) were cleaned for 15 min in RBS solution (Carl Roth, Karlsruhe, Germany), acetone (Carl Roth, Karlsruhe, Germany, ≥99.5%) and isopropanol (Carl Roth, Karlsruhe, Germany, ≥99.8%), subsequently using an ultrasonic bath at room temperature and dried with N₂ gas followed by UV-ozone treatment for 15 min. In case of the FTO-coated glass substrates, a 5 mm wide stripe was masked with a piece of adhesive tape (TESA, Norderstedt, Germany) for later electrical contacting purposes.

The precursor solution containing peroxotungstic acid (PTA) was synthesized as described in Ref. [14] from 3 g tungsten powder (Alfa Aesar, Kandel, Germany, ≥99.9%) by slowly adding 10 mL 30% hydrogen peroxide solution (Sigma Aldrich, Steinheim, Germany) into an Erlenmeyer flask. Afterwards, 3 mL glacial acetic acid (Alfa Aesar, Kandel, Germany, ≥99.7%) and 11 mL ethanol (Carl Roth, Karlsruhe, Germany, ≥99.8%) were added and the mixture was stirred for 2 h while cooling in an ice bath at 0–10 °C. The mixture was left at room temperature for 70 h and subsequently filtered three times to remove excess tungsten powder. This precursor solution was spin-coated onto the substrates at 3500 rpm for 30 s. Spin-coating was repeated three times to ensure a homogeneously coated substrate. These as-deposited WO₃|comp thin films were dried at 60 °C for about 2 h and then baked at 250 °C, if not mentioned otherwise for about 1 h (Table 1). In order to achieve interconnected micropores, polyethylene glycol (PEG 400 (Sigma Aldrich, Steinheim, Germany) or PEG 600 (Sigma Aldrich, Steinheim, Germany)) was added as structure-directing agent into the precursor solution in different volume ratio (1.0:10, 1.5:10, 3:10 and 5:10) and the WO₃|μp400 and WO₃|μp600 films were prepared following the same procedure as the WO₃|comp films. About 37 mg of polyisobutylene-*block*-polyethylene oxide (PIB_{50}-*b*-PEO_{45}) (BASF, Ludwigshafen, Germany) were added into 1 mL of the peroxotungstic acid precursor solution to obtain mesoporous WO₃|mp films with large spherical mesopores. Thin WO₃|μmp films exhibiting a combination of interconnected micropores and mesopores were prepared by adding around 75–150 μL PEG 600 and 42 mg PIB_{50}-*b*-PEO_{45} into 1 mL of the peroxotungstic acid precursor solution. Both precursor solutions containing PIB_{50}-*b*-PEO_{45} were additionally treated in the ultrasonic bath for at least 30 min. After complete dissolution of PIB_{50}-*b*-PEO_{45}, agglomerates were removed using a 0.2 μm syringe filter. After spin-coating, these as-deposited films were first dried at 60 °C for about 2 h and then annealed at 300 °C for around 12 h (Table 1). For benchmarking

of the present films, samples of a sputter-deposited 650 nm thick commWO$_3$ film from EControl-Glas GmbH & Co. KG (Plauen, Germany) were used, a type that had been used in commercially available electrochromic smart windows.

Table 1. Preparation conditions (utilized structure-directing agent, calcination temperature T and duration of calcination t) of different tungsten oxide thin films used for the spectroelectrochemical measurements.

Film Type	Polymer	$T/^\circ$C	t/h
WO$_3$ | comp	None	250 (350; 450; 550)	1
WO$_3$ | μp400	PEG 400	250	1
WO$_3$ | μp600	PEG 600	250 (350; 450; 550)	1
WO$_3$ | mp	PIB$_{50}$-b-PEO$_{45}$	300	12
WO$_3$ | μmp	PIB$_{50}$-b-PEO$_{45}$ + PEG 600	300	12

2.2. Thin Film Characterization

The surface morphology and the cross-sections were analyzed by scanning electron microscopy (SEM) in a Zeiss MERLIN (Carl Zeiss Microscopy Deutschland GmbH, Oberkochen, Germany) at an emission current of 78–100 pA and an acceleration voltage of 2–5 kV. The elemental composition of the films was examined in the Zeiss MERLIN at an emission current of 2000 pA and an acceleration voltage of 9 kV by energy-dispersive X-ray spectroscopy (EDX) using a X-Max 50 mm^2 EDX detector (Oxford Instruments, Abingdon, UK). Quantification of the elements W, O, Sn and C was carried out with the software Aztec 4.3 (Oxford Instruments, Abingdon, UK).

The crystallinity of the WO$_3$ thin films was investigated by grazing incidence X-ray diffractometry (GIXRD) using a PANanalytical X'Pert Pro MRD instrument (Malvern Panalytical B.V., Almelo, Netherlands) with Cu-Kα-radiation. In situ GIXRD was performed during step-wise heat treatment of a film from 30–700 °C to determine the crystallization temperature. The diffractograms were analyzed using the software HighScore Plus 3.0e.

The thickness d of the films was measured with an Alpha-Step profilometer from Tencor Instruments (Milpitas, CA, USA) as an average over at least 10 samples at different sites and verified by the analysis of the cross-section of the samples by SEM. Using the Alpha-Step profilometer the surface roughness was also determined. Ellipsometry of the films was measured on polished silicon wafers by means of a variable angle spectroscopic ellipsometer (VASE) from Woollam (Lincoln, NE, USA) and the data were fitted with the WVase32 software. The thickness d_E and the porosity P_E of the films was determined using the Bruggeman effective medium approximation and the compact WO$_3$ film as reference sample.

Krypton physisorption measurements were performed in an automated gas sorption station (Autosorb iQ2, Quantachrome Corporation, Boynton Beach, FL, USA) at 77 K by using a cryostat (CryoSync, Quantachrome Corporation, Boynton Beach, FL) in a relative pressure range of $p/p_0 = 0.05$–0.30 to obtain the surface areas of the films. Thin films prepared on silicon wafers were cut and filled into glass tubes with a cylindrical end. Surface areas were determined by applying the Brunauer–Emmett–Teller (BET) model supported by the software ASiQwin 4.0. The mass of tungsten in the different films m(W) was determined by microwave plasma atomic emission spectroscopy (MP-AES) with a 4210 MP-AES from Agilent Technologies (Santa Clara, CA, USA) using a nitrogen plasma. The films were dissolved in a defined volume of 5% NH$_3$ solution overnight. Sodium tungstate dissolved in NH$_3$ solution was used for calibration purposes.

The mass of tungsten oxide m(WO$_3$) in the different thin films was calculated using the content of tungsten m(W) measured by MP-AES, the molar mass of W, and that of WO$_3$. m(WO$_3$) was then used to calculate the density ρ of the films based on the volume V of the films as the product of the geometric film area A and the thickness d of the films plus a film volume existing between FTO crystallites. Material that was spin-coated onto the edges of the substrates, which would lead to higher ρ than the true value was considered in another

correction. 1 cm^2 was cut from the central part of some samples, analyzed as described and on average led to values of ρ equaling 78% of those determined after analysis of entire samples prepared in the same way. This factor of 0.78 was used to correctly determine ρ for all samples. Based on ρ, the porosity $P_{chem} = 1 - \rho\,(WO_3$ with additives$)/\rho(WO_{3\,|}$comp$)$ was calculated.

Thermogravimetry (TG) was performed using a Setsys Evolution 16/18 (Setaram, Lyon, France) on the precursor solutions with and without the addition of polymers after they were dried at 60 °C overnight. Raman spectroscopy was performed using a Renishaw InVia Raman microscope system (Renishaw plc., New Mills, UK) equipped with a helium–neon laser with a wavelength of 633 nm that was focused onto the sample using an objective with 50× magnification. With the Software Origin (OriginLab), a fast Fourier transformation (FFT) was performed to increase the resolution of the measured data.

Spectroelectrochemical analysis of the WO₃ thin films was carried out in a cell (Zahner, Kronach, Germany) with a closed environment in order to avoid the presence of oxygen during the measurements while allowing to carry out electrochemical characterization and to measure the optical properties *in operando*. The respective thin film was mounted as working electrode in the cell with a platinum wire counter electrode (Goodfellow, 99.995%) and a Ag/AgCl leak-free reference electrode (Innovative Instruments, Inc., Tampa, FL, USA) with 100 mg LiClO₄ (Sigma Aldrich, Steinheim, Germany, 99.99%) in 1 L propylene carbonate (PC) (Sigma Aldrich, Steinheim, Germany, ≥99.7%) as electrolyte (0.94 M). Cyclic voltammetry (CV) was carried out between −1.0 V and 1.0 V at different scan rates employing an IviumStat potentiostat/galvanostat (Ivium Technologies B.V., Eindhoven, Netherlands). Chronoamperometry (CA) was performed for up to 50 cycles by switching between −1.0 V and 1.0 V at a time interval of 300 s each or for 60 s at −1.0 V and 100 s at 1.0 V. To analyze the distribution of the Li⁺ ions within the films, a bias potential of −1.0 V was applied for 1 s to 300 s. The optical spectra of the films were simultaneously measured with a tec5 (Steinbach, Germany) UV/Vis spectrometer. At least two specimens of each kind were analyzed to ensure reproducibility. The amount of intercalated Li⁺ ions x was calculated from the charge density obtained from the CV and CA analysis [39].

Electrochemical impedance spectroscopy (EIS) of the films was performed at different potentials (−0.25 V, −0.50 V, −0.75 V, −1.0 V) with an AC amplitude of 10 mV and a frequency of 5 MHz to 100 mHz using a Zahner IM6 potentiostat (Kronach, Germany). The same cell as for the spectroelectrochemical analysis and a low-leak reference electrode (Innovative Instruments, Inc., Tampa, FL, USA) was chosen for these measurements. Before measuring the impedance spectra, the desired potential was applied for 15 min to reach a quasi-steady-state. Between the different impedance measurements, a potential of 1.0 V was applied for 15 min to deintercalate the ions and reoxidize the films. The evaluation of the impedance spectra was carried out with RelaxIS 3.

X-ray photoelectron spectroscopy (XPS) was performed on the films before and after intercalation of Li⁺ ions with a PHI Versaprobe II spectrometer (Physical Electronics, Inc., Chanhassen, MN, USA) using monochromatized Al-Kα (1486.6 eV) radiation allowing excitation at 45° to the surface normal. Survey spectra of the samples were measured at a pass energy of 93.5 eV. Detailed spectra of the W 4f, Li 1s, O 1s, C 1s and Cl 2p core levels were taken at a pass energy of 23.5 eV. Spectra were recorded before and after etching for 120 s, 240 s and 360 s by an Ar⁺ gun and an e⁻ gun to provide charge neutralization. The obtained spectra were fitted using the software CasaXPS (version 2.3.18, Casa Software Ltd., Teignmouth, UK). Energy calibration of the spectra was carried out using the C 1s signal at a binding energy of 284.8 eV. A Shirley background was used and all the spectra were fitted with a Gaussian/Lorentzian line shape. The depth profile of the films before and after the intercalation with Li⁺ ions was also investigated by time-of-flight secondary ion mass spectrometry (ToF-SIMS) using a ToF.SIMS 5 (IONTOF GmbH, Münster, Germany) equipped with a Bi⁺ primary ion gun (25 keV, 1.2 pA, 100 μm × 100 μm) for analysis and a Cs⁺ gun (1 keV, 120 nA, 200 μm × 200 μm) for depth profiling. All measurements were performed in the negative ion mode with a cycle time of 100 μs. Depth profiles were

acquired in spectrometry mode including a noninterlaced sputtering mode. Between two sputter frames, the analysis was carried out after a pause time of 2 s in random raster mode collecting two frames and 1 shot/pixel. Data evaluation was performed using the software SurfaceLab 7.0 (IONTOF GmbH, Münster, Germany). Aside from the Li$^-$ signals, signals of WO$_3{}^-$ and SnO$^-$ were detected with increasing sputter time to determine the position of the interface between WO$_3$ and the substrate which is defined by the drop or rise to 50% [40] of the intensity of the WO$_3{}^-$ or SnO$^-$ signals, respectively.

3. Results and Discussion

3.1. Morphology and Structure of the Films

From the cross-section of the pure tungsten oxide WO$_{3\,|\,}$comp thin films prepared from the precursor solution without additives (Figure S1c), a full coverage of the substrate by WO$_3$ with a film thickness of around 100 nm can be observed, thinner than the reported 250 nm in [14]. This could be caused by differences in the details of experimental conditions during spin-coating. The samples reveal a smooth and compact film structure with less than 2 nm RMS surface roughness (WO$_{3\,|\,}$comp) on the crystalline FTO substrate as also observed in [14]. While the addition of PEG 400 or PEG 600 in the volume ratio of 3:10 or 5:10 into the precursor solution led to inhomogeneous films, the addition of PEG in the volume ratio of up to 1.5:10 provided films of WO$_{3\,|\,}$µp400 and WO$_{3\,|\,}$µp600 with a smooth coverage of the substrate (Figures 1a and S1b) with RMS surface roughness similar to the WO$_{3\,|\,}$comp films (Figure S1a). The cross-section of these films indicates a grainy film structure and film thicknesses of about 130–150 nm (Figures 1d and S1d). Such a grainy film structure has been also observed for WO$_3$ thin films prepared via spin-coating from a peroxotungstic acid precursor solution with PEG 20,000 as structure-directing agent and annealed at 300 °C [30]. Using PIB$_{50}$-*b*-PEO$_{45}$ as structure-directing agent results in around 200–230 nm thick WO$_{3\,|\,}$mp films (Figure 1e) with isolated spherical mesopores of around 10–20 nm diameter (Figure 1b,e). These pore sizes are comparable to the ones obtained for mesoporous titanium oxide using a similar block copolymer [35,38]. Films prepared with PIB$_{50}$-*b*-PEO$_{45}$ as additive were light-brownish in color, indicating some remaining carbon within the films. The combination of PEG 600 and PIB$_{50}$-*b*-PEO$_{45}$ as structure-directing agents led to 230–250 nm thick WO$_{3\,|\,}$µmp films with interconnected mesopores (Figure 1c,f).
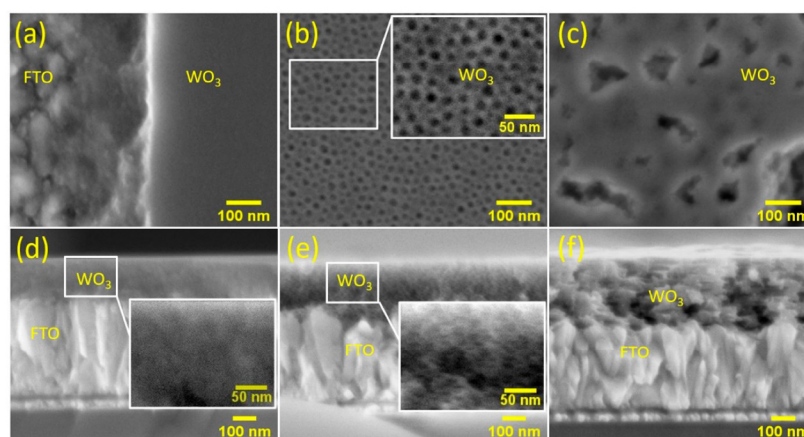
Figure 1. Top view (**a**–**c**) and cross-section (**d**–**f**) of the WO$_{3\,|\,}$µp600 (**a**,**d**), WO$_{3\,|\,}$mp (**b**,**e**), and WO$_{3\,|\,}$µmp (**c**,**f**) thin films on FTO. The left part of the film in (**a**) was scratched off to provide a comparison to the bare substrate.

The amorphous character of the films which were annealed at temperatures $T \leq 300$ °C is revealed by GIXRD at room temperature (30 °C) as depicted in Figure 2 for a WO$_3$|µp600 film. No reflexes between 20–60° are observable which would be characteristic of crystalline WO$_3$. All other reflexes correspond to FTO as confirmed by a GIXRD measurement of a bare FTO glass substrate. Annealing the film during the GIXRD analysis showed the transition of an amorphous film into a crystalline film. At 400 °C, reflexes assigned to triclinic WO$_3$ (JCPDS card 83-0947) start to appear and become more obvious from 450 °C on. For WO$_3$|comp as well as for the WO$_3$|µp400, WO$_3$|mp and WO$_3$|µmp films, similar series were obtained, indicating the presence of triclinic WO$_3$ only after annealing the samples at 450 °C (Figure S2). The crystallite size of the films annealed at 450 °C was estimated from the reflexes at 2Θ around 23° and 42° using the Scherrer equation [41–43]. An average crystallite size of around 21 nm was obtained which is well in line with the crystallite size reported in [44] for WO$_3$ films prepared by dip-coating and annealed at 500 °C. Zhao et al. [14] and Wu et al. [30] have also obtained triclinic WO$_3$ from peroxotungstic acid solutions. At 600 °C and 650 °C, the relative intensity of the substrate signals increased, presumably caused by thermal expansion of the sample leading to a higher contribution from the substrate. At 700 °C, the glass of the substrate started to melt leading to a decrease of the intensity of all reflexes.
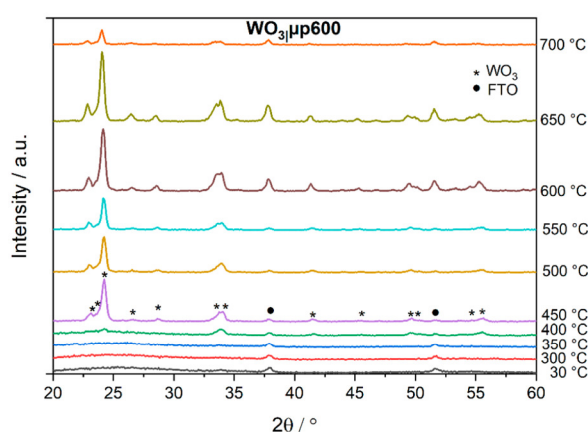

Figure 2. In situ GIXRD patterns of a WO$_3$|µp600 film that was annealed up to 700 °C with reflexes assigned to triclinic WO$_3$ (JCPDS: 83-0947) and FTO marked with asterisks and dots, respectively.

The amorphous character of the WO$_3$ thin films annealed at temperatures $T \leq 300$ °C was confirmed by Raman spectroscopy. In the Raman spectra (Figure S3) measured for the films prepared without and with PEG at $T \leq 300$ °C a broad peak at 770 cm^{-1} was observed caused by vibrations of W^{6+}-O bonds [12,45] while a relatively sharp peak at 950 cm^{-1} reflects the stretching of W^{6+}=O bonds characteristic for amorphous WO$_3$ [12,45,46]. For the WO$_3$|µp600 thin film, another broad peak at 220 cm^{-1} was noticed which might correspond to the bridging of O-W^{4+}-O bonds and indicates the presence of W^{4+} ions and oxygen vacancies within the films [12,45].

Thermogravimetry (TG) of the dried precursor, resembling films following spin-coating, was performed to monitor the decomposition of the polymers during heat treatment and to detect possible phase transformations of WO$_3$. In Figure 3a, the TG curves for the dried peroxotungstic acid precursor solutions with and without PEG are shown. Starting from room temperature up to a temperature of 100 °C, a small loss in mass of around 1% followed by a larger loss from 100 °C to 200 °C was observed caused by the desorption of water and organic solvents as well as the transformation of peroxotungstic acid to WO$_3$ [14,27,29]. For the precursors with PEG, mainly its decomposition contributed to this mass loss [27]. As expected, the drop in mass from room temperature to 250 °C is

larger for the precursor containing PEG 600 since a larger amount of polymer is present. Within the three hours of treatment at 250 °C, the mass of the precursor without additives decayed by 2% whereas the precursors containing PEG 400 or PEG 600 reduced their mass by only 1% or 0.4%. All three precursors quickly stabilized indicating that keeping them for about 1 h at 250 °C is sufficient for the preparation of amorphous WO₃ thin films. The subsequent small loss of mass (2%) upon further heating to 700 °C can be assigned to the phase transition of amorphous to crystalline WO₃ [14,27,29], which was independently proven by XRD (Figures 2 and S2). The TG curves for the precursors containing the block copolymer PIB₅₀-*b*-PEO₄₅ or PIB₅₀-*b*-PEO₄₅ in combination with PEG 600 (Figure 3b) follow the same trend upon heating to 300 °C. At this temperature, however, a mass loss of about 3% was observed over 12 h, indicating continued decomposition of the polymer. Upon subsequent heating to 800 °C, a significant mass loss of another 3% (WO₃|mp) or 7% (WO₃|μmp) was observed consisting of both, crystallization of WO₃ [27] and completion of polymer decomposition in the case of WO₃|μmp. For WO₃|mp, however, the mass loss of the precursor is similar to the one of the precursor without any additives confirming that residuals of the polymer were still present in the films. Since amorphous WO₃ thin films were aimed at, a temperature not higher than 300 °C (Figures 2 and S2) had to be chosen for the heat treatment of the films and it cannot be excluded that the WO₃|mp thin films might still contain some polymer fragments. Comparing the initial loss of mass for the different precursors reveal that the precursor without any additives and the one containing PIB₅₀-*b*-PEO₄₅ have lost about the same amount of mass (15–18%) up to a temperature of 250 °C while the precursors with PEG 600 have lost more than half of their original mass. The reason for the similar decrease in mass for the pure precursor and the one with PIB₅₀-*b*-PEO₄₅ can be explained by the small polymer content and its only partial decomposition. While for the precursors with PIB₅₀-*b*-PEO₄₅, around 37 mg of PIB₅₀-*b*-PEO₄₅ was added in 1 mL precursor solution, the precursor solution with PEG 600 in a volume ratio of 1.5:10 contained 165.5 mg PEG 600 in 1 mL precursor solution. The observed larger initial loss of mass is explained by almost complete decomposition of PEG at 250 °C.
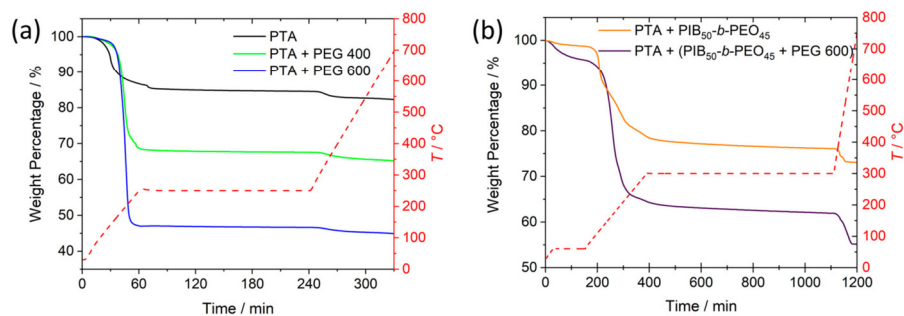

Figure 3. TG curves of the dried peroxotungstic acid precursor (**a**) without PEG (black), with PEG 400 (green), with PEG 600 (blue) and (**b**) with PIB₅₀-*b*-PEO₄₅ (orange) and PIB₅₀-*b*-PEO₄₅ + PEG 600 (purple). The dashed red lines show the temperature profile.

3.2. Elemental Composition, Density, Surface Area and Porosity

To verify that WO₃ and not any other related compound was obtained when using the precursor solutions containing different polymers as additives, the O:W ratio of the films was determined by EDX (Table 2, (O:W)$_{EDX}$). Since the tungsten oxide films are thinner than 300 nm and the penetration depth of EDX into the sample is in the micrometer range [47] emission from the substrate has to be accounted for. The spectra revealed the presence of tin in addition to tungsten and oxygen as well as some carbon contamination. Assuming a ratio of O:Sn = 2 for the FTO substrate, meaningful values of (O:W)$_{EDX}$ in the films can still be calculated. At first glance, (O:W)$_{EDX}$ was found to be around 3 for all the films (Table 2) which can be considered a confirmation that WO₃ was obtained from the different precursor

solutions. However, $(O:W)_{EDX}$ decreases for the films prepared with PEG indicating the presence of a higher concentration of oxygen vacancies. It has been reported before that PEG can inhibit the crystallization of the films and might lead to formation of oxygen-deficient WO_3 [48]. For the $WO_{3|\mu mp}$ films, $(O:W)_{EDX}$ deviates in a larger range compared to the other samples. Thus, the presence of mesopores interconnected by micropores (Figure 1c,f) might lead to locally differing transmission of X-rays emitted from Sn in FTO within a given sample area and, therefore, to larger variations in $(O:W)_{EDX}$. Further, for the $WO_{3|mp}$ films, the amount of carbon detected in the films was higher directly indicating that polymer fragments were still present in the films.

Table 2. Average elemental composition (and standard deviation) of the different tungsten oxide thin films obtained from EDX and the calculated $(O:W)_{EDX}$ ratios.

Film Type	W/At%	O/At%	Sn/At%	C/At%	$(O:W)_{EDX}$
$WO_{3|comp}$	10.0 ± 0.5	66.6 ± 0.2	17.5 ± 0.6	5.9 ± 0.2	3.16 ± 0.06
$WO_{3|\mu p400}$	12.9 ± 0.9	66.0 ± 0.3	14.0 ± 1.6	7.1 ± 0.7	2.94 ± 0.05
$WO_{3|\mu p600}$	12.7 ± 1.0	66.1 ± 0.2	14.7 ± 1.3	6.6 ± 0.2	2.90 ± 0.04
$WO_{3|mp}$	14.0 ± 0.9	63.8 ± 1.4	10.3 ± 2.0	11.9 ± 2.5	3.08 ± 0.08
$WO_{3|\mu mp}$	16.8 ± 1.3	65.8 ± 1.4	9.9 ± 1.0	7.5 ± 1.7	2.82 ± 0.20

X-ray photoelectron spectroscopy (XPS) was performed to complement the elemental analysis by EDX and, in particular, to obtain direct insight into the W oxidation state in pristine films. The overview spectra, which are quite similar for all the films (Figures 4a and S4a–S7a), only show the expected elements such as tungsten and oxygen as well as some carbon impurities, to similar extent in all samples. The W 4f spectra (Figures 4b and S4b–S7b) exhibit a doublet at binding energies around 38 eV and 36 eV, which corresponds to W^{6+} $4f_{5/2}$ and W^{6+} $4f_{7/2}$ states [14,24,49,50]. The small shoulders at lower binding energies of about 36.4 eV and 34.2 eV point out the presence of W^{5+} $4f_{5/2}$ and W^{5+} $4f_{7/2}$ states assigned to defects in the film surface [24,49]. The positions of these peaks are in good accordance with the ones reported for WO_3 thin films prepared via sol–gel processes [14,24] or sputter deposition [50]. The O 1s spectra (Figures 4c and S4c–S7c) show a main peak around 530.8 eV which can be assigned to the W=O bonds [24]. The shoulder with less intensity at higher binding energy of about 532.0 eV can be assigned to W–OH groups [24,51].
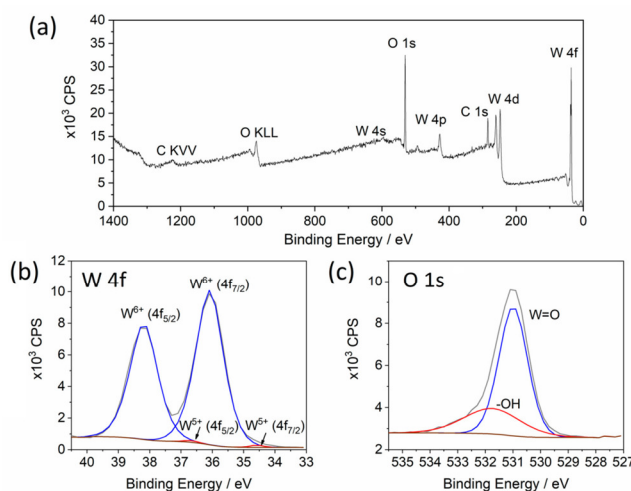

Figure 4. Full scan (**a**), range of W 4f (**b**) and range of O 1s (**c**) of an XPS spectrum measured at a $WO_{3|\mu p600}$ thin film.

From the peak areas of the O 1s spectra and the W 4f spectra, the O:W ratio at the surface (Table 3, (O:W)$_{XPS}$) was determined [52]. The values of (O:W)$_{XPS}$ are higher than the (O:W)$_{EDX}$ values (Table 2). The reason for this lies in the surface sensitivity of XPS as opposed to EDX [47] leading to a higher contribution of hydroxyl groups at the surface and therefore to higher values for (O:W)$_{XPS}$. However, the trend of a decreasing (O:W)$_{EDX}$ with PEG as precursor additive was confirmed by (O:W)$_{XPS}$ (Table 3). In the films prepared with any of the additives but in particular for WO$_{3|}$μp400 and WO$_{3|}$μp600, a higher concentration of W^{5+} was seen when compared to WO$_{3|}$comp (Table 4). Hence, as reported in [48], PEG can lead to porous films with more defects and, in particular, more oxygen vacancies, represented by the existence of W^{5+} states.

Table 3. Elemental composition of the different tungsten oxide thin films obtained from XPS, and the calculated (O:W)$_{XPS}$ ratios.

Film Type	W 4f/%	-OH/%	O=W/%	C/%	(O:W)$_{XPS}$
WO$_{3|}$comp	15.72	9.46	44.23	29.79	3.42
WO$_{3|}$μp400	16.37	9.19	43.27	30.48	3.20
WO$_{3|}$μp600	15.42	8.50	41.03	34.34	3.21
WO$_{3|}$mp	16.80	12.60	43.59	26.23	3.34
WO$_{3|}$μmp	18.09	6.79	52.40	21.86	3.27

Table 4. Concentration of W^{5+} in pristine (p) and intercalated (i) WO$_3$ thin films obtained from XPS and the degree of reduction for these experiments expressed as Li$^+$ content x in Li$_x$WO$_3$.

Film Type	W^{5+}(p)/%	W^{5+}(i)/%	x at -1.0 V
WO$_{3|}$comp	0.26	32.30	0.66
WO$_{3|}$μp400	1.42	37.50	0.62
WO$_{3|}$μp600	2.76	31.71	0.62
WO$_{3|}$mp	0.94	16.43	0.27
WO$_{3|}$μmp	0.68	19.36	0.42

The C 1s signal seems to be dominated by adventitious carbon and no conclusion can be drawn about any residual polymer fragments since even for the WO$_{3|}$comp film prepared without any additives a larger amount of carbon was detected than for the WO$_{3|}$mp film (Table 3), for which residual carbon was apparent in the color and in EDX. Therefore, the amount of carbon detected by XPS cannot give any evidence for polymer fragments remaining in the films.

During the stepwise etching with Ar$^+$, the amount of W^{6+} states for all the films decreased while the amount of W^{5+} states increased and subsequently even W^{4+}, and tungsten in even lower ionization states (W^{x+}) and metallic W^0 states arose indicating the stepwise reduction of WO$_3$ under Ar$^+$-bombardment even up to metallic tungsten as shown in Figure S8. These observations are well in line with the results obtained for Ar$^+$ bombardment of WO$_3$ films prepared via thermal evaporation [49].

Film characteristics derived from wet chemical analysis and profilometry compared to those independently obtained from the analysis of ellipsometry are summarized in Table 5. ρ of the WO$_{3|}$comp films was found similar to that reported for bulk WO$_3$ ($\rho_{WO_3} = 7.2$ g cm^{-3} [53]). By addition of PEG or PIB$_{50}$-b-PEO$_{45}$ as structure-directing agents, ρ of the prepared films decreased, according to the strategy. The porosity P_{chem} derived from microwave plasma atomic emission spectroscopy of the films dissolved in NH$_3$ solution increased according to the decreasing ρ of the films (Table 5). The porosity was independently calculated from the ellipsometry data, yielding P_E, which directly confirmed the range of porosity of the samples, but with a trend to slightly lower values than P_{chem} (Table 5). For the ellipsometric analysis, the films were prepared on smooth silicon wafers as opposed to rough FTO substrates. Such difference and the fundamentally different method of analysis can well explain the small differences between d and d_E and the small systematic

difference between P_{chem} and P_E. Both methods, however, independently yield the same trend of increasing porosity when using the polymers as structure-directing agents with $P(WO_{3|}\mu p400) < P(WO_{3|}\mu p600) << P(WO_{3|}mp) << P(WO_{3|}\mu mp)$. The combination of PIB_{50}-*b*-PEO_{45} and PEG 600 as additives clearly provided the highest porosity as already revealed by SEM (Figure 1c).

Table 5. Average thickness *d* obtained from profilometry and d_E obtained from ellipsometry, density ρ and values of the porosity P_{chem} and P_E obtained from wet chemical analysis and ellipsometry, respectively.

Film Type	*d*/nm	d_E/nm	ρ/g cm^{-3}	P_{chem}/%	P_E/%
WO$_{3|}$comp	98	95	7.15	-	-
WO$_{3|}\mu$p400	138	163	6.31	11.8	12.3
WO$_{3|}\mu$p600	145	161	5.88	17.9	14.4
WO$_{3|}$mp	215	297 *	4.84	32.3	19.2
WO$_{3|}\mu$mp	230	349 *	4.21	41.2	29.9

* not to be compared to *d* since different set of thicker films was analyzed.

The specific surface area S_{BET} of the as-prepared films was analyzed from the BET plots obtained from Kr physisorption (77 K) shown in Figure S9. The WO$_{3|}$mp sample was annealed at 550 °C for 1 h before the BET analysis to remove any residual polymer and obtain a measure for the intrinsic surface area of WO$_3$, albeit transformation to crystalline WO$_3$ under such conditions. For the WO$_{3|}$comp films prepared without additives, no significant S_{BET} could be determined, as expected for a compact thin film. For the WO$_{3|}\mu$p600 films, a significant surface area of around 3 m^2/g was obtained, comparable to the surface area reported for WO$_3$ powder (~2 m^2/g) [54]. Such surface area is compatible with the presence of micropores between grains of the films (Figure 1d). The values of S_{BET} of the WO$_{3|}$mp films and WO$_{3|}\mu$mp films turned out in the same range as reported for WO$_3$ nanoflakes (~10 m^2/g [55]) and mesoporous WO$_3$ (~32 m^2/g [31]). $S_{BET} \cong 10$ m^2/g determined for the WO$_{3|}$mp films thereby confirmed the presence of mesopores within the films but the considerably higher $S_{BET} \cong 20$ m^2/g of the WO$_{3|}\mu$mp films shows the significantly increased accessibility of the mesopores by the simultaneous presence of micropores serving as interconnecting channels. These S_{BET} values appear quite small, compared to the surface area and pore volume usually measured for templated metal oxides. Note that the BET surface area is referred to the mass and that WO$_3$ has a quite high density (ca. 4.2–7.2 g cm^{-3}), thus resulting in lower S_{BET} values compared to a material with identical porosity, but smaller skeleton density, e.g., SiO$_2$ ($\rho \cong 2.2$ g·cm^{-3} [53]). For instance, a value of $S_{BET} \cong 20$ m^2/g (WO$_{3|}\mu$mp), assuming an identical pore space, translates into a value of $S_{BET} \cong 65$ m^2/g for a corresponding SiO$_2$ material, which is in accordance with a network of connected spherical mesopores of ca. 20 nm in diameter.

3.3. Redox Characteristics and Intercalation of Li$^+$

In order to analyze the electrochromic reduction reaction and the diffusion of Li$^+$ ions in the films, cyclic voltammetry (CV) was performed at different scan rates as shown for a WO$_{3|}\mu$mp film in Figure 5 and for all other types of films in Figure S10. Following a CV curve with a just slightly different shape during a first conditioning cycle (Figure 6a), reproducible CV curves were obtained at each scan rate representing a reversible intercalation and deintercalation of Li$^+$ upon reduction and reoxidation as expected for amorphous WO$_3$ films [7].

The reversibility *K* of the bleaching and coloration process can be determined from the ratio q_{out}/q_{in} of the extracted and inserted charge densities [56]. During the first conditioning cycle (Table 6) and especially for the WO$_{3|}$comp and WO$_{3|}$mp films, the reversibility is rather low indicating that not all inserted ions can be deintercalated but are trapped within the films. Slow or irreversible movement in compact WO$_3$ can be expected. For the porous WO$_{3|}$mp films, however, this originally came unexpected and points at

49

partial pore filling by residual polymer or polymer fragments, as also concluded from a brownish color after annealing during film preparation and relevant mass losses at higher temperature during TG analysis. For the WO$_3$|µp400, WO$_3$|µp600 and WO$_3$|µmp films, the reversibility is close to 100% confirming that only a few ions are trapped within the films [39,57]. Hence, diffusion in the microporous network and in the absence of residual polymer fragments assures complete extraction of Li$^+$ even during the first bleaching process. However, from the second cycle on, all the films showed a high reversibility which means that less ions were trapped inside the films and that the sites where ions might be trapped were already occupied during the first coloration. In this respect, the films are similar to the commercially sputtered commWO$_3$ film.
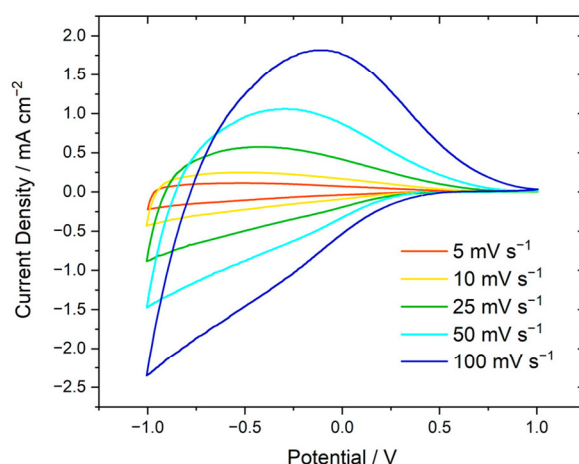
Figure 5. Cyclic voltammograms at the second cycle at different scan rates of a WO$_3$|µmp film in LiClO$_4$ in PC.
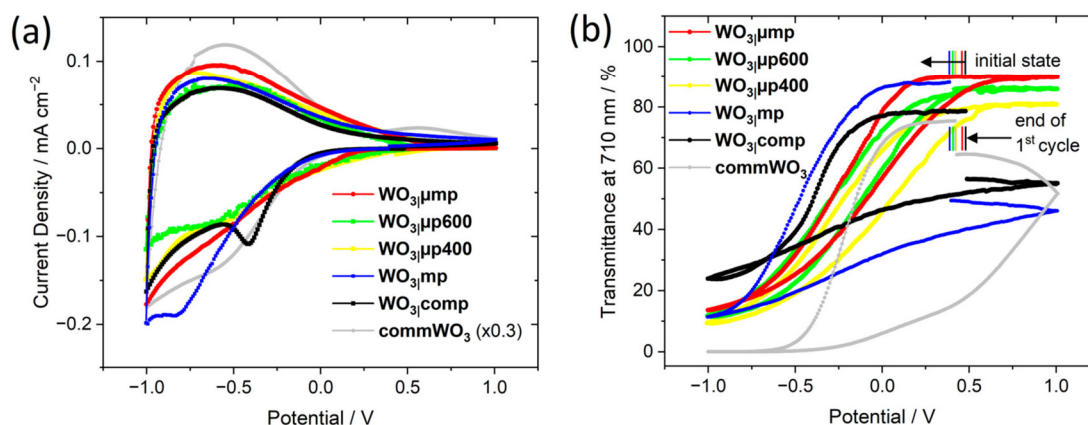
Figure 6. CV of the first cycle at a scan rate of 5 mV s^{-1} (**a**) and transmittance at 710 nm (**b**) in dependence of the applied potential during the CV of thin films of WO$_3$|comp (black), WO$_3$|µp400 (yellow), WO$_3$|µp600 (green), WO$_3$|mp (blue) and WO$_3$|µmp (red) as well as commWO$_3$ (grey) in LiClO$_4$ in PC. The initial states of each sample are marked by vertical lines and the arrows indicate the direction of cycling.

Table 6. Reversibility of the electrochromic switching determined from the first (K_1) and second (K_2) cycle of the CV measurements at a scan rate of 5 mVs^{-1} measured for at least 2 specimens of a given kind (commWO$_3$ only measured once).

Film Type	K_1/%	K_2/%
WO$_3$ comp	66–84	92–100
WO$_3$ μp400	92–96	94–97
WO$_3$ μp600	87–98	91–99
WO$_3$ mp	69–77	95–96
WO$_3$ μmp	93–96	95–97
commWO$_3$	96	97

The anodic peak current densities $j_{p,a}$ and the cathodic current densities at negative scan reversal $j_{r,c}$ (Figures 5 and S10) were plotted against the square root of the scan rate $v^{1/2}$ following the Randles Ševčík equation at room temperature

$$j = 2.69 \times 10^5 \cdot n^{3/2} \cdot D^{1/2} \cdot c \cdot v^{1/2} \tag{1}$$

where n is the number of electrons transferred in the reaction (1 in the present case [14]) and c is the concentration of Li$^+$ in the bulk of the electrolyte [14,56] to determine two approximations of the effective diffusion coefficient of Li$^+$ and electrons in the films, $D = D_{a,CV}$ in the anodic branch and $D = D_{c,CV}$ in the cathodic branch. Diffusion of Li$^+$ in the electrolyte can be considered much faster than that in the films, and it has not to be considered separately. The average values of the effective diffusion coefficients determined for a given type of sample are shown in Table 7. The values of the effective diffusion coefficient are in the range of 10^{-11}–10^{-9} cm^2·s^{-1}, similar to the values reported for sol–gel derived [14,29,58] or sputter-deposited [59] WO$_3$ thin films. Slightly larger effective diffusion coefficients were found for WO$_3$ μp400 and WO$_3$ μp600 than for WO$_3$ comp. Obviously, the ions can diffuse more easily through the film network along the microporous pathways available within the films prepared with PEG 400 or PEG 600. For WO$_3$ mp, on the other hand, an effective diffusion coefficient even smaller than for WO$_3$ comp was obtained. Despite the mesopores detected in SEM, the remaining polymer fragments of PIB$_{50}$-*b*-PEO$_{45}$ within the films seem to significantly attenuate the diffusion of Li$^+$. An effective diffusion coefficient about 6 times higher than that for WO$_3$ comp, WO$_3$ μp400 or WO$_3$ μp600 was observed in WO$_3$ μmp using a combination of both, PEG and PIB$_{50}$-*b*-PEO$_{45}$ as structure-directing agents. This combination provided films with similarly fast diffusion of Li$^+$ as obtained for commWO$_3$ (Table 7).

Table 7. Effective diffusion coefficients $D_{a,CV}$ and $D_{c,CV}$ determined from CV.

Film Type	$D_{a,CV}$/cm^2 s^{-1}	$D_{c,CV}$/cm^2 s^{-1}
WO$_3$ comp	6.0×10^{-11}	3.4×10^{-10}
WO$_3$ μp400	7.7×10^{-11}	3.5×10^{-10}
WO$_3$ μp600	1.1×10^{-10}	4.7×10^{-10}
WO$_3$ mp	6.0×10^{-11}	2.5×10^{-10}
WO$_3$ μmp	6.2×10^{-10}	1.1×10^{-9}
commWO$_3$	1.4×10^{-9}	2.8×10^{-9}

3.4. Electrochromic Switching Characteristics

To investigate the switching processes of the films, their optical transmittance T_λ was measured *in operando* during CV analysis. As expected, the reduction of WO$_3$ and the intercalation of Li$^+$ led to a decrease of T_λ (Figure 6b) and deeply blue-colored films as shown by the transmittance spectra at a potential of -1.0 V (Figures 7 and S11) and the color impressions, which were calculated as reported in [60].
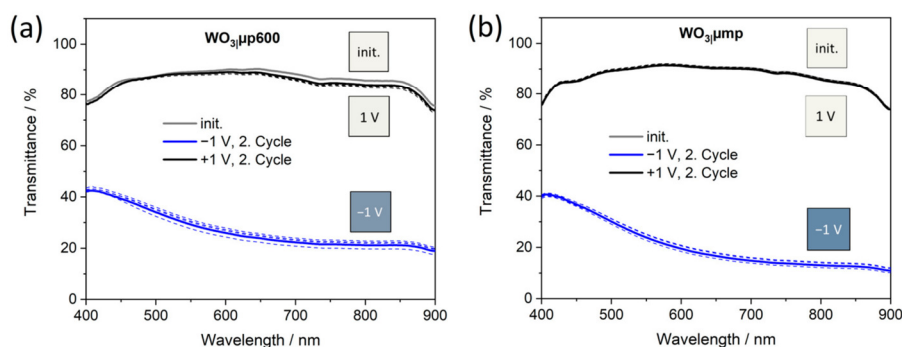
Figure 7. Transmittance spectra of (**a**) WO$_3$|µp600 and (**b**) WO$_3$|µmp thin films measured in contact to LiClO$_4$ in PC at a scan rate of 5 mV s^{-1} in the initial state (init.), in the bleached (1 V) and in the colored (-1 V) states. The insets show the calculated color impressions for the second cycle of the films.

By reoxidation of WO$_3$ and deintercalation of the ions, T_λ reversibly increased [1,6]. For the WO$_3$|comp and the WO$_3$|mp films (Figure S11b,c), T_λ in the bleached state was found lower compared to the initial state indicating partial irreversibility and the presence of trapped ions [39,57] within the films. This is in accordance with their slightly lower reversibility K_1 (Table 6). The WO$_3$|µp400, WO$_3$|µp600 and WO$_3$|µmp films (Figures 7 and S11a) could be fully bleached reaching transmittance characteristics close to the initial state. Facile deintercalation rather than trapping of ions as already revealed by the high reversibility (Table 6) is thereby confirmed.

Comparing the change in transmittance at a wavelength of 710 nm upon reduction and reoxidation of the films (Table 8) reveals that for WO$_3$|µp400, WO$_3$|µp600 and WO$_3$|µmp films the transmittance modulation ΔT_{710nm} is larger than for the WO$_3$|comp or WO$_3$|mp films. These observations correlate well with the values of the effective diffusion coefficient (Table 7). Residual polymer fragments in the WO$_3$|mp films might possibly hinder the diffusion of the ions within the mesoporous film structure leading to a change in transmittance comparable to compact films. Facile diffusion of ions supported by micropores present in the films prepared in the presence of PEG allows a high transmittance modulation, which has been also observed earlier for WO$_3$ prepared by dip-coating from similar precursor solutions [27]. The combination of PEG 600 with PIB$_{50}$-b-PEO$_{45}$ led to films reaching even higher values for the transmittance modulation compared to the films prepared with PEG only (Table 8) indicating facilitated diffusion of ions through the film network composed of interconnected mesopores and pore clusters already revealed by SEM (Figure 1f). For the WO$_3$|comp and WO$_3$|mp films, the transmittance started to change during the intercalation step at a more negative potential of around -0.25 V compared to films of WO$_3$|µp400, WO$_3$|µp600 and WO$_3$|µmp (Figure 6b). Such a delayed change in transmittance indicates a slower initial intercalation of the ions within the WO$_3$|comp and WO$_3$|mp films. For both films, the CV curves at the first cycle (Figure 6a) also stay at smaller current and show a small peak at around -0.4 V and -0.7 V, respectively. Such characteristics are expected for a hindered reaction, typically observed for crystalline WO$_3$ films [33] but observed here for the amorphous WO$_3$|comp and WO$_3$|mp films, indicative of an initial barrier for ion intercalation in line with the compact film structure or the presence of remaining polymer fragments. Nevertheless, from -0.25 V to -1.0 V the slope of the transmittance is comparable for all the films. During the bleaching process, however, a significantly steeper slope of the transmittance–potential curves can be observed for films of WO$_3$|µp400, WO$_3$|µp600 and WO$_3$|µmp suggesting a significantly more facile deintercalation of Li$^+$ through the porous film network.

Table 8. Mean values and standard deviation of the transmittance modulation $\Delta T_{710\text{nm}}$, the Li$^+$ content x in Li$_x$WO$_3$ and the coloration efficiency $CE_{710\text{nm}}$ obtained from CV at a scan rate of 5 mV s^{-1} or from CA measurements.

Film Type	$\Delta T_{710\text{nm}}$/%		x		$CE_{710\text{nm}}$/cm^2 C^{-1}	
	CV	CA	CV	CA	CV	CA
WO$_3$|comp	28.8 ± 8.4	25.4 ± 2.7	0.37 ± 0.07	0.38 ± 0.05	53.2 ± 12.6	34.5 ± 5.9
WO$_3$|µp400	68.2 ± 3.5	63.5 ± 1.7	0.43 ± 0.04	0.53 ± 0.08	75.4 ± 3.9	58.6 ± 5.6
WO$_3$|µp600	70.0 ± 4.3	64.2 ± 6.6	0.41 ± 0.05	0.57 ± 0.05	74.5 ± 7.9	54.3 ± 8.8
WO$_3$|mp	31.5 ± 1.8	40.8 ± 3.3	0.31 ± 0.06	0.45 ± 0.05	67.7 ± 4.9	40.7 ± 1.6
WO$_3$|µmp	75.3 ± 2.0	75.7 ± 0.2	0.44 ± 0.10	0.68 ± 0.04	85.2 ± 5.2	65.0 ± 4.2
commWO$_3$	59.6	88.5	0.32	0.45	68.3	67.1

Another important parameter for the comparison of switching characteristics of the electrochromic films is provided by the coloration efficiency *CE*. It is defined as the change in optical density ΔOD with the intercalated charge density q (see Equation (2)) [2,7]. $CE_{710\text{nm}}$ of the films at 710 nm, a wavelength for which the change was most significant, was determined from a linear fit in a plot of $\Delta OD = \log T_{\text{bleach}} - \log T_{\text{col}}$ over q, the charge inserted during the switching process.

$$CE = \frac{\Delta OD}{q} \tag{2}$$

$CE_{710\text{nm}}$ for the WO$_3$\|µp400, WO$_3$\|µp600 and WO$_3$\|µmp films was found considerably higher than for WO$_3$\|comp or WO$_3$\|mp (Table 8). Less charge is needed to allow a high transmittance modulation for the films with interconnected micropores compared to the compact or just mesoporous films. Such enhancement of *CE* by using appropriate structure-directing agents is in good accordance with earlier reports [27,31]. The highest obtained values for $\Delta T_{710\text{nm}}$ and $CE_{710\text{nm}}$ for the porous films were reached for WO$_3$\|µmp, similar or even better than those measured for commWO$_3$, the commercial benchmark sample, speaking in favor of the present films with a combination of mesopores interconnected by micropores. Interestingly, the *CE* values reported here are significantly higher than those previously reported for WO$_3$ films with ordered spherical mesopores caused by a similar block copolymer, and also similar thickness [34]. The observed higher *CE* in the present study is indicative of differences in the pore space: the mesoporous films reported in Sallard et al. [34] were prepared without additional PEG and, thus, without the improved connectivity between the spherical mesopores in WO$_3$\|µmp. Hence, this comparison clearly supports the need for connecting micropores to maximize the electrochromic response.

CV measurements were also performed for WO$_3$\|comp and WO$_3$\|µp600 following their annealing at temperatures higher than 250 °C (Table S1). For the films calcined at 350 °C, $D_{\text{a,CV}}$ was found in the same order of magnitude as for WO$_3$\|comp calcined at 250 °C (Table 7) and also the values of $\Delta T_{710\text{nm}}$ and $\Delta CE_{710\text{nm}}$ lie in the range of the upper limit of the obtained values for the films annealed at 250 °C (Table 8). These observations confirm facile diffusion of Li$^+$ in amorphous WO$_3$ that by GIXRD was observed to persist up to 350 °C (Figures 2 and S2). After calcination at $T \geq 450$ °C, the values of $\Delta T_{710\text{nm}}$ and $CE_{710\text{nm}}$ decreased and were found close to the lower limit of the values for the films calcined at 250 °C and a drastic change can be clearly seen for the effective diffusion coefficients, which are up to two orders of magnitude smaller than $D_{\text{a,CV}}$ determined after annealing at 250 °C. Slow diffusion in crystalline films formed after calcination at $T \geq 400$ °C (GIXRD, Figures 2 and S2) confirmed the disadvantage of a crystalline film structure for electrochromic performance as observed earlier [14,61,62]. However, the direct comparison of WO$_3$\|comp films fabricated without additives with WO$_3$\|µp600 prepared with PEG 600 as additive (Table S1) shows a benefit of a microporous starting structure even for a crystalline film resulting in a more facile diffusion of ions.

53

As shown in Figure 1, the WO$_3$|µp400, WO$_3$|µp600 and WO$_3$|µmp films were thicker than the films prepared without additives. Therefore, to check if the observed improvement of the transmittance modulation over WO$_3$|comp was provided by such increased thickness of the films and to directly compare the performance to commWO$_3$, thicker films of WO$_3$|comp, WO$_3$|µp600 and WO$_3$|µmp with similar thickness were prepared by subsequent preparation of several films onto each other. The thicker films (Figure 8) changed into an almost as deep blue as commWO$_3$ at, however, even slightly improved transparency in the bleached state (Figure S11d). Despite deep initial coloration, a reversible ΔT_{710nm} (Figure 8) of just 0.35% was measured for a 646 nm thick WO$_3$|comp film allowing a reversible change between 0.76% and 0.41% only, indicating heavily trapped ions after the initial coloration step. In contrast, for a 702 nm thick WO$_3$|µp600 film impressive ΔT_{710nm} = 65.9% and for a 620 nm thick WO$_3$|µmp film ΔT_{710nm} = 84.8% were achieved, values even slightly larger than those obtained for the 230–250 nm thick WO$_3$|µmp films (Table 8). It is thereby directly confirmed that the observed improvements of the switching characteristics are a direct consequence of a fast intercalation and deintercalation of Li$^+$ ions in the films facilitated by their porous morphology.
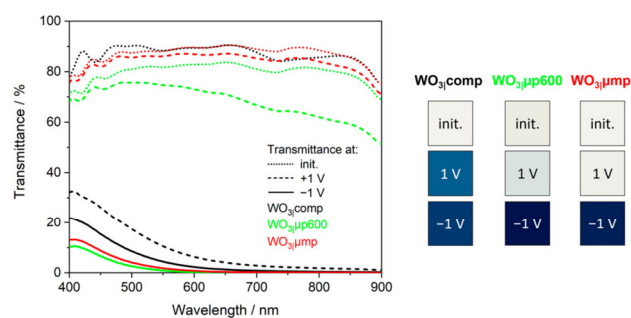
Figure 8. Transmittance spectra of 646 nm thick WO$_3$|comp (black), 702 nm thick WO$_3$|µp600 (green) and 620 nm thick WO$_3$|µmp (red) films measured in contact to LiClO$_4$ in PC at a scan rate of 5 Mv s^{-1} in the initial states (init.), the bleached (1 V) and the colored (−1 V) states at the second cycle. The corresponding calculated color impressions are shown to the right.

3.5. Long-Term Stability of Switching Characteristics

Response times t_{col} and t_{bleach} (Table 9) corresponding to the time needed to color or bleach, respectively, the films to 90% of ΔT_{710nm} [24,28] were calculated from the transmittance curves (Figure 9, Figure 10, Figures S12 and S13). t_{col} shorter than 6 s were consistently achieved for all films speaking in favor of a generally fast intercalation. However, rather long t_{bleach} > 40 s was determined for WO$_3$|comp, WO$_3$|mp and commWO$_3$ whereas the WO$_3$|µp400, WO$_3$|µp600 and WO$_3$|µmp were bleached within t_{bleach} < 25 s with short response times of just 2–3 s obtained for some samples. This tendency is again in conformity with the study of Sallard et al. [34], where response times of t_{col} ca. 20–30 s and t_{bleach} ca. 70 s were observed for samples similar to WO$_3$|mp. Despite higher ΔT_{710nm} for the commercial WO$_3$ film (Figure S12d), the short bleaching times of the films with micropores confirmed a facile switching of these films (Figure 9, Figure 10, Figures S12 and S13). The trend of t_{bleach} > t_{col} for all films fits to the slower transmittance change during positive scans in CV (Figure 6b) and $D_{c,CV}$ > $D_{a,CV}$ (Table 7). While the intercalation of Li$^+$ into all presently studied films is fast, their extraction is slow for compact films (WO$_3$|comp and commWO$_3$) and for WO$_3$|mp with remaining polymer fragments. By using PEG 400, PEG 600 or both, PIB$_{50}$-b-PEO$_{45}$ and PEG 600 as additives, micropores were created that provide pathways for fast deintercalation of the ions.

Table 9. Response times t_{col} and t_{bleach} of the different films obtained from CA measurements after prior opposite polarization for either 60 s, 100 s, or 300 s.

Film Type	t_{col}/s (300 s)	t_{bleach}/s (300 s)	t_{col}/s (60 s)	t_{bleach}/s (100 s)
WO$_3$|comp	4.5	129.0	5.1	48.8
WO$_3$|µp400	5.2	10.4	9.1	23.2
WO$_3$|µp600	4.8	14.1	5.5	17.1
WO$_3$|mp	5.1	160.6	4.6	43.6
WO$_3$|µmp	1.7	1.7	1.7	1.5
commWO$_3$	4.1	148.4	-	-
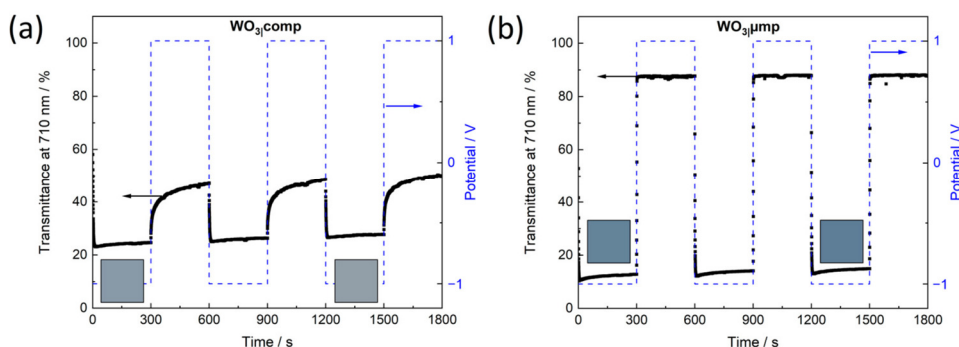
Figure 9. Optical transmittance at 710 nm of (**a**) WO$_3$\|comp and (**b**) WO$_3$\|µmp in LiClO$_4$ in PC, recorded during chronoamperometry between the potentials depicted as dashed profiles. The insets show the calculated color impressions of the films at the first and the third cycle at the colored states.
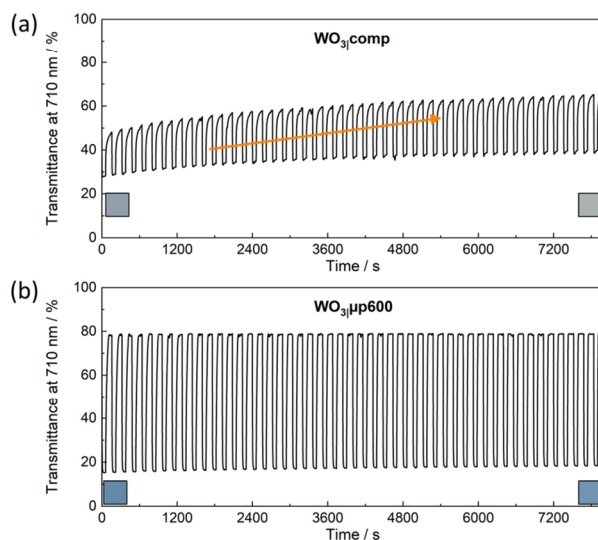
Figure 10. Optical transmittance at 710 nm of (**a**) WO$_3$\|comp and (**b**) WO$_3$\|µp600 in LiClO$_4$ in PC, recorded during chronoamperometry with 50 cycles between −1 V applied for 60 s and 1 V applied for 100 s. The arrow in (**a**) indicates the shift of the transmittance to higher values. The insets show the calculated color impressions at the 4. And the 53. Cycle of the films at the colored states.

A tendency of smaller CE_{710nm} was revealed in CA compared to CV (Table 8). The direct fast application of -1.0 V leads to higher current densities and chances of local overcharging at the beginning of the coloration process as opposed to a slow, well-defined change of the potential during CV. Overcharging or undesired side reactions can result in lower CE_{710nm}. Comparing the different kinds of films, however, CE_{710nm} follows the same trend as observed before during CV. From CV, CE_{710nm} even higher for $WO_3|\mu p400$, $WO_3|\mu p600$ and $WO_3|\mu mp$ compared to commWO₃ were reached as opposed to similar CE_{710nm} for $WO_3|comp$, $WO_3|mp$ and commWO₃.

Reversibility of the switching process deserves further attention. Films of $WO_3|comp$ showed a monotonous upward shift of T_λ when the films were switched back and forth between -1.0 V and 1.0 V for 300 s each over three cycles (Figure 9a). This trend continued when the films were studied over 50 more cycles (Figure 10a). The compact film obviously contained a considerable concentration of trapped ions [57]. It has been found earlier [63,64] that the concentration of intercalated ions x in Li_xWO_3 in the films, clearly influenced the equilibria of $W^{6+} \rightleftharpoons W^{5+}$ and $W^{5+} \rightleftharpoons W^{4+}$ leading to the observed changes in the optical absorption of WO₃. It was observed that up to $x = 0.3$–0.5, the transmittance first decreased and then shifted back to higher transmittance for larger x whereby after exceeding $x \approx 0.7$ the films became optically irreversible showing a light-brownish color. The range of $x < 0.3$–0.7 in the present experiments was chosen to provide a good compromise between intense coloration and high reversibility. However, in Figure S14a it can be seen that after the first intercalation of $WO_3|comp$ for 300 s at -1.0 V (1. Cycle) ions were trapped within the films leading to a bluish film even after reversal to 1.0 V (Figure S14c). The color impressions of the film after 53 cycles indicate that the concentration of trapped ions must have increased subsequently until the films became light-brownish with T_λ for both -1.0 V and 1.0 V shifted to higher values (Figure S14a,c). For $WO_3|mp$, despite mesoporous morphology, the remaining polymer in the film also led to trapped ions and, thus, a similar trend towards increasing T_λ (Figure S13a) as obtained for $WO_3|comp$. Hence, long coloration times are disadvantageous for such films and lead to the observed irreversibilities. For the $WO_3|\mu p400$, $WO_3|\mu p600$ and $WO_3|\mu mp$ films, however, T_λ in the bleached as well as in the colored states remained widely constant at 1.0 V and -1.0 V, respectively (Figures 10b, S13b,c and S14b,c). These films point out the possibility to endure multiple reversible switching at a high stability of the films. The porous network in these films without significant amounts of residual polymer fragments enables a facile intercalation and deintercalation of the Li^+ ions allowing the observed reversible switching of these films.

The reversibility dependent on the applied negative potential is compared for $WO_3|comp$ and $WO_3|\mu p600$ in Figure S15. It could be observed that independent of the negative potential, $WO_3|\mu p600$ could be fully bleached again at 1.0 V reaching a transmittance equal to the one in the initial state. For $WO_3|comp$, however, the transmittance was lower than in the initial state already after prior polarization at -0.25 V only, indicating trapped ions already for weakly reduced $WO_3|comp$. For both films it can be observed that the spectral shape also changed with increasing negative potential. The transmittance at longer wavelengths decreased less than expected when compared to the change at short wavelengths to a degree that around 600–900 nm the transmittance even increased from -0.75 V to -1.0 V, most clearly seen for $WO_3|comp$ (Figure S15a). This trend can be explained by a Li^+ concentration increased to $x \approx 0.6$ at -1.0 V, a value higher than the limit of $x \geq 0.5$, for which such spectral changes were already reported [63,64].

3.6. Chemical Analysis of Reduced Films

The spectroelectrochemical analysis has shown that PEG 600 in combination with PIB_{50}-b-PEO_{45} as structure-directing agents led to WO₃ films with optimum electrochromic switching characteristics (Table 8, Figures 7b, 9b and S13c). For films prepared with just PEG 600 or PEG 400 as additive, switching characteristics almost as good (Table 8, Figures 7a, 10b, S11a, S12a,b and S13b) were achieved. From a technological point of view,

application of PEG only provides other advantages over using both, PEG and PIB$_{50}$-*b*-PEO$_{45}$. The preparation of the films is not only saving the additional demanding precursor but also saves time and energy since a heat treatment of the films is only needed at 250 °C for one hour as opposed to 300 °C for 12 h. Therefore, and in order to allow further optimization of such films in the future, details of the intercalation reactions and of the charge transport were studied for WO$_3$|µp400 and WO$_3$|µp600 and compared to WO$_3$|comp.

The presence of reduced states of WO$_3$ was directly proven by XPS analysis (Figure S16 vs. Figures 4 and S4–S7) after applying −1.0 V for 300 s in the electrochemical cell and subsequent transfer to vacuum. All films showed an increase in the concentration of W^{5+} from around 0.3–2.8% in the pristine state to 16–38% in the reduced state (Figure S8b, Table 4), comparable to the values of 30–35% reported for colored WO$_3$ films prepared by a cathodic arc plasma [65]. A trend of higher concentrations of W^{5+} (at least at the surface) in WO$_3$|µp400 and WO$_3$|µp600 and to lower concentrations in WO$_3$|mp and WO$_3$|µmp, also when compared to WO$_3$|comp was observed. Efficient reduction of microporous WO$_3$ was thereby confirmed. Despite high coloration of WO$_3$|µmp and low coloration of WO$_3$|mp, both these mesoporous films showed a similarly low concentration of W^{5+} and degree of reduction *x*, in line with a high CE_{710nm} observed for WO$_3$|µmp, but rather low CE_{710nm} for WO$_3$|mp (Table 8). Ar$^+$-sputtering of the reduced films with intercalated Li$^+$ allowed to discuss the depth profile of the redox reactions. The concentration of W^{5+} for the reduced films decreased and then saturated with proceeding etching time, i.e., deeper in the films (Figure S8). This is consistent with a reduction reaction proceeding from the surface towards the inner volume of the films as would be expected for a movement of e$^-$ still faster also in porous WO$_3$ than Li$^+$, which can be expected to be fast within the pores but slow within solid, albeit porous WO$_3$, as confirmed by increased but still quite moderate D_{CV} (Table 7). The subsequent reduction to W^{4+}, W^{x+} and W^0 occurred faster than in the pristine films, reasonable in view of a start already in a reduced state of WO$_3$ (Figure S16).

To directly prove the impact of the microporous network and to complement this analysis, the distribution of Li$^+$ in the reduced films was also analyzed by ToF-SIMS (Figures 11 and S17). The WO$_3$$^-$ and the SnO$^-$ signals (Figure 11) are used for correlating the sputter times and the etched thickness of the films. For the WO$_3$|µp400 and WO$_3$|µp600 samples, the decrease in intensity of the WO$_3$$^-$ signal and the increase in intensity of the SnO$^-$ signal occurred at longer sputter times compared to the WO$_3$|comp films, well in line with a higher film thickness for WO$_3$|µp400 and WO$_3$|µp600 (Table 5). A rather constant sputter rate of about 0.3 nm/s was obtained for all films. All depth profiles (Figure S17) confirm that an intercalation for around 60 s is sufficient to completely charge the WO$_3$ film since the depth profiles of the films intercalated for 60 s or 300 s are quite similar, as also revealed by transmittance spectra measured for the films after 60 s and 300 s of intercalation (Figure S18). For WO$_3$|comp films, an accumulation of Li$^+$ at the film surface up to a depth (sputter time) of around 20 nm (60 s) can be clearly observed (Figures 11 and S17a) after reduction for $t \geq 60$ s, confirming a compact film structure and, thus, a low accessibility of the inner volume of the film for Li$^+$. In strong contrast, reduced WO$_3$|µp400 and WO$_3$|µp600 did not show any Li$^+$ accumulation at the surface, speaking in favor of a more homogeneous reduction of the films enabled by a good accessibility of the inner parts of the films for Li$^+$. An increase of the Li$^-$ signal at increased depths and for increased intercalation times observed for all films (Figure S17) points at intercalation of Li$^+$ also in the inner parts of the films, but, since unrealistically high Li$^-$ concentrations were detected close to the interface with FTO, seems to be superimposed by artefacts of the measurements caused by changing ionization probabilities (matrix effects) and by different sputter probabilities of the elements [66,67], which hinders a more detailed analysis of the depth profiles.
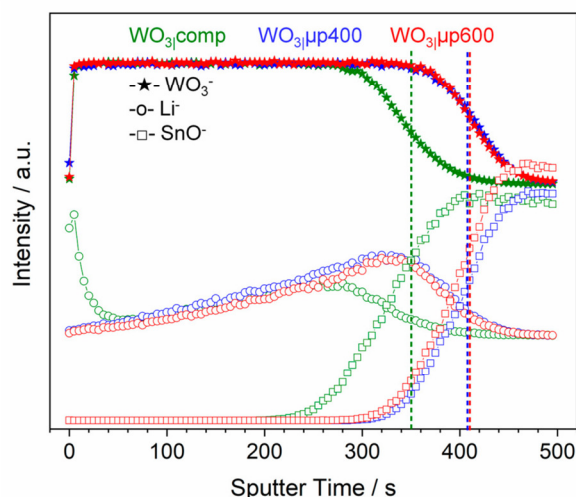
Figure 11. Depth profiles obtained from ToF-SIMS analysis of the WO$_3^-$ (-★-), Li$^-$ (-o-) and SnO$^-$ (-□-) signals for thin films of WO$_3$|comp (green), WO$_3$|μp400 (blue) and WO$_3$|μp600 (red) films intercalated at −1.0 V for 300 s. Dashed lines mark the approximate position of the interface between WO$_3$ and FTO estimated from the WO$_3^-$ and SnO$^-$ signals.

3.7. Charge Transport within Microporous vs. Compact Tungsten Oxide

The direct influence of the microporous network on electrode kinetics of the electrochromic reaction was independently analyzed by impedance spectroscopy in different redox states of WO$_3$|comp and WO$_3$|μp600 films. The resulting Nyquist plots (Figure 12) can be fitted well with the equivalent circuit shown in Figure 12a. This circuit is typically used for the description of intercalation processes in electrochromic films [68,69]. R_1 corresponds to a series resistance caused by the electrolyte and the substrate [69–72]. R_{ct} is assigned to the resistance of the charge transfer from the WO$_3$ surface to the electrolyte and describes the intercalation of the ions into the WO$_3$ film as well as the interfacial redox processes [68,69,71–73]. The electrochemical double layer consisting of the electrons at the electrode surface and ions on the electrolyte side can be modelled by a constant phase element or a capacitance [68,69,71–73]. A more accurate fit of the present data was obtained by using a constant phase element CPE_{dl}. A semi-infinite type Warburg impedance Z_w represents the diffusion of Li$^+$ ions in the WO$_3$ films [68,69,71,73] but had to be replaced by a finite-length-type Warburg element $Z_{w,s}$ [72,73] for the impedance spectra measured at a potential of −1.0 V, which led to more reliable fits of the data. C_L refers to a limiting capacitance caused by the finite length of the WO$_3$ film and considers a diffusion limited by charge accumulation in the film at low frequencies [68,69,74].

As expected, the series resistance R_1 in the high frequency range of the Nyquist plot (Figure 12) was found quite constant around 30–35 Ω for compact or microporous WO$_3$ and at different applied potentials. Similarly, Q_{CPE} and α representing the double layer capacitance and C_L representing the limiting capacitance of WO$_3$ showed no significant changes either with potential or among the films speaking in favor of a rather constant arrangement of ions and electrons at the electrode surface and of a rather constant maximum charge uptake. The resistance R_{ct}, however, for WO$_3$|comp decreased from about 51 Ω at −0.25 V to 9 Ω at −1.0 V, a trend directly seen by a decreasing radius of the semicircle in the moderate frequency range (Figure 12a). At negative potentials, a driving force is established to insert Li$^+$ into the films and the barrier to enter is decreased. The higher value of R_{ct} at −0.25 V compared to the value at −1.0 V points out that a higher barrier has still to be overcome to insert Li$^+$ at −0.25 V, possibly caused by slow transport of ions and/or

electrons within the WO$_3$|comp structure. For WO$_3$|µp600, R_{ct} of about 248 Ω at −0.25 V was found considerably higher than for WO$_3$|comp. Since ion transport should not be hindered in a microporous compared to a compact material, the reason should be sought in an attenuated electron transport. The porous morphology and a thicker film can both lead to a larger number of grain boundaries posing additional barriers for electron transport. However, R_{ct} of the microporous film decreased to around 38 Ω at a potential of −0.75 V and then to about 11 Ω at −1.0 V. Hence, the values of R_{ct} at −1.0 V are quite similar for both types of films indicating a similar facile electron transport within the films at this potential and allowing fast intercalation of Li$^+$. For both types of films, the impedance values at 1.0 V (Figure 12c,d) are much higher than at −1.0 V representing a high barrier for intercalation of the ions in the bleached state as already observed in earlier reports [75,76].
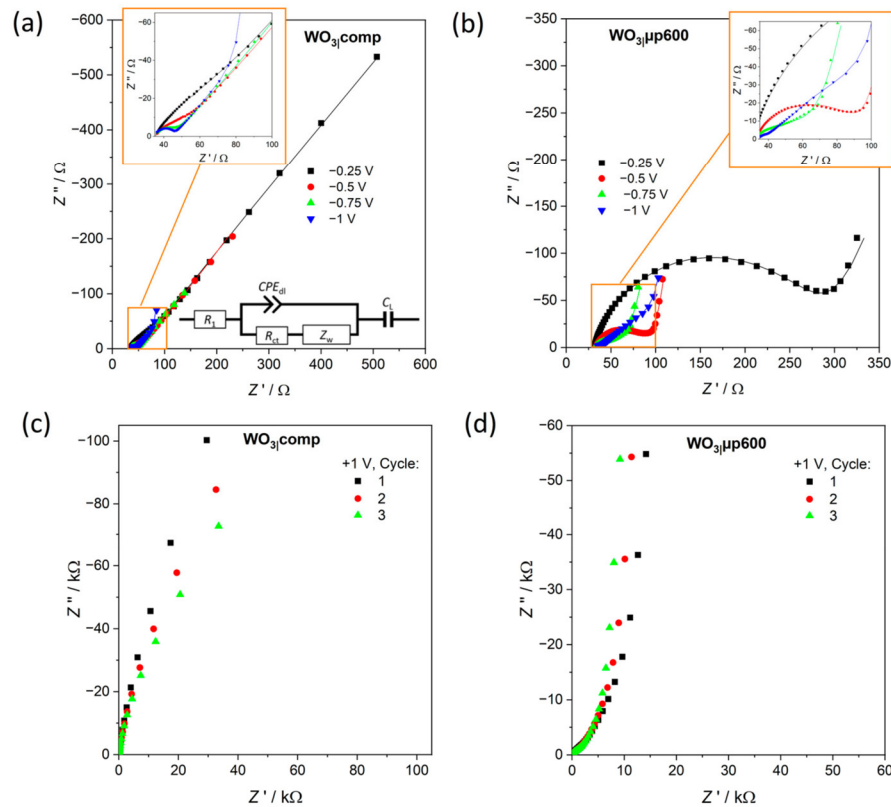
Figure 12. Nyquist plots of a WO$_3$|comp film (**a,c**) and a WO$_3$|µp600 film (**b,d**) at different negative applied potentials and at the bleached state (1 V). The insets show the impedance data at high frequencies (**a,b**) and the equivalent circuit (**a**) used for fitting the data with the resistances R_1 and R_{ct}, the Warburg impedance Z_w, the constant phase element CPE_{dl} and the capacitance C_L.

The Warburg coefficient A_w obtained from fits of the impedance spectra allows to obtain an independent measure of Li$^+$ diffusion by the ion diffusion coefficient D_I in the films with the active surface area A, the molar gas constant R and the temperature T [77]:

$$D_I = \frac{R^2 T^2}{2 A^2 n^4 F^4 c^2 A_w^2} \tag{3}$$

The WO$_3$|comp film (Table S2) provided generally smaller D_I compared to the WO$_3$|µp600 film, which is well in line with the tendency observed from the effective diffusion coefficients obtained from the CV measurements. However, D_I in the range of 10^{-13}–10^{-11} cm^2 s^{-1} were found around two orders of magnitude smaller than $D_{c,CV}$ and $D_{a,CV}$. This is a consequence of the fact that D_{CV} are effective diffusion coefficients describing the combined diffusion of electrons and ions while D_I is characteristic for the diffusion of ions only. Since CV was performed across the whole range of potentials and since the fits of the impedance spectra at -1.0 V needed a dedicated Warburg element, values at intermediate potentials (-0.25 V to -0.75 V) are used for comparison purposes. Throughout this range, D_I was found significantly larger for WO$_3$|µp600 than for WO$_3$|comp, well in line with larger D_{CV} for WO$_3$|µp600, confirming faster ion transport in WO$_3$|µp600. The difference in D_{CV}, however, was found smaller than that in D_I presumably caused by slower electron transport in WO$_3$|µp600 which also is considered by the effective diffusion coefficient D_{CV}.

4. Conclusions

Thin films of tungsten oxide with significantly increased internal surface area were prepared by spin-coating using different polymers as structure-directing agents to influence the internal film structure and, thus, the electrochromic performance. The combination of PIB$_{50}$-*b*-PEO$_{45}$, a block copolymer that is known to form micelles under the present preparation conditions, and the homopolymer polyethylene glycol PEG 600 as templates led to WO$_3$|µmp films with interconnected spherical mesopores desirable for the intercalation and deintercalation of charge-balancing Li$^+$ ions allowing high transmittance modulations between the bleached and the colored states of the films, short response times and high effective diffusion coefficients. The use of just PIB$_{50}$-*b*-PEO$_{45}$ provided mesoporous WO$_3$|mp films but residual polymer fragments or the presence of widely isolated pores separated by rather thick walls of compact WO$_3$ leading to trapping of ions similar to the compact WO$_3$|comp films prepared without any additives. Thin films homogeneously containing interconnected micropores were obtained with PEG 400 (WO$_3$|µp400) or PEG 600 (WO$_3$|µp600) as additives, showing electrochromic characteristics almost as good as the WO$_3$|µmp films. Reversible and stable switching processes as well as a homogeneous distribution of the intercalated ions within the films were obtained for all three types of films that contained the interconnected micropores, WO$_3$|µp400, WO$_3$|µp600 and WO$_3$|µmp. Furthermore, the use of PEG only leading to purely microporous films, i.e., to forego additional mesopores, allows a fabrication of tungsten oxide thin films at presumably lower cost and in an environmentally even more benign way favored by a considerably shorter heat treatment at even lower temperature. Nevertheless, the presence of both, micropores as well as interconnected mesopores of defined shape could still provide significant advantages in transmittance modulation, response times and coloration efficiency over films modified by just PEG as additive (WO$_3$|µp400, WO$_3$|µp600 as well as films reported in the literature [24,27,28]). These results are in excellent agreement with the enhanced Li$^+$ permeation found in corresponding TiO$_2$ films, also containing spherical mesopores (10–15 nm) connected by small mesopores (ca. 3 nm in diameter) [33]. In conclusion, films using a combination of 10–20 nm mesopores connected through micropores or small mesopores (i.e., <3 nm in diameter) can offer an attractive pathway towards facile diffusion of ions throughout the film network in particular for thicker films of even more intense coloration as long as the mesopores are well accessible for ions. The present study thus confirms that suitable porosity can indeed substantially improve Li$^+$-based electrochromic properties.

60

References

1. Granqvist, C.G. Electrochromics for smart windows: Oxide-based thin films and devices. *Thin Solid Films* **2014**, *564*, 1–38. [CrossRef]
2. Mortimer, R.J.; Rosseinsky, D.R.; Monk, P.M.S. *Electrochromic Materials and Devices*, 1st ed.; Wiley-VCH Verlag GmbH & Co. KGaA: Weinheim, Germany, 2013.
3. Wang, Z.; Wang, X.; Cong, S.; Chen, J.; Sun, H.; Chen, Z.; Song, G.; Geng, F.; Chen, Q.; Zhao, Z. Towards full-colour tunability of inorganic electrochromic devices using ultracompact fabry-perot nanocavities. *Nat. Commun.* **2020**, *11*, 302. [CrossRef] [PubMed]
4. Ke, Y.; Chen, J.; Lin, G.; Wang, S.; Zhou, Y.; Yin, J.; Lee, P.S.; Long, Y. Smart Windows: Electro-, Thermo-, Mechano-, Photochromics, and Beyond. *Adv. Energy Mater.* **2019**, *9*, 1902066. [CrossRef]
5. Granqvist, C.G. Progress in electrochromics: Tungsten oxide revisited. *Electrochim. Acta* **1999**, *44*, 3005–3015. [CrossRef]
6. Deb, S.K. Opportunities and challenges in science and technology of WO$_3$ for electrochromic and related applications. *Sol. Energy Mater. Sol. Cells* **2008**, *92*, 245–258. [CrossRef]
7. Granqvist, C.G. Electrochromic tungsten oxide films: Review of progress 1993–1998. *Sol. Energy Mater. Sol. Cells* **2000**, *60*, 201–262. [CrossRef]

8. Park, S.-I.; Quan, Y.-J.; Kim, S.-H.; Kim, H.; Kim, S.; Chun, D.-M.; Lee, C.S.; Taya, M.; Chu, W.-S.; Ahn, S.-H. A Review on Fabrication Processes for Electrochromic Devices. *Int. J. Precis. Eng. Manuf.-Green Technol.* **2016**, *3*, 397–421. [CrossRef]
9. Li, C.; Hsieh, J.H.; Hung, M.-T.; Huang, B.Q. Electrochromic study on amorphous tungsten oxide films by sputtering. *Thin Solid Films* **2015**, *587*, 75–82. [CrossRef]
10. Washizu, E.; Yamamoto, A.; Abe, Y.; Kawamura, M.; Sasaki, K. Optical and electrochromic properties of RF reactively sputtered WO₃ films. *Solid State Ion.* **2003**, *165*, 175–180. [CrossRef]
11. Ashrit, P.V.; Bader, G.; Truong, V.-V. Electrochromic properties of nanocrystalline tungsten oxide thin films. *Thin Solid Films* **1998**, *320*, 324–328. [CrossRef]
12. Ozkan, E.; Lee, S.-H.; Tracy, C.E.; Pitts, J.R.; Deb, S.K. Comparison of electrochromic amorphous and crystalline tungsten oxide films. *Sol. Energy Mater. Sol. Cells* **2003**, *79*, 439–448. [CrossRef]
13. Agnihotry, S.A.; Sharma, R.; Kar, M.; Saxena, T.K. Towards electrochromic stability in sol–gel-derived tungsten oxide films: Cyclic voltammetric and spectrophotometric investigations. *Sol. Energy Mater. Sol. Cells* **2006**, *90*, 15–24. [CrossRef]
14. Zhao, B.; Zhang, X.; Dong, G.; Wang, H.; Yan, H. Efficient electrochromic device based on sol–gel prepared WO₃ films. *Ionics* **2015**, *21*, 2879–2887. [CrossRef]
15. Deepa, M.; Singh, D.P.; Shivaprasad, S.M.; Agnihotry, S.A. A comparison of electrochromic properties of sol–gel derived amorphous and nanocrystalline tungsten oxide films. *Curr. Appl. Phys.* **2007**, *7*, 220–229. [CrossRef]
16. Pauporté, T. A Simplified Method for WO₃ Electrodeposition. *J. Electrochem. Soc.* **2002**, *149*, C539–C545. [CrossRef]
17. Nishio, K.; Sei, T.; Tsuchiya, T. Preparation of Electrochromic Tungsten Oxide Thin Film by Sol-Gel Process. *J. Ceram. Soc. Jpn* **1999**, *107*, 199–203. [CrossRef]
18. Zayim, E.Ö.; Tepehan, F.Z. Structural and Electrochromic Properties of Sol-Gel Made Tantalum Oxide and Tungsten Oxide Films. *Key Eng. Mater.* **2004**, *264–268*, 435–438. [CrossRef]
19. Yamanaka, K.; Oakamoto, H.; Kidou, H.; Kudo, T. Peroxotungstic Acid Coated Films for Electrochromic Display Devices. *Jpn. J. Appl. Phys.* **1986**, *25*, 1420–1426. [CrossRef]
20. Chemseddine, A.; Henry, M.; Livage, J. Sol-gel derived electrochromic layers. *Rev. Chim. Min.* **1984**, *21*, 487–495.
21. Yang, H.; Shang, F.; Gao, L.; Han, H. Structure, electrochromic and optical properties of WO₃ film prepared by dip coating-pyrolysis. *Appl. Surf. Sci.* **2007**, *253*, 5553–5557. [CrossRef]
22. Bentley, J.; Desai, S.; Bastakoti, B.P. Porous Tungsten Oxide: Recent Advances in Design, Synthesis, and Applications. *Chem. Eur. J.* **2021**, *27*, 9241–9252. [CrossRef] [PubMed]
23. Gupta, J.; Shaik, H.; Kumar, K.N. A review on the prominence of porosity in tungsten oxide thin films for electrochromism. *Ionics* **2021**, *27*, 2307–2334. [CrossRef]
24. Bertus, L.M.; Faure, C.; Danine, A.; Labrugere, C.; Campet, G.; Rougier, A.; Duta, A. Synthesis and characterization of WO₃ thin films by surfactant assisted spray pyrolysis for electrochromic applications. *Mater. Chem. Phys.* **2013**, *140*, 49–59. [CrossRef]
25. Djaoued, Y.; Ashrit, P.V.; Badilescu, S.; Brüning, R. Synthesis and Characterization of Macroporous Tungsten Oxide Films for Electrochromic Application. *J. Sol-Gel Sci. Technol.* **2003**, *28*, 235–244. [CrossRef]
26. Cremonesi, A.; Bersani, D.; Lottici, P.P.; Djaoued, Y.; Ashrit, P.V. WO₃ thin films by sol–gel for electrochromic applications. *J. Non-Cryst. Solids* **2004**, *345–346*, 500–504. [CrossRef]
27. Lu, S.; Wang, C.; Wang, H.; Liu, J.; Yan, H. Excellent electrochromic properties of tungsten oxide films with a mesoporous structure. *J. Mater. Sci. Mater. Electron.* **2017**, *28*, 10049–10055. [CrossRef]
28. Deepa, M.; Kar, M.; Singh, D.P.; Srivastava, A.K.; Ahmad, S. Influence of polyethylene glycol template on microstructure and electrochromic properties of tungsten oxide. *Sol. Energy Mater. Sol.* **2008**, *92*, 170–178. [CrossRef]
29. Fang, Y.; Sun, X.; Cao, H. Influence of PEG additive and annealing temperature on structural and electrochromic properties of sol–gel derived WO₃ films. *J. Sol-Gel Sci. Technol.* **2011**, *59*, 145–152. [CrossRef]
30. Wu, W.-T.; Liao, W.-P.; Chen, L.-Y.; Chen, J.-S.; Wu, J.-J. Outperformed electrochromic behavior of poly(ethylene glycol)-template nanostructured tungsten oxide films with enhanced charge transfer/transport characteristics. *Phys. Chem. Chem. Phys.* **2009**, *11*, 9751–9758. [CrossRef]
31. Kim, K.-W.; Yun, T.Y.; You, S.-H.; Tang, X.; Lee, J.; Seo, Y.; Kim, Y.-T.; Kim, S.H.; Moon, H.C.; Kim, J.K. Extremely fast electrochromic supercapacitors based on mesoporous WO₃ prepared by an evaporation-induced self-assembly. *NPG Asia Mater.* **2020**, *12*, 84. [CrossRef]
32. Cheng, W.; Baudrin, E.; Dunn, B.; Zink, J.I. Synthesis and electrochromic properties of mesoporous tungsten oxide. *J. Mater. Chem.* **2001**, *11*, 92–97. [CrossRef]
33. Brezesinski, T.; Rohlfing, D.F.; Sallard, S.; Antonietti, M.; Smarsly, B.M. Highly Crystalline WO₃ Thin Films with Ordered 3D Mesoporosity and Improved Electrochromic Performance. *Small* **2006**, *2*, 1203–1211. [CrossRef] [PubMed]
34. Sallard, S.; Brezesinski, T.; Smarsly, B.M. Electrochromic Stability of WO₃ Thin Films with Nanometer-Scale Periodicity and Varying Degrees of Crystallinity. *J. Phys. Chem. C* **2007**, *111*, 7200–7206. [CrossRef]
35. Sallard, S.; Schröder, M.; Boissière, C.; Dunkel, C.; Etienne, M.; Walcarius, A.; Oekermann, T.; Wark, M.; Smarsly, B.M. Bimodal mesoporous titanium dioxide anatase films templated by a block polymer and an ionic liquid: Influence of the porosity on the permeability. *Nanoscale* **2013**, *5*, 12316–12329. [CrossRef] [PubMed]
36. Livage, J.; Guzman, G. Aqueous precursors for electrochromic tungsten oxide hydrates. *Solid State Ion.* **1996**, *84*, 205–211. [CrossRef]

37. Gorbunova, O.V.; Baklanova, O.N.; Gulyaeva, T.I.; Trenikhin, M.V.; Drozdov, V.A. Poly(ethylene glycol) as structure directing agent in sol–gel synthesis of amorphous silica. *Microporous Mesoporous Mater.* **2014**, *190*, 146–151. [CrossRef]
38. Cop, P.; Hess, K.; Werner, S.; Meinusch, R.; Smarsly, B.M.; Kozuka, H. Comparison of In-Plane Stress Development in Sol-Gel- and Nanoparticle-Derived Mesoporous Metal Oxide Thin Films. *Langmuir* **2019**, *35*, 16427–16437. [CrossRef]
39. Wen, R.-T.; Granqvist, C.G.; Niklasson, G.A. Eliminating degradation and uncovering ion-trapping dynamics in electrochromic WO₃ thin films. *Nat. Mater.* **2015**, *14*, 996–1001. [CrossRef]
40. Kim, K.J.; Jang, J.S.; Moon, D.W.; Kang, H.J. A method to determine the interface position and layer thickness in SIMS depth profiling of multilayer films. *Metrologia* **2010**, *47*, 253–261. [CrossRef]
41. Scherrer, P. Bestimmung der Größe und der inneren Struktur von Kolloidteilchen mittels Röntgenstrahlen. *Nachr. Ges. Wiss. Göttingen* **1918**, *2*, 98–100.
42. Patterson, A.L. The Scherrer Formula for X-Ray Particle Size Determination. *Phys. Rev.* **1939**, *56*, 978–981. [CrossRef]
43. Spieß, L.; Teichert, G.; Schwarzer, R.; Behnken, H.; Genzel, C. *Moderne Röntgenbeugung: Röntgendiffraktometrie für Materialwissenschaftler, Physiker und Chemiker*, 2nd ed.; Vieweg + Teubner: Wiesbaden, Germany, 2009.
44. Srivastava, A.K.; Agnihotry, S.A.; Deepa, M. Sol–gel derived tungsten oxide films with pseudocubic triclinic nanorods and nanoparticles. *Thin Solid Films* **2006**, *515*, 1419–1423. [CrossRef]
45. Shapovalov, V.I.; Lapshin, A.E.; Gagarin, A.G.; Efimenko, L.P. Chemical Composition and Crystal Structure of Tungsten Oxide Films. *Glass Phys. Chem.* **2014**, *40*, 553–569. [CrossRef]
46. Gabrusenoks, J.V.; Cikmach, P.D.; Lusis, A.R.; Kleperis, J.; Ramans, G.M. Electrochromic Colour Centres in Amorphous Tungsten Trioxide Thin Films. *Solid State Ion.* **1984**, *14*, 25–30. [CrossRef]
47. Haynes, W.M.; David, R.L.; Bruno, T.J. *Handbook of Chemistry and Physics*, 97th ed.; CRC Press: Boca Raton, FL, USA, 2016.
48. Cremonesi, A.; Djaoued, Y.; Bersani, D.; Lottici, P.P. Micro-Raman spectroscopy on polyethylene-glycol assisted sol–gel meso and macroporous WO₃ thin films for electrochromic applications. *Thin Solid Films* **2008**, *516*, 4128–4132. [CrossRef]
49. Xie, F.Y.; Gong, L.; Liu, X.; Tao, Y.T.; Zhang, W.H.; Chen, S.H.; Meng, H.; Chen, J. XPS studies on surface reduction of tungsten oxide nanowire film by Ar⁺ bombardment. *J. Electron. Spectrosc. Relat. Phenom.* **2012**, *185*, 112–118. [CrossRef]
50. Wang, X.G.; Jang, Y.S.; Yang, N.H.; Yuan, L.; Pang, S.J. XPS and XRD study of the electrochromic mechanism of WOₓ films. *Surf. Coat. Technol.* **1998**, *99*, 82–86. [CrossRef]
51. Dupin, J.-C.; Gonbeau, D.; Vinatier, P.; Levasseur, A. Systematic XPS studies of metal oxides, hydroxides and peroxides. *Phys. Chem. Chem. Phys.* **2000**, *2*, 1319–1324. [CrossRef]
52. Leftheriotis, G.; Papaefthimiou, S.; Yianoulis, P.; Siokou, A.; Kefalas, D. Structural and electrochemical properties of opaque sol–gel deposited WO₃ layers. *Appl. Surf. Sci.* **2003**, *218*, 275–280. [CrossRef]
53. Lide, D.R. *Handbook of Chemistry and Physics*, 81st ed.; CRC Press: Boca Raton, FL, USA, 2000.
54. Salleh, F.; Saharuddin, T.S.T.; Samsuri, A.; Othaman, R.; Yarmo, M.A. Effect of Zirconia and Nickel Doping on the Reduction Behavior of Tungsten Oxide in Carbon Monoxide Atmosphere. *Int. J. Chem. Eng. Appl.* **2015**, *6*, 389–394. [CrossRef]
55. Zhao, Y.; Chen, H.; Wang, X.; He, J.; Yu, Y.; He, H. Flower-like tungsten oxide particles: Synthesis, characterization and dimethyl methylphosphonate sensing properties. *Anal. Chim. Acta* **2010**, *675*, 36–41. [CrossRef] [PubMed]
56. Bard, A.J.; Faulkner, L.R. *Electrochemical Methods: Fundamentals and Applications*, 2nd ed.; Wiley: New York, NY, USA, 2001.
57. Zhou, K.; Wang, H.; Liu, J. Coloration and Ion Insertion Kinetics Study in Electrochromic WO₃ Films by Chronoamperometry. *Int. J. Electrochem. Sci.* **2020**, *15*, 7821–7832. [CrossRef]
58. Deepa, M.; Joshi, A.G.; Srivastava, A.K.; Shivaprasad, S.M.; Agnihotry, S.A. Electrochromic Nanostructured Tungsten Oxide Films by Sol-gel: Structure and Intercalation Properties. *J. Electrochem. Soc.* **2006**, *153*, C365–C376. [CrossRef]
59. Maho, A.; Nicolay, S.; Manceriu, L.; Spronck, G.; Henrist, C.; Cloots, R.; Vertruyen, B.; Colson, P. Comparison of Indium Tin Oxide and Indium Tungsten Oxide as Transparent Conductive Substrates for WO₃-Based Electrochromic Devices. *J. Electrochem. Soc.* **2017**, *164*, H25–H31. [CrossRef]
60. Lupo, C.; Eberheim, F.; Schlettwein, D. Facile low-temperature synthesis of nickel oxide by an internal combustion reaction for applications in electrochromic devices. *J. Mater. Sci.* **2020**, *55*, 14401–14414. [CrossRef]
61. Sivakumar, R.; Shanthakumari, K.; Thayumanavan, A.; Jayachandran, M.; Sanjeeviraja, C. Coloration and bleaching mechanism of tungsten oxide thin films in different electrolytes. *Surf. Eng.* **2007**, *23*, 373–379. [CrossRef]
62. Sahu, D.R.; Hung, C.-Y.; Wang, S.-C.; Huang, J.-L. Existence of electrochromic reversibility at the 1000th cyclic voltammetry for spin coating WO₃ film. *Ionics* **2017**, *23*, 3227–3233. [CrossRef]
63. Berggren, L.; Jonsson, J.C.; Niklasson, G.A. Optical absorption in lithiated tungsten oxide thin films: Experiment and theory. *J. Appl. Phys.* **2007**, *102*, 083538. [CrossRef]
64. Berggren, L.; Niklasson, G.A. Optical charge transfer absorption in lithium-intercalated tungsten oxide thin films. *Appl. Phys. Lett.* **2006**, *88*, 081906. [CrossRef]
65. Chen, P.-W.; Chang, C.-T.; Ko, T.-F.; Hsu, S.-C.; Li, K.-D.; Wu, J.-Y. Fast response of complementary electrochromic device based on WO₃/NiO electrodes. *Sci. Rep.* **2020**, *10*, 8430. [CrossRef]
66. Pillatsch, L.; Östlund, F.; Michler, J. FIBSIMS: A review of secondary ion mass spectrometry for analytical dual beam focussed ion beam instruments. *Prog. Cryst. Growth Charact. Mater.* **2019**, *65*, 1–19. [CrossRef]
67. Vickerman, J.C.; Briggs, D. *ToF-SIMS: Materials Analysis by Mass Spectrometry*, 2nd ed.; IM Publications LLP: Chichester, UK; SurfaceSpectra Ltd.: Manchester, UK, 2013.

68. Lee, S.-H.; Cheong, H.M.; Tracy, C.E.; Mascarenhas, A.; Pitts, J.R.; Jorgensen, G.; Deb, S.K. Alternating current impedance and Raman spectroscopic study on electrochromic a-WO₃ films. *Appl. Phys. Lett.* **2000**, *76*, 3908–3910. [CrossRef]
69. Shim, H.-S.; Kim, J.W.; Sung, Y.-E.; Kim, W.B. Electrochromic properties of tungsten oxide nanowires fabricated by electrospinning method. *Sol. Energy Mater. Sol. Cells* **2009**, *93*, 2062–2068. [CrossRef]
70. Kondalkar, V.V.; Mali, S.S.; Kharade, R.R.; Mane, R.M.; Patil, P.S.; Hong, C.K.; Kim, J.H.; Choudhury, S.; Bhosale, P.N. Langmuir–Blodgett self organized nanocrystalline tungsten oxide thin films for electrochromic performance. *RSC Adv.* **2015**, *5*, 26923–26931. [CrossRef]
71. Sequeira, C.A.C.; Santos, D.M.F. Tungsten Oxide Electrochromic Windows with Lithium Polymer Electrolytes. *J. Electrochem. Soc.* **2010**, *157*, J202–J207. [CrossRef]
72. Yoo, S.J.; Lim, J.W.; Sung, Y.-E.; Jung, Y.H.; Choi, H.G.; Kim, D.K. Fast switchable electrochromic properties of tungsten oxide nanowire bundles. *Appl. Phys. Lett.* **2007**, *90*, 173126. [CrossRef]
73. Mattson, M.S. Li insertion into WO₃: Introduction of a new electrochemical analysis method and comparison with impedance spectroscopy and the galvanostatic intermittent titration technique. *Solid State Ion.* **2000**, *131*, 261–273. [CrossRef]
74. Wang, L.S.; Hichwa, B.P.; Sapers, S.P.; Mathew, J.G.H.; O'Brien, N.A. Impedance Spectroscopy Study of Physical Vapor Deposited Amorphous WO₃ Electrochromic Thin Films. *Electrochem. Soc. Proc.* **1996**, *95*, 63–75.
75. Evecan, D.; Gurcuoglu, O.; Zayim, E.O. Electrochromic device application of tungsten oxide film with polymer electrolytes. *Microelectron. Eng.* **2014**, *128*, 42–47. [CrossRef]
76. Pehlivan, E.; Niklasson, G.A.; Granqvist, C.G.; Georén, P. Ageing of electrochromic WO₃ coatings characterized by electrochemical impedance spectroscopy. *Phys. Status Solidi A* **2010**, *207*, 1772–1776. [CrossRef]
77. Wang, L.; Zhao, J.; He, X.; Gao, J.; Li, J.; Wan, C.; Jiang, C. Electrochemical Impedance Spectroscopy (EIS) Study of LiNi$_{1/3}$Co$_{1/3}$Mn$_{1/3}$O₂ for Li-ion Batteries. *Int. J. Electrochem. Sci.* **2012**, *7*, 345–353.

Supplementary Materials for

Enhancing the Spectroelectrochemical Performance of WO$_3$ Films by Use of Structure-Directing Agents During Film Growth

Thi Hai Quyen Nguyen[a,b], **Florian Eberheim**[a,b], **Sophie Göbel**[a,b], **Pascal Cop**[b,c], **Marius Eckert**[a,b], **Tim P. Schneider**[a,b], **Lukas Gümbel**[a,b], **Bernd M. Smarsly**[b,c] **and Derck Schlettwein**[a,b*]

[a] Institute of Applied Physics, Justus-Liebig-University Giessen, Heinrich-Buff-Ring 16, 35392 Giessen, Germany
[b] Center for Materials Research (ZfM), Justus-Liebig-University Giessen, Heinrich-Buff-Ring 16, 35392 Giessen, Germany
[c] Institute of Physical Chemistry, Justus-Liebig-University Giessen, Heinrich-Buff-Ring 17, 35392 Giessen, Germany
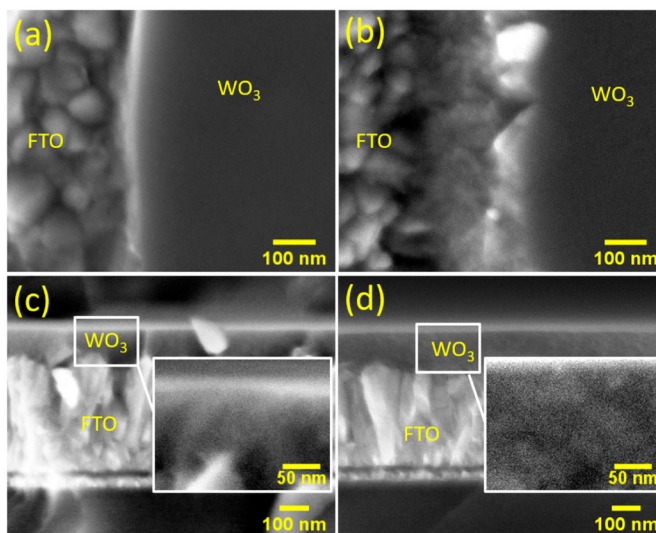*Corresponding author at email: schlettwein@uni-giessen.de

1

Figure S1. Top view (**a,b**) and cross-section (**c,d**) of WO₃|comp (**a,c**) and WO₃|μp400 (**b,d**) thin films on FTO. The left part of the film in (**a,b**) was scratched off to provide a comparison to the bare substrate.
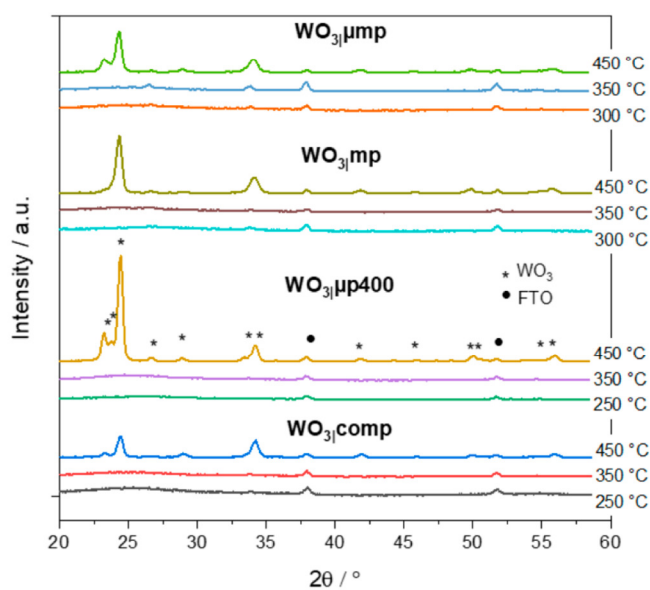

Figure S2. GIXRD patterns of WO₃|comp, WO₃|μp400, WO₃|mp and WO₃|μmp thin films calcined at different temperatures with reflexes assigned to triclinic WO₃ (JCPDS: 83-0947) and FTO marked with asterisks and dots, respectively.
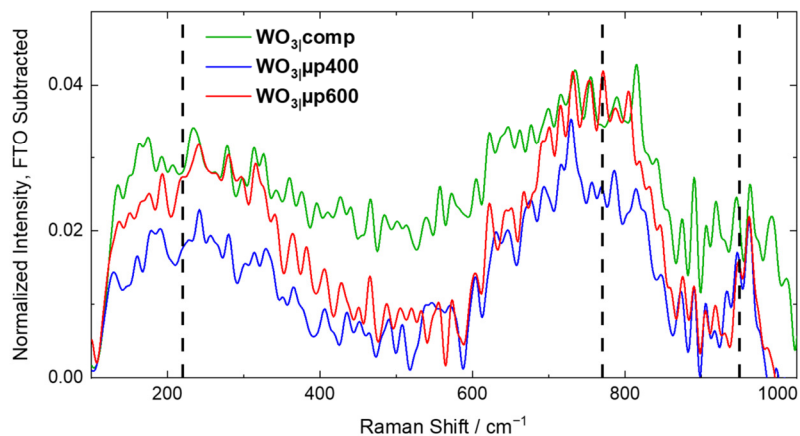
Figure S3. Normalized Raman spectra of thin films of WO₃ₗcomp (green), WO₃ₗμp400 (blue) and WO₃ₗμp600 (red).

Figure S4. Full scan (**a**), range of W 4f (**b**) and range of O 1s (**c**) of an XPS spectrum measured at a WO₃ₗcomp thin film.

3
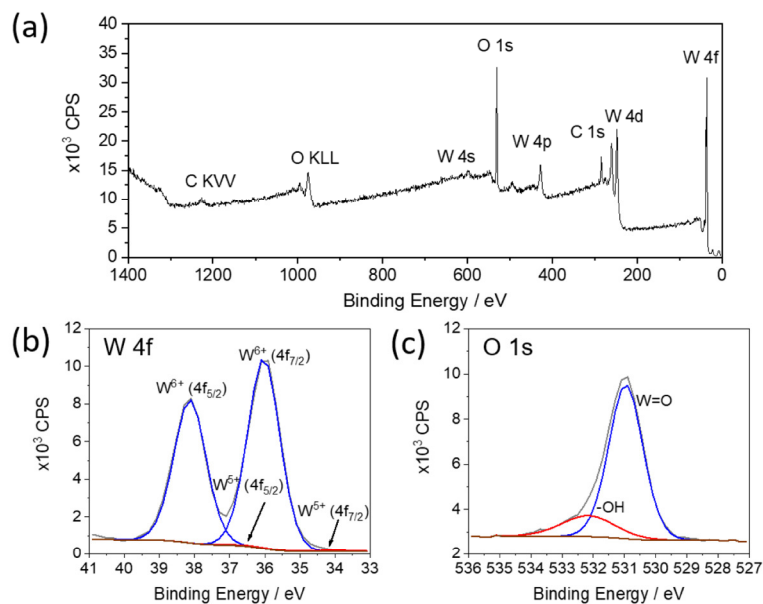
Figure S5. Full scan (**a**), range of W 4f (**b**) and range of O 1s (**c**) of an XPS spectrum measured at a WO₃ₗµp400 thin film.
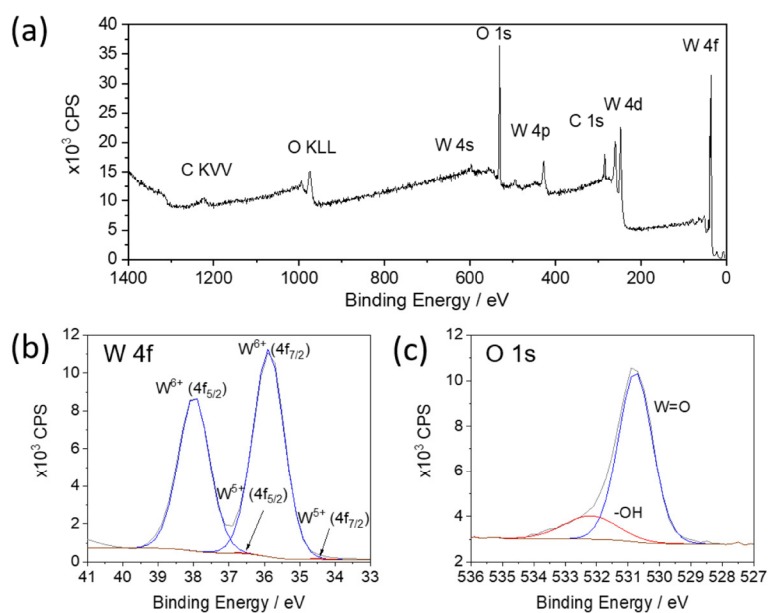

Figure S6. Full scan (**a**), range of W 4f (**b**) and range of O 1s (**c**) of an XPS spectrum measured at a WO₃ₗmp thin film.

4

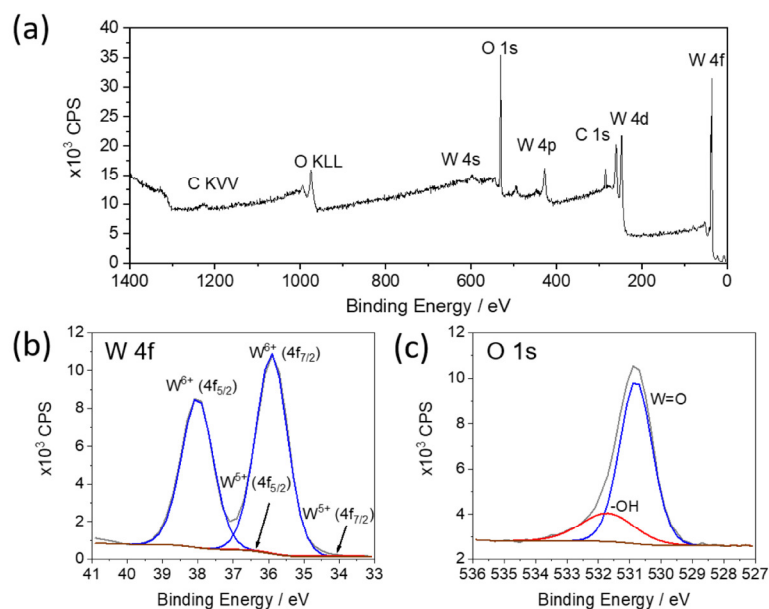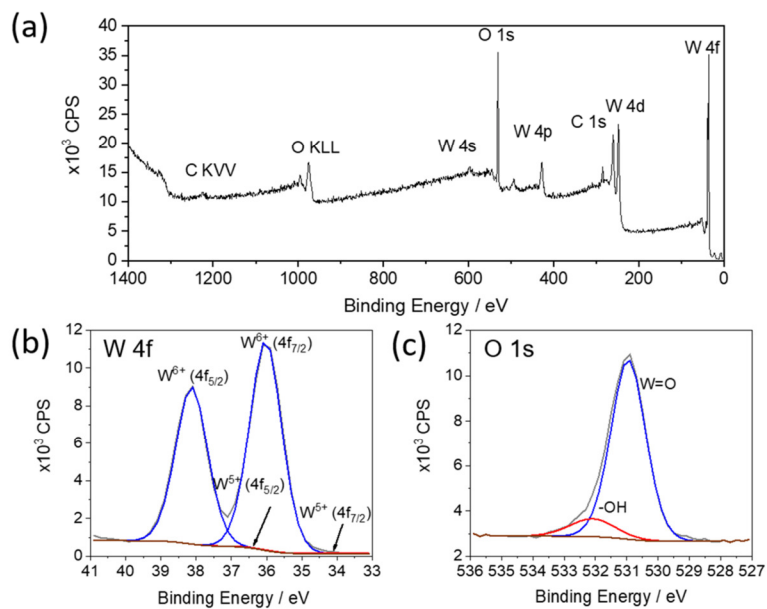**Figure S7.** Full scan (**a**), range of W 4f (**b**) and range of O 1s (**c**) of an XPS spectrum measured at a WO₃ıμmp thin film.
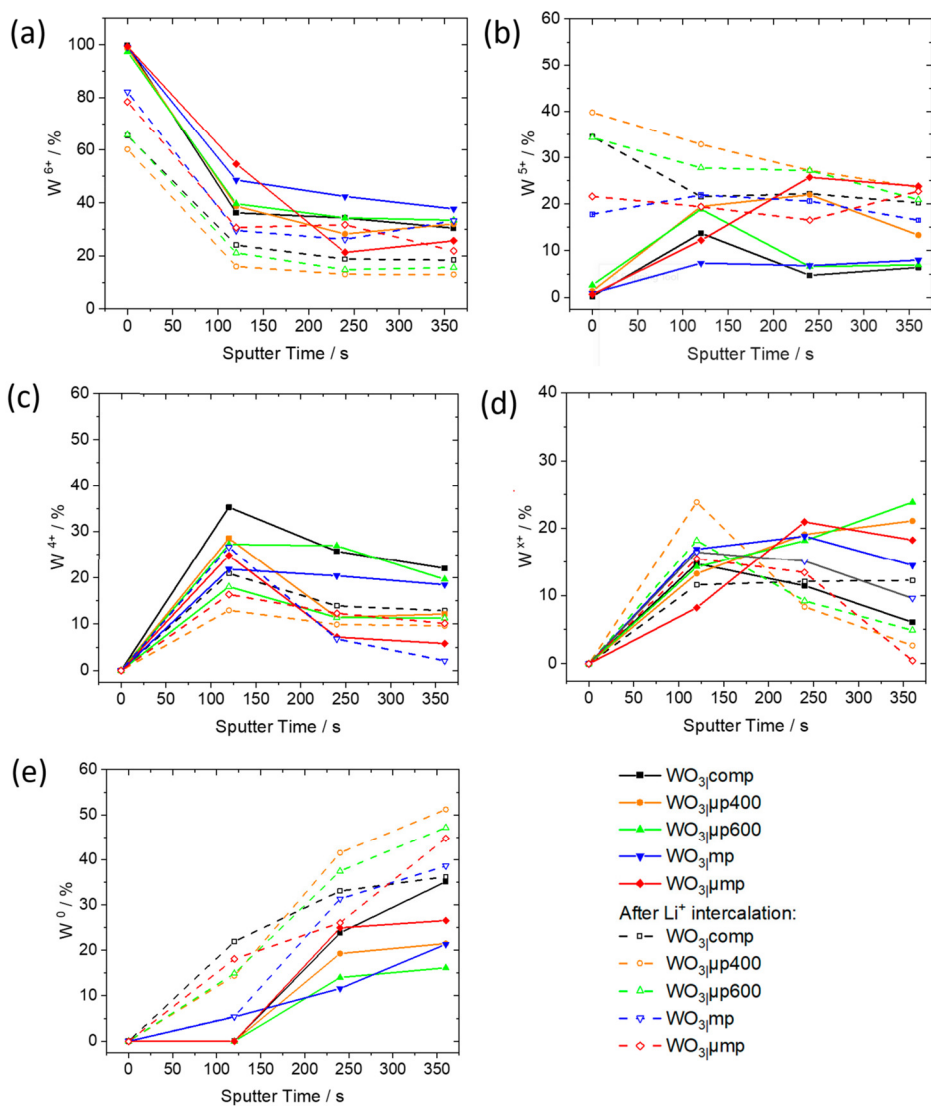
Figure S8. Amount of W^{6+} (**a**), W^{5+} (**b**), W^{4+} (**c**), W^{x+} (**d**) and W^0 states (**e**) in dependence of the sputter time obtained by XPS for thin films of WO$_{3|}$comp (black), WO$_{3|}\mu$p400 (orange), WO$_{3|}\mu$p600 (green), WO$_{3|}$mp (blue) and WO$_{3|}\mu$mp (red) as prepared (solid lines) and following intercalation (dashed lines). The lines between data points are meant to guide the eye.

6

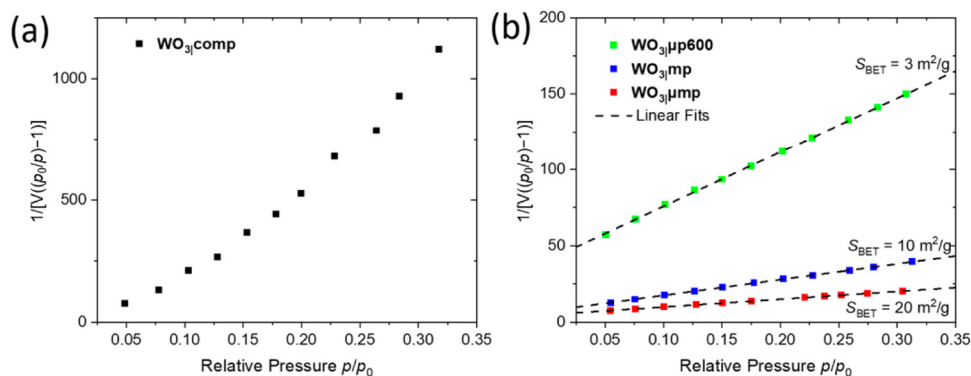**Figure S9.** BET plot of (**a**) WO₃|comp and (**b**) WO₃|μp600 (green), WO₃|mp (blue) and WO₃|μmp (red) thin films obtained from gas sorption analysis. The dashed black lines represent linear fits to the data.
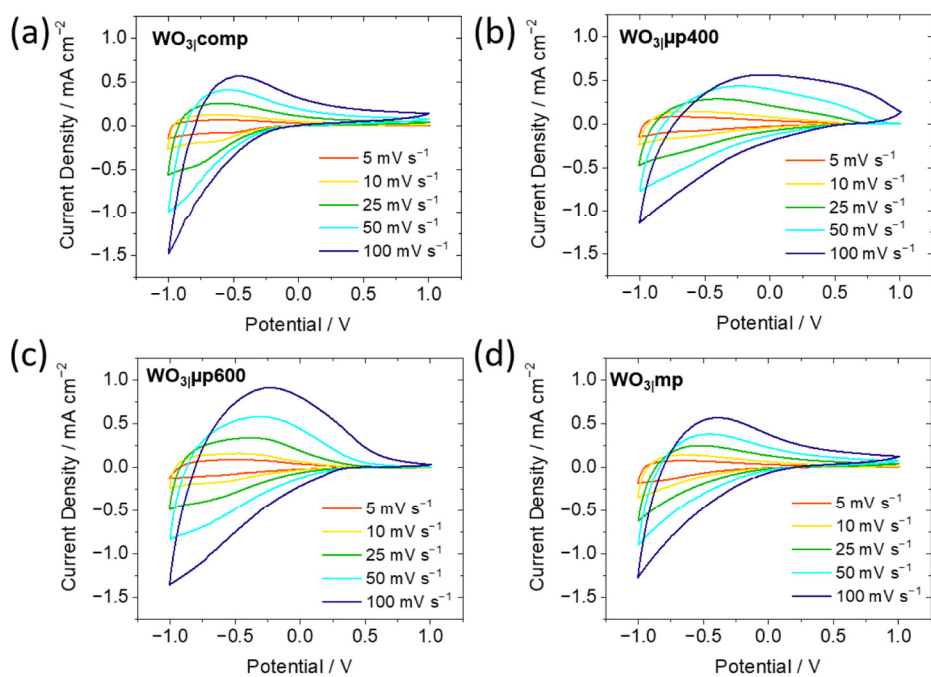

Figure S10. Cyclic voltammograms at the second cycle at different scan rates for thin films of (**a**) WO₃|comp, (**b**) WO₃|μp400, (**c**) WO₃|μp600 and (**d**) WO₃|mp in LiClO₄ in PC.

7
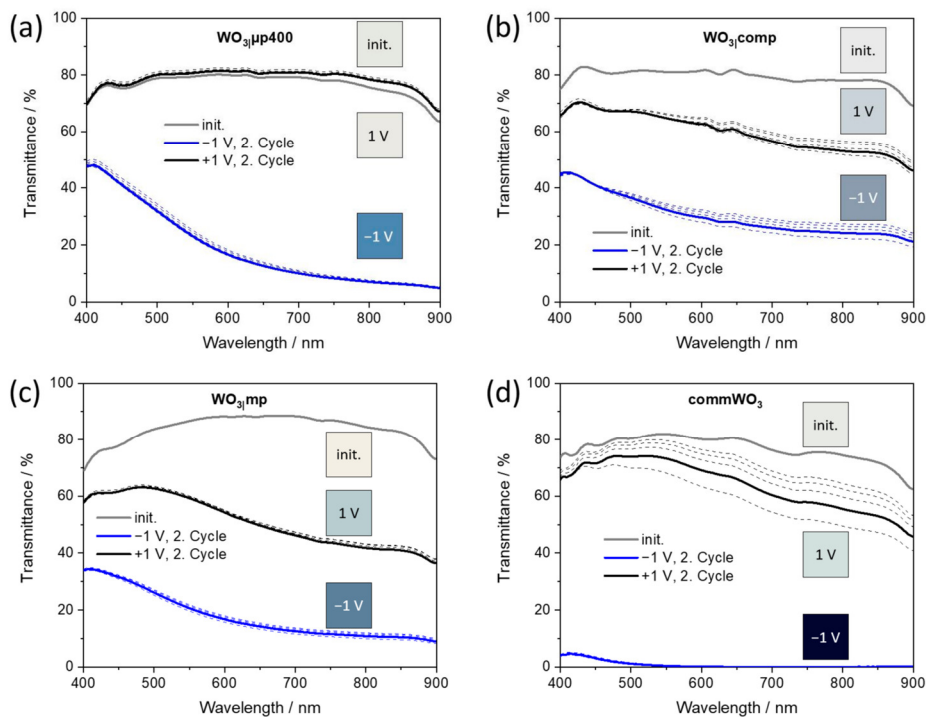
Figure S11. Transmittance spectra of (**a**) WO$_{3|}$μp400, (**b**) WO$_{3|}$comp, (**c**) WO$_{3|}$mp and (**d**) commWO$_3$ thin films measured in contact to LiClO$_4$ in PC at a scan rate of 5 mV s^{-1} in the initial state (init.), in the bleached (1 V) and the colored (−1 V) states for different cycles. The insets show the calculated color impressions for the second cycle of the films.

Table S1. Effective diffusion coefficient $D_{a,CV}$ determined from CV for scan rates of 5–100 mV s^{-1}, transmittance modulation ΔT_{710nm} and coloration efficiency CE_{710nm} obtained from CV at a scan rate of 5 mV s^{-1} of the films prepared with or without PEG 600 and annealed at different temperatures T.

Film Type	T / °C	$D_{a,CV}$ / cm^2 s^{-1}	ΔT_{710nm} / %	CE_{710nm} / cm^2 C^{-1}
WO$_{3|}$comp	350	3.1×10^{-11}	46.4	53.0
	450	6.2×10^{-13}	15.3	34.5
	550	1.6×10^{-13}	12.2	34.3
WO$_{3|}$μp600	350	3.1×10^{-11}	69.0	78.0
	450	1.0×10^{-11}	48.5	44.1
	550	4.0×10^{-12}	31.0	43.1

8
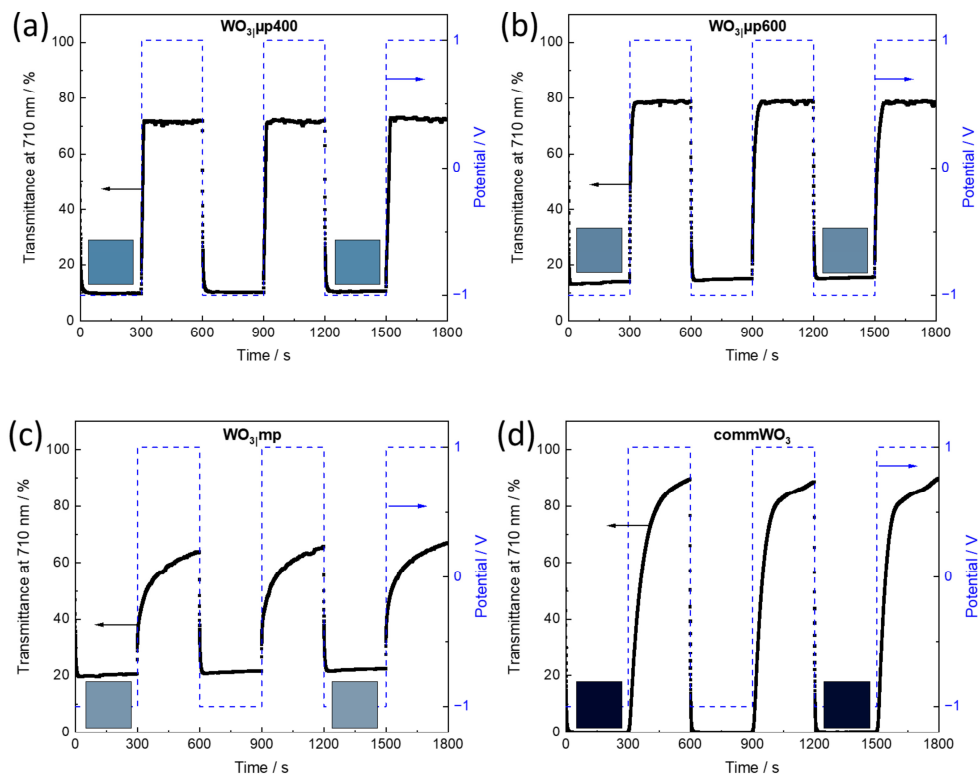
Figure S12. Optical transmittance at 710 nm of (**a**) WO₃|μp400, (**b**) WO₃|μp600, (**c**) WO₃|mp and (**d**) commWO₃ in contact to LiClO₄ in PC, recorded during chronoamperometry between the voltages depicted as dashed profiles. The insets show the calculated color impressions for the first and the third cycle of the films in the colored states.

9
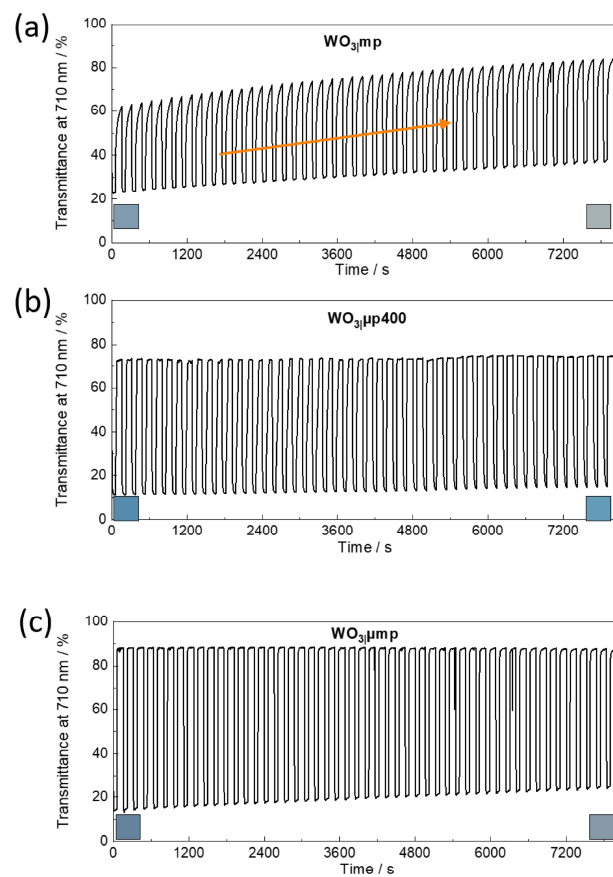
Figure S13. Optical transmittance at 710 nm of (**a**) WO₃ǀmp, (**b**) WO₃ǀμp400 and (**c**) WO₃ǀμmp in contact to LiClO₄ in PC, recorded during chronoamperometry with 50 cycles between −1 V applied for 60 s and 1 V applied for 100 s. The arrow in (**a**) indicates the shift of the transmittance to higher values. The insets show the calculated color impressions for the 4. and the 53. cycle of the films in the colored states.

10
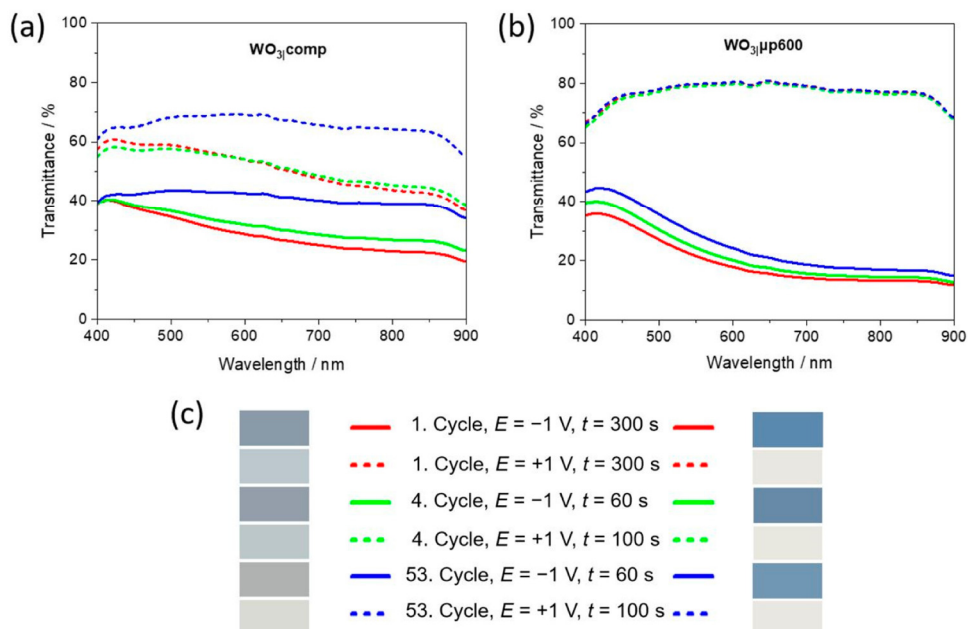
Figure S14. Transmittance spectra of WO₃|comp (**a**) and WO₃|μp600 (**b**) measured during chronoamperometry in contact to LiClO₄ in PC in the bleached (1 V) and the colored (−1 V) states at the first cycle (red), 4. cycle (green) and 53. cycle (blue). The calculated coloration impressions in the different states of these films are shown in (**c**).
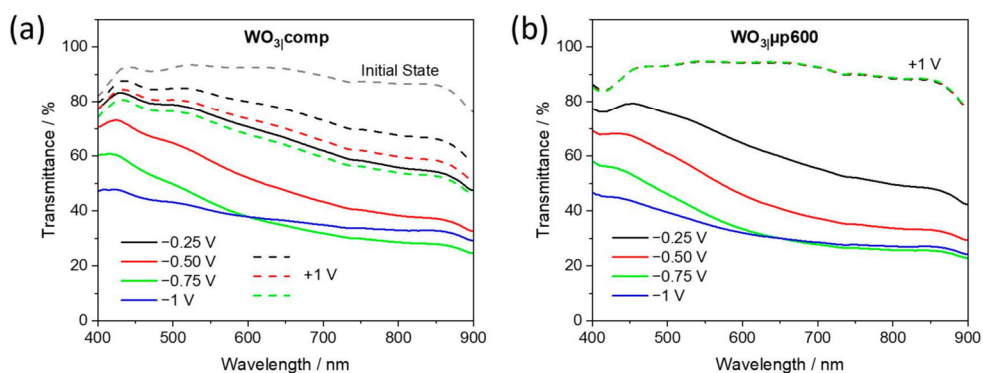
Figure S15. Transmittance spectra of a WO₃|comp film (**a**) and a WO₃|μp600 film (**b**) at the initial state and at different applied potentials during chronoamperometry in contact to LiClO₄ in PC.

11
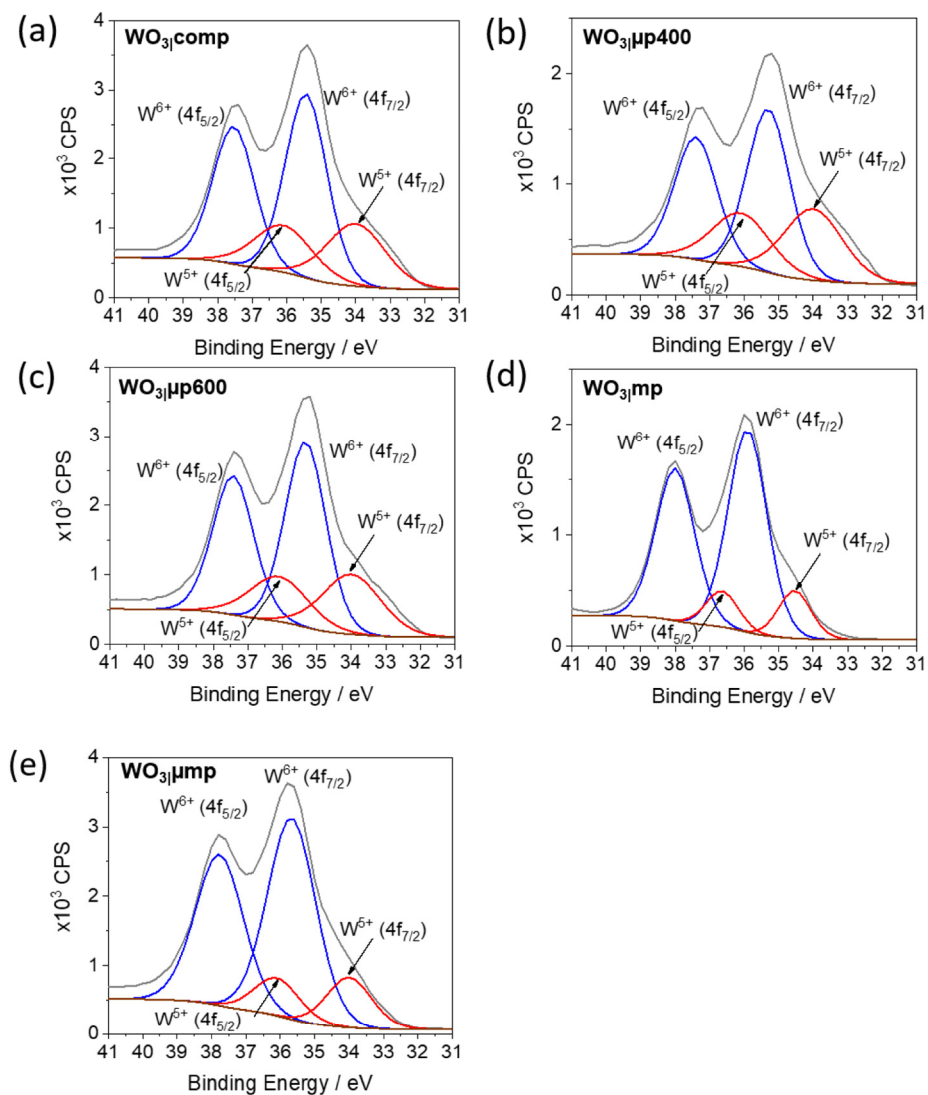
Figure S16. W 4f XPS spectra of intercalated thin films of WO$_3$|comp (**a**), WO$_3$|µp400 (**b**), WO$_3$|µp600 (**c**), WO$_3$|mp (**d**) and WO$_3$|µmp (**e**).

12
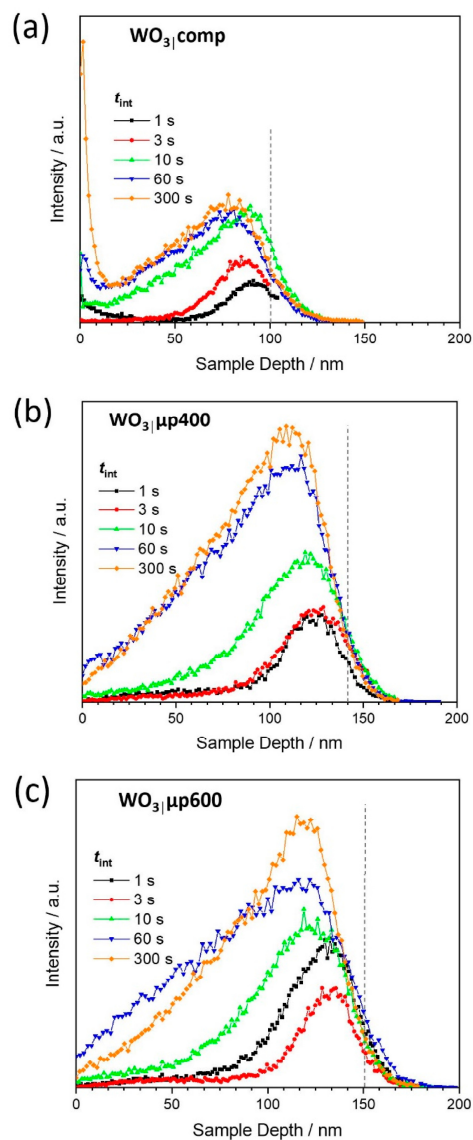
Figure S17. Depth profiles of the Li⁻ signal of (**a**) WO₃|comp, (**b**) WO₃|μp400 and (**c**) WO₃|μp600 films intercalated for different time spans t_{int} obtained from ToF-SIMS analysis. The approximate position of the interface between WO₃ and FTO is marked by dashed lines determined from depth profiles of the WO₃⁻ and SnO⁻ signals of the films.

13
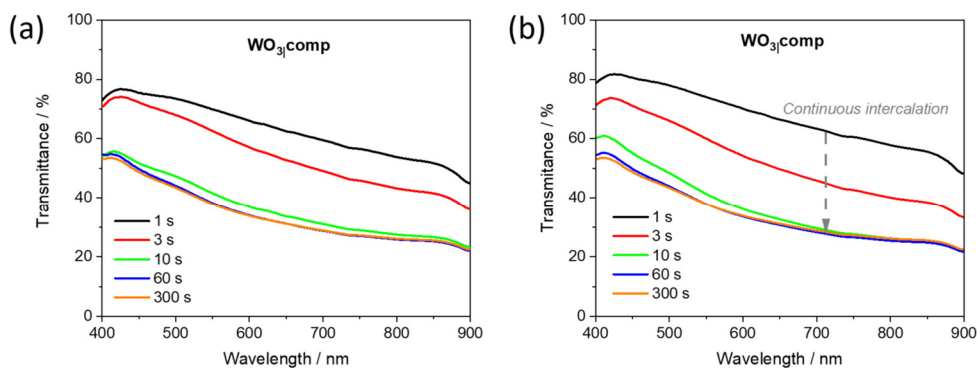
Figure S18. Transmittance spectra of different WO₃|comp films intercalated for various time spans (**a**) and of a specific WO₃|comp film at different intercalation time (**b**) measured during chronoamperometry in contact to LiClO₄ in PC at the colored (−1 V) state.

Table S2. Values of the resistances R_1 and R_{ct}, the parameters Q_{CPE} and α assigning to the CPE element, the limiting capacitance C_L, the Warburg coefficient A_W and the diffusion coefficient D_I obtained from A_W.

| Sample, applied potential	R_1 / Ω	R_{ct} / Ω	Q_{CPE} / Fs$(\alpha-1)$	α	C_L / F	A_W / Ωs$^{-1/2}$	D_I / cm² s^{-1}
WO₃|comp, −0.25 V	35.30	51.28	0.000457	0.7	0.0289	445.98	0.2×10^{-13}
WO₃|comp, −0.5 V	35.56	16.93	0.000375	0.7	0.0630	147.82	1.8×10^{-13}
WO₃|comp, −0.75 V	35.25	10.51	0.000098	0.8	0.1221	71.04	7.8×10^{-13}
WO₃|comp, −1.0 V	35.29	9.00	0.000034	0.9	0.0261	44.50	20×10^{-13}
WO₃|μp600, −0.25 V	30.85	248.31	0.000143	0.8	0.0325	47.41	17×10^{-13}
WO₃|μp600, −0.5 V	32.45	60.85	0.00050	0.7	0.0299	13.64	211×10^{-13}
WO₃|μp600, −0.75 V	31.71	37.95	0.00339	0.5	0.0394	17.65	126×10^{-13}
WO₃|μp600, −1.0 V	31.73	10.70	0.004	0.4	0.0281	89.78	4.9×10^{-13}

14

3.2   Additional Work in the Context of Publication 1

The findings from Publication 1 show that the addition of structure-directing agents into the precursor solution allowed for versatile modification of the porosity and internal film structure, crucial for the electrochromic performance of the WO$_3$ thin films. The presence of interconnected micropores or interconnected mesopores in the WO$_3$ films allowed facile transport of the ions through the film network leading to enhancement of the electrochromic properties of the WO$_3$ films. Additional aspects in sample preparation, role of pores in ion diffusion and the interplay of different layers in electrochromic devices were studied. Their discussion is presented here to serve a conclusive discussion.

Parallel to these studies and in cooperation with Pascal Cop, precursor solutions based on tungsten chloride [177,182] with either PIB$_{50}$-b-PEO$_{45}$ or PEG 600 as additives were used for the fabrication of WO$_3$ thin films. The spectroelectrochemical results of these films, however, revealed electrochromic switching characteristics only as good as the WO$_3$|comp films prepared with the peroxotungstic acid precursor solution. To analyze if the electrochromic switching of the films obtained from the tungsten chloride precursor solutions could be enhanced, a thin layer of gold was used as an alternative electron conductor. The gold layer was supposed to allow a fast electron injection into WO$_3$ and, thus, enhance the electrochromic switching properties as observed in [182]. For this purpose, a thin layer of gold was deposited on glass or on FTO-coated glass. In the case of the pure glass, a thin film of chromium was deposited in between serving as adhesive material for the gold layer on glass similar as reported in [182]. The spectroelectrochemical analyses of the WO$_3$ thin films deposited on the gold layer led to no improved switching characteristics confirming that the injection of the electrons from FTO or gold to WO$_3$ was similarly fast. The main drawback was the slightly bluish tint of the thin gold layers leading to an overall decrease in transparency of the samples in the bleached state. Therefore, detailed investigations, which were discussed in Publication 1, were restricted to the WO$_3$ thin films obtained from the peroxotungstic acid precursor solutions and deposited on FTO as electron conductive layer.

The fabrication of mesoporous WO$_3$ thin films from the peroxotungstic acid precursor solution in the presence of PIB$_{50}$-b-PEO$_{45}$ (WO$_3$|mp) could be improved in recent cooperation with Sophie Göbel leading to thin films of WO$_3$|mp* with enhanced electrochromic characteristics which are similar to those obtained with just PEG as additive [183]. Annealing the films at slightly higher temperatures than 300 °C but still lower than 350 °C allows for preparing mesoporous and widely amorphous films with

presumably proper decomposition and removal of polymers from the WO$_3$ thin films [183]. After the heat treatment these films were more transparent than those annealed at just 300 °C clearly indicating a more complete decomposition of residual polymer fragments present within the films and, thus, providing a higher accessibility of the films for Li$^+$ ions [183].

During the study of the WO$_3$ films in a three-electrode configuration by EIS it was found that the impedance of the reference electrode itself had a strong influence on the impedance measurements of the samples, particularly in the range of intermediate to high frequencies. It has been reported that the use of a reference electrode with high impedance might perturb the impedance measurement leading to artefacts rather than meaningful data points in the high frequency range [184–186]. In order to avoid distortions of the impedance measurement, the impedance of the reference electrode had to be quite small [185,186]. For this reason, the impedance measurements of the WO$_3$ films shown in Publication 1 were performed using a low-leak reference electrode with an impedance of ~1 kΩ instead of ~10 kΩ for the leak-free reference electrode which was used for the spectroelectrochemical analyses of the WO$_3$ thin films. The impedance of the reference electrodes were estimated from independent EIS measurements using an aqueous solution of KCl as electrolyte. The use of the low-leak reference electrode allowed for reliable data acquisition in the range of low frequencies as well as in the intermediate frequency range. Nevertheless, still no meaningful data points were obtained for the highest frequencies so that only data points from the intermediate to the low frequency range could be used for fitting the spectra. Therefore, further investigations on the choice of alternative reference electrodes would be interesting to be able to also gain reliable data points at the highest frequencies which might provide additional insight into, e.g. the contact resistance between the substrate and the WO$_3$ thin film [187].

Besides polymers, numerous different surfactants had been used as structure-directing agents for the preparation of WO$_3$ thin films [188–190]. Among them, Triton was utilized in a few studies [191–193]. However, the studies in which the films were prepared by spin-coating with Triton as an additive [192,193] did not focus on the electrochromic properties of WO$_3$. Therefore, in collaboration with Matthias Reichhardt and Leonardo Basso, the influence of Triton on the electrochromic properties of WO$_3$ was investigated. The amount of Triton added into the peroxotungstic acid precursor solution as well as the temperature and duration of the heat treatment of the as-deposited samples were varied to obtain WO$_3$ thin films with improved electrochromic properties [194,195].

The addition of Triton in a volume ratio of 2:10 into the precursor solution followed by annealing the films at 350 °C for 4 h resulted in homogeneous thin films of WO$_3$ with electrochromic switching characteristics [195] similar to those obtained for the WO$_3$|µp600 and WO$_3$|µmp films (Publication 1). Hence, quite different approaches using different structure-directing agents for the fabrication of WO$_3$ thin films with good electrochromic performance could be established in this work.

3.2.1 Role of Pores for Diffusion and Charge Transport in WO$_3$ Thin Films

Further studies related to Publication 1 were carried out to distinguish between the diffusion rate of the ions within solid WO$_3$ and within pores of the film. Hence, large ions needed to be chosen that were able to diffuse into the pores but not into the solid WO$_3$. For this purpose, the reversible ferrocenium/ferrocene (Fc$^+$/Fc) redox couple was chosen since it is significantly larger than the typical intercalating ions such as Li$^+$ [196–199]. Cyclic voltammetry was performed at various scan rates on different WO$_3$ thin films as working electrode and using 5 mM ferrocene and 0.1 M tetrabutylammonium perchlorate (TBAP) in propylene carbonate (PC) as electrolyte solution. In addition, a plain FTO-coated glass substrate was analyzed serving as a reference sample.

In Figure 3.1, the CV curves measured at a scan rate of 10 mV s^{-1} are shown for the different samples with the current densities normalized to the geometric surface area of the samples. Pronounced cathodic as well as anodic peaks (Figure 3.1 (a)) can be observed especially for FTO, the WO$_3$|µmp film and the WO$_3$|mp* film (which was prepared by Sophie Göbel after adjustment of the annealing temperature for preparing films with accessible mesopores) that allow for an estimation of the redox potential of the Fc$^+$/Fc redox couple as an average value of the cathodic and the anodic peak potential [141]. In the case of FTO as electrode material, the redox potential of the Fc$^+$/Fc redox couple is found at around 0.32 V comparable to the value reported in the literature [200–202]. The values of the redox potential obtained with the WO$_3$|µmp film and the WO$_3$|mp* film as electrodes are quite similar (0.23 V and 0.21 V, respectively). The ratio of the cathodic and anodic peak current densities $j_{p,c}/j_{p,a}$ is close to 1 for all the electrodes shown in Figure 3.1 (a) speaking in favor of a reversibility of the redox reactions [141]. The WO$_3$|µmp or WO$_3$|mp* films showed the highest reversibility indicated by peak-to-peak separations ΔE_p of around 0.36 V and 0.26 V, respectively, smaller than $\Delta E_p = 0.65$ V determined for FTO, indicating smaller overvoltage for well accessible WO$_3$.

While $\left|E_{p,c} - E_{p/2}\right|$ is around 0.11 V for WO$_3$|μmp, WO$_3$|mp* and FTO, $\left|E_{p,a} - E_{p/2}\right| = 0.17$ V is found for the WO$_3$|μmp film close to the value of 0.11 V obtained for the WO$_3$|mp* film whereas $\left|E_{p,a} - E_{p/2}\right| = 0.24$ V is found for FTO pointing at an overvoltage in the oxidation of Fc at FTO as the main difference. The smaller overpotentials needed for the WO$_3$|μmp and the WO$_3$|mp* films speak in favor of more active sites due to a larger accessible internal film surface compared to plain FTO, despite the fact that the values of ΔE_p and $\left|E_p - E_{p/2}\right|$ differ from the values of around 60/n mV characteristic for diffusion-controlled reversible redox reactions with fast electron transfer [141]. For the films of WO$_3$|comp, WO$_3$|μp600 and WO$_3$|mp (Figure 3.1 (b)), no clear cathodic and anodic peaks can be distinguished in the CV curves, typical for irreversible redox reactions [141]. However, as expected, the open circuit potentials and the potential range in which oxidation of Fc and reduction of Fc$^+$ occur roughly lie in the same range as for WO$_3$|μmp, WO$_3$|mp* and FTO.
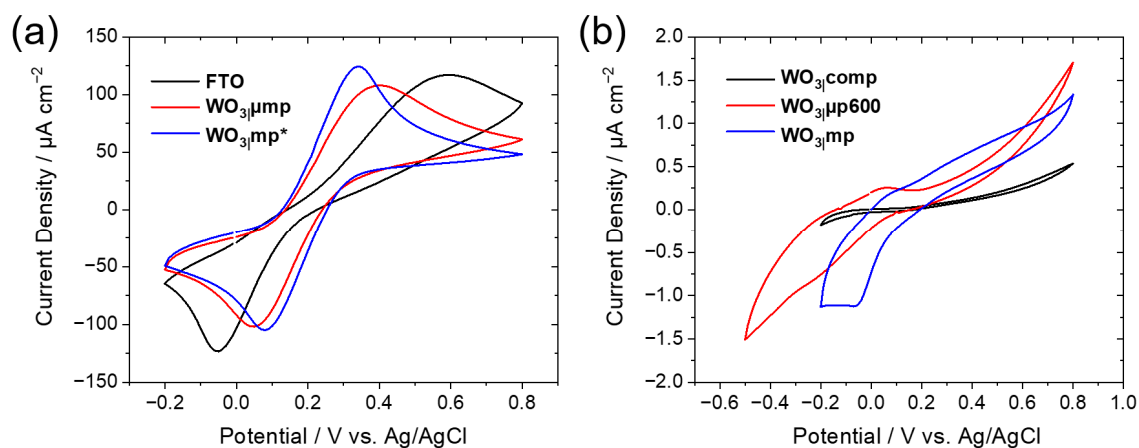
Figure 3.1: Cyclic voltammograms of ferrocene in PC measured at 10 mV s^{-1} using (a) FTO, WO$_3$|μmp and WO$_3$|mp* and (b) WO$_3$|comp, WO$_3$|μp600 and WO$_3$|mp as electrodes.

The current densities at the WO$_3$|μmp and WO$_3$|mp* films are found in a similar range as for the plain FTO (Figure 3.1 (a)), speaking for a limitation of the current by diffusion in the electrolyte. However, for the WO$_3$|comp film as well as the films of WO$_3$|μp600 and WO$_3$|mp (Figure 3.1 (b)), the current densities are found two orders of magnitude smaller indicating a hindrance by a process slower than the diffusion of Fc in the electrolyte.

These observations correlate well with those reported for TiO$_2$ films which were prepared using a different combination of PIB$_{50}$-b-PEO$_{45}$ and C$_{16}$mimCl as structure-directing agents and analyzed in an aqueous electrolyte solution containing Fe(CN)$_6^{3-}$ ions [178].

The TiO$_2$ mesoporous films showed only low peak currents and a larger peak potential separation indicating a poor interconnection of the mesopores and a hindrance of the reaction at the FTO surface [178]. For the TiO$_2$ films consisting of worm-like pores and interconnected mesopores the peak currents were in the same range as those for the plain FTO substrate because of well-accessible FTO [178].

Plotting $j_{p,c}$ and $j_{p,a}$ (Figure 3.1) in dependence of the square root of the scan rate $v^{1/2}$ according to the Randles-Ševčík equation (Equation 2.7, Figure 3.2) can be useful to determine the effective diffusion coefficients, D_c and D_a, of the reduction and oxidation process of the Fc$^+$/Fc redox couple where c is the concentration of ferrocene in the bulk of the electrolyte and n is the number of electrons transferred in the reaction ($n = 1$ in this case) [141], which may, however, contain some contribution of electron transport in WO$_3$. For at least three CV curves measured at different scan rates, values of $j_{p,c}$ and $j_{p,a}$ could be determined for each of the samples and yielded linear plots speaking in favor of diffusion-limitation in all cases. The values of D_a are found smaller than those of D_c, in particular, when using films of WO$_3$|comp and WO$_3$|mp as electrodes, possibly caused by a larger solvation shell of Fc compared to Fc$^+$ [203]. Reference values for D_a of Fc in PC in the range of $(2.8 - 6.5) \cdot 10^{-6}$ cm^2 s^{-1} were reported [202–205]. Comparable values of D_a are expected for FTO. Due to the irreversible curve shape, however, these values are not reached. Consistent with a more ideal shape in the cathodic branch, nevertheless, the value of $D_c = 8.0 \cdot 10^{-7}$ cm^2 s^{-1} almost reaches the literature range as opposed to $D_a = 2.0 \cdot 10^{-7}$ cm^2 s^{-1} found for the strongly irreversible anodic branch.
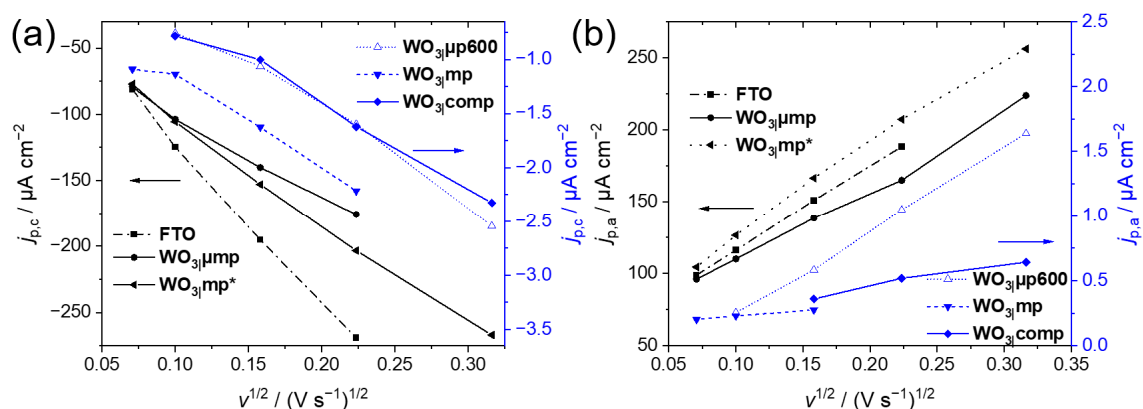

Figure 3.2: Current densities (a) $j_{p,c}$ and (b) $j_{p,a}$ in dependence of the square root of the scan rate $v^{1/2}$ for different WO$_3$ thin films as electrodes and FTO as reference.

With the WO$_3$|µmp and WO$_3$|mp* films, despite almost ideal shape of the CV, effective diffusion coefficients for the Fc$^+$/Fc redox couple of still $(1.4 - 3.5) \cdot 10^{-7}$ cm^2 s^{-1} are found. These lower values of D may well reflect a somewhat slower diffusion in pores as opposed to the bulk electrolyte. With WO$_3$|comp, WO$_3$|µp600 and WO$_3$|mp as electrode materials, however, the effective diffusion coefficients are much smaller and comparable to each other, in the range of $10^{-13} - 10^{-11}$ cm^2 s^{-1} (Table 3.1), indicating significant contributions of slow electron transport, reasonable if one assumes that micropores and the mesopores partially filled with remaining polymer are not accessible to Fc$^+$/Fc and require significantly longer electron pathways. These results show that the presence of interconnected mesopores in the WO$_3$|µmp film as well as accessible mesopores in the WO$_3$|mp* film provide a reaction limited by diffusion of Fc and/or Fc$^+$ in the electrolyte similar to the characteristics at plain FTO.

Table 3.1: Effective diffusion coefficients D_c and D_a of the Fc$^+$/Fc redox couple obtained by CV with different samples as electrodes.

Sample	D_c / cm^2 s^{-1}	D_a / cm^2 s^{-1}
FTO	$8.0 \cdot 10^{-7}$	$2.0 \cdot 10^{-7}$
WO$_3$|comp	$2.7 \cdot 10^{-11}$	$2.2 \cdot 10^{-12}$
WO$_3$|µp600	$3.5 \cdot 10^{-11}$	$2.0 \cdot 10^{-11}$
WO$_3$|mp	$3.5 \cdot 10^{-11}$	$3.5 \cdot 10^{-13}$
WO$_3$|mp*	$3.5 \cdot 10^{-7}$	$2.0 \cdot 10^{-7}$
WO$_3$|µmp	$2.0 \cdot 10^{-7}$	$1.4 \cdot 10^{-7}$

Rotating disk electrode experiments were additionally performed at different angular velocities using FTO, the WO$_3$|comp film and the WO$_3$|µmp film as electrodes to analyze the influence of the diffusion layer thickness in the bulk electrolyte on the kinetics of the redox reaction of the Fc$^+$/Fc redox couple. The WO$_3$|comp film showed no diffusion-limited current in agreement with a limitation of the reaction by charge transport in or charge transfer from WO$_3$ due to smaller accessibility of the films. For FTO and the WO$_3$|µmp film, reciprocal values of the measured current densities $1/j_m$ for a given potential in the diffusion-limited regime were observed that are linearly dependent on the reciprocal square root of the angular velocity $\omega^{-1/2}$, as predicted by the Koutecký-Levich equation (Equation 2.9) [141] and diffusion coefficients D_{RDE} of Fc were determined from the slope (Figure 3.3), assuming a kinematic viscosity of around 0.023 cm^2 s^{-1} as reported for a 0.1 M LiClO$_4$ in PC electrolyte solution [206].

$D_{\text{RDE}}(\text{FTO}) = 1.9 \cdot 10^{-6}\ \text{cm}^2\,\text{s}^{-1}$ and $D_{\text{RDE}}(\text{WO}_{3|}\mu\text{mp}) = 2.1 \cdot 10^{-6}\ \text{cm}^2\,\text{s}^{-1}$ are found close to the expected literature values [202–205], well confirming the validity of a dominant limitation by diffusion of Fc in the bulk electrolyte. For the WO$_{3|}\mu$mp film, however, additional kinetic limitations were present as indicated by an intercept significantly different from zero and well in line with the smaller D_{a} (Table 3.1). Such an intercept is characteristic for a superimposed kinetic limitation [141], presumably caused by subsequent diffusion through the pore system, consistent with the morphology of this electrode. Similar characteristics have been observed for the diffusion of benzoquinone through poly(vinyl ferrocene) [156].
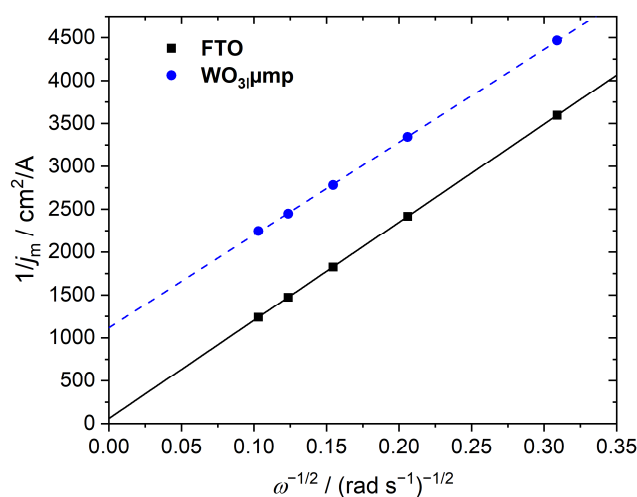

Figure 3.3: Reciprocal measured current densities $1/j_{\text{m}}$ in dependence of the reciprocal square root of the angular velocity $\omega^{-1/2}$ for WO$_{3|}\mu$mp or FTO as well as linear fits according to the Koutecký-Levich equation.

The values of the diffusion coefficients D_{c}, D_{a} and D_{RDE} of the Fc$^+$/Fc redox couple are around two orders of magnitude higher than the effective diffusion coefficients determined for the mixed transport of Li$^+$ ions and electrons in the WO$_{3|}\mu$mp films in contact with LiClO$_4$ in PC which are shown in Publication 1. This can be explained by the fact that the effective diffusion coefficient from Publication 1 is dictated by the diffusion of ions through the pores and also in the film volume of WO$_3$ whereas in the case of the Fc$^+$/Fc redox couple only the faster diffusion of the Fc$^+$/Fc redox couple through the pore network contributes to the diffusion coefficient.

The highly contrasting characteristics of WO$_3$|µp600 and WO$_3$|µmp in these reactions with Fc$^+$/Fc at first sight appear surprising in view of the high similarity of such samples in the electrochromic reaction with Li$^+$ (Publication 1). Such difference can be explained, however, by a poor accessibility of the narrow pore system of WO$_3$|µp600 for the large Fc as opposed to a good accessibility for the smaller Li$^+$ in contrast to a good accessibility of the considerably wider pores of WO$_3$|µmp for both species.

These results show that the improved effective diffusion coefficient obtained in Publication 1 is based on the facilitated diffusion of Li$^+$ through the accessible internal porous network leading to enhanced electrochromic performance of the films.

3.2.2 Charge Transport in Electrochromic Devices

To complement the impedance analyses shown in Publication 1 and in order to resolve the interplay of different charge transport processes, the impedance of complete electrochromic cells was investigated in cooperation with Leonardo Basso. These cells were constructed to resemble the architecture of established electrochromic devices (Figure 2.1).
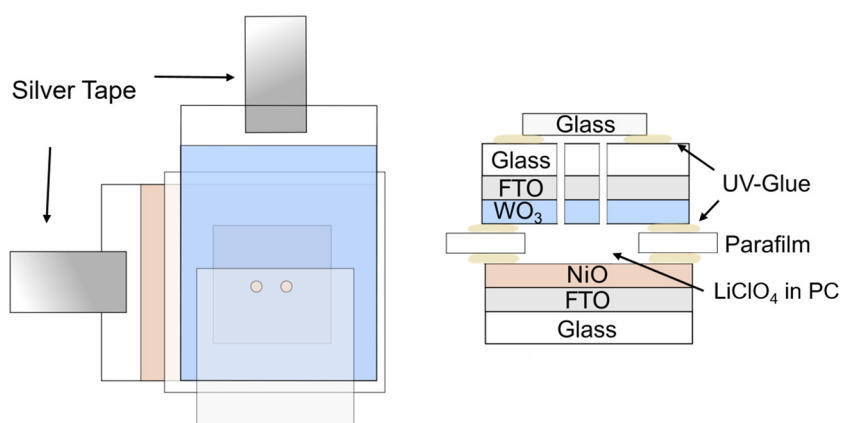
Figure 3.4: Sketch of an electrochromic device: Top view (left) and cross-section (right).

The electrochromic devices ECD|comp and ECD|µp600 consisted of either a WO$_3$|comp or WO$_3$|µp600 thin film as the working electrode and a thin film of NiO as the counter electrode which was prepared as described in [207]. Both films were deposited on FTO-coated glass. The thin films were combined using Parafilm M as a spacer and sealed together with UV-glue which is shown in Figure 3.4. LiClO$_4$ in PC as electrolyte was

filled into the cell through the holes in the glass which were drilled prior to deposition of WO$_3$. Afterwards, the holes were sealed by a cover glass and UV-glue. A piece of silver tape was attached on each FTO-coated glass for electric contact. Impedance measurements were performed with an AC amplitude of 10 mV at -2.5 V, a potential at which WO$_3$ is in its colored state. In a separate experiment performed by Leonardo Basso using a traditional electrochemical cell and a reference electrode (RE), this was confirmed by a voltage between WO$_3$ and the RE around -1.04 V and between the RE and NiO around 1.37 V at -2.5 V between WO$_3$ and NiO [208].

An equivalent circuit shown in Figure A.1 (a) was presented and used in [209] for fitting impedance spectra of a complete electrochromic device consisting of a sputtered WO$_3$ film, a sputtered NiO film and LiClO$_4$ in PC as electrolyte. In particular, R_0 was assigned to the series resistance caused by the substrate and the wires [209]. The interfaces between the electron conductive layer and the electrochromic film or the ionic storage layer could be described by the contact resistances R_1 and R_5 along with the capacitances C_1 and C_5 [209]. Similarly, the charge transfer resistances R_2 and R_4 accompanied by the capacitances C_2 and C_4 represented the interfaces between the electrochromic film or the ionic storage layer with the electrolyte [209]. Insights into the charge transport within the electrochromic film or the ionic storage layer might be gained from the contribution of the sum of R_1 and R_2 or R_4 and R_5, respectively. The electrolyte was described with the diffusion resistance R_3 and the semi-infinite type Warburg impedance element Z_w representing the diffusion of the intercalating ions [209]. The capacitance C_3 stood for the capacitance effect of the electrolyte [209].

The obtained Nyquist plots (Figures A.1 (b) and (c)) could be fitted with the equivalent circuit shown in Figure A.1 (a). Since the experimental impedance data could also be represented by significantly simplified models (Figures A.2 and 3.5), the relevance of each physical quantity assigned by the complex model (Figure A.1 (a)) is limited. Nevertheless, the obtained parameters are discussed since they provide a direct comparison to independent experimental results and since their meaning is preserved in the simpler models. For both electrochromic devices (Table A.1), the diffusion resistance R_3 of the electrolyte is much smaller than the values reported in [209] indicating that the contributions of some other components in the impedance spectra were not clearly separated from each other but tend to overlap [141]. Nevertheless, the series resistances R_0 are found in a similar range as the values obtained from the analysis of the WO$_3$ thin films in the half-cell configuration reported in Publication 1. This is expected since the identical equipment and wires were used in both cases. The capacitances C_1 to C_5 also

exhibit no relevant differences among the cells suggesting a constant contribution of electrons and ions in the devices. The contact resistances to FTO, however, are for both devices significantly smaller at one electrode (R_1) than at the other electrode (R_5). Since the NiO thin films were prepared under similar conditions for both devices and the values of R_5 are comparable to each other, it can be assumed that R_5 can be assigned to the contact resistance between FTO and NiO while R_1 represents the contact resistance between FTO and WO$_3$ speaking in favor of a better contact of the WO$_3$ films on FTO. R_1 of ECD|µp600 is about a factor of 6 smaller than of ECD|comp indicating an improved contact of WO$_3$|µp600 on FTO compared to WO$_3$|comp. For each device, the charge transfer resistances at the film/electrolyte interfaces, R_2 and R_4, are comparable speaking in favor of a constant charge transfer at WO$_3$ and NiO. Nevertheless, the value of R_2 of ECD|comp is about 8 times higher than that of ECD|µp600. This corresponds well with the accumulation of Li$^+$ ions at the surface of the WO$_3$|comp films as revealed by ToF-SIMS analysis of the thin films after intercalation of Li$^+$ shown in Publication 1. The accumulation of Li$^+$ possibly acted as a barrier between the WO$_3$ thin film and the electrolyte that impeded the charge transfer. The WO$_3$|µp600 films consisting of interconnected micropores, however, provided a homogeneous distribution of Li$^+$ within the films. The absence of an accumulation of Li$^+$ ions at the film surface of WO$_3$|µp600 enabled a facile charge transfer between WO$_3$|µp600 and the electrolyte. The sum of R_1 and R_2 or R_4 and R_5 might serve as a valuable estimation for the overall resistance of the WO$_3$ or NiO films towards charge transport. For both devices, the sum of R_1 and R_2 is significantly smaller than that of R_4 and R_5 indicating more facile charge transport through WO$_3$ compared to NiO. The sum of R_1 and R_2 of ECD|µp600 is smaller compared to ECD|comp at almost constant sum of R_4 and R_5, speaking in favor of a facile charge transport through the microporous WO$_3$|µp600 film. From the Warburg coefficient A_w (Table A.1) the diffusion coefficient D_I of the Li$^+$ ions could be determined using Equation 2.13. D_I obtained from the complete electrochromic devices are found in the lower range of D_I determined at different applied potentials in Publication 1 (D_I(WO$_3$|comp) = $(0.2 - 20) \cdot 10^{-13}$ cm^2 s^{-1}; D_I(WO$_3$|µp600) = $(4.9 - 211) \cdot 10^{-13}$ cm^2 s^{-1}) using the half-cell configuration, possibly caused by the different type of cell configurations leading to different cell components contributing to the Warburg impedance Z_w. For the complete devices, in particular, the ionic transport in WO$_3$ as well as in NiO is represented by Z_w whereas the diffusion of ions in the electrolyte can be regarded as significantly faster [206] than in the films and is, thus, not relevant for Z_w. ECD|comp exhibits a smaller D_I compared to ECD|µp600 which is in good agreement with the tendency of D_I obtained from the half-cell configurations.

Hence, a clear difference is still preserved for D_I determined for the complete devices speaking in favor that the diffusion of ions in NiO did not relevantly limit the overall ionic transport compared to WO$_3$|comp. Faster transport of ions in ECD|µp600 provided by the microporous WO$_3$|µp600 film is, thereby, confirmed.

In view of the small number of characteristic features in the experimental impedance spectra of the devices, the equivalent circuit presented in Figure A.1 (a) seems to be overparameterized for the impedance spectra of this work. If the equivalent circuit is simplified to the one shown in Figure A.2 (a), fits are obtained that provide an equally good match of the data. This equivalent circuit unites R_1, R_2, C_1 and C_2 into R_{1+2} and C_{1+2} and R_4, R_5, C_4 and C_5 into R_{4+5} and C_{4+5}, respectively. The capacitance C_3 was replaced with a constant phase element CPE_3 to allow a more accurate fit of the data. The resistances, R_{1+2} and R_{4+5}, assigned to the charge transport into and through each of the electrochromic films (Table A.2) are significantly smaller for one of the films (R_{1+2}, presumably WO$_3$) than for the other (R_{4+5}, presumably NiO) for both devices. Such assignment is derived from the fact that R_{4+5} is found in the same order of magnitude (same kind of NiO) whereas R_{1+2} shows a factor of 10 (different WO$_3$) indicating a facilitated charge transport to and through the WO$_3$ films. ECD|µp600 shows a smaller R_{1+2} and a higher diffusion coefficient D_I obtained from the Warburg coefficient A_w than ECD|comp. The diffusion resistances R_3 of the electrolyte was still smaller than reported in [209] and the values C_{1+2}, C_{4+5} and Q_{CPE3} also show no significant trends among the cells. These results along with the series resistances R_0 are well in line with those obtained from fitting the data with the equivalent circuit shown in Figure A.1 confirming that a simple equivalent circuit might be sufficient to clarify these simple Nyquist plots of ECD|comp and ECD|µp600 with one dominating semicircle as, by the way, also reported in [209].

However, the equivalent circuit presented in Figure A.2 still exhibits many parameters. Further simplification of the equivalent circuit leads to that shown in Figure 3.5 (a), typically used for fitting impedance spectra of electrochromic thin films studied in a half-cell configuration [30,160,161,168], still provided meaningful fit results for all parameters (Figure 3.5 and Table 3.2). As expected, the series resistance R_0 caused by the substrate and the electrolyte and the limiting capacitance C_L assigned to the charge accumulation in the film at low frequencies are similar to the values shown in Tables A.1, A.2 and in Publication 1. The resistance R_{ct} summarizes the charge transport within the WO$_3$ and NiO thin films as well as the respective charge transfer to/from the electrolyte.

A constant phase element *CPE* describing all the interfaces in the devices was used instead of a capacitance to allow for more precise fits of the data. The Warburg impedance Z_w represents the ion diffusion in the thin films of WO$_3$ and NiO.
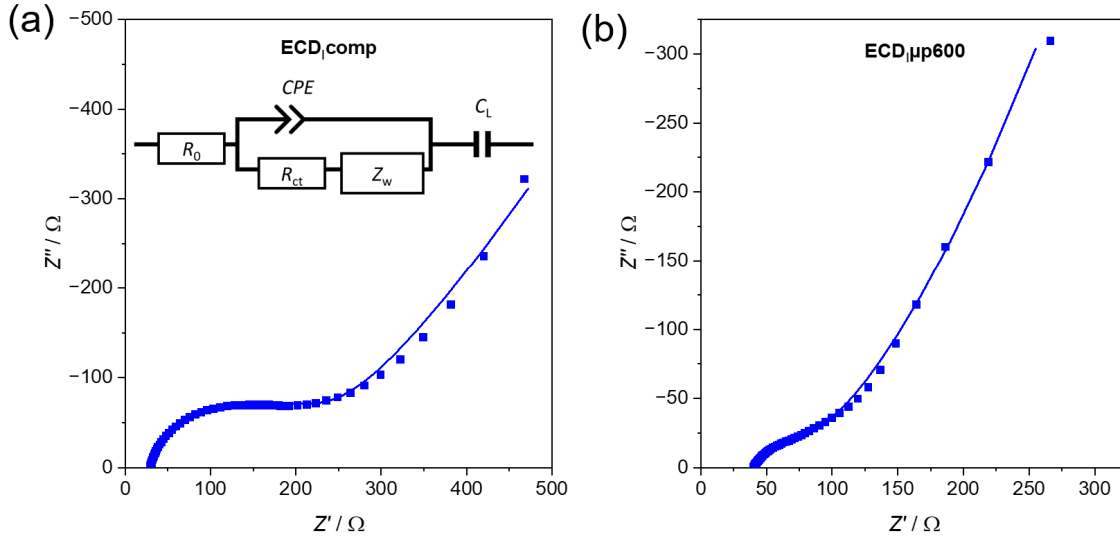

Figure 3.5: Nyquist plots of (a) ECD|comp and (b) ECD|μp600. The inset (a) show the equivalent circuit used for fitting (solid lines) the experimental data (points).

If NiO would strongly influence the overall transport, no clear differences would be expected in the fitting results of the devices using different WO$_3$ thin films. However, the data obtained from the fits (Table 3.2) show a clear difference for ECD|μp600 with a higher D_I and a smaller R_{ct} than for ECD|comp indicating a facilitated transport of ions and electrons in ECD|μp600. The finding for the whole cells shows that the difference between the thin films of WO$_3$|comp and WO$_3$|μp600 translates into significantly different device properties. These properties can be resolved by such a very simple equivalent circuit presented in Figure 3.5 that had already been used in Publication 1 for the analyses of individual WO$_3$ thin films in the half-cell configuration. The values of R_{ct} are in good agreement with the results obtained from the ToF-SIMS analysis of the WO$_3$ thin films after intercalation of Li$^+$ (Publication 1). Li$^+$ ions were homogeneously distributed in the WO$_3$|μp600 films. As opposed to WO$_3$|comp, no accumulation of Li$^+$ ions at the film surface was present. A facile charge transfer between WO$_3$|μp600 and the electrolyte, well in line with the smaller R_{ct} obtained for ECD|μp600, was, therefore, observed. Such correlation between two independent analyses clearly confirm that the very simple equivalent circuit (Figure 3.5) allowed for a good description of the impedance data and led to meaningful fit results.

Table 3.2: Values of the resistances R_0 and R_{ct}, the parameters Q_{CPE} and α representing the CPE element, the limiting capacitance C_L, the Warburg coefficient A_w and the diffusion coefficient D_I obtained from A_w of ECD|comp and ECD|µp600.

	ECD|comp	ECD|µp600
R_0 / Ω	27.66	40.39
R_{ct} / Ω	201.18	53.42
Q_{CPE} / F s$^{(\alpha-1)}$	0.000088	0.000412
α	0.7	0.7
C_L / µF	32295	12723
A_w / Ω s$^{-1/2}$	205.93	146.98
D_I / cm^2 s^{-1}	$1.80 \cdot 10^{-13}$	$3.54 \cdot 10^{-13}$

In summary, a very simple equivalent circuit (Figure 3.5) is sufficient to describe the overall transport processes within the devices. The facilitated charge transport processes for WO$_3$|µp600 could still be preserved in a full electrochromic device configuration and led to overall enhanced transport properties in ECD|µp600 as revealed by the higher D_I and significantly lower R_{ct} compared to ECD|comp. Separate impedance analysis of the NiO thin films in a half-cell configuration would be of interest to confirm the transport processes occurring for these films in contact with the electrolyte providing more precise insight into the contribution of NiO to the impedance spectra of the complete electrochromic devices.

4 Thin Films of F_{40}PcCu as a New Electrochromic Material (Publication 2)

Background for Publication 2

A second series of experiments in the course of this Ph.D. thesis was devoted to the investigation of mixed ionic and electronic transport and the corresponding switching characteristics of different substituted phthalocyanine thin films as an alternative group of electrochromic materials. This part followed up on earlier studies on the electrochromic properties of vapor-deposited thin films of copper perfluoro phthalocyanine F_{16}PcCu and copper octakis-perfluoroisopropyl-perfluoro phthalocyanine F_{64}PcCu, published by Juliane Weissbecker [54] and Stefanie Nagel [53] from the same group. The degree of fluorination in copper phthalocyanines clearly influences the intermolecular coupling induced by van der Waals interactions and, thus, the rate of diffusion of ions and transfer of electrons in the films [54]. Films of F_{16}PcCu showed strong intermolecular coupling, well in line with their crystallinity, leading to a facile electron transfer [54–56] whereas the diffusion of ions was attenuated and limited the rate of the electrochromic switching process [54]. Sterically hindered F_{64}PcCu with eight bulky perfluoroisopropyl groups exhibited a weak interaction between the molecules which led to amorphous thin films providing a facile ion diffusion while the rate of the electrochromic reaction was limited by the transfer of electrons [53,54].

The results from the earlier studies [53,54] triggered attempts to tune the substitution pattern to provide a molecule with an intermediate strength of intermolecular interaction in the solid state. A moderate degree of intermolecular interactions offers the chance of a simultaneous fast transport of both ions and electrons in such films ("goldilocks principle" of an optimum at an intermediate coupling strength).

Context of Publication 2

Based on this approach, a golden mean of F_{16}PcCu and F_{64}PcCu was sought and established in Publication 2. In cooperation with Marius Pelmuş, Christopher Colomier and Sergiu M. Gorun, a new type of phthalocyanine, copper tetrakis-perfluoroisopropyl-perfluoro phthalocyanine F_{40}PcCu, was designed and studied. In F_{40}PcCu, two of the four isoindole units have been substituted as in F_{16}PcCu and the other two have been modified as in F_{64}PcCu. Homogeneous F_{40}PcCu thin films of different thickness could be prepared by vapor deposition as revealed by SEM and atomic force microscopy (AFM). The influence of the film thickness on the intermolecular coupling was monitored by *in situ* UV-Vis spectroscopy during film growth. The measured absorption spectra of F_{40}PcCu exhibited a Soret- and Q-band typical for phthalocyanines [47,116]. The absorption spectra of F_{64}PcCu in the solid state were reported to be quite similar to the solution spectrum, in good agreement with the presence of a very weak intermolecular coupling of the molecules in the films [56]. For F_{40}PcCu, a clear broadening and splitting of the Q-band were found for the films in comparison to the solution spectra, indicating a higher interaction of the molecules in the solid state than in solution [50,210]. However, the Q-band of the F_{40}PcCu thin films were still not as broad as in F_{16}PcCu [54]. A moderate degree of intermolecular interaction of the F_{40}PcCu molecules in the films is thereby confirmed which is stronger than that of F_{64}PcCu but still weaker than that of F_{16}PcCu.

Electrochemical and spectroelectrochemical measurements of the F_{40}PcCu films were performed in aqueous KCl electrolyte solution to analyze the rate of the transport of electrons and ions in the films and the changes in the optical absorption spectra.

Reproducible CV curves could be achieved after conditioning, representing high R_{EC} of the redox reaction of the F_{40}PcCu films along with intercalation and extraction of the charge-balancing K^+ ions as already observed for other fluorinated phthalocyanine films [53,54]. Compared to thin films of F_{16}PcCu or F_{64}PcCu [54], the redox reactions of the F_{40}PcCu films showed no transport limitation up to a significant larger scan rate and also higher effective diffusion coefficients obtained via chronoamperometry. This speaks in favor of moderate interactions of the F_{40}PcCu molecules in the solid state which led to facilitated transport of electrons and ions through the films.

The optical absorption spectra revealed reversible changes of the F_{40}PcCu films during the redox reaction including the appearance of a new absorption band of around 540 nm upon reduction typical for phthalocyanine rings in their reduced state as found for F_{16}PcCu [54] and F_{64}PcCu [53,54].

Chronoamperometry and *in situ* UV-Vis spectroscopy was performed over multiple cycles to study the electrochromic switching and the stability of the material upon reduction and re-oxidation. Fast electrochromic switching along with high R_{EC} of the F_{40}PcCu films was provided over at least 200 cycles with short response times of about 0.3 s.

4.1   Publication 2: The influence of intermolecular coupling on electron and ion transport in differently substituted phthalocyanine thin films as electrochromic materials: a chemistry application of the Goldilocks principle

Derck Schlettwein and Sergiu M. Gorun planned and supervised the project. The F_{40}PcCu molecule was synthesized by cooperation partners from the Seton Hall University (Marius Pelmuş, Christopher Colomier and Sergiu M. Gorun). The characterization of the molecules in solution were carried out by the cooperation partners from Seton Hall University as well as by me. All thin films of F_{40}PcCu were prepared and characterized by me. I planned, performed and evaluated all electrochemical measurements on these thin films, drafted the manuscript, fine-tuned it with Derck Schlettwein and we discussed it with all co-authors.

PCCP

Physical Chemistry Chemical Physics

rsc.li/pccp

ROYAL SOCIETY
OF CHEMISTRY

PAPER

Sergiu M. Gorun, Derck Schlettwein *et al.*
The influence of intermolecular coupling on electron and ion transport in differently substituted phthalocyanine thin films as electrochromic materials: a chemistry application of the Goldilocks principle

PCCP

PAPER

The influence of intermolecular coupling on electron and ion transport in differently substituted phthalocyanine thin films as electrochromic materials: a chemistry application of the Goldilocks principle†

Thi Hai Quyen Nguyen,[a] Marius Pelmuş, [ID][b] Christopher Colomier, [ID][b] Sergiu M. Gorun [ID] *[b] and Derck Schlettwein [ID] *[a]

The transport of both electrons and ions in organic mixed ionic and electronic conductors such as phthalocyanines, is essential to allow redox reactions of entire films and, hence, to impart electrochromism. Thin films of a new type, tetrakis-perfluoroisopropyl-perfluoro phthalocyanine, **F$_{40}$PcCu** of different thicknesses were obtained *via* vapor deposition. The extent of the intermolecular coupling within the **F$_{40}$PcCu** films established by van der Waals interactions was investigated by *in situ* optical spectroscopy during film growth. The transfer of electrons and diffusion of counter cations in these films, as well as their electrochromic performance were characterized by electrochemical and spectroelectrochemical measurements with an aqueous solution of KCl as electrolyte. A moderate degree of intermolecular interaction of the **F$_{40}$PcCu** molecules in the solid state was observed, compared to non-fluoroalkylated perfluoro phthalocyanine, **F$_{16}$PcCu** and octakis-perfluoroisopropyl-perfluorophthalocyanine, **F$_{64}$PcCu**, which exhibit stronger and weaker coupling, respectively. The replacement of F by perfluoroisopropyl is, thereby, established as a valuable approach to tune this coupling of chromophores and, hence, the transport coefficients of electrons and ions in the solid films. Reversible changes of the films upon reduction and intercalation of K$^+$ counter ions and re-oxidation and expulsion of the counter ions were confirmed by simultaneously measured optical absorption spectra. Thin films of **F$_{40}$PcCu** showed a well-balanced, equally fast transport of electrons and ions. The films provided a fast and reversible switching process over at least 200 cycles indicating the stability of these materials.

[a] *Institute of Applied Physics and Laboratory of Materials Research, Justus-Liebig-University Gießen, Heinrich-Buff-Ring 16, 35392 Gießen, Germany. E-mail: schlettwein@uni-giessen.de*

[b] *Department of Chemistry and Biochemistry and Center for Functional Materials, Seton Hall University, 400 South Orange Ave, South Orange, NJ 07079, USA. E-mail: sergiu.gorun@shu.edu*

† Electronic supplementary information (ESI) available: Mass spectrometry, FT-IR spectra, concentration-dependent UV-Vis spectra, grazing incidence X-ray diffraction (GIXRD) pattern. See DOI: 10.1039/c9cp06709d

1 Introduction

Molecular thin films play an increasingly important role in electronic and optoelectronic devices as dielectric, conducting or semiconducting materials.[1] One specific example is their use as electrochromic layers, *i.e.* layers which reversibly change their color and/or light transmission upon their reduction or oxidation. Such layers are of potential use in display applications or as smart windows or smart mirrors.[2,3] When compared to classic electrochromic materials like WO$_3$, organic materials

offer faster switching due to their higher extinction coefficients which allow the use of thinner films.[4,5] In order to establish such higher switching rates, the diffusion of ions and the mobility of electrons in the films have to be optimized since both are needed at a given molecular site in the films in order for the redox reaction to occur. As a consequence, organic mixed ionic and electronic conductors (OMIEC) are needed for this purpose, a group of materials recently established in the literature.[6] For a number of such materials, namely polymer electronic (or hole-) conductors, water is needed in the films in order to provide channels of ionic conduction – polymers are chosen that are easily swollen with water.[7,8] Electrochromic reactions, however, have also been established for pure molecular semiconductors, namely phthalocyanines (Pc).[9]

In early studies, unsubstituted Pc (*e.g.*, **H$_{16}$PcCu**, Fig. 1a) showed partially reversible electrochromic oxidation.[10] Substitution of aromatic hydrogen atoms by electron-withdrawing groups facilitate an electrochromic reduction characterized by a highly increased reversibility.[11] Unsubstituted Pc, as well as

This journal is © the Owner Societies 2020

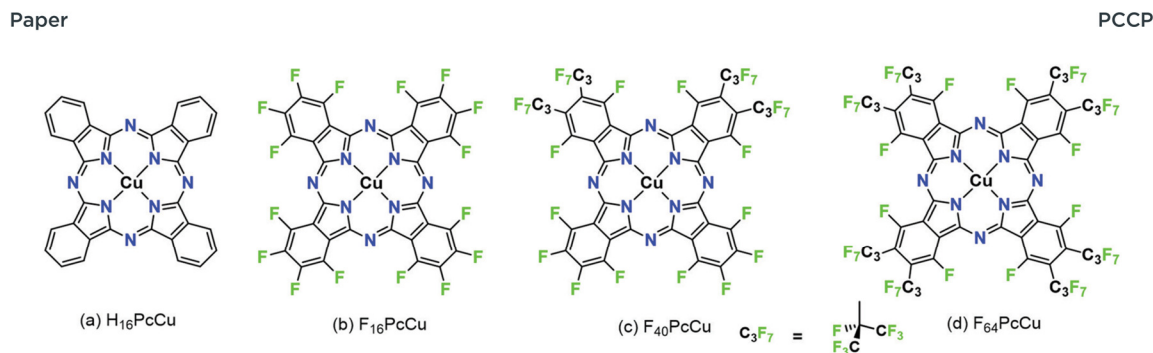*Phys. Chem. Chem. Phys.*, 2020, **22**, 7699–7709 | **7699**

Fig. 1 Structural formulae of copper phthalocyanines with different degree of fluorination.

suitably substituted Pc can be sublimed to form thin films by physical vapor deposition (PVD) on a variety of substrates. In the solid state, such Pc molecules typically form molecular crystals bound by van der Waals (vdW) interactions.[12] The weak intermolecular interactions result in polycrystallinity for a given molecule, e.g. α- and β-phases of unsubstituted Pc[13] or a variety of structures in thin films of, e.g. perfluorinated F$_{16}$Pc.[14] Different intermolecular orientations in these different crystalline phases leads to significant differences in the electronic coupling of the central aromatic chromophore systems and, hence, significant differences in their optical absorption spectra.[15] The strength of intermolecular vdW interactions in Pc molecules in solids can further be rationally tuned by a judicious choice of the substituents of the aromatic macrocycles, detected in the absorption spectra of thin films.[16,17] In a direct comparison of vapor-deposited thin films of a perfluorinated copper phthalo-cyanine, F$_{16}$PcCu (Fig. 1b), with those of a copper phthalocyanine in which the eight non-peripheral 8 H-atoms of the parent H$_{16}$PcCu had been substituted by F-atoms and the other, periph-eral 8 H-atoms were substituted by perfluoroisopropyl groups, F$_{64}$PcCu (Fig. 1d) it could be shown that the films of F$_{16}$PcCu exhibit strong electronic coupling, also leading to their crystal-linity, whereas those of sterically hindered F$_{64}$PcCu showed very weak coupling, in line with amorphous growth.[18]

Films of both F$_{64}$PcCu and F$_{16}$PcCu exhibited electrochromic switching upon their reduction and subsequent re-oxidation. However, in accordance with the strength of vdW interactions and, hence, electronic coupling of the aromatic macrocycle, the rate of switching in films of F$_{16}$PcCu was limited by ion diffusion (high electron mobility), as opposed to the switching rate in films of F$_{64}$PcCu that was limited by electron conduction (fast ion diffusion). These limiting cases, linked to the limiting structural features imparted by the lack or presence of bulky fluoroalkyl substituents, respectively, suggested that the optimiza-tion of the substitution pattern and, thus, of the vdW interactions of Pc molecules in the solid state could result in a molecule exhibiting sufficiently strong interactions favoring a high electronic coupling and thus electron mobility, but also still sufficiently weak to facilitate fast diffusion of charge-compensating ions in films.

Following this strategy (the "Goldilocks principle"), F$_{40}$PcCu was synthesized and characterized in the present work, Fig. 1c. In F$_{40}$PcCu 12 H-atoms of H$_{16}$PcCu are formally substituted by F but only 4 by perfluoroisopropyl groups. F$_{40}$PcCu exhibits an intermediate degree of steric hindrance, electronic deficiency and likely an intermediate strength of vdW interactions, therefore, a likely optimized balance between electron mobility and ion diffusion. Fast, reversible electrochromic switching is indeed realized in this optimized OMIEC and the consequences for technical application of potential devices are discussed below.

2 Experimental

2.1 Synthesis

Tetrafluorophthalonitrile, 1, 0.016 g (0.08 mmol), perfluoro-(4,5-diisopropyl)phthalonitrile, 2, 0.1 g (0.2 mmol), and copper(II) acetate monohydrate, 0.015 g (0.08 mmol), were mixed with a few drops of nitrobenzene in a glass vial, sealed with a Teflon cap and heated in a microwave reactor at 185 °C for 12 minutes. The crude products were separated via gravity column chromatography using silica gel 60 (63–200 μm) and a 0–15% gradient of ethyl acetate in hexanes, followed by an isocratic 30% ethyl acetate/hexanes blend to yield a mixture of F$_{64}$PcCu, F$_{52}$PcCu and F$_{40}$PcCu. The phthalocyanines were separated using flash chromatography in 0–50% CH$_2$Cl$_2$/hexanes. F$_{40}$PcCu was isolated as a deep-blue solid in 17% yield. UV-Vis (TFT): λ_{max} (log ε) 686 (5.33), 616 (4.64), 360 (4.85) nm (L mol^{-1} cm^{-1}); UV-Vis (ethanol): λ_{max} (log ε) 676 (4.95), 640 (4.74), 612 (4.49), 372 (4.62), 316 (4.52) nm (L mol^{-1} cm^{-1}); HRMS (ESI, negative mode, Fig. S1 in ESI†): calculated for C$_{44}$F$_{40}$N$_8$Cu + Cl$^-$ [M + Cl]$^-$ 1497.8586, found 1497.8611 (δ = 16.7 ppm), FT-IR (KBr disk) ν, cm^{-1} (intensity), Fig. S2 (ESI†): 2918.53 (w), 2850.76 (w); 1527.97 (w), 1491.21 (w) C=C aromatic; 1251.43 (s), 1171.29 (m), 1104.90 (w), C–F aliphatic and aromatic; 964.30 (w), 729.74 (w), 752.33 (w), 470.64 (w).

2.2 Chemicals and molecular characterization

All solvents (ACS grade or better) and reagents were purchased from commercial sources and used as received, unless stated otherwise. Copper acetate monohydrate and the fluorinated tetrafluorophthalonitrile, 1, (Fig. 2) were purchased from TCI Co., Ltd. Perfluoro-(4,5-diisopropyl)phthalonitrile, 2, was prepared as described in the literature.[19] F$_{16}$PcCu was purchased from TCI in sublimed grade, F$_{64}$PcCu was prepared as described in ref. 16.
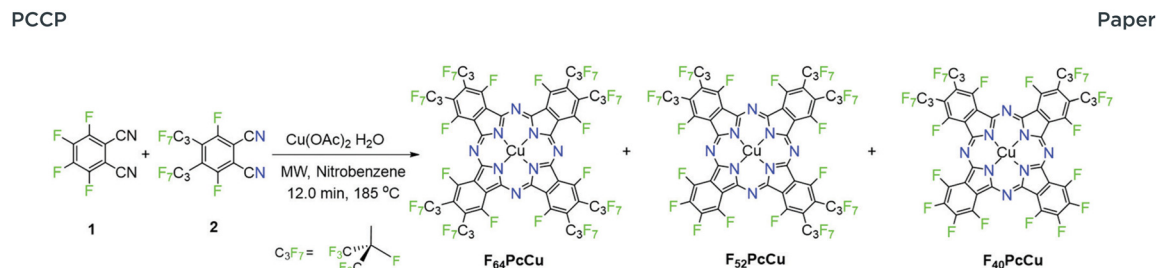
Fig. 2 Reaction scheme for the synthesis of perfluorinated copper phthalocyanines.

The microwave-assisted syntheses were performed using a CEM Discover system (CEM Corporation). Flash chromatography was carried out using a Combi*Flash Rf+*, (Teledyne ISCO). UV-Vis spectra were recorded on a Cary 500 Scan UV-Vis-NIR spectrophotometer. FT-IR spectra were recorded on a Nicolet 4700 FT-IR spectrophotometer using KBr pellets. High-resolution mass spectrometry (HRMS) data were obtained at Rutgers University (Newark, NJ) by direct injection of ethanolic solutions in an Apex-ultra 70 hybrid FT-MS. For the electrochemical investigations by CV (cyclic voltammetry) at a scan rate of 0.1 V s^{-1} and SWV (square wave voltammetry at a pulse amplitude of 50 mV, a frequency of 10 Hz and a potential step of 5 mV), solutions of the molecules in 0.1 M tetrabutylammonium tetrafluoroborate (TBATFB, Fluka, 99%, electrochemical grade) in trifluorotoluene (TFT, Sigma-Aldrich, ≥99%) were used. The measurements were carried out employing an IviumStat potentiostat/galvanostat, equipped with Pt wires as working electrode and counter electrode, respectively, and a leak-free Ag/AgCl reference electrode (LF-2, Innovative Instruments, Inc.) for which the potential was calibrated against ferrocene/ferrocenium (Sigma-Aldrich, 98%) at 0.4 V *vs.* Ag/AgCl[20] in dimethylformamide (Sigma-Aldrich, 99.8%). All experiments were performed at room temperature in a glovebox under dry nitrogen.

2.3 Preparation of thin films

Glass substrates coated with FTO (Kaivo, <15 Ohm sq^{-1}) were cut into 10 mm × 25 mm pieces. The FTO-coated glass pieces were cleaned for 15 min in RBS solution (Roth), acetone (Roth, ≥99.5%) and isopropanol (Roth, ≥99.8%), respectively, using an ultrasonic bath at room temperature. The cleaned substrates were dried with N$_2$ gas. A piece of adhesive tape from TESA was attached to the shorter edge of the substrate in order to keep an area of the substrate uncovered for later electrical contacting.

Thin films with different thicknesses of **F$_{40}$PcCu** were prepared on FTO-coated glass by physical vapor deposition in a vacuum chamber with a quartz crystal microbalance which was calibrated as reported in ref. 16 for monitoring the deposited mass and calculating an average film thickness based on an estimated density (2.2 g cm^{-3}) as an average value from the known values of **F$_{16}$PcCu** and **F$_{64}$PcCu**.[13,16] The vapor deposition was carried out at a pressure of <10^{-6} mbar and an evaporation rate of about 0.5–1 nm min^{-1} by resistively heating the powder of **F$_{40}$PcCu** in a BN crucible (Kurt J. Lesker Ltd). In order to analyze the thickness-dependent film growth of **F$_{40}$PcCu**, an optical fiber was attached to the vacuum chamber

and a pre-cleaned quartz glass (TED PELLA, INC.) was mounted into the chamber as a substrate. A lower deposition rate of 0.2 nm min^{-1} was chosen to allow measurements of the optical absorption spectra by a tec 5 diode array spectrometer during deposition at a pressure of <10^{-5} mbar. The sample was rotated between two positions to alternately vapor-deposit the film and measure the spectra as reported earlier.[16]

2.4 Characterization of thin films

The film coverage on the substrate and cross-sections of the films were analyzed by scanning electron microscopy (SEM) in a Zeiss MERLIN at an emission current of 100 pA and an acceleration voltage of 5 kV. The film morphology was investigated by atomic force microscopy (AFM) in air using a Smart SPM 1000 (AIST-NT) with NanoWorld Pointprobe SEIHR Non-Contact/Soft Tapping probes (tip radius < 12 nm) in an oscillating mode. Images were processed by the Gwyddion 2.55 program using the plane subtraction method and adjusting the individual lines by the median of differences. The crystallinity of the thin films was analyzed by grazing incidence X-ray diffractometry using a PAN-analytical X'Pert Pro MRD instrument with Cu-K$_\alpha$-radiation. The spectroelectrochemical analysis of the films was performed in a 1 M aqueous KCl (Aldrich, ≥99.5%) solution with a three-electrode setup. To remove the dissolved oxygen from the solution, N$_2$ gas was flushed through the solution before the measurements. During the measurements, N$_2$ gas was passed above the surface of the solution only, to avoid fluctuation of the solution. To contact the fluorinated phthalocyanine films for the spectroelectrochemical characterization, a Cu wire was attached with conductive Ag paste (Ferro GmbH) on the uncovered substrate area. Afterwards, the metal wire and the substrate area were sealed with Araldite Rapid epoxy resin. The prepared sample was mounted as working electrode in a glass cell (Starna) with a platinum wire counter electrode (Goodfellow, 99.995%) and a Ag/AgCl reference electrode (REF201 Red Rod, Radiometer analytical). Cyclic voltammetry between 0.6 V and −1.1 V at different scan rates and chronoamperometry between the bias potentials of 0.6 V and −1.0 V at a time delay of 3 s were carried out employing an IviumStat potentiostat/galvanostat. Optical spectra were simultaneously measured *in situ* by placing the working electrode into the beam of the tec5 diode array spectrometer. The charge measured during long-term switching experiments is underestimated by a factor of about 3.8 which is caused by a rather low sampling frequency (5 Hz compared to 1 kHz) needed to ensure reliable data acquisition by the spectrometer.

3 Results and discussion

3.1 Synthesis and properties of F$_{40}$PcCu

The synthesis method, Fig. 2, uses two different precursors with different propensities to form phthalocyanines. The ratio of precursors **1** vs. **2** is $2:2$ in **F$_{40}$PcCu**, but a ratio of $0.08/0.2 = 0.8:2$ was used in order to minimize the formation of the $4:0$ complex **F$_{16}$PcCu**. The complexes $1:3$, **F$_{52}$PcCu** and $0:4$, **F$_{64}$PcCu**, Fig. 2, also form, but the reported **1** vs. **2** ratio seems to give **F$_{40}$PcCu** in modest but maximum isolated yield. Further optimizations of either the reaction conditions or the purification method were not pursued. The structure of **F$_{40}$PcCu**, Fig. 2, depicts the complex in its "*cis*" form, with the two coordinating, C$_3$F$_7$-substituted isoindole rings, labeled 'isoR' adjacent, *i.e.* the N$_{isoR}$–Cu–N$_{isoR}$ angle is 90°. Alternatively the rings can be "*trans*", the N$_{isoR}$–Cu–N$_{isoR}$ angle being 180°. The assignment, in the absence of a single-crystal X-ray structure is based on the structure of the analogous F$_{40}$PcCo complex, for which an X-ray crystal structure has been reported.[21]

The spectral position of the Q-band of **F$_{40}$PcCu** in solution (Fig. 3) corresponds to that reported for F$_{40}$PcZn or F$_{40}$PcCo,[22] for which the "*cis*" structure of the substituents was proven, in good agreement with literature reports on Q-band differences for complexes in either "*cis*" or "*trans*" structure.[23,24] Our assignment of a "*cis*" structure for **F$_{40}$PcCu**, therefore, is fully consistent with the literature.

F$_{40}$PcCu exhibits solvent dependent UV-Vis spectra, Fig. 3. The main Q-band in TFT, 686 nm, appears at least twice as intense as the one in ethanol, 676 nm. The Beer–Lambert plots of concentration dependent spectra, Fig. S3 and S4 (ESI†), are linear, but the variation of absorbance of the Q-band with concentration is approximately double in TFT vs. ethanol. Taken together, the data suggest that a higher degree of aggregation exists in ethanol, consistent with ethanol axial coordination in **F$_{64}$PcCu**.[25]

Cyclic voltammetry (CV) and square wave voltammetry (SWV) were performed for solutions of **F$_{40}$PcCu** in direct comparison to solutions of **F$_{16}$PcCu** and **F$_{64}$PcCu** in order to discuss the
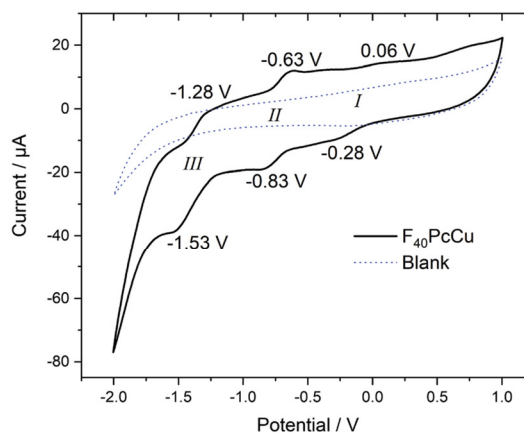

Fig. 4 Cyclic voltammetry at 0.1 V s^{-1} of **F$_{40}$PcCu** dissolved in 0.1 M TBATFB in TFT compared to a blank scan of the electrolyte in the absence of **F$_{40}$PcCu**.

influence of substituents on the redox potential of reduction reactions under otherwise identical conditions. The CV results for the new complex **F$_{40}$PcCu** are shown in Fig. 4 and the main findings are summarized together with the SWV results for all complexes in Table 1. Values measured for **F$_{16}$PcCu** reveal a potential for the first reduction (*I*) of -0.2 V and of the second reduction (*II*) of -0.9 V. The potential of *I* is found slightly less negative than the reported -0.6 V measured for the Zn-complex of F$_{16}$Pc in dimethylformamide, whereas that of *II* is found in accordance with the reported value (-0.9 V).[26] The values for **F$_{64}$PcCu** are found similar to those reported under comparable conditions[17] of $I = -0.06$ V, $II = -0.56$ V and $III = -1.17$ V.

The redox potentials indicate that **F$_{64}$PcCu** is easiest to reduce, followed by **F$_{40}$PcCu**, and **F$_{16}$PcCu**. This is consistent with the stronger electron-withdrawing effect of the C$_3$F$_7$ substituents vs. F atoms. The broad characteristics in the region of *I* speak in favor of a parallel reduction of differently aggregated species of **F$_{40}$PcCu** at this concentration needed to obtain reasonably high signals above background. Some small additional waves are detected which can be caused by solvent interaction with monomeric species, as also observed earlier for **F$_{64}$PcCu**.[17]

3.2 Film growth of F$_{40}$PcCu

Uniformly blue thin films, obtained after vapor deposition of **F$_{40}$PcCu** showed a compact film morphology consisting of

Fig. 3 UV-Vis spectra of **F$_{40}$PcCu** in ethanol (EtOH) and trifluorotoluene (TFT).

Table 1 Redox potentials (*E* in V vs. Ag/AgCl) of the redox waves of **F$_{16}$PcCu**, **F$_{40}$PcCu** and **F$_{64}$PcCu** in solution obtained from CV (0.1 V s^{-1}) and SWV experiments

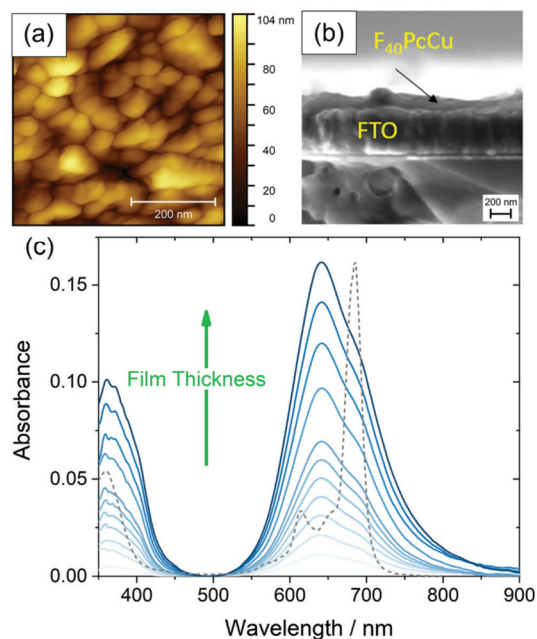| Wave	Method					
	CV			SWV		
E/V	*I*	*II*	*III*	*I*	*II*	*III*
F$_{16}$PcCu	-0.21	—	—	-0.19	-0.88	-1.64
F$_{40}$PcCu	-0.11	-0.73	-1.40	—	-0.71	-1.40
F$_{64}$PcCu	0.05	-0.53	—	0.02	-0.49	-1.40

Fig. 5 Morphology of a 35 nm thin film of **F$_{40}$PcCu** on FTO measured by AFM (a), cross-section of a 35 nm thin film F$_{40}$PCu on FTO observed by SEM (b) and optical absorbance spectra acquired during film preparation of **F$_{40}$PcCu** with a film thickness *d* of 0–35 nm on quartz glass at room temperature, the optical spectrum of **F$_{40}$PcCu** in TFT (see Fig. 3) is shown as a dashed line (c).

individually contacted grains around 60–100 nm lateral diameter, in a similar range compared to **F$_{64}$PcCu** (200 nm)[18] or **F$_{16}$PcCu** (50 nm)[18] as revealed by AFM (Fig. 5a). The covering film of **F$_{40}$PcCu** on FTO is also observed in the SEM cross-section (Fig. 5b). The extent of intermolecular electronic coupling of **F$_{40}$PcCu** in thin films was monitored by *in situ* measurements of the optical absorption spectra during film growth (Fig. 5c). For all spectra, the Soret band below 400 nm[27] and the Q-band around 500–800 nm[27,28] characteristic for phthalocyanines were found. When compared to solution spectra (Fig. 3 and dashed line in Fig. 5c), which is dominated by the characteristic vibronic fine structure, the films showed significant broadening and a splitting of the Q-band revealing more intense interaction of the molecules in the solid state compared to solutions.[28,29] The splitting leads to a maximum at shorter wavelength which indicates dominance of face-to-face coupling of the molecules (H-aggregation) in solid state.[28,29] The presence of an absorption maximum around 640 nm and a shoulder at about 690 nm implies a structure similar to the α-structure of unsubstituted phthalocyanines with a herringbone orientation of the molecules.[15] Ultrathin films of **F$_{16}$PcCu** in the range of a few monolayers[30,31] showed similar features typical for the β-bilayer structure with a parallel stacking of the molecules. Since the **F$_{40}$PcCu** molecule contains bulky perfluoroisopropyl substituents, a molecular orientation appears likely where the chromophores are

not fully stacked as in the β-bilayer structure, but are oriented slightly inclined thereby approaching an orientation similar to the classic α-structure. The X-ray diffraction pattern (Fig. S5, ESI†) of a thin film of **F$_{40}$PcCu** on FTO exhibits two reflections at around 6° and 19°. Their broad shape indicates the presence of films with a rather well-defined intermolecular orientation, but with still widely amorphous character. The positions of the peaks correspond to the (200) and (600) reflections of a herringbone orientation of the molecules parallel to the substrate as reported earlier for **F$_{16}$PcCu** and PcCu thin films.[32,33] These results, therefore, confirm the presence of an α-structure as also derived from the optical analysis. The films grew at constant band positions and constant band splitting from the monolayer regime up to the film thicknesses studied in this work (Fig. 5c) which yields proof for a constant intermolecular coupling of the **F$_{40}$PcCu** molecules within the film and, hence, for a homogeneous structure of the film. Such an observation has also been reported earlier for **F$_{64}$PcCu**.[16] However, the spectra of solid **F$_{64}$PcCu** matched well the solution spectrum indicating a very weak interaction of the molecules in the solid state caused by the strong suppression of electronic coupling by the bulky perfluoroisopropyl side groups.[16] Thus, the lower degree of fluorination in **F$_{40}$PcCu** provides a strength of intermolecular coupling in solid state that is stronger than that for **F$_{64}$PcCu**, but weaker than that for **F$_{16}$PcCu**.[16,34]

3.3 Rate of the electron and ion transport in the F$_{40}$PcCu films

In order to analyze the electron and ion transport within the **F$_{40}$PcCu** films, cyclic voltammetry (CV) was performed at different scan rates ν. The initial cycle of the as-deposited films showed subtle differences in shape compared to subsequent cycles. Such conditioning, already reported for other fluorinated phthalocyanine films[17,18] was assigned to an initial hindrance of counter ion intercalation into the van der Waals-bonded molecular crystals. However, after about 6 cycles, reproducible CV curves could be obtained for all the prepared **F$_{40}$PcCu** films (Fig. 6a), a change which can be assigned to the reversible reduction and re-oxidation of the **F$_{40}$PcCu** films with concurrent intercalation and expulsion of K$^+$ ions. In Fig. 6b and c the current density *j* was divided by the scan rate to compare the CV curves for different scan rates in one plot. One main peak of reduction and one peak of re-oxidation were observed. The smaller reduction peak at less negative potentials (around −0.4 V) was mainly observed for lower scan rates and thinner films and is most likely indicative of a small concentration of molecules in a slightly different environment. With increasing scan rate, the peak potential of the main reduction process E_{red} shifted slightly towards more negative potentials, while the peak potential E_{reox} of the re-oxidation process underwent a larger shift towards less negative values, typical for kinetically hindered reactions. When the positions of the main reduction peak of around $-1.04\ V \leq E_{red}(\mathbf{F_{40}PcCu}) \leq -0.91\ V$ and the re-oxidation peak of around $-0.78\ V \leq E_{reox}(\mathbf{F_{40}PcCu}) \leq -0.30\ V$ measured for the stabilized CV curves of the **F$_{40}$PcCu** films (10 to 50 nm average film thickness) are compared to other fluorinated Pc, some differences are observed. Thus, the reduction of **F$_{40}$PcCu** requires a higher driving force than that of **F$_{16}$PcCu** or **F$_{64}$PcCu**

This journal is © the Owner Societies 2020

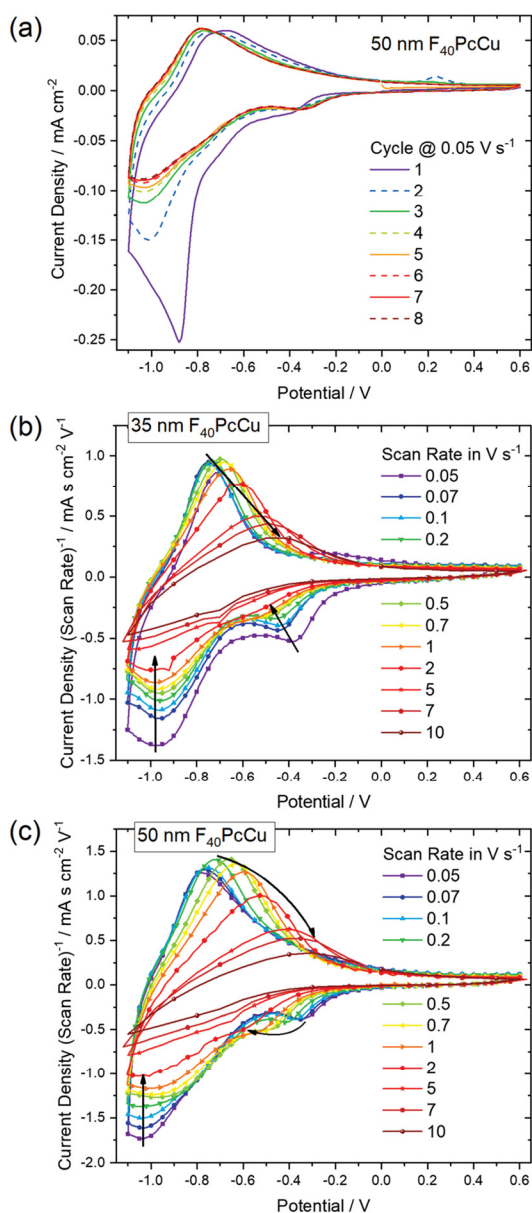*Phys. Chem. Chem. Phys.*, 2020, **22**, 7699–7709 | **7703**

102

Fig. 6 Cyclic voltammograms of **F$_{40}$PcCu** films in contact with 1 M aqueous KCl (a) with a film thickness of 50 nm during conditioning at a scan rate of 0.05 V s^{-1} and at different scan rates after conditioning of (b) a 35 nm and (c) a 50 nm thin film. In (b) and (c) the current density is divided by the scan rate to represent the CV curves in one plot.

-0.62 V $\leq E_{reox}($**F$_{64}$PcCu**$) \leq -0.55$ V.[18] From the average value of $E_{red}($**F$_{40}$PcCu**$)$ and $E_{reox}($**F$_{40}$PcCu**$)$ the redox potential -0.91 V $\leq E($**F$_{40}$PcCu**$) \leq -0.74$ V was estimated depending on the scan rate and thickness of the films. The values are more negative compared to the redox potential for **F$_{16}$PcCu** or **F$_{64}$PcCu** with -0.78 V $\leq E($**F$_{16}$PcCu**$) \leq -0.64$ V[18] and $E($**F$_{64}$PcCu**$) \approx -0.68$ V,[18] respectively suggesting that a slightly higher driving force is needed for reducing **F$_{40}$PcCu** in solid state. This trend was found clearly more pronounced than in solution, speaking in favor of a higher intermolecular interaction energy in the neutral film of **F$_{40}$PcCu** relative to the reduced film with inter-calated K$^+$ when compared to films of **F$_{64}$PcCu** or **F$_{16}$PcCu**. From the values of the main reduction and the re-oxidation peak of the films up to a scan rate of 2 V s^{-1} an average peak potential difference of $\Delta E_p($**F$_{40}$PcCu**$) = 0.30$ V was obtained, in the range of the values reported for films of **F$_{16}$PcCu** and **F$_{64}$PcCu** indicating (quasi-) reversibility of the redox processes[35,36] within all studied perfluorinated Pc films.[18]

To gain a deeper insight into the dependence of j on ν and, hence, the transport limitation within the films, the logarithm of the peak current densities of the cathodic (j_{pc}) as well as those of the anodic branches (j_{pa}) were plotted against the logarithm of the scan rates for different average film thicknesses (Fig. 7). A linear dependence of j on ν (slope of 1, solid black line) is assigned to films with reversible redox reactions without diffusion limitation, expected for an ideal adsorbed monolayer.[35] For reactions which are limited by the diffusion rate of counter ions, a dependence of j on the square root of ν is expected (slope of 0.5, dashed black line).[35] A slope of 0.6 (dotted black line) can be typically assigned to films where the reaction is limited by electron hopping between the redox centers.[37–39] Despite a decreasing j/ν for higher ν in the CV of Fig. 6,
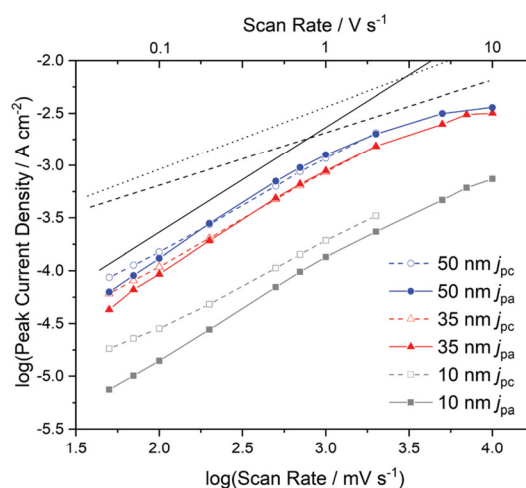

Fig. 7 Dependence of the cathodic (j_{pc}) and anodic (j_{pa}) peak current densities on the scan rate, determined by cyclic voltammetry with **F$_{40}$PcCu** films of different thickness. The black dashed line indicates a slope of 0.5, the dotted line a slope of 0.6 and the solid line a slope of 1.

with -0.92 V $\leq E_{red}($**F$_{16}$PcCu**$) \leq -0.76$ V and -0.79 V $\leq E_{red}($**F$_{64}$PcCu**$) \leq -0.75$ V.[18] The values of E_{reox} for the re-oxidation process of **F$_{40}$PcCu**, however, were comparable with the reported values for **F$_{16}$PcCu** with -0.71 V $\leq E_{reox}($**F$_{16}$PcCu**$) \leq -0.38$ V, but in a slightly larger range compared to **F$_{64}$PcCu** with

a linear dependence of the peak current on scan rates up to 1 V s^{-1} can still be fitted for the thicker films ($d \geq 35$ nm) in the reduction reaction and for all films in the re-oxidation reaction. Hence, the reduction of the films takes place with just a minor limitation by the transfer of electrons or counter ions and the re-oxidation reveals independence of any transport limitation, representing a high reversibility of the redox reactions of the films in this range of ν significantly larger than was observed for F$_{16}$PcCu and F$_{64}$PcCu films where a linear dependence could be observed only for $\nu < 0.2$ V s^{-1}.[18] For F$_{16}$PcCu this was only valid for $d \leq 20$ nm and for F$_{64}$PcCu for $d \leq 50$ nm.[18] For $\nu > 0.2$ V s^{-1} the F$_{64}$PcCu films thinner than 50 nm showed a dependence of $j \sim \nu^{0.6}$ characteristic for a limitation by electron hopping in the films and sufficiently fast diffusion of the counter ions through the F$_{64}$PcCu films, facilitated by the presence of the large perfluoroisopropyl substituents.[18] At scan rates $\nu > 1$ V s^{-1} the linear dependence of j on ν is no longer observed, but the reaction clearly becomes transport-limited. A clear assignment to a characteristic slope is no longer possible because for F$_{40}$PcCu films with $d \geq 35$ nm a dependence of $j \sim \nu^{0.5}$ was indicated, whereas the 10 nm F$_{40}$PcCu film approached $j \sim \nu^{0.6}$. Therefore, limitation by either the counter ions (slope of 0.5) or by hopping of electrons (slope of 0.6) cannot be distinguished, the transport of both seems to be equally fast. It should be noted that F$_{40}$PcCu films show no transport limitation up to a scan rate 5 times higher than that reported for F$_{16}$PcCu and F$_{64}$PcCu.[18] Thus, the two isoindole units with two perfluoroisopropyl substituents in F$_{40}$PcCu instead of four such units in F$_{64}$PcCu[16] (Fig. 1) lead to a film structure with optimized attributes of both F$_{16}$PcCu and F$_{64}$PcCu which allows a fast electron as well as a fast ion transport through the film.

As a quantitative measure for the rate of transport in the F$_{40}$PcCu films, an effective diffusion coefficient D was obtained from chronoamperometric measurements. After the initialization of the film during the first cycle, the subsequent cycles were invariable. The integrated current density yielded an average charge of 1.5 electrons for each deposited molecule of F$_{40}$PcCu considering the molecular weight of 1464.01 g mol^{-1}. The measured cathodic and anodic current densities of the second cycle were plotted against the reciprocal square root of time $t^{-1/2}$ (Fig. 8) corresponding to the Cottrell eqn (1) valid for semi-infinite diffusion

$$ j = nFcD^{1/2}\pi^{-1/2}t^{-1/2} \tag{1} $$

where F is Faraday's constant, n is the number of electrons transferred in the reaction and c is the concentration in the bulk of the electrolyte.[35] The characteristics, Fig. 8, are reminiscent of those reported for films of redox polymers like poly(fluorenone-bithiophene)[40] or for redox polyelectrolyte multilayers.[41] In the long time regime the current density decreased to lower than expected values, an observation which can be explained by the finite film thickness leading to deviations from semi-infinite diffusion. In the short time regime of 4.4–10 ms (10–15 s$^{-1/2}$) the data followed the expected linear Cottrellian behavior and allow a quantitative analysis.

For the 35 nm thin film, values for the effective diffusion coefficient of $D_c(35$ nm$) = 4.4 \times 10^{-10}$ cm^2 s^{-1} and $D_a(35$ nm$) = 1.4 \times 10^{-9}$ cm^2 s^{-1} were obtained from the fits of the cathodic and anodic current densities, respectively, Fig. 8a. The values estimated for a 50 nm thin film are in the same range, with $D_c(50$ nm$) = 5.3 \times 10^{-10}$ cm^2 s^{-1} and $D_a(50$ nm$) = 1.9 \times 10^{-9}$ cm^2 s^{-1}. For both films, the values of D_a for the re-oxidation were found higher than those of D_c for the reduction, as found earlier for F$_{16}$PcCu.[18] Such smaller effective diffusion coefficient upon reduction might be caused by a slow removal of the solvation shell[42] before intercalation into the solid film of F$_{40}$PcCu.

The values of the diffusion coefficient reported for F$_{16}$PcCu, $D_c(F_{16}$PcCu$) = 8 \times 10^{-11}$ cm^2 s^{-1} and $D_a(F_{16}$PcCu$) = 1.5 \times 10^{-10}$ cm^2 s^{-1}, as well as $D_c(F_{64}$PcCu$) = D_a(F_{64}$PcCu$) = 5 \times 10^{-11}$ cm^2 s^{-1} for F$_{64}$PcCu were significantly smaller[18] compared to the values for F$_{40}$PcCu. Thus, the faster diffusion in F$_{40}$PcCu is a direct confirmation for the successfully enhanced overall
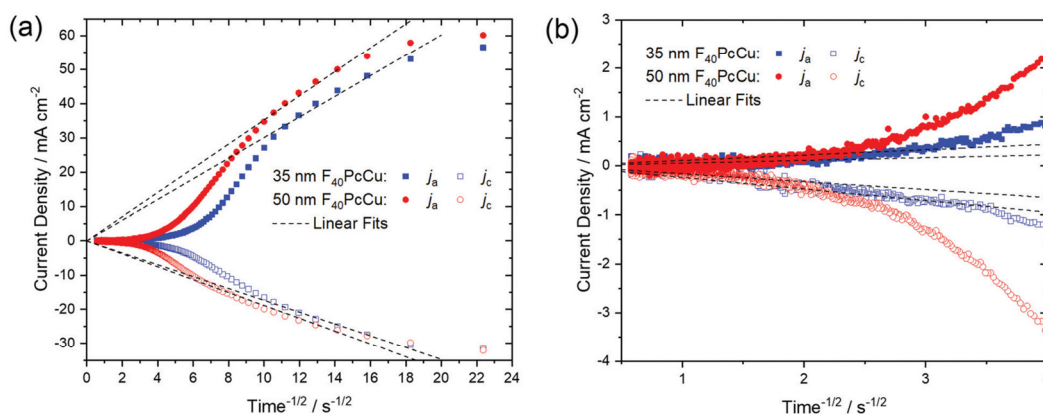

Fig. 8   (a) Cathodic (j_c) and anodic (j_a) current densities dependent on the reciprocal square root of time obtained from chronoamperometric analysis of a 35 nm (blue) and 50 nm (red) thin F$_{40}$PcCu film. (b) Plot of the data for long times. The linear fits according to the Cottrell equation are marked in dashed lines.

diffusion of electrons and K^+ within the film. By zooming into the range of the data at longer times around $4 \ s^{-1/2}$, as shown in Fig. 8b, another linear region was observed. The fits in this time regime yielded considerably smaller diffusion coefficients of $D = 0.5-8.5 \times 10^{-12} \ cm^2 \ s^{-1}$, representing a lower limit for the diffusion into those parts of films which are least accessible, either because of poor electronic conduction or difficult intercalation of ions. However, for the overall yield of the reaction and, hence, prospective technical application of the reactions, the high values of D in the early stage of the reactions are most significant since they represent the highest currents and, hence, the largest contribution. Along with the results from the CV measurements (Fig. 7) revealing a transport limitation in the films dominated by neither electrons nor ions, but given by a similarly fast movement of both with $j \sim \nu$ up to $1 \ V \ s^{-1}$, it can be concluded that the moderate intermolecular coupling of the **F₄₀PcCu** molecules provides facilitated pathways for both ions and electrons in the films.

3.4 Spectroelectrochemical characterization of F₄₀PcCu films

Optical absorption spectra of the **F₄₀PcCu** films were measured *in situ* during the electrochemical measurements to (i) investigate the changes of the electronic structure of the molecules in the solid state caused by the redox processes and (ii) to analyze the performance of these films as possible electrochromic smart windows.

The changes in the electronic structure of the **F₄₀PcCu** films observed in the stabilized CV curves are clearly reflected in the absorption spectra of the films, as shown in Fig. 9. As expected, the bands of the neutral films upon immersion into the aqueous KCl solution were found almost equal to those of the as-deposited films (Fig. 5). However, a small but significant shift of the Q-band maximum to about 630 nm was caused by this different environment. In contrast to earlier experiments with **F₁₆PcCu**,[18] the electrochemical conditioning of **F₄₀PcCu** did not lead to any changes in the spectra, *i.e.* the intermolecular

coupling was found unchanged following the first eight cycles of reduction and re-oxidation.

The reduction of **F₄₀PcCu** led to remarkable changes in the Q-band position as well as in the absorptions between the Soret and the Q-band, while the absorption of the Soret band was just slightly decreased without any remarkable shift. The absorption maximum at 630 nm decreased in intensity while the shoulder at around 690 nm transformed into a local maximum. A new absorption maximum at around 540 nm and a broad absorption in the NIR at 800 nm and beyond, both typical for phthalocyanine rings in their reduced state (Pc(−3)Cu(ɪɪ)) arose (Fig. 9a) as also observed for **F₁₆PcCu**[18] and for **F₆₄PcCu**.[17,18] Upon re-oxidation these spectral changes were reversed (Fig. 9b). Well-defined isosbestic points were detected at 390 nm, characteristic of a uniformly smaller absorption by the Soret band in the reduced state. Small ranges of intersecting spectra ("isosbestic ranges") were detected around 580 nm and around 730 nm upon re-oxidation of the films, indicating widely uniform transitions also in the Q-band range, which is known to be very sensitive to parameters of intermolecular coupling in Pc.[28] These ranges were considerably wider upon reduction of the film, consistent with the two contributions in the cathodic wave of the CV (Fig. 6). The presence of isosbestic points and "isosbestic ranges" indicates the reversible $A \leftrightarrow B$ transformation of neutral species A to a reduced species B with characteristic spectra for neutral (re-oxidized) A and reduced B species, similar to results for **F₆₄PcCu** films reported earlier[17,18] confirming the presence of a reversible redox reaction, with no permanent change in the material.

In order to check if a complete reduction and re-oxidation of the films was ensured even for faster scan rates, which would be beneficial for fast switching in electrochromic layers, the change in optical absorption between the reduced (−1.1 V) and the re-oxidized state (0.6 V) of the films was determined in dependence of the scan rate (Fig. 10). Absorption signals at 540 nm and 630 nm, for which most significant changes were detected upon reduction and re-oxidation were selected (marked with arrows in Fig. 9).
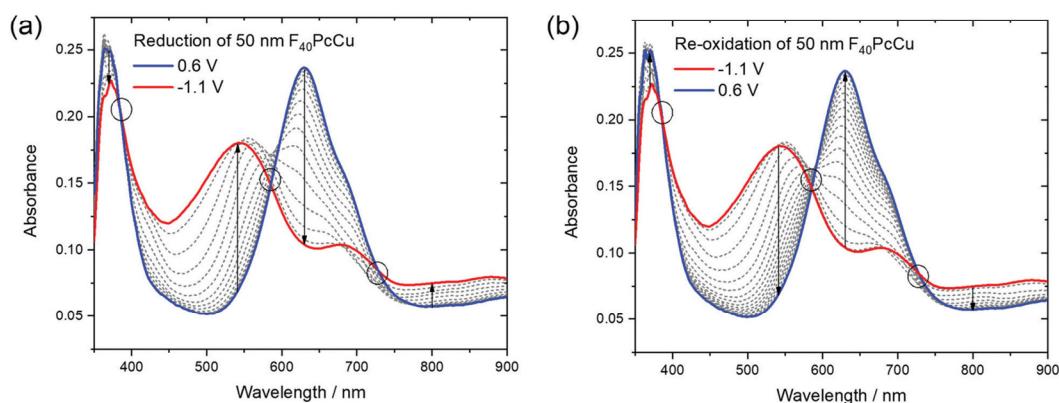

Fig. 9   Optical absorption spectra of a 50 nm thin film of **F₄₀PcCu** measured during cyclic voltammetry at $0.05 \ V \ s^{-1}$ upon (a) reduction and (b) re-oxidation of the film. The isosbestic points and ranges are marked by circles.
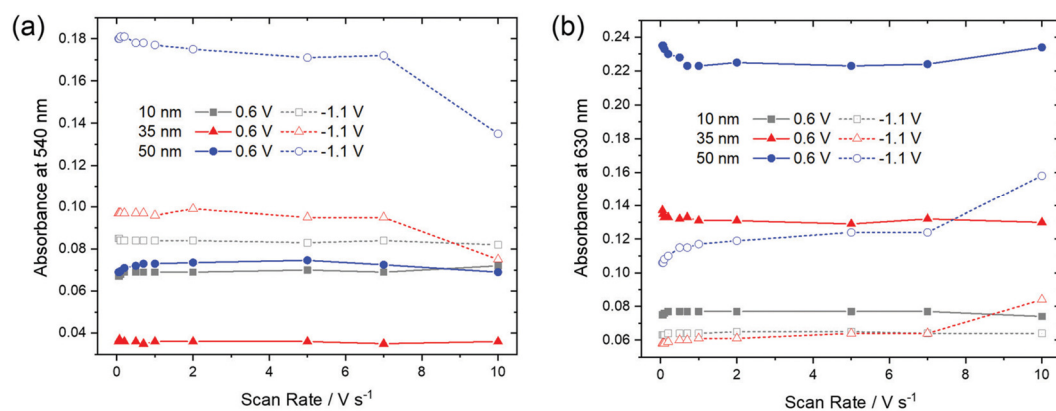
Fig. 10   Optical absorbance at (a) 540 nm and (b) 630 nm as a function of scan rate of **F₄₀PcCu** films of different thickness in the re-oxidized (0.6 V) or reduced (−1.1 V) states.

For the thinnest, 10 nm film of **F₄₀PcCu** the absorbances at 540 nm and 630 nm remained largely constant for all scan rates. The main observation, however, is that the thicker films showed significant changes at higher scan rates. Upon reduction (−1.1 V), the absorbance at 540 nm has a lower value, indicating incomplete reduction of the film. Correspondingly, a higher
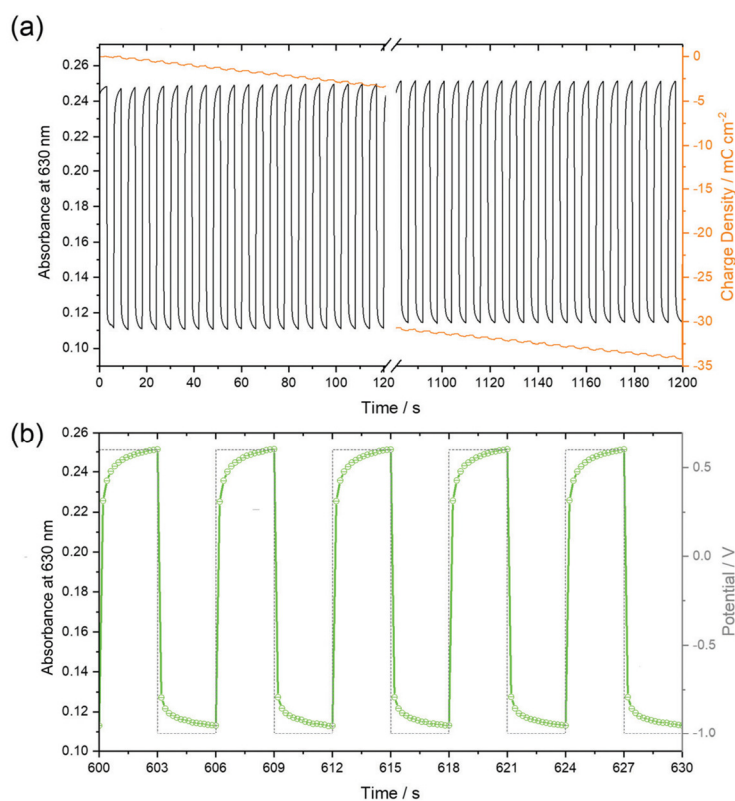
Fig. 11   Optical absorption at 630 nm of a 50 nm thin **F₄₀PcCu** film, recorded during chronoamperometry over 20 minutes (a) and at high resolution for an intermediate time interval (b) between the potentials depicted as dashed profiles in (b). The variation of the charge density within 200 cycles is shown as orange lines in (a).

absorbance was found at 630 nm, characteristic of remaining neutral molecules. These features are most significant for the 50 nm thin film for which changes were noticeable at scan rates $\nu > 1 \text{ V s}^{-1}$. Both trends clearly point at an incomplete reduction of the films at high scan rates. Upon re-oxidation (0.6 V), however, absorbance remained almost constant even for higher scan rates and thicker films, confirming the fast re-oxidation processes, also indicated by the higher effective diffusion coefficient determined during re-oxidation (Fig. 8).

3.5 Long-term, repeated switching characteristics of F$_{40}$PcCu films

The stability of the time-dependent switching characteristics was studied by chronoamperometry of 50 nm thin films over 20 minutes (Fig. 11). It is remarkable that the absorbance, as shown in Fig. 11a for the 50 nm thin film in both the reduced and neutral states remained constant for all subsequent 200 cycles, thus defining a reversible switching process which, in turn, indicated a high stability of the films. Despite this stability, the total charge monotonously shifted to negative values indicative of a background current at the negative potential as already observed by CV (Fig. 6), in earlier studies at F$_{16}$PcCu and F$_{64}$PcCu films, and assigned to water reduction.[17,18] Obviously, this side reaction had no influence on the spectral properties of the film, a feature also found for F$_{16}$PcCu and F$_{64}$PcCu films using Li$^+$ or K$^+$ as counter ions.[17,18] The higher time resolution (Fig. 11b) indicates fast decrease of the absorbance at 630 nm upon reduction (−1.0 V) and recovery upon re-oxidation (0.6 V). The response times, $0.2 \text{ s} \leq t_{\text{red}} \leq 0.4 \text{ s}$ and $0.3 \text{ s} \leq t_{\text{reox}} \leq 0.4 \text{ s}$ were determined, corresponding to the time needed to switch the absorption to 90% of the change to the reduced or the neutral state, respectively. The present response times (Fig. 11) are shorter than the 1.3 s and 0.6 s values, determined in earlier work for the reduction and re-oxidation of F$_{64}$PcCu films,[17] revealing a faster switching behavior of the present films caused by facilitated transport of both electrons and K$^+$ counter ions in F$_{40}$PcCu as directly seen in cyclic voltammetry (Fig. 7) and the chronoamperometric measurements (Fig. 8). The films provide fast and reversible switching capabilities, stable over many cycles, ideal for their use as electrochromic materials.

4 Conclusions

A new type of perfluorinated phthalocyanine, namely F$_{40}$PcCu has been designed to exhibit simultaneously both efficient electron and ion transport properties. The molecule in solution shows the expected absorption bands of phthalocyanines and exhibits facile reduction and re-oxidation. Thin films, obtained by physical vapor deposition exhibited spectral broadening of the absorption spectra characteristic for thin films of weakly coupling chromophores in solid state. Electrochromic cells could be obtained by a contact of each individual grain of the films with the FTO support and the aqueous electrolyte. The reversible switching observed upon reduction and re-oxidation

indicates a high stability of the films with no permanent change in the material. Changes of the absorption spectra in the reduced state typical for phthalocyanines (Pc(−3)Cu(II)) were noticed. The electrochemical characteristics of thin films showed that F$_{40}$PcCu films exhibited intermolecular coupling within the grains, weaker than that for F$_{16}$PcCu, but stronger than that for F$_{64}$PcCu, leading to a facilitated transport of both electrons and counter ions up to scan rates of about 1 V s^{-1}. Short response times during the switching process were determined for both the reduction and re-oxidation of the films. However, at very high scan rates the films could not be fully reduced, whereas a fast re-oxidation of the films was still observed. The apparent diffusion coefficient ranges from 10^{-10} to 10^{-9} cm^2 s^{-1} depending on film thicknesses, a characteristic of fast reversible switching attractive for the use of the new material in electrochromic smart windows.

Conflicts of interest

There are no conflicts of interest to declare.

Acknowledgements

References

1 H. Klauk, *Organic Electronics*, Wiley-VCH, Weinheim, 2006.
2 C. G. Granqvist, *Thin Solid Films*, 2014, **564**, 1–38.
3 R. Baetens, B. P. Jelle and A. Gustavsen, *Sol. Energy Mater. Sol. Cells*, 2010, **94**, 87–105.
4 P. R. Somani and S. Radhakrishnan, *Mater. Chem. Phys.*, 2002, **77**, 117–133.
5 R. J. Mortimer, A. L. Dyer and J. R. Reynolds, *Displays*, 2006, **27**, 2–18.
6 M. Berggren, X. Crispin, S. Fabiano, M. P. Jonsson, D. T. Simon, E. Stavrinidou, K. Tybrandt and I. Zozoulenko, *Adv. Mater.*, 2019, **31**, e1805813.
7 A. L. Dyer, A. M. Österholm, D. E. Shen, K. E. Johnson and J. R. Reynolds, in *Electrochromic Materials and Devices*, ed. R. J. Mortimer, D. R. Rosseinsky and P. M. S. Monk, Wiley-VCH, Weinheim, 2015, ch. 5, vol. 1, pp. 113–184.
8 L. Beverina, G. A. Pagani and M. Sassi, *Chem. Commun.*, 2014, **50**, 5413–5430.
9 M. M. Nicholson, in *Phthalocyanines: Properties and Applications*, ed. C. C. Leznoff and A. B. P. Lever, VCH, Weinheim, 1993, ch. 2, vol. 3, pp. 71–118.

10 J. M. Green and L. R. Faulkner, *J. Am. Chem. Soc.*, 1983, **105**, 2950–2955.

11 B. Schumann, D. Wöhrle and N. I. Jaeger, *J. Electrochem. Soc.*, 1985, **132**, 2144–2149.

12 C. Wang, H. Dong, L. Jiang and W. Hu, *Chem. Soc. Rev.*, 2018, **47**, 422–500.

13 M. K. Engel, in *The Porphyrin Handbook*, ed. K. M. Kadish, K. M. Smith and R. Guilard, Academic Press, San Diego, 2003, vol. 20, pp. 1–242.

14 T. Hosokai, A. Gerlach, A. Hinderhofer, C. Frank, G. Ligorio, U. Heinemeyer, A. Vorobiev and F. Schreiber, *Appl. Phys. Lett.*, 2010, **97**, 63301.

15 L. Cornelius, M. Beu, C. Keil and D. Schlettwein, *Phys. Status Solidi RRL*, 2012, **6**, 214–216.

16 C. Keil, O. Tsaryova, L. Lapok, C. Himcinschi, D. Wöhrle, O. R. Hild, D. R. T. Zahn, S. M. Gorun and D. Schlettwein, *Thin Solid Films*, 2009, **517**, 4379–4384.

17 S. Nagel, M. Lener, C. Keil, R. Gerdes, Ł. Łapok, S. M. Gorun and D. Schlettwein, *J. Phys. Chem. C*, 2011, **115**, 8759–8767.

18 J. Weissbecker, A. Loas, S. M. Gorun and D. Schlettwein, *Electrochim. Acta*, 2015, **157**, 232–244.

19 S. M. Gorun, B. A. Bench, G. Carpenter, M. W. Beggs, J. T. Mague and H. E. Ensley, *J. Fluorine Chem.*, 1998, **91**, 37–40.

20 A. B. P. Lever, E. R. Milaeva and G. Speier, in *Phthalocyanines: Properties and Applications*, ed. C. C. Leznoff and A. B. P. Lever, VCH, Weinheim, 1993, vol. 3, ch. 1.

21 H. H. Patel, PhD thesis, Seton Hall University, 2015.

22 E. N. Carrión, A. Loas, H. H. Patel, M. Pelmuş, K. Ramji and S. M. Gorun, *J. Porphyrins phthalocyanines*, 2018, **22**, 371–397.

23 K. J. M. Nolan, M. Hu and C. C. Leznoff, *Synlett*, 1997, 593–594.

24 H. Konami, Y. Ikeda, M. Hatano and K. Mochizuki, *Mol. Phys.*, 1993, **80**, 153–160.

25 H. Moons, Ł. Łapok, A. Loas, S. van Doorslaer and S. M. Gorun, *Inorg. Chem.*, 2010, **49**, 8779–8789.

26 K. Hesse and D. Schlettwein, *J. Electroanal. Chem.*, 1999, **476**, 148–158.

27 D. Schlettwein, N. I. Jaeger and T. Oekermann, in *The Porphyrin Handbook*, ed. K. M. Kadish, K. M. Smith and R. Guilard, Academic Press, San Diego, 2003, vol. 16, pp. 247–284.

28 C. G. Claessens, U. Hahn and T. Torres, *Chem. Rec.*, 2008, **8**, 75–97.

29 A. W. Snow, in *The Porphyrin Handbook*, ed. K. M. Kadish, K. M. Smith and R. Guilard, Academic Press, San Diego, 2003, vol. 17, pp. 129–176.

30 C. Keil, PhD thesis, Justus-Liebig-University, 2012.

31 D. G. de Oteyza, E. Barrena, J. O. Ossó, S. Sellner and H. Dosch, *J. Am. Chem. Soc.*, 2006, **128**, 15052–15053.

32 R. Ye, M. Baba, Y. Ohishi, K. Mori and K. Suzuki, *Mol. Cryst. Liq. Cryst.*, 2006, **444**, 203–210.

33 G. Liu, T. Gredig and I. K. Schuller, *Europhys. Lett.*, 2008, **83**, 56001.

34 W. Michaelis, D. Wöhrle and D. Schlettwein, *J. Mater. Res.*, 2004, **19**, 2040–2048.

35 A. J. Bard and L. R. Faulkner, *Electrochemical Methods*, Wiley, New York, 2001.

36 J.-M. Savéant, *Elements of Molecular and Biomolecular Electrochemistry*, John Wiley & Sons, Hoboken, NJ, 2006.

37 E. Laviron, *J. Electroanal. Chem.*, 1980, **112**, 1–9.

38 E. Laviron, L. Roullier and C. Degrand, *J. Electroanal. Chem.*, 1980, **112**, 11–23.

39 E. Laviron, *J. Electroanal. Chem.*, 1981, **122**, 37–44.

40 M. D. Levi, R. Demadrille, A. Pron, M. A. Vorotyntsev, Y. Gofer and D. Aurbach, *J. Electrochem. Soc.*, 2005, **152**, E61–E67.

41 M. Tagliazucchi, D. Grumelli, C. Bonazzola and E. J. Calvo, *J. Nanosci. Nanotechnol.*, 2006, **6**, 1731–1740.

42 K. Xu, A. von Cresce and U. Lee, *Langmuir*, 2010, **26**, 11538–11543.

This journal is © the Owner Societies 2020

Phys. Chem. Chem. Phys., 2020, **22**, 7699–7709 | **7709**

Electronic Supplementary Information

The Influence of Intermolecular Coupling on Electron and Ion Transport in Differently Substituted Phthalocyanine Thin Films as Electrochromic Materials: a Chemistry Application of the Goldilocks Principle

Thi Hai Quyen Nguyen,[a] Marius Pelmus,[b] Christopher Colomier,[b] Sergiu M. Gorun,[b] Derck Schlettwein[a*]*

[a] Institute of Applied Physics and Laboratory of Materials Research, Justus-Liebig-University Gießen, Heinrich-Buff-Ring 16, 35392 Gießen, Germany.

[b] Department of Chemistry and Biochemistry and Center for Functional Materials, Seton Hall University, 400 South Orange Ave, South Orange, NJ 07079, USA.

* corresponding authors email: schlettwein@uni-giessen.de; sergiu.gorun@shu.edu.

Figure S1. HRMS spectra of **$F_{40}PcCu$**. Experimental (top) vs. theoretical (bottom) isotopic distribution.
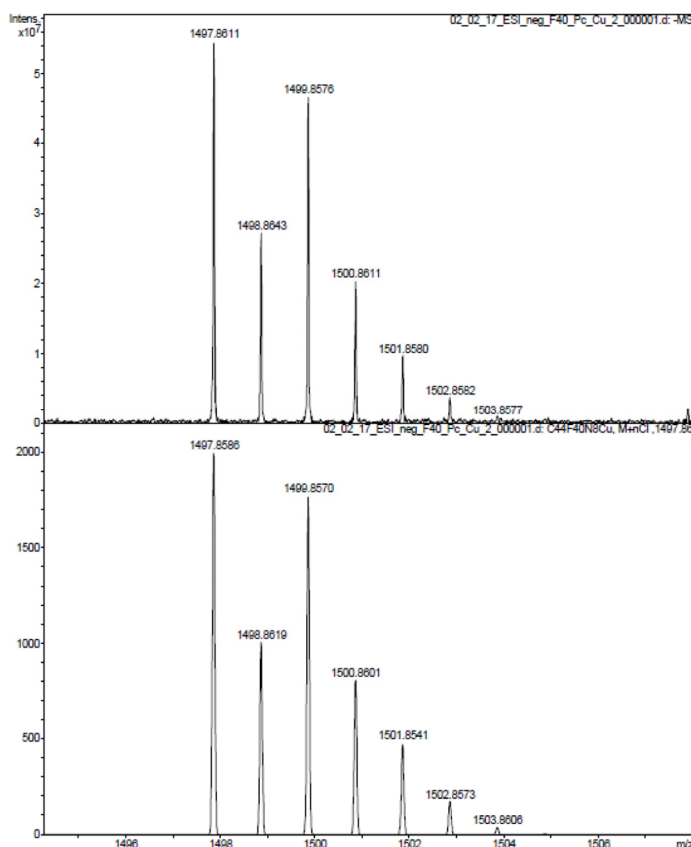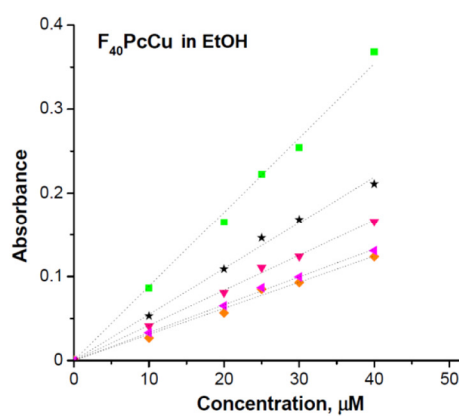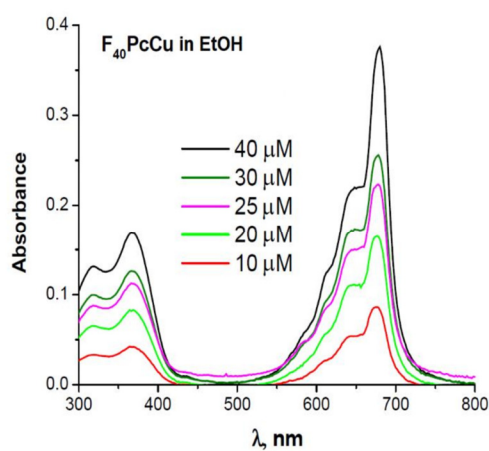
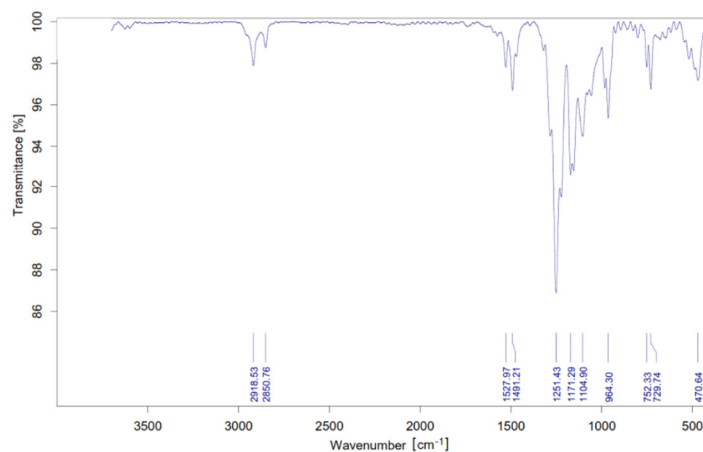**Figure S2.** FT-IR spectrum of **F$_{40}$PcCu**, KBr disk

Figure S3. Concentration-dependent UV-Vis spectra of 10-40 µM solutions of **F$_{40}$PcCu** in ethanol (EtOH), (left). Beer-Lambert plots (right).

Symbol	λ, nm	Slope	R^2
■	676	0.00885	0.99796
★	640	0.00548	0.99813
◆	612	0.00311	0.99659
▼	372	0.00418	0.9991
◀	316	0.00332	0.99943

Figure S4. Concentration-dependent UV-Vis spectra of 10-40 µM solutions of **F$_{40}$PcCu** in trifluorotoluene (TFT), (left). Beer-Lambert plots (right).

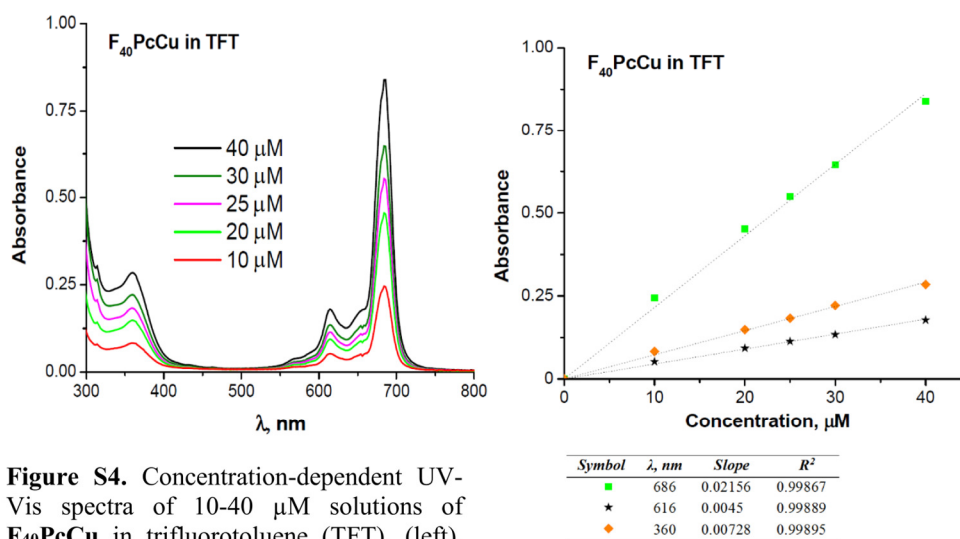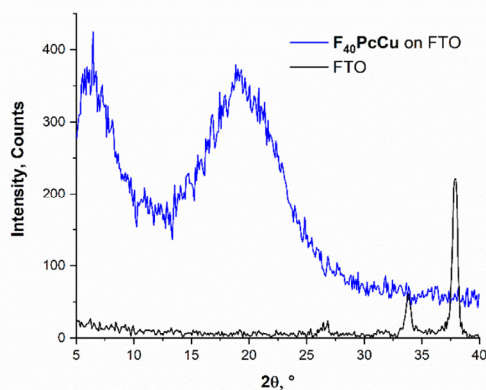| Symbol	λ, nm	Slope	R^2
■	686	0.02156	0.99867
★	616	0.0045	0.99889
◆	360	0.00728	0.99895

Figure S5. Grazing incidence X-ray diffraction (GIXRD) of a 50 nm thin film of **F$_{40}$PcCu** on FTO compared to pristine FTO.

4.2 Additional Work in the Context of Publication 2

The replacement of copper in the molecule by an equivalent transition metal ion still allowing the occurrence of charge transfer transitions at the phthalocyanine ring rather than at the central metal ion, e.g. Zn^{2+} [120–122] should result in thin films providing similar electrochromic switching properties as observed for F_{16}PcZn [123] in comparison with F_{16}PcCu [54]. Recently, in collaboration with Marius Pelmuş and Sergiu M. Gorun, copper has, therefore, been replaced by zinc as central metal ion resulting in the new material F_{40}PcZn. Thin films of F_{40}PcZn could be successfully prepared by vapor deposition. The optical absorption spectra of the F_{40}PcZn films measured during cyclic voltammetry of the films in contact with aqueous KCl electrolyte solution (Figure 4.1) showed close similarity to the F_{40}PcCu films. The spectra revealed comparable changes in absorbance upon reduction and re-oxidation. Upon reduction, a new absorption band around 540 nm arose, characteristic for reduced phthalocyanine rings [53,54] and identical to F_{40}PcCu. As a difference to F_{40}PcCu, a small shoulder around 580 nm remained during re-oxidation, presumably caused by a stable partially reduced intermediate or by neutral F_{40}PcZn in a different intermolecular arrangement [211].
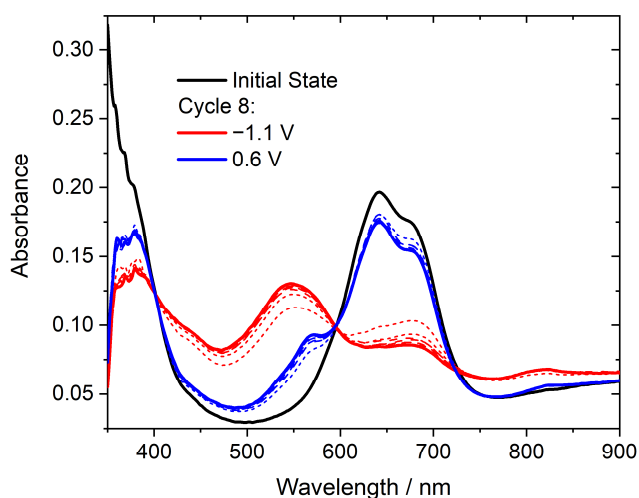

Figure 4.1: Optical absorption spectra of a 50 nm thin film of F_{40}PcZn in contact with aqueous KCl measured in the neutral state before (Initial State) and during cyclic voltammetry at 0.05 V s^{-1} upon reduction (−1.1 V) and re-oxidation (0.6 V).

As for other substituted phthalocyanines, the present experiments proved versatile use of different central metals.

5 Mixed Electrochromic Thin Films of $F_{16}PcCu$ and $F_{64}PcCu$ (Publication 3)

Background for Publication 3

The results of Publication 2 and the additional experiments show that the modification of the substitution pattern of the phthalocyanine ligand represents a valuable approach to optimize the intermolecular coupling of the molecules in the solid state and, thus, the transport of electrons and ions in the films, directly connected to reaching very attractive electrochromic switching characteristics. The synthesis of new molecules, however, often requires multiple complex steps and additional workload. Without the need of alteration on the intramolecular level, a simple and more convenient method to combine the properties of different materials would be the preparation of thin films using a mixture of already available molecules.

Mixed films consisting of different copper phthalocyanine molecules were already successfully prepared with $F_{16}PcCu$ and $H_{16}PcCu$, even if not in the context of electrochromism, as reported in two independent studies [139,140]. A clear influence of the mixing ratios on the crystallinity and, hence, on the conductivity of the films was found [139,140].

A similar strategy was followed in Publication 3 utilizing a mixture of $F_{16}PcCu$ and $F_{64}PcCu$ as well-established molecules to possibly achieve the golden mean of the properties of both materials in one film, similar as obtained for $F_{40}PcCu$ thin films in Publication 2. In this approach, the mixture of differently fluorinated ligands will not be sought on an intramolecular, but on an intermolecular level.

Context of Publication 3

Thin films containing $F_{16}PcCu$ and $F_{64}PcCu$ of different thicknesses and mixing ratios were fabricated and characterized in cooperation with Michael Schäfer. SEM analysis of the films revealed the successful preparation of homogeneous thin films by simultaneous vapor deposition of $F_{16}PcCu$ and $F_{64}PcCu$.

The strength of the intermolecular coupling in the films was studied using UV-Vis spectroscopy. Similar to $F_{40}PcCu$ thin films, all the films exhibited the characteristic Soret- and Q-band [47,116] in the optical absorption spectra. In collaboration with Marius Pelmuş, a broadening of the Q-band was found for all the films in comparison to the solution spectra, except for $F_{64}PcCu$. The absorption spectrum of pure $F_{64}PcCu$ in the solid state was quite similar to that in solution as already observed in [56], well in line with weak intermolecular coupling in the film. Mixed films of $F_{16}PcCu$ and $F_{64}PcCu$ in a ratio of 1:1 exhibited a broadened and split Q-band confirming an intermediate strength of intermolecular coupling comparable to $F_{40}PcCu$ caused by rather strongly interacting $F_{16}PcCu$ and weakly interacting $F_{64}PcCu$. The comparison of the spectra of the 1:1 $F_{16}PcCu{:}F_{64}PcCu$ mixed films with that of an $F_{16}PcCu{:}F_{64}PcCu$ bilayer obtained by sequential deposition revealed a desired mixture of both molecules on the molecular level as opposed to a formation of separate phases of $F_{16}PcCu$ and $F_{64}PcCu$.

Similar to the study of the films of $F_{40}PcCu$ shown in Publication 2, electrochemical and spectroelectrochemical measurements of the 1:1 $F_{16}PcCu{:}F_{64}PcCu$ mixed films were carried out in aqueous KCl electrolyte solution and directly compared with the films of $F_{16}PcCu$ [54], $F_{40}PcCu$ (Publication 2) and $F_{64}PcCu$ [53,54].

Significant changes during the conditioning process were not only found in the CV curves but also in the simultaneously measured absorption spectra. Such changes in the absorbance indicated a loss of the β-structure of $F_{16}PcCu$ portions [212] in the mixed films upon the initial cycle as similarly seen for the pure $F_{16}PcCu$ films [54]. After the conditioning process, reproducible CV curves and reversible changes in the absorption spectra were obtained for the mixed films. This is comparable to the films of $F_{16}PcCu$ [54], $F_{40}PcCu$ (Publication 2) and $F_{64}PcCu$ [53,54] and points out the high R_{EC} of the redox reaction of the films. The CV measurements revealed that the scan rate, up to which the redox reactions proceeded without transport limitation, was significantly larger for the $F_{40}PcCu$ films (Publication 2). However, for an 85 nm thin mixed film the redox reactions still proceeded without considerable transport limitation at scan rates for which the reactions of $F_{16}PcCu$ and $F_{64}PcCu$ films with even smaller thickness already became transport-limited by either ions or electrons, respectively [54].

The effective diffusion coefficient determined from the chronoamperometric analysis upon re-oxidation for the mixed films was found lower than for the $F_{40}PcCu$ films (Publication 2) but equal or higher than the values reported for $F_{16}PcCu$ or $F_{64}PcCu$ films of similar thickness [54]. Electrochromic switching of the mixed films could still be

established with response times of about 1 s. The difference of the absorbance between the reduced and the re-oxidized states of the mixed films became smaller after subsequent cycles as revealed by chronoamperometry and *in situ* UV-Vis spectroscopy, unlike the case of the $F_{40}PcCu$ films (Publication 2). These changes might presumably be caused by partial ablation of the mixed films, in particular of $F_{64}PcCu$ portions.

5.1 Publication 3: Electron and Ion Transport in Mixed Electrochromic Thin Films of Perfluorinated Phthalocyanines

Derck Schlettwein planned and supervised the project. Chemical synthesis and parts of the UV-Vis spectroscopy measurements of the molecules in solution were carried out by the cooperation partners from the Seton Hall University (Marius Pelmuş and Sergiu M. Gorun). The preparation of thin films of different mixing ratios of $F_{16}PcCu$ and $F_{64}PcCu$, the fabrication of the bilayer structure and the analysis of these films by UV-Vis spectroscopy were carried out by Michael Schäfer. I planned, performed and interpreted the electrochemical and spectroelectrochemical measurements of the 1:1 mixed $F_{16}PcCu:F_{64}PcCu$ films and took care of the preparation and characterization of such films, including the GIXRD and SEM measurements at the Institute of Physical Chemistry. I drafted the manuscript, fine-tuned it with Derck Schlettwein and we discussed it with all co-authors.

Electron and Ion Transport in Mixed Electrochromic Thin Films of Perfluorinated Phthalocyanines

Thi Hai Quyen Nguyen[a], Michael Schäfer[a], Marius Pelmuş[b], Sergiu M. Gorun[b], Derck Schlettwein[a,*]

[a] Institute of Applied Physics and Laboratory of Materials Research, Justus Liebig University Giessen, Heinrich-Buff-Ring 16, 35392 Giessen, Germany
[b] Department of Chemistry and Biochemistry and Center for Functional Materials, Seton Hall University, 400 South Orange Ave, South Orange, NJ 07079, USA

ARTICLE INFO

ABSTRACT

Thin films of a mixture of the perfluorinated phthalocyanines 1,2,3,4,8,9,10,11,15,16,17,18,22,23,24,25-hexadeca-fluorophthalocyaninato copper(II) (F_{16}PcCu) and 1,4,8,11,15,18,22,25-octakis-fluoro-2,3,9,10,16,17,23,24-octakis-perfluoro(isopropyl) phthalocyaninato copper(II) (F_{64}PcCu) of different thicknesses and mixing ratios were prepared by simultaneous vapor deposition. A moderate extent of the intermolecular coupling between F_{16}PcCu and F_{64}PcCu within the mixed films comparable to that reported earlier for tetrakisperfluoroisopropyl-perfluoro phthalocyanine (F_{40}PcCu) was revealed by UV/Vis spectroscopy. The electrochromic properties as well as the transport of electrons and counter cations in the 1:1 F_{16}PcCu:F_{64}PcCu mixed films were investigated by electrochemical and spectroelectrochemical characterization using an aqueous solution of KCl as electrolyte. The transport coefficients of electrons and ions of these films were comparable to those reported for F_{40}PcCu films, for which a well-balanced, equally fast transport of both electrons and ions had been seen. Fast, reversible, and stable switching characteristics of the mixed films, upon reduction and intercalation of K^+ counterions and re-oxidation with extraction of the counterions, were observed by cyclic voltammetry, chronoamperometry, and simultaneously measured optical absorption spectra.

1. Introduction

Phthalocyanines (Pc) as organic ionic and electronic conductors exhibit electrochromic properties which can be tuned by the central metal ion and substituents at the aromatic ring system and draw interest for the application as electrochromic thin films in devices such as smart windows and mirrors [1,2]. A clear influence of the degree of fluorination in copper phthalocyanines on the intermolecular coupling of the molecules within thin films and, hence, on the rate of electron and ion transport was observed [3,4]. Thin films of these phthalocyanines can be prepared by a variety of methods such as physical vapor deposition [5], chemical vapor deposition [6], or electrochemical deposition [7]. In comparison to classic inorganic electrochromic materials like tungsten oxide, organic materials exhibit a variable range of color changes upon reduction and oxidation, as well as higher molar extinction coefficients which enable the preparation of thinner films leading to faster switching processes [1,2,8]. To allow for fast switching rates

the interplay of fast transport of electrons as well as a fast diffusion of ions are necessary since both of them contribute to the redox reaction.

Electrochromic oxidation had been already observed for unsubstituted phthalocyanines (Pc) [9], but a more reversible electrochromic reduction of phthalocyanines could be obtained following the substitution of aromatic hydrogen atoms by electron-withdrawing cyano-groups [10,11] or by fluorine atoms [12,13]. These substitutions are responsible for positive shifts of about 0.7 V and 0.5 V of the redox potentials relative to the unsubstituted Pc, respectively. In the solid state, unsubstituted Pc or perfluorinated F_{16}Pc crystallize in different modifications and intermolecular coupling which results in different spectral characteristics [14,15]. The degree of fluorination of the aromatic ring system in copper phthalocyanines exhibits a significant influence on the intermolecular coupling and, hence, on the electron and ion transport. This leads to modification of thin-film properties such as light absorption and conductivity [16,17], essential for the application in organic field-effect transistors (OFET) [18], organic light-emitting diodes (OLED) [19], or organic photovoltaic cells (OPV) [20].

Thin films of F_{16}PcCu as well as F_{64}PcCu exhibited reversible electrochromic switching upon reduction and re-oxidation in con-

* Corresponding author.
  E-mail address: schlettwein@uni-giessen.de (D. Schlettwein).

T.H.Q. Nguyen, M. Schäfer, M. Pelmuş et al.
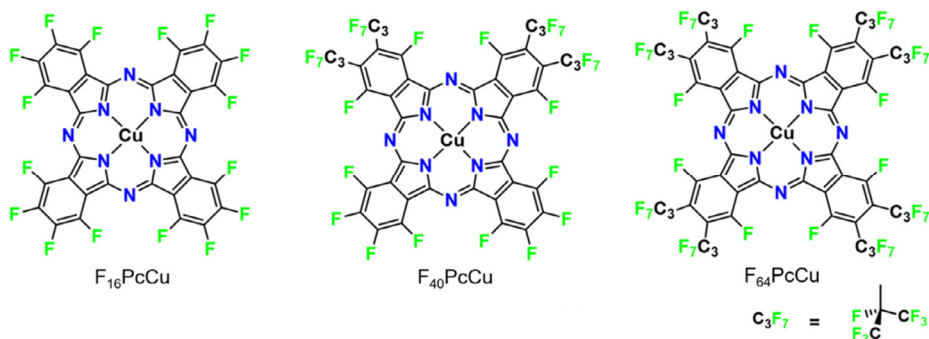
Scheme 1. Structural formula of F_{16}PcCu, F_{40}PcCu, and F_{64}PcCu.

tact with neutral aqueous electrolytes [3,21]. No influence of the counter anion, but a clear influence of the intercalating cation was observed with 1 M KCl, displaying the most reliable switching characteristics for thin films of, e.g., F_{16}PcCu and F_{16}PcZn [3,13]. Solid F_{16}PcCu consists of crystals with an interplanar molecular distance of around 3.2 Å revealing tight π-π stacking of the molecules [16,22,23]. Efficient transport of electrons was observed with an electronic conductivity significantly higher than for F_{64}PcCu [24,25]. The diffusion of charge-balancing counter cations, however, was significantly hampered [3]. An opposite situation occurs for F_{64}PcCu since the presence of 8 bulky perfluoroisopropyl groups (Scheme 1) resulted in amorphous films with a weak intermolecular coupling [25]. For crystals of F_{64}PcCu, it was observed that the peripheral perfluoroisopropyl groups inhibited the intermolecular stacking interactions [3,26]. π-π stacking interactions played a minor role since the inter-ligand distances in these crystals were higher than 5 Å leading to fast diffusion of cations, but decreased electronic conductivity [3,25,27]. Recently, a new type of perfluorinated phthalocyanine, F_{40}PcCu (Scheme 1), in which two of the four six-membered rings of the ligand have been preserved as in F_{16}PcCu, but two have been modified with perfluoroisopropyl groups as in F_{64}PcCu, has been reported to deliver a moderate degree of intermolecular coupling within the films, leading to a well-balanced, equally fast transport of electrons and ions [4]. Such optimized substitution pattern within a phthalocyanine molecule suggested that a mixture of two differently substituted phthalocyanines might result in mixed films with combined properties of both materials. A similar strategy had already proven successful for mixed films consisting of F_{16}PcCu and H_{16}PcCu, for which variation of the mixing ratios influenced the crystallinity and, thus, the conductivity of the films [28,29].

In the present work, thin films of a mixture of F_{16}PcCu and F_{64}PcCu were prepared by simultaneous physical vapor deposition to test the above hypothesis, presumably achieve the golden mean of the properties of both materials and mimic properties of F_{40}PcCu, a molecule in which the structural motifs of F_{16}PcCu and F_{64}PcCu had been successfully mixed on an intramolecular level. The optical, electrochemical, and spectroelectrochemical properties of the mixed films were characterized and compared to the results reported earlier for thin films of pure F_{16}PcCu, pure F_{64}PcCu, or F_{40}PcCu. An improvement of the electrochromic switching characteristics compared to the pure films of F_{16}PcCu or F_{64}PcCu could be obtained with a facilitated diffusion of the ions and an enhanced transport of the electrons similar to films of F_{40}PcCu, promising for the use of such mixed films in electrochromic devices.

2. Experimental

2.1. Preparation of thin films

FTO-coated (Sigma-Aldrich, 7 Ohm sq^{-1} or Kaivo, < 15 Ohm sq^{-1}) and ITO-coated (Delta-Technologies, 10 Ohm sq^{-1}) glass substrates were cut into 10 mm x 25 mm pieces, cleaned with RBS detergent solution (Roth), acetone (Roth, ≥ 99.5%) and isopropanol (Roth, ≥ 99.8%) in an ultrasonic bath at room temperature for 15 min each and blow-dried using N_2 gas.

Sublimation-purified F_{16}PcCu was purchased from TCI, F_{64}PcCu was synthesized and purified as reported in Ref. [25]. To prepare thin films of a mixture of F_{16}PcCu and F_{64}PcCu with different mixing ratios and different total film thicknesses on FTO- and ITO-coated glass, a vacuum chamber with two resistively heated BN crucibles (Kurt J. Lesker Ltd.) was used to enable simultaneous physical vapor deposition of both materials. The evaporation rate of both materials was monitored by two independent quartz crystal microbalances, which were calibrated as reported in Ref. [25] to provide the overall film thickness based on the densities of F_{16}PcCu (1.97 g cm^{-3}) and F_{64}PcCu (2.46 g cm^{-3}) [14,25]. The vapor deposition was carried out at a pressure of ≤ 10^{-5} mbar and an evaporation rate of about 0.25–0.75 nm Min^{-1}. For each deposition process, three substrates with a stripe of each substrate masked for later electrical contacting were mounted in a row on the sample holder of the chamber. This allowed the deposition of a mixed film on the central substrate and pure F_{16}PcCu and F_{64}PcCu films on the substrates at the side positions with cross-contamination of the respective other compound by about < 2% (for a 1:1 composition in the center), as determined by an independent calibration. For comparison purposes, a bilayer structure was prepared by deposition of F_{16}PcCu on the substrate followed by F_{64}PcCu.

2.2. Characterization and measurements

The coverage of the substrate by the films and the cross-sections of the samples were analyzed by scanning electron microscopy (SEM) in a Zeiss MERLIN at an emission current of 100 pA and an acceleration voltage of 5 kV. The crystallinity of the films was examined by grazing incidence X-ray diffractometry using a PANanalytical X'Pert Pro-MRD and Cu-K$_\alpha$-radiation.

The intermolecular interactions of the F_{16}PcCu and F_{64}PcCu molecules within the mixed films were investigated and compared with the bilayer structure by measuring the optical absorption spectra with a tec 5 diode array spectrometer. UV-
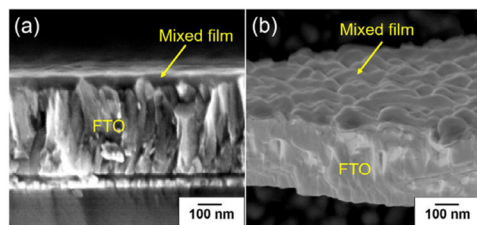
T.H.Q. Nguyen, M. Schäfer, M. Pelmuş et al.

Fig. 1. Cross-section (a) and tilted cross-section (b) of a 50 nm thin 1:1 F$_{16}$PcCu:F$_{64}$PcCu mixed film measured by SEM.

Vis spectra of F$_{16}$PcCu and F$_{64}$PcCu dissolved in hot chlorobenzene (~60 °C, Sigma-Aldrich, ≥99.8%) were measured using a Perkin Elmer Lambda 365 spectrometer. UV/Vis spectra of the molecules in toluene (Macron Fine Chemicals, reagent grade) with 20% absolute ethanol (Koptec) were recorded on a Cary 500 UV-Vis-NIR spectrophotometer (Agilent/Varian).

The spectroelectrochemical analyses of the films were carried out in a 1 M aqueous KCl (Aldrich, ≥ 99.5%) solution with a three-electrode-setup. To remove dissolved oxygen, the solution was purged with N$_2$ gas before the measurements. During the measurements, N$_2$ gas was passed above the surface of the solution to provide inert conditions, but avoid forced convection in the solution. To mount the perfluorinated phthalocyanine films for the spectroelectrochemical characterization, a Cu wire was attached with conductive Ag paste (Ferro GmbH) on the uncovered part of the substrate. Afterward, Araldite Rapid epoxy resin was used to seal the metal wire and the substrate area. The prepared sample was used as the working electrode in a glass cell (Starna) with a Ag/AgCl reference electrode (Red Rod, Radiometer analytical) and a platinum wire counter electrode (Goodfellow, 99.995%). Cyclic voltammetry at different scan rates between 0.6 and -1.1 V and chronoamperometry between the bias potentials of 0.6 and -1.0 V at a time delay of 3 s were performed using an IviumStat potentiostat/galvanostat. The measured values of the current of the first three ms after switching the potential were neglected in order to consider the response time of the setup, which was determined by an independent measurement. The effective electrode area of the samples was estimated from the charging current of the double layer capacitance (current after 4 ms) considering its linear dependence on the film thickness and assuming that the area of an infinitely thin film equals the geometric sample area (1.5 cm^2). The charge measured in long-term switching experiments beyond 5 s is underestimated when compared to that from short-term switching experiments by a factor of about 3.8 due to a low sampling frequency (5 Hz compared to 1 kHz) necessary for reliable data acquisition by the spectrometer. Molar charges were calculated based on the molecular mass of 863.9 g mol^{-1} (F$_{16}$PcCu) and 2064.1 g mol^{-1} (F$_{64}$PcCu). Optical absorption spectra were recorded *in operando* with the working electrode positioned in the beam of the tec5 diode array spectrometer.

3. Results and discussion

3.1. Film growth of mixed films

After a simultaneous vapor deposition of F$_{16}$PcCu and F$_{64}$PcCu, homogeneous thin films with color ranging from blue to green, dependent on the mixing ratio of both phthalocyanines, were obtained. SEM cross-section analysis (Fig. 1) showed complete coverage of the FTO substrate area and a compact film morphology, consisting of contacted grains around 50 – 200 nm in lateral diameter, typical for F$_{16}$PcCu (50 nm) [3] and F$_{64}$PcCu (200 nm) [3].
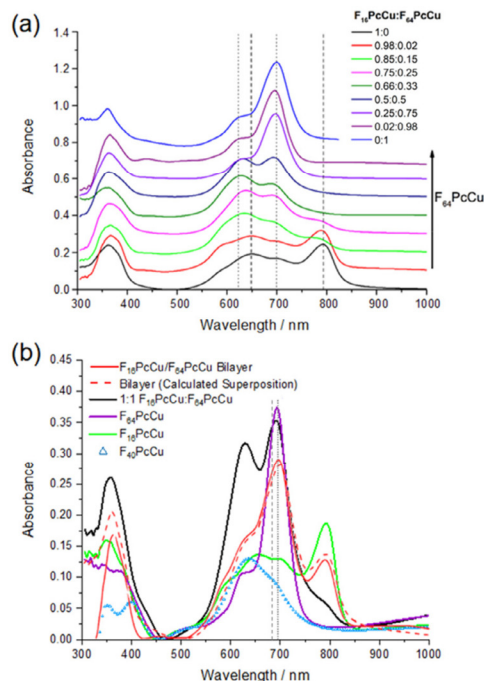

Fig. 2. (a) Normalized optical absorbance spectra of 50 nm thin films prepared with different mixing ratios of F$_{16}$PcCu:F$_{64}$PcCu with vertical lines representing the main contributions of F$_{16}$PcCu (dashed) and F$_{64}$PcCu (dotted). (b) Absorbance spectra of films of 1:1 F$_{16}$PcCu:F$_{64}$PcCu (d = 85 nm), pure F$_{64}$PcCu (d = 42.5 nm) and pure F$_{16}$PcCu (d = 42.5 nm) prepared within the same deposition process, compared to a spectrum of a F$_{16}$PcCu (25 nm)/F$_{64}$PcCu (25 nm) bilayer and a superposition of the pure F$_{16}$PcCu and F$_{64}$PcCu absorption spectra. For comparison purposes, a spectrum of F$_{40}$PcCu (d = 35 nm) is also shown. The dashed and dotted vertical lines represent the absorbance maximum measured for solutions (Fig. S1) of F$_{16}$PcCu and F$_{64}$PcCu in chlorobenzene (~60 °C), respectively.

The extent of intermolecular electronic coupling of F$_{16}$PcCu and F$_{64}$PcCu in the mixed films was investigated by measurements of the optical absorption spectra of films prepared with different mixing ratios (Fig. 2a). To allow for better comparison, the intensity of each absorption spectrum was normalized to the intensity of a 50 nm thick film by dividing by d/50 nm. For all the films, the Soret band below 400 nm and the Q-band around 500 – 800 nm characteristic for phthalocyanines [5,30] were found in the spectra. When compared to the solution spectra (Fig. S1), the films exhibited a broadening of the Q-band. However, the absorption spectra of F$_{64}$PcCu as a thin film and in solution were almost similar consistent with the existence of only weak intermolecular interaction of the molecules within the film. For F$_{16}$PcCu, various crystal structures have been observed characteristic for different intermolecular arrangement, leading to an altered coupling of the optical transition moments and, therefore, to differently split bands in the Q-band range [15]. The pure F$_{16}$PcCu film exhibited a broad absorption band with a maximum at around 790 nm, characteristic for the β-structure [15,16]. The presence of a band at around 660 nm can be assigned to the β-bilayer-structure of F$_{16}$PcCu and the band at around 700 nm indicates a disordered interfacial layer [15,16]. The admixture of F$_{64}$PcCu led to a decrease in intensity of the absorption at 790 nm, suggesting a disturbance of the β-structure similar to that observed for films of F$_{16}$PcCu doped with 10% H$_{16}$PcCu [28] and for 1:1 F$_{16}$PcCu:H$_{16}$PcCu mixed films [29].

At a proportion of 15% F_{64}PcCu within the F_{16}PcCu film, the bands between 650 nm and 700 nm became more pronounced revealing a dominance of the β-bilayer-structure and disordered interfacial layer in the mixed film. With the further addition of F_{64}PcCu (25% - 33%), a blueshift of the Q-band occurred indicating an attenuation of the intermolecular coupling of the transition dipoles, suggesting a molecularly dispersed F_{16}PcCu rather than solid crystalline F_{16}PcCu [28]. For a mixed film consisting of F_{16}PcCu and F_{64}PcCu in a ratio of 1:1, absorption maxima at around 625 and 690 nm were present. For the pure F_{64}PcCu film, only the maximum at 700 nm remained in the spectrum whereas the maximum at 625 nm transformed into a shoulder, as reported earlier [25]. Upon dissolution of such films, it was revealed that both molecules were retrieved from the mixed films without change of the intramolecular structure (Fig. S1). The broadened and split Q-band observed for films prepared in a mixing ratio of 1:1 revealed a stronger interaction of the molecules compared to pure F_{64}PcCu films, caused by the presence of F_{16}PcCu providing a more intense coupling, as also independently observed for thin films of F_{40}PcCu [4]. The 1:1 F_{16}PcCu:F_{64}PcCu thin films grew at constant band splitting and constant band positions for the different film thicknesses studied in this work (Fig. S2), which implies a constant interaction of both molecules within the film and, therefore, a homogeneous growth of the film, likewise reported earlier for pure F_{64}PcCu and F_{40}PcCu films [4,25]. Hence, the presence of both F_{16}PcCu and F_{64}PcCu molecules with a low and high degree of fluorination, respectively, leads to a moderate intermolecular coupling between both molecules within the films, similar to films of F_{40}PcCu.

The spectra of the mixed films were compared with those of a compositionally ordered bilayer structure prepared by sequential deposition of F_{16}PcCu and F_{64}PcCu (Fig. 2b). The measured absorption spectrum of the bilayer (red line) is compared to spectra of pure F_{16}PcCu, pure F_{64}PcCu, and a superposition of the two (red dashed line). The measured absorption spectrum of the bilayer coincided quite well with the superposition of the absorption characteristics of the pure F_{16}PcCu and pure F_{64}PcCu films, respectively. From 550 to 630 nm the bilayer exhibited characteristics similar to a film of F_{16}PcCu, while from 630 to 750 nm it reflected characteristics of F_{64}PcCu. Superposition of the spectra reveals a significant shoulder at 625 nm. In particular, the band at 790 nm assigned to the β-structure of F_{16}PcCu is still very pronounced confirming the presence of both molecules in two separate phases without disturbance of the film structure of F_{16}PcCu by adjacent F_{64}PcCu. Such observation is typical for independently growing films on top of each other and was also reported for bilayers consisting of F_{16}PcCu and H_{16}PcCu [29]. A comparison of the absorption spectra of the F_{16}PcCu/F_{64}PcCu bilayer structure with that of the 1:1 F_{16}PcCu:F_{64}PcCu mixed film (Fig. 2b) revealed significant differences in the position and intensity of the absorption bands. For the mixed film, the absorption at around 625 nm appeared at a similar intensity as the band at 690 nm. A large portion of the spectrum exhibits characteristics of solid F_{16}PcCu [3,28], blue-shifted compared with isolated molecules (Fig. S1). Correspondingly, the absorption at 790 nm strongly decreased, indicating that a small portion of F_{16}PcCu is present as the β-polymorph. The loss of crystallinity upon mixing was confirmed by X-ray diffraction (Fig. S3). While the pure F_{16}PcCu film exhibits a reflection at around 6° corresponding to the (200) reflection as reported earlier [31], no reflections were observed for the 1:1 F_{16}PcCu:F_{64}PcCu mixed film. Thus, by simultaneous deposition of both materials under the present conditions, phase-separation of F_{16}PcCu and F_{64}PcCu could be avoided and mixing of both molecules occurred on a molecular level, allowing intermolecular coupling between the two phthalocyanine species within the film.
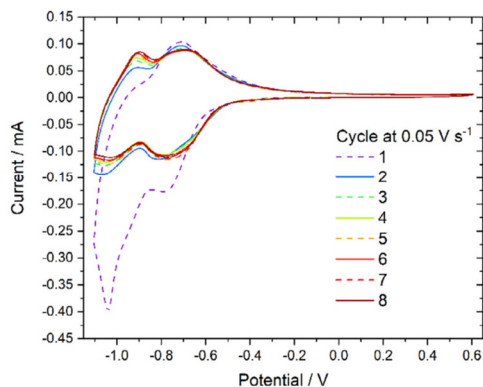

Fig. 3. First eight cyclic voltammograms of a 1:1 F_{16}PcCu:F_{64}PcCu mixed film (d = 50 nm) in contact with 1 M aqueous KCl during conditioning at a scan rate of 0.05 V s^{-1}.
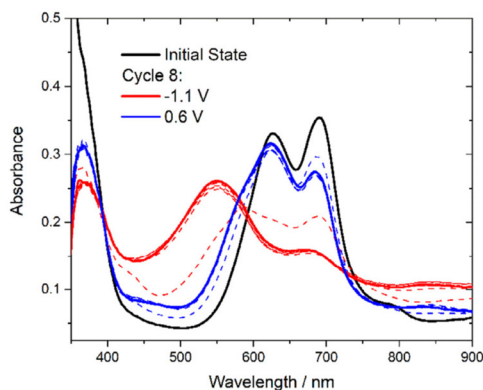

Fig. 4. Optical absorption spectra of a 1:1 F_{16}PcCu:F_{64}PcCu mixed film (d = 85 nm) in contact with 1 M aqueous KCl taken in the neutral state before (Initial State) and after eight cycles of electrochemical initialization (0.6 V), at intermediate potentials (dashed lines) and in the reduced state (-1.1 V).

3.2. Electrochromic reduction and re-oxidation

The initial cycle of reduction and re-oxidation of the as-deposited films immersed in 1 M aqueous KCl as electrolyte exhibited some differences in shape compared to subsequent cycles (Fig. 3). As already observed for films of F_{16}PcCu, F_{64}PcCu, or F_{40}PcCu [3,4], such conditioning process indicates an initial hindrance of the intercalation of counterions into the phthalocyanine films, subsequently lifted by structural relaxation upon further cycling.

Changes among the initial and subsequent cycles during the conditioning process were also noticed in the absorption spectra of the films in the re-oxidized state compared to the original spectra of the films before the initial reduction (Fig. 4). Films of pure F_{64}PcCu showed only minor changes in the absorption spectra during conditioning [3]. For films of F_{16}PcCu, however, the redox process led to a decrease of the band at 790 nm while the other bands, especially the one at 660 nm, gained in significance, representing an irreversible loss of the crystalline β-structure and increased contributions of other crystalline phases of F_{16}PcCu [3,16]. The presently observed spectral changes of the F_{16}PcCu:F_{64}PcCu
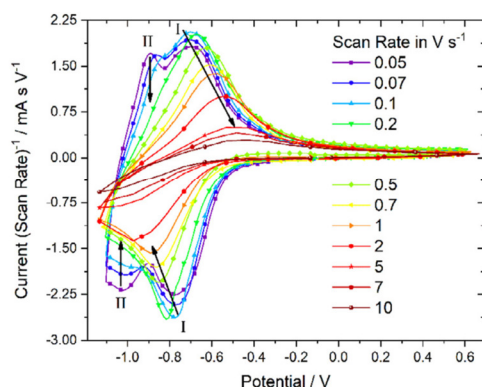
Fig. 5. Cyclic voltammetry at a 50 nm 1:1 F$_{16}$PcCu:F$_{64}$PcCu thin film in contact with 1 M aqueous KCl dependent on scan rate after conditioning. The current is divided by the scan rate to show all curves in one plot.

mixed films upon initialization (Fig. 4), however, also do show disappearance of the β-structure, but do not support the formation of other crystalline phases. Rather, they support the formation of disordered F$_{16}$PcCu. The shoulder at 790 nm, characteristic for the crystalline β-structure (Fig. 2) is no longer detected; the intensity of the absorption band at 690 nm is decreased and a band at 625 nm starts to dominate the spectral range, caused by the superposition of the main absorption of re-oxidized F$_{16}$PcCu and a shoulder of F$_{64}$PcCu in the original, as well as re-oxidized state [3]. After about 6 cycles, constant CV curves were obtained (Fig. 3), accompanied by the almost invariable shape of the corresponding absorption spectra for all the mixed films (Figs. 4 and S4). Following an initial conditioning reaction consisting in a phase change of the F$_{16}$PcCu portions from crystalline to disordered, a reversible reduction and re-oxidation of the films accompanied by the intercalation and expulsion of the K$^+$ ions was revealed, also by the spectral changes.

3.3. Rate of ion and electron transport

Following initialization, cyclic voltammetry (CV) was performed at different scan rates v (Figs. 5 and S5) to investigate the ion and electron transport within the 1:1 F$_{16}$PcCu:F$_{64}$PcCu mixed films and compare the results to existing data for pure films of F$_{16}$PcCu, F$_{40}$PcCu, and F$_{64}$PcCu. To provide a charge equivalent and represent all CV curves for different scan rates in one plot, the current I was divided by the scan rate. The stable voltammograms are dominated by the signal for the first reduction of the molecules ($E_{red,I}$, $I_{p,red}$) and the corresponding re-oxidation ($E_{ox,I}$, $I_{p,ox}$). Only for the smallest scan rates, $v \leq 0.1$ V s^{-1}, a second pair of peaks exists with the reduction peak $E_{red,II} \approx -1.0$ V and the re-oxidation peak $E_{ox,II} \approx -0.9$ V. For pure F$_{16}$PcCu films an additional pair of peaks was found in the same potential range due to the partial, second reduction of the complex [3].

At higher scan rates, $E_{red,I}$ shifted towards more negative potentials and, correspondingly, $E_{ox,I}$ of the re-oxidation process shifted towards less negative values, characteristic for kinetically hindered reactions. The redox potentials E_{redox} estimated as average values of each $E_{red,I}$ and $E_{ox,I}$ showed no trend in dependence to the scan rate and remained almost constant with deviations smaller than ± 0.04 V from the values obtained at a scan rate of 0.05 V s^{-1}. Hence, for comparison purposes, only the values determined at the scan rate of 0.05 V s^{-1} are shown in Table 1.

As hypothesized, the CV curves of the F$_{16}$PcCu:F$_{64}$PcCu films showed characteristics of films studied earlier, consisting of pure perfluorinated Pc [3]. The positions of $E_{red,I}$ (Table 1) of the mixed films (35 to 85 nm average overall film thickness) and the redox potentials E_{redox} fell into a similar range as those for pure F$_{16}$PcCu or F$_{64}$PcCu, slightly less negative than the values for F$_{40}$PcCu, whereas the positions of $E_{ox,I}$ were quite similar for all materials [3,4]. The electron-withdrawing substituents decrease the electron density in the π-system and lower the energy of the electronic levels resulting in a more positive redox potential and, hence, a facile reduction process [5,32,33]. Such a trend could be observed for F$_{64}$PcCu vs. with F$_{16}$PcCu, while for F$_{40}$PcCu a more negative value for the redox potential compared to both F$_{16}$PcCu or F$_{64}$PcCu [3,4] was found, as opposed to having an intermediate value. This apparent anomaly might be caused by the asymmetric arrangement of the substituents within the ligand, [34,35] which lacks the 4-fold effective symmetry axis of F$_{16}$PcCu and F$_{64}$PcCu (Scheme 1). The difference of peak potentials (0.05 V $\leq \Delta E_p \leq$ 0.11 V) for the 1:1 F$_{16}$PcCu:F$_{64}$PcCu thin films, obtained at a scan rate of 0.05 V s^{-1} remained almost constant for $v < 0.2$ V s^{-1} and was smaller than the values reported for films of other fluorinated phthalocyanines: 0.13 V $\leq \Delta E_p \leq$ 0.54 V for F$_{16}$PcCu [3], 0.22 V $\leq \Delta E_p \leq$ 0.30 V for F$_{40}$PcCu [4] and 0.13 V $\leq \Delta E_p \leq$ 0.22 V for F$_{64}$PcCu [3]. These values confirm the (quasi-) reversibility of the redox reactions [36,37]. At the significantly higher scan rate of 2 V s^{-1}, peak potential differences $\Delta E_p \leq$ 0.52 V were obtained for the 1:1 F$_{16}$PcCu:F$_{64}$PcCu mixed films of different thickness, showing quasi-reversibility even for such high scan rates.

Integration of the cyclic voltammograms (Fig. S6) yields the charge upon reduction and re-oxidation of the films. Complete reduction and re-oxidation of the molecules by $n = 1$ electron for each molecule was revealed in all films at slow scan rates, decreasing to values as small as $n = 0.2$ at the highest scan rate of 10 V s^{-1}, indicative of transport limitation of the reaction. Within the studied thickness range, however, a constant yield of the electrochemical reactions was found for a given scan rate, leading to currents and charges roughly proportional to the film thickness and, hence, largely constant values of n at a given scan rate.

To further analyze the transport limitation in the mixed films that was evident from the strong shift of $E_{red,I}$ and $E_{ox,I}$ and the decreased charge with increasing scan rate, the logarithm of the peak current of the cathodic ($I_{p,red}$) and anodic ($I_{p,ox}$) branches were plotted against the logarithm of the scan rate for films with different average thicknesses (Fig. 6). For reversible redox reactions without diffusion limitation, a linear dependence of I on v (slope of 1, solid black line) is expected [36]. Diffusion limitation

Table 1
Peak potentials $E_{red,I}$ of the reduction, $E_{ox,I}$ of the re-oxidation and estimated redox potentials E_{redox} of the 1:1 F$_{16}$PcCu:F$_{64}$PcCu mixed films ($d = 35$–85 nm) at a scan rate of 0.05 V s^{-1} in contact with aqueous KCl solution. The reported values for F$_{16}$PcCu ($d = 5.0$–67.5 nm), F$_{64}$PcCu ($d = 12.4$–117.1 nm) and F$_{40}$PcCu ($d = 10$–50 nm) under identical conditions are listed for comparison.

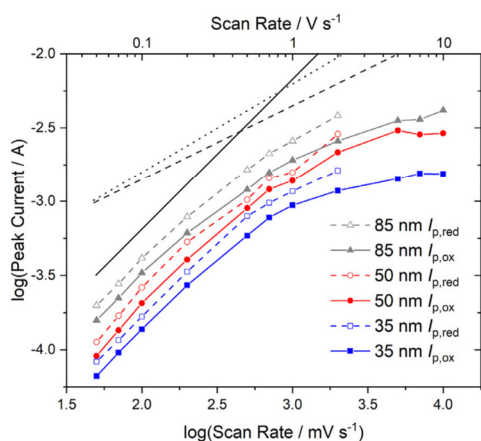| Material	$E_{red,I}$ / V	$E_{ox,I}$ / V	E_{redox} / V	
1:1 F$_{16}$PcCu:F$_{64}$PcCu	$-0.81 \leq E_{red,I} \leq -0.77$	$-0.72 \leq E_{ox,I} \leq -0.69$	$-0.76 \leq E_{redox} \leq -0.74$	This work
F$_{16}$PcCu	$-0.92 \leq E_{red,I} \leq -0.76$	$-0.71 \leq E_{ox,I} \leq -0.38$	$-0.78 \leq E_{redox} \leq -0.64$	Ref. [3]
F$_{64}$PcCu	$-0.79 \leq E_{red,I} \leq -0.75$	$-0.62 \leq E_{ox,I} \leq -0.55$	-0.68	Ref. [3]
F$_{40}$PcCu	$-1.04 \leq E_{red,I} \leq -0.91$	$-0.78 \leq E_{ox,I} \leq -0.61$	$-0.91 \leq E_{redox} \leq -0.76$	Ref. [4]

5

Fig. 6. Cathodic ($I_{p,red}$) and anodic ($I_{p,ox}$) peak current dependent on the scan rate obtained from cyclic voltammetry at 1:1 F$_{16}$PcCu:F$_{64}$PcCu mixed films of different thickness in contact with 1 M aqueous KCl. The solid line indicates a slope of 1, the dotted line a slope of 0.6 and the dashed line a slope of 0.5 while connecting lines of data points are just meant to guide the eye.

of reversible redox reactions leads to a dependence of I on the square root of v (slope of 0.5, dashed black line) [36]. A slope of 0.6 (dotted black line) is typical for films with reactions limited by electron hopping between redox centers [38–40]. Although I/v decreases with higher v (Fig. 5) indicative of kinetic hindrance and incomplete reactions, a linear dependency of the peak current on the scan rate (slope 1 in Fig. 6) is still valid up to 0.2 V s^{-1} for $I_{p,red}$ and $I_{p,ox}$ for all the films. Therefore, in this range of v, the reduction as well as the re-oxidation process proceed without significant limitation by the transport of electrons or counterions in the films. For F$_{16}$PcCu, such characteristics were restricted to films with $d \leq 20$ nm and for F$_{64}$PcCu to films with $d \leq 50$ nm as opposed to $d \leq 85$ nm for the present mixed F$_{16}$PcCu:F$_{64}$PcCu films [3]. At scan rates $v > 0.2$ V s^{-1} the linear dependency of I on v is no longer valid leading to a limitation of the redox processes where none of the characteristic slopes is approached. For the reduction reaction, a dependence of $I_{p,red} \sim v^{0.5}$ or $I_{p,red} \sim v^{0.6}$ cannot be unequivocally assigned despite a slope larger than 0.5, while for the re-oxidation no assignment to any of the expected slopes can be made since the data seem to approach a slope even smaller than 0.5. Hence, transport of electrons and counterions might be equally fast, with ions perhaps being slightly slower during reduction. For $v > 0.2$ V s^{-1}, films of pure F$_{64}$PcCu approached $I \sim v^{0.6}$ typical for a limitation of the redox reaction by electron transport [3]. Films of pure F$_{40}$PcCu ($d \leq 50$ nm) exhibited no transport limitation up to 1 V s^{-1} which is 5 times higher than the limit for the pure F$_{16}$PcCu, F$_{64}$PcCu, or F$_{16}$PcCu:F$_{64}$PcCu mixed films [4]. Beyond this range, however, F$_{40}$PcCu showed similar characteristics as F$_{16}$PcCu:F$_{64}$PcCu without a clear dependence $I \sim v^{0.5}$ (limited by ion diffusion) or $I \sim v^{0.6}$ (limited by electron hopping) distinguishable [4]. The present F$_{16}$PcCu:F$_{64}$PcCu mixed films, therefore, seem to provide a similar, optimized balanced transport of electrons and counterions established by, on average, the same concentration of two isoindole units with two perfluoroisopropyl substituents per molecule in the film.

While films of F$_{16}$PcCu already became transport-limited for $d > 20$ nm, and films of F$_{64}$PcCu for $d > 50$ nm [3], the 1:1 F$_{16}$PcCu:F$_{64}$PcCu mixed film with $d = 85$ nm containing considerably more active material than the respective pure films still

showed a non-limited reaction, at least for small v. We conclude that the introduction of perfluoroisopropyl groups by the inclusion of F$_{64}$PcCu leads to a decreased intermolecular coupling of both molecules, as also revealed by the optical absorption spectra (Fig. 2), which allows a well-balanced ion and electron transport in the mixed films, leading to the facile reduction and re-oxidation of even higher amounts of F$_{16}$PcCu than in pure films.

Quantitative measures for the transport rates in the mixed films were obtained via chronoamperometry. The integrated current density during potential steps between 0.6 and -1.0 V (or opposite) for 3 s each yielded an average charge of $n = 0.8$ electrons per molecule in the 1:1 F$_{16}$PcCu:F$_{64}$PcCu mixed films, representing the average of the values found for F$_{16}$PcCu ($n = 1$) and F$_{64}$PcCu ($n = 0.6$), significantly lower than $n = 1.5$ for F$_{40}$PcCu [3,4]. In Fig. 7a and b, the measured cathodic (j_{red}) and anodic current densities (j_{ox}) were plotted as a function of the reciprocal square root of time $t^{-1/2}$ according to the Cottrell Eq. (1) valid for semi-infinite diffusion [36]:

$$j = nFcD^{1/2}\pi^{-1/2}t^{-1/2}. \tag{1}$$

In this equation n is the number of electrons transferred in the reaction, F is Faraday's constant, c is the concentration in the bulk of the electrolyte (1 M aqueous KCl in our case) and D here represents an effective diffusion coefficient referring to the combined transport of both electrons and cations through the films [41]. Characteristics similar to those shown in Fig. 7 have been already observed for films of F$_{40}$PcCu and redox polymers, for example poly(fluorenone-bithiophene) [4,41]. For longer times the current density decreased to values lower than expected due to deviations from semi-infinite diffusion, caused by the finite film thickness [36,41,42]. In the short-time domain, from 4 up to 14 ms, the mixed films showed a deviation from the linear Cottrell plot that was not observed in films of F$_{40}$PcCu [4]. Such deviation might be due to kinetic limitations [36], also observed, e.g., for poly(fluorenone-bithiophene) [41]. Plots of $jt^{1/2}$ against log(t) (Fig. 7c) as in Ref. [41] illustrates the deviation from the Cottrelian behavior evidenced by the appearance of minima and maxima instead of a time-invariant plateau.

For intermediate times of about 7 – 40 ms (5 – 12 s$^{-1/2}$) the data of the mixed films followed the Cottrell behavior. From the slope of the fits in Fig. 7a and the maxima and minima of Fig. 7c, values for effective diffusion coefficients were determined. It should be noted that the deviations from the Cottrell behavior might result in underestimated values for the diffusion coefficient. For the 35 nm 1:1 F$_{16}$PcCu:F$_{64}$PcCu thin film, effective diffusion coefficients of D_{red}(35 nm) = 0.1·10^{-10} cm^2 s^{-1} and D_{ox}(35 nm) = 0.8·10^{-10} cm^2 s^{-1} were calculated for the cathodic and anodic current densities, respectively. The 50 nm mixed film yielded values of D_{red}(50 nm) = 0.2·10^{-10} cm^2 s^{-1} and D_{ox}(50 nm) = 1.2·10^{-10} cm^2 s^{-1}. For a 85 nm mixed film values of D_{red}(85 nm) = 0.3·10^{-10} cm^2 s^{-1} and D_{ox}(85 nm) = 1.5·10^{-10} cm^2 s^{-1} were obtained. D values were quite similar for all film thicknesses, but slightly larger for thicker films, possibly caused by subtle differences in film morphology. The values are also similar to D_{red} for F$_{64}$PcCu [3]. Generally, D_{red} was found smaller than D_{ox} as also seen earlier for F$_{16}$PcCu and F$_{40}$PcCu [3,4]. The reason for a smaller effective diffusion coefficient observed during reduction might be a slow removal of the solvation shell of the counterions [43] entering the film. D_{ox}, which, therefore, is most characteristic for diffusion in the active material can be directly compared to earlier measurements. The value of D_{ox} for the 85 nm mixed film is higher than that reported for a 91.9 nm thin F$_{64}$PcCu film (D_{ox} = 5.0·10^{-11} cm^2 s^{-1}), equal to D_{ox} reported for a 67.5 nm thin F$_{16}$PcCu film (D_{ox} = 1.5·10^{-10} cm^2 s^{-1}) [3]. The presently
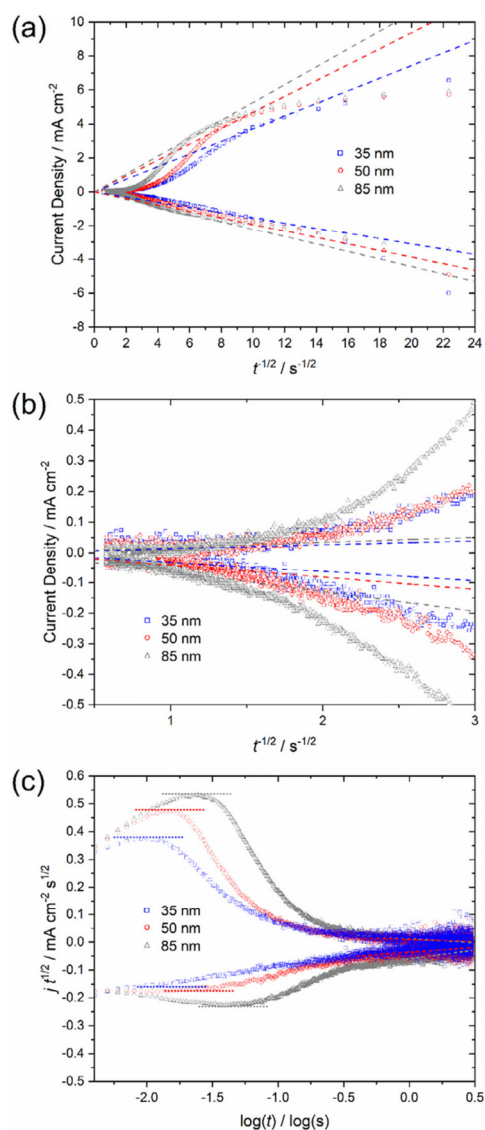
Fig. 7. (a) Dependence of the cathodic (j_{red}) and anodic (j_{ox}) currents density on the reciprocal square root of time observed during the chronoamperometric analysis of a 35 nm, 50 nm and 85 nm thin 1:1 F$_{16}$PcCu:F$_{64}$PcCu mixed film in contact with 1 M aqueous KCl. (b) Plot of the data for the long-time regime. (c) Plot of $jt^{1/2}$ against the logarithm of time. The linear fits following the Cottrell equation are marked in dashed lines.

determined values for the mixed films, however, are smaller than $D_{ox} = (14 - 19) \cdot 10^{-10}$ cm^2 s^{-1} measured for F$_{40}$PcCu films of similar thickness (35 and 50 nm) with nominally the same F-content [4].

For times longer than about 400 ms (1.6 s$^{-1/2}$ in Fig. 7b), another linear fit yields effective diffusion coefficients D_{long}(1:1 F$_{16}$PcCu:F$_{64}$PcCu) = (0.1 – 2.2)·10^{-12} cm^2 s^{-1} as the lower limit for the diffusion into poorly accessible domains of the films caused by either a difficult intercalation of the ions or poor electronic conduction, as it was also observed for F$_{40}$PcCu films [4], which showed slightly higher D_{long} = (0.5 – 8.5)·10^{-12} cm^2 s^{-1}. Such range of D_{long} is confirmed by a fit to the peak current densities during cyclic voltammetry at slow scan rates (Fig. S7). For technical applications, however, values of D_{ox} are of higher relevance since they represent fast switching capabilities and higher currents.

Another possibility to analyze the experimental data is the Anson-plot of the charge as a function of the square root of time (Fig. 8). A linear dependence is expected, characteristic for the diffusion coefficient [44]. The extrapolation of the fits in the Cottrell region (Fig. 8) resulted in a positive intercept t_{int} on the $t^{1/2}$ axis characteristic for slow interfacial kinetics [36]. In this case, the rate constant k can be determined from the $k = m \pi /(4 n F c t_{int}^{1/2})$ relationship [36] where m is the slope of the fits yielded $k = (0.9 - 8.9) \cdot 10^{-4}$ cm s^{-1} for the 1:1 F$_{16}$PcCu:F$_{64}$PcCu mixed films, a range similar to that reported for Li$^+$ intercalation in highly-oriented pyrolytic graphite ($10^{-5} - 10^{-4}$ cm s^{-1}) [45].

3.4. Spectroelectrochemical investigation of switching characteristics

During the electrochemical measurements, optical absorption spectra of the 1:1 F$_{16}$PcCu:F$_{64}$PcCu mixed films were measured *in operando* to analyze the changes of the electronic structure of the molecules and to reveal switching characteristics. Upon reduction (Fig. 9a) of the mixed films remarkable changes in the Q-band (500 – 750 nm) and in the range between the Q- and Soret band were noticed whereas the Soret band (350 – 430 nm) remained at the same position and its absorbance decreased only slightly. The Q-band absorption maximum at 625 nm turned into a local minimum. Also, at scan rates $v \leq 0.2$ V s^{-1} the absorption maximum at 690 nm first decreased and then slightly increased in intensity. Such a trend was even more pronounced for the 35 nm thin film (Fig. S8a). Similar spectral changes were already observed for thin films of pure F$_{16}$PcCu and assigned to the second reduction of F$_{16}$PcCu molecules [3]. Thereby, such partially occurring second reduction of F$_{16}$PcCu was also revealed in the present mixed films.

A new absorption maximum around 550 nm and a broad absorption reaching beyond 800 nm arose for all scan rates, as also observed earlier for pure F$_{16}$PcCu, F$_{40}$PcCu or F$_{64}$PcCu [3,4,21] and characteristic for phthalocyanine rings in their reduced state. Redox reactions for copper or zinc phthalocyanines typically occur on the phthalocyanine ring while for phthalocyanine complexes with polyvalent metals with e.g. iron or cobalt, the redox processes can involve the ligand as well as the metal atom [32,46,47]. The re-oxidation of the mixed films led to reversed changes of the absorption spectra (Fig. 9b). An isosbestic point was detected in both directions at 390 nm and at ~580 and ~730 nm "isosbestic ranges" were found (Figs. 9, S8b) implying a widely uniform reversible $A \rightleftarrows B$ transformation of neutral species A to a reduced species B with characteristic spectra for each form, respectively, as reported for F$_{40}$PcCu and F$_{64}$PcCu films [3,4,21]. For $v \leq 0.2$ V s^{-1} and in particular for the 35 nm thin film (Fig. S8a), the increase of the absorption intensity at 690 nm upon reduction led to an additional "isosbestic range" at ~650 nm indicating a further transformation $B \rightleftarrows C$ of the reduced species B to a doubly reduced species C, as reported earlier for pure F$_{16}$PcCu films [3] and also indicated by the presence of a second pair of peaks in the CV curves at low scan rates (Figs. 5 and S5). For $v > 0.2$ V s^{-1} the second reduction step, characterized by its peak pair as well as the corresponding spectral changes, was no longer observed.

The completeness of reduction and re-oxidation at increased switching rates was investigated by plotting the change in optical absorption between the reduced (-1.1 V) and the re-oxidized state (0.6 V) of the mixed films as a function of the scan rate (Fig. 10). Since significant changes upon reduction and re-oxidation were observed at 550 and 625 nm (Fig. 9), absorption signals at
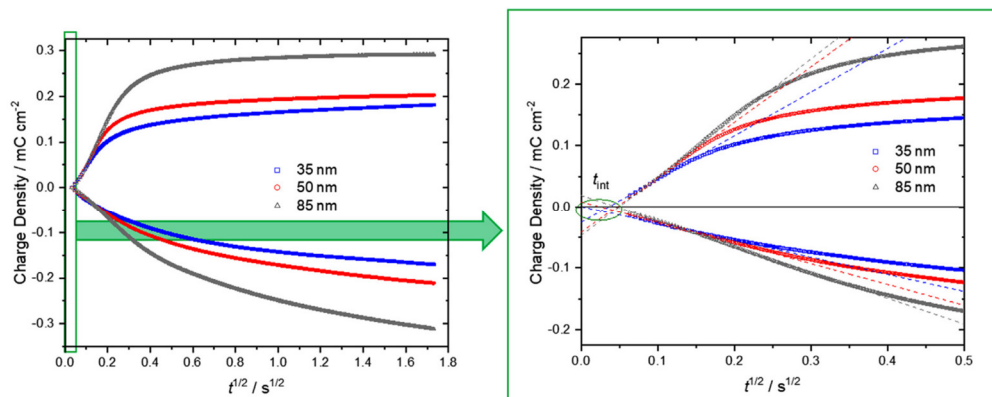
Fig. 8. Charge of the cathodic (q_{red}) and anodic (q_{ox}) branches as a function of the square root of time of 1:1 $F_{16}PcCu$:$F_{64}PcCu$ mixed films of different thickness in contact with 1 M aqueous KCl. The linear fits in the Cottrell region for determining the constant k are marked in dashed lines (For interpretation of the references to colour in this figure legend, the reader is referred to the web version of this article.).
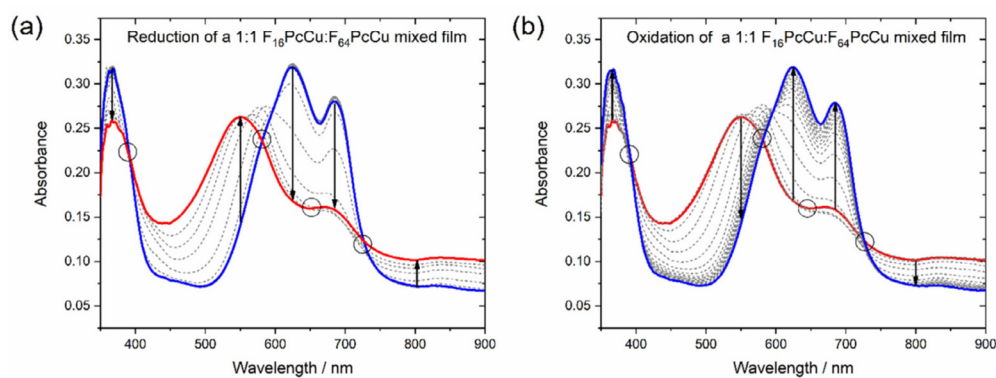

Fig. 9. Optical absorption spectra of a 1:1 $F_{16}PcCu$:$F_{64}PcCu$ mixed film ($d = 85$ nm) measured during cyclic voltammetry in contact with 1 M aqueous KCl at 0.05 V s^{-1} upon reduction (a) and re-oxidation (b). The isosbestic points and ranges are highlighted by circles.
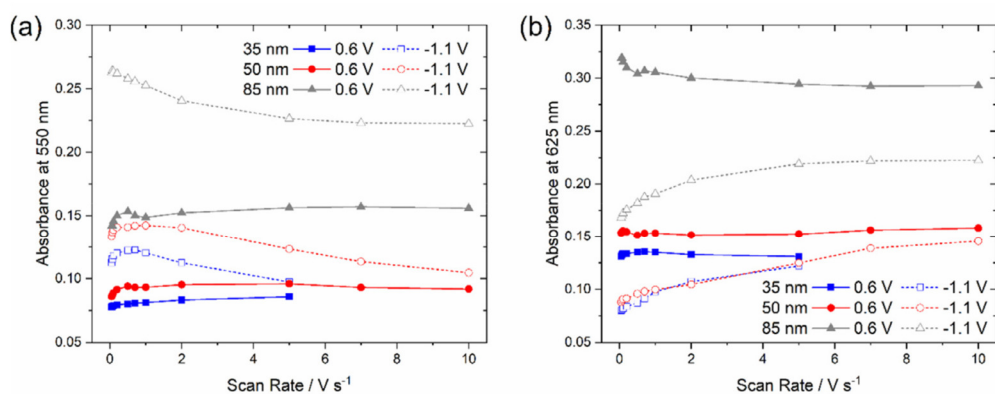

Fig. 10. Optical absorption at 550 nm (a) and 625 nm (b) as a function of the scan rate of 1:1 $F_{16}PcCu$:$F_{64}PcCu$ mixed films of different thickness in contact with 1 M aqueous KCl in the reduced (-1.1 V) and re-oxidized (0.6 V) states.
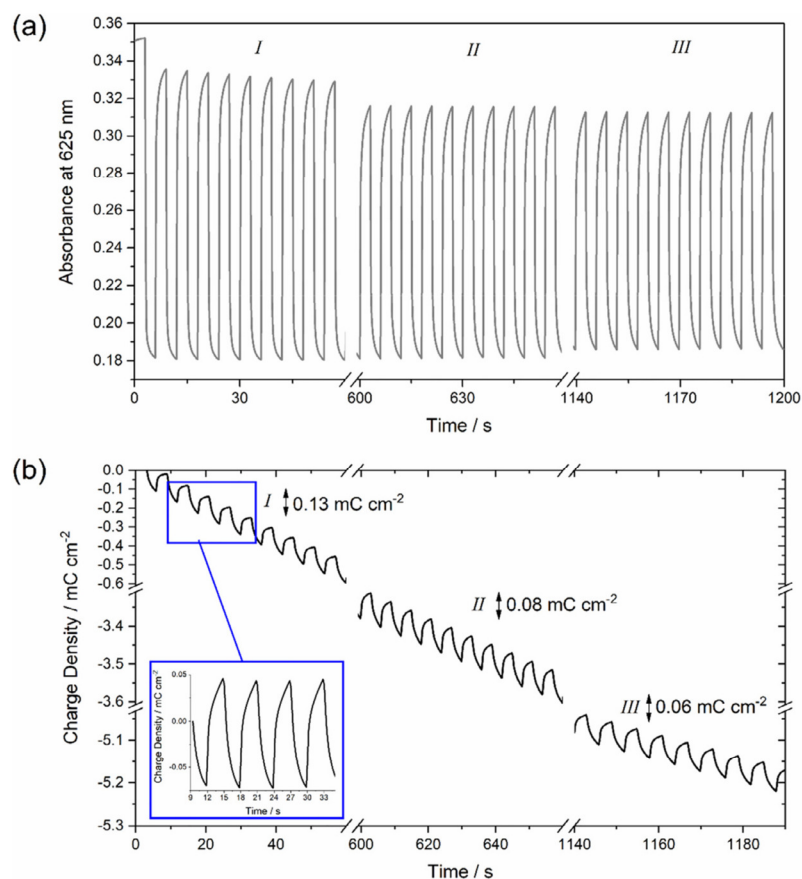
Fig. 11. Optical absorption at 625 nm of an 85 nm mixed film in contact with 1 M aqueous KCl (a), measured upon switching between 0.6 and -1.0 V kept for 3 s each, as well as the charge density observed simultaneously (b), arrows indicate the observed amplitude in the different regimes. The inset in (b) shows the signal after background-correction.

these wavelengths were selected. For all films the absorbance increase at 550 nm upon reduction (-1.1 V) was smaller at higher scan rates, indicating an incomplete reduction of the film. Accordingly, a higher absorbance at 625 nm was found, suggesting that some molecules in the film remained neutral. Nevertheless, upon re-oxidation (0.6 V) the absorbance change of all but the thickest (85 nm) films remained almost constant for all scan rates, thus confirming fast re-oxidation processes, as already noticed by the higher effective diffusion coefficient measured during re-oxidation. Such an observation was also made for films of F_{40}PcCu [4].

The spectral characteristics clearly show that the mixed films could still be reduced and re-oxidized almost completely, up to the highest scan rate of 10 V s^{-1} thus demonstrating a fast switching process for mixed films consisting of different substituted phthalocyanines.

The films could be repeatedly switched between the two redox states. Chronoamperometry was performed over 200 cycles with 3 s (1200 s total time) at alternately 0.6 or -1.0 V, as exemplarily shown for an 85 nm thin film of 1:1 F_{16}PcCu:F_{64}PcCu in Fig. 11. After 600 s, the amplitude of charge densities decreased (Fig. 11b) while the absorption at 625 nm shifted to lower values upon re-oxidation and slightly higher values upon reduction (Fig. 11a), both indicative of incomplete reduction. After another

540 s, the charge amplitudes further decreased leading to additional small changes in the absorbance, accompanied by subsequent partial ablation of the films (predominantly of F_{64}PcCu, Fig. S1) upon rinsing with water after removal from the electrolyte solution. Compared to the rather large changes in charge amplitudes, the absorbance change remained quite constant upon frequent fast reduction and re-oxidation. The drift of the charge density to negative values indicates the presence of a background current at negative potential, presumably caused by water reduction, which was also observed earlier in studies of F_{16}PcCu, F_{40}PcCu, and F_{64}PcCu films [3,4,21]. For each section of Fig. 11, response times t_{red} upon reduction and t_{ox} upon re-oxidation were determined, corresponding to the time that was needed to reach 90% of the absorbance change in a given step. Both were found in the range of seconds and increased upon repeated switching (Table 2) indicating attenuated switching as already revealed by the decreased charge amplitude, caused either by attenuated electron transport or attenuated ion transport. t_{red} of the mixed film is always shorter than t_{ox} despite smaller D_{red} compared to D_{ox} (Fig. 7). D_{red} and D_{ox}, however, were determined in the ms regime. The response times, requiring almost complete reactions, on the other hand, seem to be determined by diffusion into poorly accessible domains of the films.

9

Table 2

Response times t_{red} upon reduction and t_{ox} upon re-oxidation of an 85 nm mixed film for each section of Fig. 11.

Section	t_{red} / s	t_{ox} / s
I	0.4	0.8
II	0.7	1.1
III	0.9	1.2

4. Conclusions

Films containing a mixture of two well-established perfluorinated phthalocyanines, namely, $F_{16}PcCu$ and $F_{64}PcCu$ could be prepared by simultaneous physical vapor deposition. The optical absorption spectra of the mixed films revealed the formation of a widely molecularly dispersed mixture with moderate intermolecular interactions between $F_{16}PcCu$ and $F_{64}PcCu$. This can be interpreted as a blend of properties between quite strongly interacting $F_{16}PcCu$ and quite weakly interacting $F_{64}PcCu$. Electrochromic behavior with reversible switching between the reduced and re-oxidized state was found for the 1:1 $F_{16}PcCu$:$F_{64}PcCu$ films using an aqueous electrolyte at almost the same driving force as necessary for the reduction of either of the pure compounds. During the conditioning process, irreversible changes of the CV curves occurred, which were also reflected in changes of the absorption spectra standing for an irreversible loss of remaining crystallinity in the $F_{16}PcCu$ portion of the films. Upon reduction, changes in the absorption spectra characteristic for ring-reduced phthalocyanines were detected. Mixed films of up to 85 nm thickness could be reduced and re-oxidized even for scan rates as high as 10 V s^{-1} or, during chronoamperometry, at response times (90% yield) of about 1 s. This mixture of 1:1 $F_{16}PcCu$:$F_{64}PcCu$ led to a facilitated transport of both electrons and ions up to this film thickness, advantageously higher than for pure $F_{16}PcCu$ or $F_{64}PcCu$ films. The determined effective diffusion coefficient lies in the range of 10^{-11} to 10^{-10} cm^2 s^{-1} depending on film thickness speaking in favor of fast reversible switching, similar to films of $F_{40}PcCu$, a molecule with nominal identical content of perfluorinated and perfluoroisopropyl-substituted ligand rings as in the 1:1 $F_{16}PcCu$:$F_{64}PcCu$ film.

This work shows that mixed molecular thin films may provide simple means to achieve device properties superior to those of the pure constituents, without the need of performing new, often challenging, synthetic work to optimize properties on an intramolecular level.

Declaration of Competing Interest

The authors declare that they have no known competing financial interests or personal relationships that could have appeared to influence the work reported in this paper.

Credit authorship contribution statement

Thi Hai Quyen Nguyen: Conceptualization, Methodology, Validation, Investigation, Writing – original draft, Writing – review & editing, Visualization. **Michael Schäfer:** Investigation, Visualization. **Marius Pelmuş:** Investigation, Writing – review & editing. **Sergiu M. Gorun:** Conceptualization, Validation, Resources, Writing – review & editing, Supervision, Project administration, Funding acquisition. **Derck Schlettwein:** Conceptualization, Validation, Resources, Writing – review & editing, Supervision, Project administration, Funding acquisition.

Supplementary materials

Supplementary material associated with this article can be found, in the online version, at doi:10.1016/j.electacta.2021.138065.

References

[1] R.J. Mortimer, A.L. Dyer, J.R. Reynolds, Electrochromic organic and polymeric materials for display applications, Displays 27 (2006) 2–18.

[2] P.R. Somani, S. Radhakrishnan, Electrochromic materials and devices: present and future, Mater. Chem. Phys. 77 (2002) 117–133.

[3] J. Weissbecker, A. Loas, S.M. Gorun, D. Schlettwein, Switching of the Rate-limiting Step in the Electrochromic Reduction of Fluorinated Phthalocyanine Thin Films by Decreased Intermolecular Coupling, Electrochim. Acta 157 (2015) 232–244.

[4] T.H.Q. Nguyen, M. Pelmuş, C. Colomier, S.M. Gorun, D. Schlettwein, The influence of intermolecular coupling on electron and ion transport in differently substituted phthalocyanine thin films as electrochromic materials: a chemistry application of the Goldilocks principle, Phys. Chem. Chem. Phys. 22 (2020) 7699–7709.

[5] D. Schlettwein, N.I. Jaeger, T. Oekermann, Photoelectrochemical Reactions at Phthalocyanine Electrodes, in: K.M. Kadish, K.M. Smith, R. Guilard (Eds.), The Porphyrin Handbook, Academic Press, San Diego, 2003, pp. 247–283.

[6] K. Ishii, S. Mitsumura, Y. Hibino, R. Hagiwara, H. Nakayama, Preparation of phthalocyanine and octacyanophthalocyanine films by CVD on metal surfaces, and in SITU observation of the molecular processes by Raman spectroscopy, Appl. Surf. Sci. 33-34 (1988) 1324–1331.

[7] T. Fukuzawa, T. Koyama, G. Schneider, K. Hanabusa, H. Shirai, J. Inorg. Functional metallomacrocycle derivatives and their polymers. 31. Preparation and electrochromic properties of novel cobaltophthalocyanine thin films on electrodes, Organomet. Polym. 4 (1994) 261–271.

[8] M.M. Nicholson, Electrochromism and Display Devices, in: C.C. Leznoff, A.B.P. Lever (Eds.), Phthalocyanines: Properties and Applications, VCH, Weinheim, 1993, pp. 71–118.

[9] J.M. Green, L.R. Faulkner, Reversible Oxidation and Rereduction of Entire Thin Films of Transition-Metal Phthalocyanines, J. Am. Chem. Soc. 105 (1983) 2950–2955.

[10] B. Schumann, D. Wöhrle, N.I. Jaeger, Reversible Reduction and Reoxidation of Entire Thin Films of Octacyanophthalocyanine, J. Electrochem. Soc. 132 (1985) 2144–2149.

[11] A. Giraudeau, A. Louati, M. Gross, J.J. Andre, J. Simon, C.H. Su, K.M. Kadish, Redox properties of octacyano-substituted zinc phthalocyanine ((CN)$_8$PcZn). New charge-transfer complex, J. Am. Chem. Soc. 105 (1983) 2917–2919.

[12] B. Schöllhorn, J.P. Germain, A. Pauly, C. Maleysson, J.P. Blanc, Influence of peripheral electron-withdrawing substituents on the conductivity of zinc phthalocyanine in the presence of gases. Part 1: reducing gases, Thin Solid Films 326 (1998) 245–250.

[13] K. Hesse, D. Schlettwein, Spectroelectrochemical investigations on the reduction of thin films of hexadecafluorophthalocyaninatozinc ($F_{16}PcZn$), J. Electroanal. Chem. 476 (1999) 148–158.

[14] M.K. Engel, Single-Crystal Structures of Phthalocyanine Complexes and Related Macrocycles, in: K.M. Kadish, K.M. Smith, R. Guilard (Eds.), The Porphyrin Handbook, Academic Press, San Diego, 2003, pp. 1–242.

[15] T. Hosokai, A. Gerlach, A. Hinderhofer, C. Frank, G. Ligorio, U. Heinemeyer, A. Vorobiev, F. Schreiber, Simultaneous in situ measurements of x-ray reflectivity and optical spectroscopy during organic semiconductor thin film growth, Appl. Phys. Lett. 97 (2010) 063301.

[16] D.G. de Oteyza, E. Barrena, J.O. Ossó, S. Sellner, H. Dosch, Thickness-Dependent Structural Transitions in Fluorinated Copper-phthalocyanine ($F_{16}CuPc$) Films, J. Am. Chem. Soc. 128 (2006) 15052–15053.

[17] W. Michaelis, D. Wöhrle, D. Schlettwein, Organic n-channels of substituted phthalocyanine thin films grown on smooth insulator surfaces for organic field effect transistors applications, J. Mater. Res. 19 (2004) 2040–2048.

[18] O.A. Melville, B.H. Lessard, T.P. Bender, Phthalocyanine-Based Organic Thin-Film Transistors: A Review of Recent Advances, ACS Appl. Mater. Interfaces 7 (2015) 13105–13118.

[19] C. Bizzarri, E. Spuling, D.M. Knoll, D. Volz, S. Bräse, Sustainable metal complexes for organic light-emitting diodes (OLEDs), Coord. Chem. Rev. 373 (2018) 49–82.

[20] M.G. Walter, A.B. Rudine, C.C. Wamser, Porphyrins and phthalocyanines in solar photovoltaic cells, J. Porphyr. Phthalocyanines 14 (2010) 759–792.

[21] S. Nagel, M. Lener, C. Keil, R. Gerdes, Ł. Łapok, S.M. Gorun, D. Schlettwein, Electrochromic Switching of Evaporated Thin Films of Bulky, Electronic Deficient Metallo-Phthalocyanines, J. Phys. Chem. C 115 (2011) 8759–8767.

10

[22] P.A. Pandey, L.A. Rochford, D.S. Keeble, J.P. Rourke, T.S. Jones, R. Beanland, N.R. Wilson, Resolving the Nanoscale Morphology and Crystallographic Structure of Molecular Thin Films: F_{16}CuPc on Graphene Oxide, Chem. Mater. 24 (2012) 1365–1370.

[23] D.G. de Oteyza, E. Barrena, S. Sellner, J.O. Ossó, H. Dosch, Structural Rearrangements During the Initial Growth Stages of Organic Thin Films of F_{16}CuPc on SiO$_2$, J. Phys. Chem. B 110 (2006) 16618–16623.

[24] C. Keil, D. Schlettwein, Development of the field-effect mobility in thin films of F_{16}PcCu characterized by electrical in situ measurements during device preparation, Org. Electron. 12 (2011) 1376–1382.

[25] C. Keil, O. Tsaryova, L. Lapok, C. Himcinschi, D. Wöhrle, O.R. Hild, D.R.T. Zahn, S.M. Gorun, D. Schlettwein, Growth and characterization of thin films prepared from perfluoro-isopropyl-substituted perfluorophthalocyanines, Thin Solid Films 517 (2009) 4379–4384.

[26] H. Moons, Ł. Łapok, A. Loas, S. van Doorslaer, S.M. Gorun, Synthesis, X-ray Structure, Magnetic Resonance, and DFT Analysis of a Soluble Copper(II) Phthalocyanine Lacking C−H Bonds, Inorg. Chem. 49 (2010) 8779–8789.

[27] H. Moons, A. Loas, S.M. Gorun, S. van Doorslaer, Photoreduction and light-induced triplet-state formation in a single-site fluoroalkylated zinc phthalocyanine, Dalton Trans. 43 (2014) 14942–14948.

[28] L. Cornelius, M. Beu, C. Keil, D. Schlettwein, Doping in mixed films of differently substituted phthalocyanines measured in-situ during film growth, Phys. Status Solidi RRL 6 (2012) 214–216.

[29] A. Opitz, B. Ecker, J. Wagner, A. Hinderhofer, F. Schreiber, J. Manara, J. Pflaum, W. Brütting, Mixed crystalline films of co-evaporated hydrogen- and fluorine-terminated phthalocyanines and their application in photovoltaic devices, Org. Electron. 10 (2009) 1259–1267.

[30] C.G. Claessens, U. Hahn, T. Torres, Phthalocyanines: From Outstanding Electronic Properties to Emerging Applications, Chem. Rec. 8 (2008) 75–97.

[31] Z. Bao, A.J. Lovinger, J. Brown, New Air-Stable n-Channel Organic Thin Film Transistors, J. Am. Chem. Soc. 120 (1998) 207–208.

[32] M. L'Her, A. Pondaven, Electrochemistry of Phthalocyanines, in: K.M. Kadish, K.M. Smith, R. Guilard (Eds.), The Porphyrin Handbook, Academic Press, San Diego, 2003, pp. 117–169.

[33] J. Mack, M.J. Stillman, Electronic Structures of Metal Phthalocyanine and Porphyrin Complexes from Analysis of the UV–Visible Absorption and Magnetic Circular Dichroism Spectra and Molecular Orbital Calculations, in: K.M. Kadish, K.M. Smith, R. Guilard (Eds.), The Porphyrin Handbook, Academic Press, San Diego, 2003, pp. 43–116.

[34] A.B.P. Lever, The Phthalocyanines—Molecules of Enduring Value; a Two-dimensional Analysis of Redox Potentials, J. Porphyr. Phthalocyanines 3 (1999) 488–499.

[35] V.N. Nemykin, N. Kobayashi, T. Nonomura, E.A. Luk'yanets, Low Symmetrical Phthalocyanines Having Spectroscopic and Electrochemical Properties Characteristic of Unexpected Accidental S_1 State Degeneracy and Non-Planar Distortions, Chem. Lett. 29 (2000) 184–185.

[36] A.J. Bard, L.R. Faulkner, Electrochemical Methods, Electrochemical Methods: Fundamentals and Applications, Wiley, New York, 2001.

[37] J.M. Savéant, Elements of Molecular and Biomolecular Electrochemistry, John Wiley & Sons, Hoboken, NJ, 2006.

[38] E. Laviron, A multilayer model for the study of space distributed redox modified electrodes: Part I. Description and discussion of the model, J. Electroanal. Chem. 112 (1980) 1–9.

[39] E. Laviron, L. Roullier, C. Degrand, A multilayer model for the study of space distributed redox modified electrodes: Part II. Theory and application of linear potential sweep voltammetry for a simple reaction, J. Electroanal. Chem. 112 (1980) 11–23.

[40] E. Laviron, A multilayer model for the study of space distributed redox modified electrodes: Part III. Influence of interactions between the electroactive centers in the first layer on the linear potential sweep voltammograms, J. Electroanal. Chem. 122 (1981) 37–44.

[41] M.D. Levi, R. Demadrille, A. Pron, M.A. Vorotyntsev, Y. Gofer, D. Aurbach, Application of a Novel Refinement Method for Accurate Determination of Chemical Diffusion Coefficients in Electroactive Materials by Potential Step Technique, J. Electrochem. Soc. 152 (2005) E61–E67.

[42] M. Tagliazucchi, D. Grumelli, C. Bonazzola, E.J. Calvo, Oxidation-Reduction Dynamics in Layer-by-Layer Self-Assembled Redox Polyelectrolyte Multilayer Modified Electrodes, J. Nanosci. Nanotechnol. 6 (2006) 1731–1740.

[43] K. Xu, A. von Cresce, U. Lee, Differentiating Contributions to "Ion Transfer" Barrier from Interphasial Resistance and Li⁺ Desolvation at Electrolyte/Graphite Interface, Langmuir 26 (2010) 11538–11543.

[44] F.C. Anson, R.A. Osteryoung, Chronocoulometry: A Convenient, Rapid and Reliable Technique for Detection and Determination of Adsorbed Reactants, J. Chem. Educ. 60 (1983) 293–296.

[45] Z.T. Gossage, J. Hui, Y. Zeng, H. Flores-Zuleta, J. Rodríguez-López, Probing the reversibility and kinetics of Li⁺ during SEI formation and (de)intercalation on edge plane graphite using ion-sensitive scanning electrochemical microscopy, Chem. Sci. 10 (2019) 10749–10754.

[46] P.C. Minor, M. Gouterman, A.B.P. Lever, Electronic Spectra of Phthalocyanine Radical Anions and Cations, Inorg. Chem. 24 (1985) 1894–1900.

[47] J.H. Zagal, Metallophthalocyanines as catalysts in electrochemical reactions, Coord. Chem. Rev. 119 (1992) 89–136.

Supplementary Information for

Electron and Ion Transport in Mixed Electrochromic Thin Films of Perfluorinated Phthalocyanines

Thi Hai Quyen Nguyen[a], Michael Schäfer[a], Marius Pelmuş[b], Sergiu M. Gorun[b], Derck Schlettwein[a*]

[a] Institute of Applied Physics *and* Laboratory of Materials Research, Justus Liebig University Giessen, Heinrich-Buff-Ring 16, 35392 Giessen, Germany

[b] Department of Chemistry and Biochemistry *and* Center for Functional Materials, Seton Hall University, 400 South Orange Ave, South Orange, NJ 07079, USA

* corresponding author at email: schlettwein@uni-giessen.de
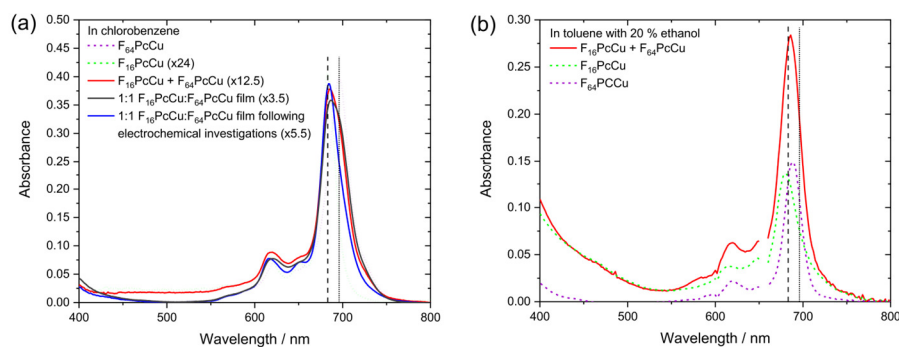
Fig. S1: (a) Absorbance spectra of $F_{16}PcCu$, $F_{64}PcCu$, and a mixed solution of the two in hot chlorobenzene compared to spectra of a dissolved freshly deposited 1:1 film and a 1:1 film following the electrochemical investigation. It is seen that the solutions of both films still consist of the two original molecules. It is also seen that the content of $F_{64}PcCu$ in the mixed films decreased upon extended electrochemical investigation, presumably contributing to the decrease of the absorbance at 700 nm during electrochemical initialization (Fig. 4, Fig. S4) and causing the decrease of absorbance (Fig. 11) upon frequent switching between the two redox states. (b) Absorbance spectra of $F_{16}PcCu$, $F_{64}PcCu$, and a mixed solution of the two in ethanol:toluene (1:4). A small blue-shift of the peak positions is observed compared to the peaks of $F_{16}PcCu$ and $F_{64}PcCu$ in hot chlorobenzene (dashed and dotted vertical lines), indicating a different coordination by the solvents. However, additional peaks caused by direct interaction of $F_{16}PcCu$ and $F_{64}PcCu$ are not observed also in these solvents.
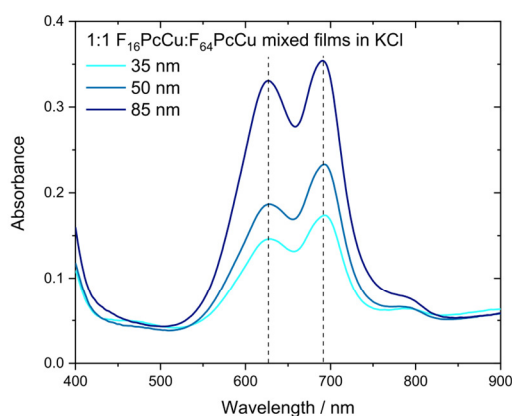

Fig. S2: Optical absorbance spectra of 1:1 $F_{16}PcCu$:$F_{64}PcCu$ mixed films of different thickness in contact with 1 M aqueous KCl.
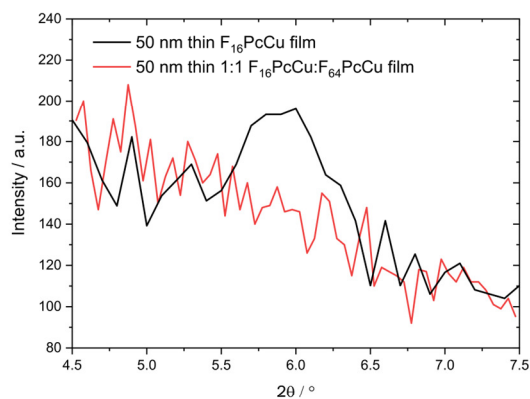
Fig. S3: Grazing incidence X-ray diffraction (GIXRD) of a 50 nm thin 1:1 $F_{16}PcCu:F_{64}PcCu$ mixed film on FTO compared to pure and 50 nm thin $F_{16}PcCu$ film.
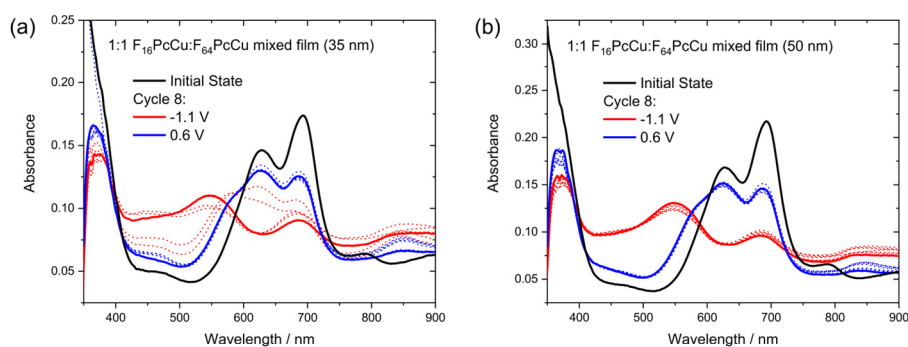

Fig. S4: Optical absorption spectra of (a) a 35 nm and (b) a 50 nm 1:1 $F_{16}PcCu:F_{64}PcCu$ thin film in contact with 1 M aqueous KCl taken in the neutral state before (Initial State) and after eight cycles of electrochemical initialization (0.6 V), at intermediate potentials (dashed lines) and in the reduced state (-1.1 V).
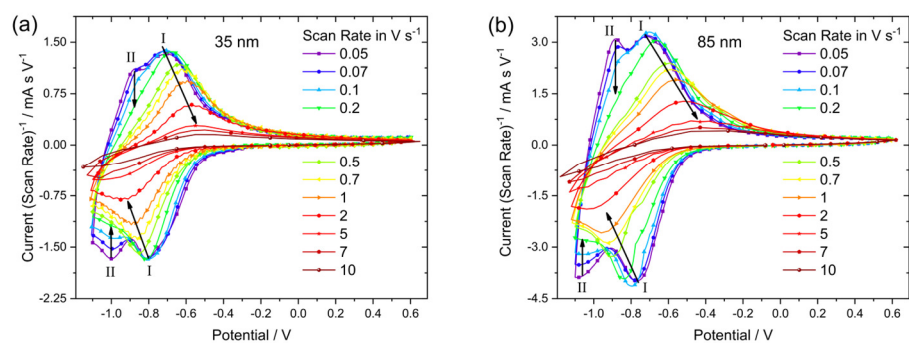
Fig. S5: Cyclic voltammetry at (a) a 35 nm and (b) a 85 nm 1:1 F$_{16}$PcCu:F$_{64}$PcCu thin film in contact with 1 M aqueous KCl dependent on scan rate after conditioning. The current is divided by the scan rate to show all curves in one plot.
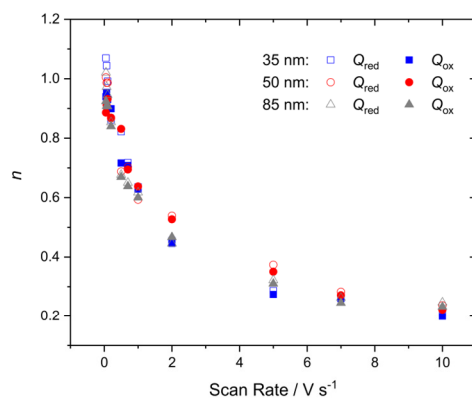

Fig. S6: Charge per molecule in the 1:1 F$_{16}$PcCu:F$_{64}$PcCu mixed films of different thickness in contact with 1 M aqueous KCl obtained from integration of the cyclic voltammograms. Values widely independent of thickness show a widely constant yield of the electrochemical reaction within the studied thickness range.
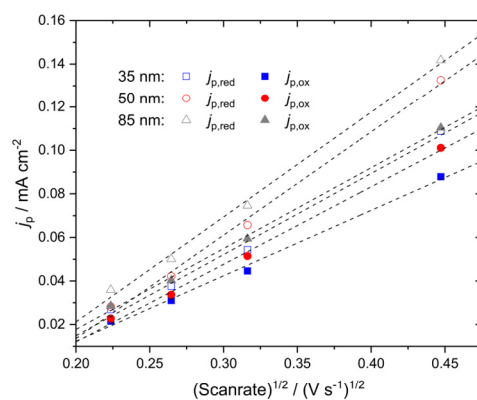
Fig. S7: Current density during cyclic voltammetry at slow scan rates and fits according to the Randles-Ševčík equation to estimate D_{long} leading to values of $2 \cdot 10^{-12}$ cm^2 s^{-1} $< D_{long} < 6 \cdot 10^{-12}$ cm^2 s^{-1} confirming the range obtained during chronoamperometry at times > 400 ms of 1:1 $F_{16}PcCu:F_{64}PcCu$ mixed films of different thickness in contact with 1 M aqueous KCl.
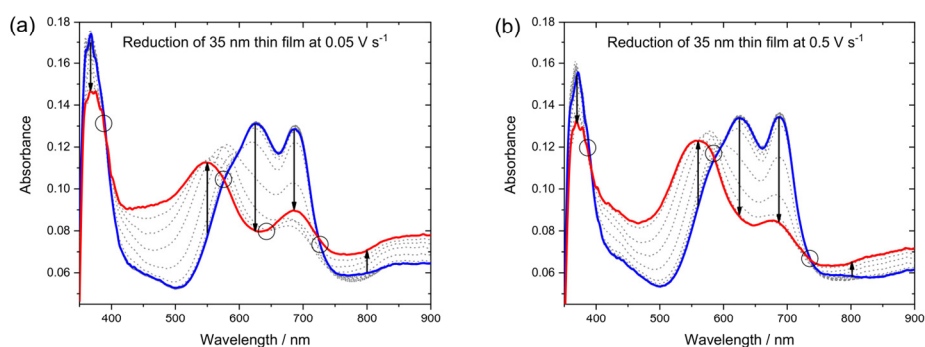

Fig. S8: Optical absorption spectra of a 1:1 $F_{16}PcCu:F_{64}PcCu$ mixed film ($d = 35$ nm) measured during cyclic voltammetry in contact with 1 M aqueous KCl upon reduction at (a) 0.05 V s^{-1} and (b) 0.5 V s^{-1}. The isosbestic points and "ranges" are highlighted by circles. An additional range around 650 nm is observed at 0.05 V s^{-1}.

Outlook from Publication 3

The results of Publication 3 show that the modification of the film composition on the material level rather than on the intramolecular level by mixing two molecules that represent well-established materials allows for simple fabrication of mixed thin films with combined optimized properties. Films of a mixture of $F_{16}PcCu$ and $F_{64}PcCu$ in a ratio of 1:1 and even with a higher film thickness than for films of $F_{64}PcCu$ or $F_{16}PcCu$ [54] provided an enhanced transport of electrons and facilitated diffusion of ions leading to improved electrochromic characteristics almost comparable to the films of $F_{40}PcCu$ [124], the specifically designed molecular optimum. Thus, if small compromises are accepted the variation of the substitution pattern of the molecules via synthesis routes can be circumvented to still obtain thin films with optimized properties of two different molecules.

6 Conclusions

Different strategies were pursued in the course of this Ph.D. project to enhance the mixed transport of electrons and ions and, thus, the electrochromic switching characteristics of thin films consisting of either tungsten oxide as the classic electrochromic material or fluorinated copper phthalocyanines as alternative counterparts by modification of their respective characteristics as thin films in electrochromic cells.

Thin films of WO_3 were fabricated via spin-coating from a precursor solution consisting of peroxotungstic acid and different structure-directing agents to tune the porosity and the internal film structure and, thus, to enable a facilitated diffusion of charge-balancing Li^+ ions through the film network resulting in improved electrochromic performance. The addition of the polymers PEG 400 or PEG 600 into the precursor solution led to $WO_3|\mu p400$ or $WO_3|\mu p600$ films, respectively, consisting of interconnected micropores which provided fast electrochromic switching with large transmittance modulation and high coloration efficiencies. Fast diffusion of Li^+ ions could be also established in a complete electrochromic device with NiO as counter electrode and $WO_3|\mu p600$ as working electrode, promising for the application of microporous WO_3 films in smart windows. The use of the block copolymer PIB_{50}-b-PEO_{45} as structure-directing agent provided $WO_3|mp$ films with isolated spherical mesopores and residual polymer fragments leading to trapping of ions and, thus, electrochromic properties comparable to compact $WO_3|comp$ films, only. Annealing the as-deposited $WO_3|mp$ films at slightly higher temperatures, however, provided mesoporous and widely amorphous $WO_3|mp*$ films with similar improved electrochromic characteristics as $WO_3|\mu p400$ or $WO_3|\mu p600$ films. Significantly optimized electrochromic characteristics could be obtained for WO_3 films which were fabricated in the presence of PIB_{50}-b-PEO_{45} combined with PEG 600. These $WO_3|\mu mp$ films containing mesopores connected by micropores needed only around 2 s to switch from the bleached to the colored state and vice versa providing an even more facilitated diffusion of ions and higher transmittance modulations and coloration efficiencies than for WO_3 films modified by just PEG as additive. The analysis of the $WO_3|\mu mp$ films with ferrocene as electroactive species revealed the high accessibility of the inner film surface even by these large ions in the films containing

accessible mesopores. Use of a rotating disk electrode allows for distinguishing between the diffusion in these pores and in the electrolyte. Fast diffusion in these pores explains the higher effective diffusion coefficients for Li^+ ions in these films compared to other WO_3 films. High chemical reversibility R_{EC} of the electrochromic switching processes could also be established for the microporous WO_3 films even at quite high film thickness. The surfactant Triton as an alternative structure-directing agent led to WO_3 thin films showing electrochromic switching characteristics similar to the films prepared with PEG or the combination of PIB_{50}-b-PEO_{45} and PEG 600. Among these, the use of PEG might be the one of choice since a significantly shorter heat treatment at lower temperature was required for the fabrication of these films leading to a preparation of WO_3 films at possibly lower cost and in an environmentally friendly manner.

Vapor-deposited thin films of the new $F_{40}PcCu$ or of a mixture of two already established Pc molecules, $F_{16}PcCu$ and $F_{64}PcCu$, were prepared to reach a moderate degree of intermolecular coupling in the solid state, and, hence, fast transport of electrons and K^+ charge-balancing ions leading to fast electrochromic switching. The presence of four perfluoroisopropyl groups in $F_{40}PcCu$ rather than eight as in $F_{64}PcCu$ or none as in $F_{16}PcCu$ provided a film structure with optimized properties beyond those of $F_{64}PcCu$ or $F_{16}PcCu$. Electrochromic switching with high R_{EC} and extremely fast response times of only ~ 0.3 s were obtained for these $F_{40}PcCu$ films confirming the presence of moderate intermolecular interactions of the molecules that enabled a well-balanced, equally fast transport of ions and electrons in the films. The redox reactions of the films of $F_{40}PcCu$ occurred, as expected, on the phthalocyanine ring which was also observed for films of $F_{40}PcZn$. The simultaneous vapor deposition of $F_{16}PcCu$ and $F_{64}PcCu$ in a ratio of 1:1 resulted in mixed films that also showed fast response times of about 1 s. Hence, compared to pure films of $F_{16}PcCu$ or $F_{64}PcCu$, these films exhibited enhanced electrochromic switching properties that were nearly as good as those of the films of $F_{40}PcCu$. Thus, the mixture of $F_{16}PcCu$ and $F_{64}PcCu$ on the molecular level established an overall intermediate strength of coupling between the molecules in the film leading to fast transport of both electrons and ions in the mixed films similar as for the films of $F_{40}PcCu$ consisting of the same content of F_4-benzo and $F_2(C_3F_7)_2$-benzo groups in the ligand, but realized directly on an intramolecular level.

The different approaches for modification of the film properties allowed to obtain WO_3 thin films with accessible pathways for facile transport of ions and thin films of phthalocyanines with a moderate degree of intermolecular coupling of the molecules in the solid state that enabled a fast transport of electrons and ions. In both cases, the

enhanced transport of electrons and/or ions led to fast and stable electrochromic switching characteristics with short response times, significantly beyond those reached earlier.
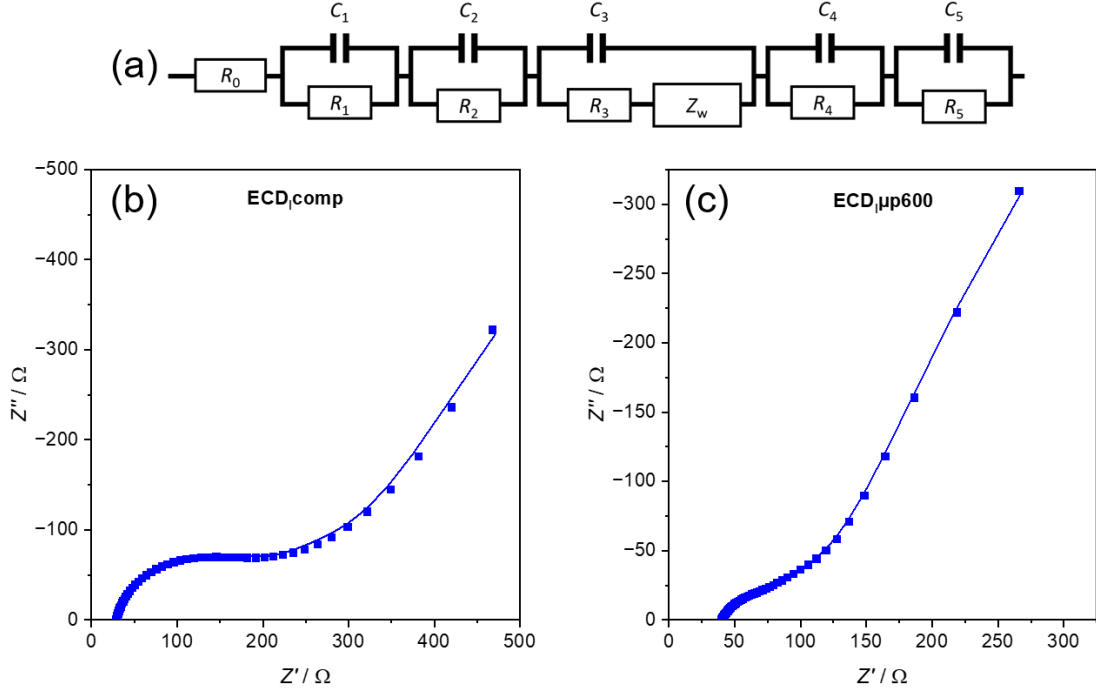
A. Appendix

Figure A.1: (a) Equivalent circuit describing a complete electrochromic device as reported in [209] and Nyquist plots of (b) ECD|comp and (c) ECD|µp600 with the experimental data (points) and fitted data (solid lines) obtained from the fits using the equivalent circuit shown in (a).

Table A.1: Values of the resistances R and capacitances C, the Warburg coefficient A_w and the diffusion coefficient D_I obtained from A_w of ECD|comp and ECD|µp600.

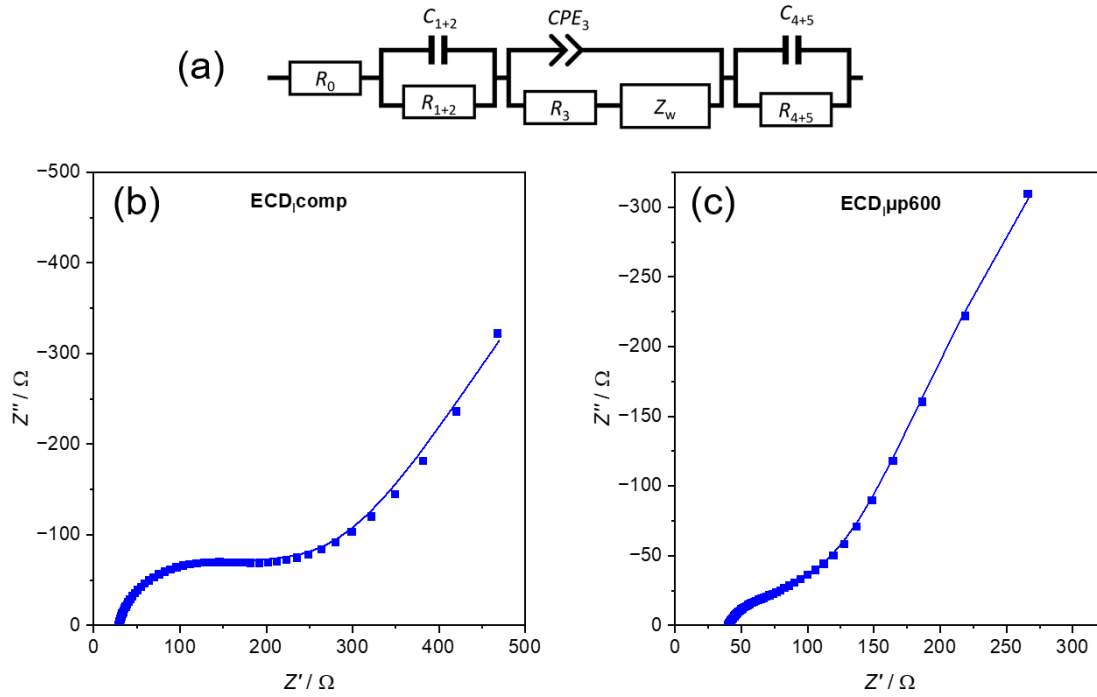|	ECD|comp	ECD|µp600		ECD|comp	ECD|µp600
R_0 / Ω	30.26	40.70			
R_1 / Ω	20.04	3.12	C_1 / µF	20	25
R_2 / Ω	86.98	10.54	C_2 / µF	25	68
R_3 / Ω	88.73	35.18	C_3 / µF	569	431
A_w / $\Omega\,s^{-1/2}$	142.26	103.71			
R_4 / Ω	70.09	18.02	C_4 / µF	151	179
R_5 / Ω	589.79	794.30	C_5 / µF	12067	8616
D_I / cm^2 s^{-1}	$3.78 \cdot 10^{-13}$	$7.12 \cdot 10^{-13}$			

Figure A.2: (a) Simplified equivalent circuit for description of a complete electrochromic device and Nyquist plots of (b) ECD|comp and (c) ECD|µp600 with the experimental data (points) and fitted data (solid lines) obtained from the fits using the equivalent circuit shown in (a).

Table A.2: Values of the resistances R, the capacitances C, the parameters Q_{CPE3} and α representing the CPE element, the Warburg coefficient A_w and the diffusion coefficient D_I obtained from A_w of ECD|comp and ECD|µp600.

	ECD|comp	ECD|µp600
R_0 / Ω	28.42	40.07
R_{1+2} / Ω	56.24	5.91
R_3 / Ω	195.55	91.92
R_{4+5} / Ω	583.04	805.21
A_w / $\Omega\,s^{-1/2}$	175.86	111.67
D_I / $cm^2\,s^{-1}$	$2.47 \cdot 10^{-13}$	$6.14 \cdot 10^{-13}$
C_{1+2} / μF	34	208
Q_{CPE3} / $F\,s^{(\alpha-1)}$	0.000313	0.001244
α	0.6	0.6
C_{4+5} / μF	16602	8248

References – Separately Mentioned from Those in the Publications

1. United Nations Environment Programme. *2021 Global Status Report for Buildings and Construction: Towards a Zero-emission, Efficient and Resilient Buildings and Construction Sector*, Nairobi, 2021. Available online: https://globalabc.org/resources/publications/2021-global-status-report-buildings-and-construction. Retrieved: June 22, 2022.

2. M. Santamouris, K. Vasilakopoulou. Present and Future Energy Consumption of Buildings: Challenges and Opportunities towards Decarbonisation. *e-Prime - Advances in Electrical Engineering, Electronics and Energy* **2021**, *1*, 100002.

3. A. Cannavale, U. Ayr, F. Fiorito, F. Martellotta. Smart Electrochromic Windows to Enhance Building Energy Efficiency and Visual Comfort. *Energies* **2020**, *13* (6), 1449.

4. M. Pittaluga. The Electrochromic Wall. *Energy Build.* **2013**, *66*, 49–56.

5. N.L. Sbar, L. Podbelski, H.M. Yang, B. Pease. Electrochromic Dynamic Windows for Office Buildings. *Int. J. Sustain. Built Environ.* **2012**, *1* (1), 125–139.

6. B.R. Park, J. Hong, E.J. Choi, Y.J. Choi, C. Lee, J.W. Moon. Improvement in Energy Performance of Building Envelope Incorporating Electrochromic Windows (ECWs). *Energies* **2019**, *12* (6), 1181.

7. J.-M. Dussault, L. Gosselin, T. Galstian. Integration of Smart Windows into Building Design for Reduction of Yearly Overall Energy Consumption and Peak Loads. *Sol. Energy* **2012**, *86* (11), 3405–3416.

8. Bibliothèque nationale de France, Dominique Perrault Architecture, DPA–X, Saint-Gobain SageGlass. *La Bibliothèque nationale de France et la métropole durable*: *COP21*, Paris, 2015. Available online: https://issuu.com/dparchitecture/docs/la_biblioth__que_nationale_de_franc. Retrieved: June 22, 2022.

9. Paladino and Company. Performance Assessment of SageGlass Electrochromic Coatings and Control Scenarios. *SageGlass Energy Performance Modeling* **2010**, 1–10.

10. J.K. Day, C. McIlvennie, C. Brackley, M. Tarantini, C. Piselli, J. Hahn, W. O'Brien, V.S. Rajus, M. de Simone, M.B. Kjærgaard, M. Pritoni, A. Schlüter, Y. Peng, M. Schweiker, G. Fajilla, C. Becchio, V. Fabi, G. Spigliantini, G. Derbas, A.L. Pisello. A Review of Select Human-Building Interfaces and Their Relationship to Human Behavior, Energy Use and Occupant Comfort. *Build. Environ.* **2020**, *178*, 106920.

11. J.S.E.M. Svensson, C.G. Granqvist. Electrochromic Coatings for "Smart Windows". *Proc. SPIE* **1984**, *502*, 30–37.

12. J.S.E.M. Svensson, C.G. Granqvist. Electrochromic Coatings for "Smart Windows". *Sol. Energy Mater.* **1985**, *12* (6), 391–402.

13. C.G. Granqvist. Electrochromics for Smart Windows: Oxide-Based Thin Films and Devices. *Thin Solid Films* **2014**, *564*, 1–38.

14. P.M.S. Monk, R.J. Mortimer, D.R. Rosseinsky. *Electrochromism: Fundamentals and Applications;* VCH: Weinheim, 1995.

15. R.J. Mortimer, D.R. Rosseinsky, P.M.S. Monk, Eds. *Electrochromic Materials and Devices;* Wiley-VCH Verlag GmbH & Co. KGaA: Weinheim, 2015.

16. I. Riess. Mixed Ionic–Electronic Conductors—Material Properties and Applications. *Solid State Ionics* **2003**, *157* (1–4), 1–17.

17. C.G. Granqvist. Electrochromic Metal Oxides: An Introduction to Materials and Devices. In *Electrochromic Materials and Devices*; R.J. Mortimer, D.R. Rosseinsky, P.M.S. Monk, Eds.; Wiley-VCH Verlag GmbH & Co. KGaA: Weinheim, 2015; pp. 3–40.

18. C.G. Granqvist. *Handbook of Inorganic Electrochromic Materials*, Elsevier Science B.V.; 1995: Amsterdam.

19. S.K. Deb. Opportunities and Challenges in Science and Technology of WO_3 for Electrochromic and Related Applications. *Sol. Energy Mater. Sol. Cells* **2008**, *92* (2), 245–258.

20. M. Casini. Smart Windows for Energy Efficiency of Buildings. *Int. J. Civ. Struct. Eng.* **2015**, *2* (1), 230–238.

21. M. Casini. Active Dynamic Windows for Buildings: A Review. *Renew. Energ.* **2018**, *119*, 923–934.

22. P.M.S. Monk, D.R. Rosseinsky, R.J. Mortimer. Electrochromic Materials and Devices Based on Viologens. In *Electrochromic Materials and Devices*; R.J. Mortimer, D.R. Rosseinsky, P.M.S. Monk, Eds.; Wiley-VCH Verlag GmbH & Co. KGaA: Weinheim, 2015; pp. 57–89.

23. D.R. Rosseinsky, R.J. Mortimer. Electrochromic Systems and the Prospects for Devices. *Adv. Mater.* **2001**, *13* (11), 783–793.

24. K.W. Shah, S.-X. Wang, D.X.Y. Soo, J. Xu. Viologen-Based Electrochromic Materials: From Small Molecules, Polymers and Composites to Their Applications. *Polymers* **2019**, *11* (11), 1839.

25. Masdar - A Mubadala Company. *Smart Windows: Electrochromic Windows for Building Optimisation*, 2018. Available online: https://www.sageglass.com/en/ resource/masdar-technology-journal-smart-windows-electrochromic-windows- building-optimisation. Retrieved: June 22, 2022.

26. A. Piccolo, F. Simone. Performance Requirements for Electrochromic Smart Window. *J. Build. Eng.* **2015**, *3*, 94–103.

27. E.S. Lee, D.L. DiBartolomeo. Application Issues for Large-Area Electrochromic Windows in Commercial Buildings. *Sol. Energy Mater. Sol. Cells* **2002**, *71* (4), 465–491.

28. R.S. Crandall, B.W. Faughnan. Measurement of the Diffusion Coefficient of Electrons in WO_3 Films. *Appl. Phys. Lett.* **1975**, *26* (3), 120–121.

29. X. Meng, F. Quenneville, F. Venne, E. Di Mauro, D. Işık, M. Barbosa, Y. Drolet, M.M. Natile, D. Rochefort, F. Soavi, C. Santato. Electrolyte-Gated WO_3 Transistors: Electrochemistry, Structure, and Device Performance. *J. Phys. Chem. C* **2015**, *119* (37), 21732–21738.

30. C. Ho, I.D. Raistrick, R.A. Huggins. Application of A-C Techniques to the Study of Lithium Diffusion in Tungsten Trioxide Thin Films. *J. Electrochem. Soc.* **1980**, *127* (2), 343–350.

31. J.-G. Zhang, D.K. Benson, C.E. Tracy, S.K. Deb. The Influence of Microstructure on the Electrochromic Properties of Li_xWO_3 Films: Part II. Limiting Mechanisms in Coloring and Bleaching Processes. *J. Mater. Res.* **1993**, *8* (10), 2657–2667.

32. N. Kumagai, M. Abe, N. Kumagai, K. Tanno, J.P. Pereira-Ramos. Kinetics of Electrochemical Insertion of Lithium into WO. *Solid State Ionics* **1994**, *70/71*, 451–457.

33. S. Xiong, P.S. Lee, X. Lu. Nanostructures in Electrochromic Materials. In *Electrochromic Materials and Devices*; R.J. Mortimer, D.R. Rosseinsky, P.M.S. Monk, Eds.; Wiley-VCH Verlag GmbH & Co. KGaA: Weinheim, 2015; pp. 251–287.

34. J. Gupta, H. Shaik, K.N. Kumar. A Review on the Prominence of Porosity in Tungsten Oxide Thin Films for Electrochromism. *Ionics* **2021**, *27* (6), 2307–2334.

35. Y.-C. Her, C.-C. Chang. Facile Synthesis of One-Dimensional Crystalline/Amorphous Tungsten Oxide Core/Shell Heterostructures with Balanced Electrochromic Properties. *CrystEngComm* **2014**, *16* (24), 5379–5386.

36. N.A. Galiote, R.L.T. Parreira, J.M. Rosolen, F. Huguenin. Self-Assembled Films from WO_3: Electrochromism and Lithium Ion Diffusion. *Electrochem. Commun.* **2010**, *12* (6), 733–736.

37. S.-I. Park, Y.-J. Quan, S.-H. Kim, H. Kim, S. Kim, D.-M. Chun, C.S. Lee, M. Taya, W.-S. Chu, S.-H. Ahn. A Review on Fabrication Processes for Electrochromic Devices. *Int. J. Pr. Eng. Man.-G.T.* **2016**, *3* (4), 397–421.

38. G. Atak, İ. Bayrak Pehlivan, J. Montero, C.G. Granqvist, G.A. Niklasson. Electrochromic Tungsten Oxide Films Prepared by Sputtering: Optimizing Cycling Durability by Judicious Choice of Deposition Parameters. *Electrochim. Acta* **2021**, *367*, 137233.

39. C. Li, J.H. Hsieh, M.-T. Hung, B.Q. Huang. Electrochromic Study on Amorphous Tungsten Oxide Films by Sputtering. *Thin Solid Films* **2015**, *587*, 75–82.

40. J. Livage, D. Ganguli. Sol–Gel Electrochromic Coatings and Devices: A Review. *Sol. Energy Mater. Sol. Cells* **2001**, *68* (3–4), 365–381.

41. B. Zhao, X. Zhang, G. Dong, H. Wang, H. Yan. Efficient Electrochromic Device Based on Sol–Gel Prepared WO_3 Films. *Ionics* **2015**, *21* (10), 2879–2887.

42. S. Lu, C. Wang, H. Wang, J. Liu, H. Yan. Excellent Electrochromic Properties of Tungsten Oxide Films with a Mesoporous Structure. *J. Mater. Sci.: Mater. Electron.* **2017**, *28* (14), 10049–10055.

43. T. Pauporté. A Simplified Method for WO_3 Electrodeposition. *J. Electrochem. Soc.* **2002**, *149* (11), C539–C545.

44. J. Bentley, S. Desai, B.P. Bastakoti. Porous Tungsten Oxide: Recent Advances in Design, Synthesis, and Applications. *Chem. Eur. J.* **2021**, *27* (36), 9241–9252.

45. C.G. Granqvist. Oxide Electrochromics: An Introduction to Devices and Materials. *Sol. Energy Mater. Sol. Cells* **2012**, *99*, 1–13.

46. R.J. Mortimer. Organic Electrochromic Materials. *Electrochim. Acta* **1999**, *44* (18), 2971–2981.

47. J. Mack, M.J. Stillman. Electronic Structures of Metal Phthalocyanine and Porphyrin Complexes from Analysis of the UV-Visible Absorption and Magnetic Circular Dichroism Spectra and Molecular Orbital Calculations. In *The Porphyrin Handbook,* Vol. 16; K.M. Kadish, K.M. Smith, R. Guilard, Eds.; Academic Press: San Diego, 2003; pp. 43–116.

48. R.J. Mortimer, A.L. Dyer, J.R. Reynolds. Electrochromic Organic and Polymeric Materials for Display Applications. *Displays* **2006**, *27* (1), 2–18.

49. P.R. Somani, S. Radhakrishnan. Electrochromic Materials and Devices: Present and Future. *Mater. Chem. Phys.* **2003**, *77* (1), 117–133.

50. C.G. Claessens, U. Hahn, T. Torres. Phthalocyanines: From Outstanding Electronic Properties to Emerging Applications. *Chem. Rec.* **2008**, *8* (2), 75–97.

51. M.M. Nicholson. Electrochromism and Display Devices. In *Phthalocyanines: Properties and Applications,* Vol. 3; C.C. Leznoff, A.B.P. Lever, Eds.; VCH: Weinheim, 1993; pp. 71–118.

52. B. Schumann, D. Wöhrle, N.I. Jaeger. Reversible Reduction and Reoxidation of Entire Thin Films of Octacyanophthalocyanine. *J. Electrochem. Soc.* **1985**, *132* (9), 2144–2149.

53. S. Nagel, M. Lener, C. Keil, R. Gerdes, Ł. Łapok, S.M. Gorun, D. Schlettwein. Electrochromic Switching of Evaporated Thin Films of Bulky, Electronic Deficient Metallo-Phthalocyanines. *J. Phys. Chem. C* **2011**, *115* (17), 8759–8767.

54. J. Weissbecker, A. Loas, S.M. Gorun, D. Schlettwein. Switching of the Rate-limiting Step in the Electrochromic Reduction of Fluorinated Phthalocyanine Thin Films by Decreased Intermolecular Coupling. *Electrochim. Acta* **2015**, *157*, 232–244.

55. C. Keil, D. Schlettwein. Development of the Field-Effect Mobility in Thin Films of $F_{16}PcCu$ Characterized by Electrical *in situ* Measurements During Device Preparation. *Org. Electron.* **2011**, *12* (8), 1376–1382.

56. C. Keil, O. Tsaryova, L. Lapok, C. Himcinschi, D. Wöhrle, O.R. Hild, D.R.T. Zahn, S.M. Gorun, D. Schlettwein. Growth and Characterization of Thin Films Prepared from Perfluoro-Isopropyl-Substituted Perfluorophthalocyanines. *Thin Solid Films* **2009**, *517* (15), 4379–4384.

57. I.F. Chang, B.L. Gilbert, T.I. Sun. Electrochemichromic Systems for Display Applications. *J. Electrochem. Soc.* **1975**, *122* (7), 955–962.

58. C.L. Bird, A.T. Kuhn. Electrochemistry of the Viologens. *Chem. Soc. Rev.* **1981**, *10* (1), 49–82.

59. S. Fletcher, L. Duff, R.G. Barradas. Nucleation and Charge-Transfer Kinetics at the Viologen/SnO_2 Interface in Electrochromic Device Applications. *J. Electroanal. Chem. Interfacial Electrochem.* **1979**, *100* (1–2), 759–770.

60. K. Ellmer. Past Achievements and Future Challenges in the Development of Optically Transparent Electrodes. *Nat. Photonics* **2012**, *6* (12), 809–817.

61. M.A. Aouaj, R. Diaz, A. Belayachi, F. Rueda, M. Abd-Lefdil. Comparative Study of ITO and FTO Thin Films Grown by Spray Pyrolysis. *Mater. Res. Bull.* **2009**, *44* (7), 1458–1461.

62. T. Kawashima, T. Ezure, K. Okada, H. Matsui, K. Goto, N. Tanabe. FTO/ITO Double-Layered Transparent Conductive Oxide for Dye-Sensitized Solar Cells. *J. Photochem. Photobiol. A* **2004**, *164* (1–3), 199–202.

63. U. Schwarz-Schampera, P.M. Herzig. *Indium: Geology, Mineralogy, and Economics;* Springer: Berlin, 2002.

64. A. Verma, A.K. Bakhshi, S.A. Agnihotry. Effect of Citric Acid on Properties of CeO_2 Films for Electrochromic Windows. *Sol. Energy Mater. Sol. Cells* **2006**, *90* (11), 1640–1655.

65. N. Özer. Optical Properties and Electrochromic Characterization of Sol–Gel Deposited Ceria Films. *Sol. Energy Mater. Sol. Cells* **2001**, *68* (3–4), 391–400.

66. G.A. Niklasson, C.G. Granqvist. Electrochromics for Smart Windows: Thin Films of Tungsten Oxide and Nickel Oxide, and Devices Based on These. *J. Mater. Chem.* **2007**, *17* (2), 127–156.

67. J. Zhang, J.P. Tu, X.H. Xia, Y. Qiao, Y. Lu. An All-Solid-State Electrochromic Device Based on NiO/WO_3 Complementary Structure and Solid Hybrid Polyelectrolyte. *Sol. Energy Mater. Sol. Cells* **2009**, *93* (10), 1840–1845.

68. T. Saito, Y. Ushio, M. Yamada, T. Niwa. Properties of Tantalum Oxide Thin Film for Solid Electrolyte. *Solid State Ionics* **1999**, *40/41*, 499–501.

69. K. Tajima, H. Hotta, Y. Yamada, M. Okada, K. Yoshimura. Fabrication of Solid Electrolyte Ta_2O_5 Thin Film by Reactive DC Magnetron Sputtering Suitable for Electrochromic All-Solid-State Switchable Mirror Glass. *J. Ceram. Soc. Jpn.* **2011**, *119* (1385), 76–80.

70. O. Bohnke, C. Rousselot, P.A. Gillet, C. Truche. Gel Electrolyte for Solid-State Electrochromic Cell. *J. Electrochem. Soc.* **1992**, *139* (7), 1862–1865.

71. A.L.-S. Eh, X. Lu, P.S. Lee. Advances in Polymer Electrolytes for Electrochromic Applications. In *Electrochromic Materials and Devices*; R.J. Mortimer, D.R. Rosseinsky, P.M.S. Monk, Eds.; Wiley-VCH Verlag GmbH & Co. KGaA: Weinheim, 2015; pp. 289–310.

72. L.M. Bertus, C. Faure, A. Danine, C. Labrugere, G. Campet, A. Rougier, A. Duta. Synthesis and Characterization of WO_3 Thin Films by Surfactant Assisted Spray Pyrolysis for Electrochromic Applications. *Mater. Chem. Phys.* **2013**, *140* (1), 49–59.

73. M. Deepa, M. Kar, D.P. Singh, A.K. Srivastava, S. Ahmad. Influence of Polyethylene Glycol Template on Microstructure and Electrochromic Properties of Tungsten Oxide. *Sol. Energy Mater. Sol. Cells* **2008**, *92* (2), 170–178.

74. C.G. Granqvist. Electrochromic Tungsten Oxide Films: Review of Progress 1993–1998. *Sol. Energy Mater. Sol. Cells* **2000**, *60* (3), 201–262.

75. W. Han, Q. Shi, R. Hu. Advances in Electrochemical Energy Devices Constructed with Tungsten Oxide-Based Nanomaterials. *Nanomaterials* **2021**, *11* (3), 692.

76. S.K. Deb. A Novel Electrophotographic System. *Appl. Opt.* **1969**, *8* (1), 192–195.

77. S.K. Deb. Optical and Photoelectric Properties and Colour Centres in Thin Films of Tungsten Oxide. *Philos. Mag.* **1973**, *27* (4), 801–822.

78. F.P. Koffyberg, K. Dwight, A. Wold. Interband Transitions of Semiconducting Oxides Determined from Photoelectrolysis Spectra. *Solid State Commun.* **1979**, *30* (7), 433–437.

79. K. Miyake, H. Kaneko, M. Sano, N. Suedomi. Physical and Electrochromic Properties of the Amorphous and Crystalline Tungsten Oxide Thick Films Prepared under Reducing Atmosphere. *J. Appl. Phys.* **1984**, *55* (7), 2747–2753.

80. H. Zheng, J.Z. Ou, M.S. Strano, R.B. Kaner, A. Mitchell, K. Kalantar-zadeh. Nanostructured Tungsten Oxide - Properties, Synthesis, and Applications. *Adv. Funct. Mater.* **2011**, *21* (12), 2175–2196.

81. J.B. Goodenough: Metallic Oxides. *Prog. Solid State Chem.* **1971**, *5*, 145–399.

82. A. Hjelm, C.G. Granqvist, J.M. Wills. Electronic Structure and Optical Properties of WO_3, $LiWO_3$, $NaWO_3$, and HWO_3. *Phys. Rev. B* **1996**, *54* (4), 2436–2445.

83. A. Magnéli. Some Aspects of the Crystal Chemistry of Oxygen Compounds of Molybdenum and Tungsten Containing Structural Elements of ReO_3 or Perovskite Type. *J. Inorg. Nucl. Chem.* **1956**, *2* (5–6), 330–339.

84. K. Bange. Colouration of Tungsten Oxide Films: A Model for Optically Active Coatings. *Sol. Energy Mater. Sol.* **1999**, *58* (1), 1–131.

85. H. Bräkken. Die Kristallstrukturen der Trioxyde von Chrom, Molybdän und Wolfram. *Z. Kristallogr. – Cryst. Mater.* **1931**, *78* (1–6), 484–488.

86. K. Meisel. Rheniumtrioxyd. III. Mitteilung. Über die Kristallstruktur des Rheniumtrioxyds. *Z. Anorg. Allg. Chem.* **1932**, *207* (1), 121–128.

87. G. Andersson. On the Crystal Structure of Tungsten Trioxide. *Acta Chem. Scand.* **1953**, *7* (1), 154–158.

88. C. Balázsi, M. Farkas-Jahnke, I. Kotsis, L. Petrás, J. Pfeifer. The Observation of Cubic Tungsten Trioxide at High-Temperature Dehydration of Tungstic Acid Hydrate. *Solid State Ionics* **2001**, *141/142*, 411–416.

89. A.R. Siedle, T.E. Wood, M.L. Brostrom, D.C. Koskenmaki, B. Montez, E. Oldfield. Solid-State Polymerization of Molecular Metal Oxide Clusters: Aluminum 12-Tungstophosphate. *J. Am. Chem. Soc.* **1989**, *111* (5), 1665–1669.

90. L.J. LeGore, R.J. Lad, S.C. Moulzolf, J.F. Vetelino, B.G. Frederick, E.K. Kenik. Defects and Morphology of Tungsten Trioxide Thin Films. *Thin Solid Films* **2002**, *406* (1–2), 79–86.

91. S. Tanisaki. Crystal Structure of Monoclinic Tungsten Trioxide at Room Temperature. *J. Phys. Soc. Jpn.* **1960**, *15* (4), 573–581.

92. R. Diehl, G. Brandt, E. Saije. The Crystal Structure of Triclinic WO_3. *Acta Crystallogr. B* **1978**, *34* (4), 1105–1111.

93. S. Tanisaki. On the Phase Transition of Tungsten Trioxide below Room Temperature. *J. Phys. Soc. Jpn.* **1960**, *15* (4), 566–573.

94. E. Salje, K. Viswanathan. Physical Properties and Phase Transitions in WO_3. *Acta Crystallogr. A* **1975**, *31* (3), 356–359.

95. P.M. Woodward, A.W. Sleight, T. Vogt. Structure Refinement of Triclinic Tungsten Trioxide. *J. Phys. Chem. Solids* **1995**, *56* (10), 1305–1315.

96. B. Gerand, G. Nowogrocki, J. Guenot, M. Figlarz. Structural Study of a New Hexagonal Form of Tungsten Trioxide. *J. Solid State Chem.* **1979**, *29* (3), 429–434.

97. B. Gerand, G. Nowogrocki, M. Figlarz. A New Tungsten Trioxide Hydrate, $WO_3 \cdot 1/3H_2O$: Preparation, Characterization, and Crystallographic Study. *J. Solid State Chem.* **1981**, *38* (3), 312–320.

98. S. Balaji, Y. Djaoued, A.-S. Albert, R.Z. Ferguson, R. Brüning. Hexagonal Tungsten Oxide Based Electrochromic Devices: Spectroscopic Evidence for the Li Ion Occupancy of Four-Coordinated Square Windows. *Chem. Mater.* **2009**, *21* (7), 1381–1389.

99. E. Salje. The Orthorhombic Phase of WO_3. *Acta Crystallogr. B* **1977**, *33* (2), 574–577.

100. W.L. Kehl, R.G. Hay, D. Wahl. The Structure of Tetragonal Tungsten Trioxide. *J. Appl. Phys.* **1952**, *23* (2), 212–215.

101. A. Magnéli. Structures of the ReO$_3$-Type with Recurrent Dislocations of Atoms: 'Homologous Series' of Molybdenum and Tungsten Oxides. *Acta Crystallogr.* **1953**, *6* (6), 495–500.

102. B.W. Faughnan, R.S. Crandall, P.M. Heyman. Electrochromism in WO$_3$ Amorphous Films. *RCA Rev.* **1975**, *36* (1), 177–197.

103. B.W. Faughnan, R.S. Crandall. Electrochromic Displays Based on WO$_3$. In *Topics in Applied Physics*: *Display Devices,* Vol. 40; J.I. Pankove, Ed.; Springer: Berlin, 1980; pp. 181–211.

104. D. Dini, F. Decker, E. Masetti. A Comparison of the Electrochromic Properties of WO$_3$ Films Intercalated with H$^+$, Li$^+$ and Na$^+$. *J. Appl. Electrochem.* **1996**, *26* (6), 657–653.

105. R. Sivakumar, K. Shanthakumari, A. Thayumanavan, M. Jayachandran, C. Sanjeeviraja. Coloration and Bleaching Mechanism of Tungsten Oxide Thin Films in Different Electrolytes. *Surf. Eng.* **2007**, *23* (5), 373–379.

106. L. Berggren, J.C. Jonsson, G.A. Niklasson. Optical Absorption in Lithiated Tungsten Oxide Thin Films: Experiment and Theory. *J. Appl. Phys.* **2007**, *102* (8), 083538.

107. L. Berggren, G.A. Niklasson. Optical Charge Transfer Absorption in Lithium-Intercalated Tungsten Oxide Thin Films. *Appl. Phys. Lett.* **2006**, *88* (8), 081906.

108. O.F. Schirmer, V. Wittwer, G. Baur, G. Brandt. Dependence of WO$_3$ Electrochromic Absorption on Crystallinity. *J. Electrochem. Soc.* **1977**, *124* (5), 749–753.

109. S.-H. Lee, H.M. Cheong, J.-G. Zhang, A. Mascarenhas, D.K. Benson, S.K. Deb. Electrochromic Mechanism in a-WO$_{3-y}$ Thin Films. *Appl. Phys. Lett.* **1999**, *74* (2), 242–244.

110. J.-G. Zhang, D.K. Benson, C.E. Tracy, S.K. Deb, A.W. Czanderna, C. Bechinger. Chromic Mechanism in Amorphous WO$_3$ Films. *J. Electrochem. Soc.* **1997**, *144* (6), 2022–2026.

111. C. Bechinger, M.S. Burdis, J.-G. Zhang. Comparison between Electrochromic and Photochromic Coloration Efficiency of Tungsten Oxide Thin Films. *Solid State Commun.* **1997**, *101* (10), 753–756.

112.   D.H. Mendelsohn, R.B. Goldner. Ellipsometry Measurements as Direct Evidence of the Drude Model for Polycrystalline Electrochromic WO_3 Films. *J. Electrochem. Soc.* **1984**, *131* (4), 857–860.

113.   R.B. Goldner, P. Norton, K. Wong, G. Foley, E.L. Goldner, G. Seward, R. Chapman. Further Evidence for Free Electrons as Dominating the Behavior of Electrochromic Polycrystalline WO_3 Films. *Appl. Phys. Lett.* **1985**, *47* (5), 536–538.

114.   J.S.E.M. Svensson, C.G. Granqvist. Modulated Transmittance and Reflectance in Crystalline Electrochromic WO_3 Films: Theoretical Limits. *Appl. Phys. Lett.* **1984**, *45* (8), 828–830.

115.   D. Wöhrle, G. Schnurpfeil, S.G. Makarov, A. Kazarin, O.N. Suvorova. Practical Applications of Phthalocyanines – from Dyes and Pigments to Materials for Optical, Electronic and Photo-electronic Devices. *Macroheterocycles* **2012**, *5* (3), 191–202.

116.   H. Isago. *Optical Spectra of Phthalocyanines and Related Compounds*: *A Guide for Beginners;* Springer: Tokyo, 2015.

117.   L. Edwards, M. Gouterman. Porphyrins: XV. Vapor Absorption Spectra and Stability: Phthalocyanines. *J. Mol. Spectrosc.* **1970**, *33* (2), 292–310.

118.   A.T. Davidson. The Effect of the Metal Atom on the Absorption Spectra of Phthalocyanine Films. *J. Chem. Phys.* **1982**, *77* (1), 168–172.

119.   T. Muto, T. Temma, M. Kimura, K. Hanabusa, H. Shirai. Elongation of the π-System of Phthalocyanines by Introduction of Thienyl Substituents at the Peripheral *β* Positions. Synthesis and Characterization. *J. Org. Chem.* **2001**, *66* (18), 6109–6115.

120.   A.B.P. Lever, E.R. Milaeva, G. Speier. The Redox Chemistry of Metallophthalocyanines in Solution. In *Phthalocyanines: Properties and Applications,* Vol. 3; C.C. Leznoff, A.B.P. Lever, Eds.; VCH: Weinheim, 1993; pp. 3–69.

121.   M. L'Her, A. Pondaven. Electrochemistry of Phthalocyanines. In *The Porphyrin Handbook,* Vol. 16; K.M. Kadish, K.M. Smith, R. Guilard, Eds.; Academic Press: San Diego, 2003; pp. 117–169.

122. P.C. Minor, M. Gouterman, A.B.P. Lever. Electronic Spectra of Phthalocyanine Radical Anions and Cations. *Inorg. Chem.* **1985**, *24* (12), 1894–1900.

123. K. Hesse, D. Schlettwein. Spectroelectrochemical Investigations on the Reduction of Thin Films of Hexadecafluorophthalocyaninatozinc (F_{16}PcZn). *J. Electroanal. Chem.* **1999**, *476* (2), 148–158.

124. T.H.Q. Nguyen, M. Pelmuş, C. Colomier, S.M. Gorun, D. Schlettwein. The Influence of Intermolecular Coupling on Electron and Ion Transport in Differently Substituted Phthalocyanine Thin Films as Electrochromic Materials: A Chemistry Application of the Goldilocks Principle. *Phys. Chem. Chem. Phys.* **2020**, *22* (15), 7699–7709.

125. B.A. Bench, A. Beveridge, W.M. Sharman, G.J. Diebold, J.E. van Lier, S.M. Gorun. Introduction of Bulky Perfluoroalkyl Groups at the Periphery of Zinc Perfluorophthalocyanine: Chemical, Structural, Electronic, and Preliminary Photophysical and Biological Effects. *Angew. Chem. Int. Ed.* **2002**, *41* (5), 747–750.

126. D. Klyamer, D. Bonegardt, T. Basova. Fluoro-Substituted Metal Phthalocyanines for Active Layers of Chemical Sensors. *Chemosensors* **2021**, *9* (6), 133.

127. W.-Y. Wen, J.A. Muccitelli. Thermodynamics of Some Perfluorocarbon Gases in Water. *J. Solution Chem.* **1979**, *8* (3), 225–246.

128. V.H. Dalvi, P.J. Rossky. Molecular Origins of Fluorocarbon Hydrophobicity. *Proc. Natl. Acad. Sci. U.S.A* **2010**, *107* (31), 13603–13607.

129. A.C. Pierre. *Introduction to Sol-Gel Processing*, 2nd ed.; Springer: Cham, 2020.

130. D.P. Birnie III. Spin Coating Technique. In *Sol-Gel Technologies for Glass Producers and Users*; M.A. Aegerter, M. Mennig, Eds.; Springer: New York, 2004; pp. 49–55.

131. N. Sahu, B. Parija, S. Panigrahi. Fundamental Understanding and Modeling of Spin Coating Process : A Review. *Indian J. Phys.* **2009**, *83* (4), 493–502.

132. M.D. Tyona. A Theoritical Study on Spin Coating Technique. *Adv. Mater. Res.* **2013**, *2* (4), 195–208.

133. D.P. Birnie III. Spin Coating: Art and Science. In *Chemical Solution Deposition of Functional Oxide Thin Films*; T. Schneller, R. Waser, M. Kosec, D. Payne, Eds.; Springer: Wien, 2013; pp. 263–274.

134. J.R. Vig. Ultraviolet-Ozone Cleaning Of Semiconductor Surfaces. In *Handbook of Semiconductor Wafer Cleaning Technology*; W. Kern, Ed.; Noyes Publications: Park Ridge, 1993; pp. 233–273.

135. K.K. Chattopadhyay, A.N. Banerjee. *Introduction to Nanoscience and Nanotechnology;* PHI Learning Private Limited: New Delhi, 2009.

136. P.M. Martin. *Introduction to Surface Engineering and Functionally Engineered Materials;* Scrivener Publishing LLC, John Wiley & Sons: Salem, Hoboken, 2011.

137. Z. Cheng, C. Wu, M. Ni. The Measurement of Cathode Evaporation Rate by Quartz Crystal Microbalance. *J. Vac. Sci. Technol. A* **1991**, *9* (3), 501–504.

138. S. Stuckenholz, C. Büchner, G. Thielsch, M. Heyde, H.-J. Freund. A Portable Quartz Micro Balance for Physical Vapor Deposition Techniques. *Rev. Sci. Instrum.* **2013**, *84* (8), 085118.

139. L. Cornelius, M. Beu, C. Keil, D. Schlettwein. Doping in Mixed Films of Differently Substituted Phthalocyanines Measured in-situ During Film Growth. *Phys. Status Solidi RRL* **2012**, *6* (5), 214–216.

140. A. Opitz, B. Ecker, J. Wagner, A. Hinderhofer, F. Schreiber, J. Manara, J. Pflaum, W. Brütting. Mixed Crystalline Films of Co-evaporated Hydrogen- and Fluorine-Terminated Phthalocyanines and Their Application in Photovoltaic Devices. *Org. Electron.* **2009**, *10* (7), 1259–1267.

141. A.J. Bard, L.R. Faulkner. *Electrochemical Methods*: *Fundamentals and Applications*, 2nd ed.; John Wiley & Sons: New York, 2001.

142. T.E. Keyes, R.J. Forster. Spectroelectrochemistry. In *Handbook of Electrochemistry*; C.G. Zoski, Ed.; Elsevier B.V.: Amsterdam, 2007; pp. 591–635.

143. N. Elgrishi, K.J. Rountree, B.D. McCarthy, E.S. Rountree, T.T. Eisenhart, J.L. Dempsey. A Practical Beginner's Guide to Cyclic Voltammetry. *J. Chem. Educ.* **2017**, *95* (2), 197–206.

144. H.H. Perkampus. *UV-VIS-Spektroskopie und ihre Anwendungen;* Springer: Berlin, 2013.

145. W. Bechmann, J. Schmidt. *Struktur- und Stoffanalytik mit spektroskopischen Methoden;* Teubner: Stuttgart, 2013.

146. J. Singh, P. Capper, A. Willoughby, S.O. Kasap, Eds. *Optical Properties of Materials and Their Applications*, 2nd ed.; John Wiley & Sons: Chichester, 2020.

147. H. Kamal, A.A. Akl, K. Abdel-Hady. Influence of Proton Insertion on the Conductivity, Structural and Optical Properties of Amorphous and Crystalline Electrochromic WO_3 Films. *Physica B* **2004**, *349* (1–4), 192–205.

148. K. Zhou, H. Wang, S. Zhang, J. Jiu, J. Liu, Y. Zhang, H. Yan. Electrochromic Modulation of Near-Infrared Light by WO_3 Films Deposited on Silver Nanowire Substrates. *J. Mater. Sci.* **2017**, *52* (21), 12783–12794.

149. S.S. Mali, D.S. Dalavi, P.N. Bhosale, C.A. Betty, A.K. Chauhan, P.S. Patil. Electro-Optical Properties of Copper Phthalocyanines (CuPc) Vacuum Deposited Thin Films. *RSC Adv.* **2012**, *2* (5), 2100–2104.

150. T.G. Mayerhöfer, S. Pahlow, J. Popp. The Bouguer-Beer-Lambert Law: Shining Light on the Obscure. *ChemPhysChem* **2020**, *21* (18), 2029–2046.

151. E. Laviron. A Multilayer Model for the Study of Space Distributed Redox Modified Electrodes: Part I. Description and Discussion of the Model. *J. Electroanal. Chem.* **1980**, *112* (1), 1–9.

152. E. Laviron, L. Roullier, C. Degrand. A Multilayer Model for the Study of Space Distributed Redox Modified Electrodes: Part II. Theory and Application of Linear Potential Sweep Voltammetry for a Simple Reaction. *J. Electroanal. Chem.* **1980**, *112* (1), 11–23.

153. E. Laviron. A Multilayer Model for the Study of Space Distributed Redox Modified Electrodes: Part III. Influence of Interactions between the Electroactive Centers in the First Layer on the Linear Potential Sweep Voltammograms. *J. Electroanal. Chem.* **1981**, *122*, 37–44.

154. G. Denuault, M. Sosna, K.-J. Williams. Classical Experiments. In *Handbook of Electrochemistry*; C.G. Zoski, Ed.; Elsevier B.V.: Amsterdam, 2007; pp. 431–469.

155. J. Wang. *Analytical Electrochemistry*, 3rd ed.; John Wiley & Sons: Hoboken, 2006.

156. J. Leddy, A.J. Bard. Polymer Films on Electrodes: Part XII. Chronoamperometric and Rotating Disk Electrode Determination of the Mechanism of Mass Transport Through Poly(vinyl Ferrocene) Films. *J. Electroanal. Chem.* **1983**, *153* (1), 223–242.

157. H.-I. Yoo, J.-H. Lee, M. Martin, J. Janek, H. Schmalzried. Experimental Evidence of the Interference between Ionic and Electronic Flows in an Oxide with Prevailing Electronic Conduction. *Solid State Ionics* **1994**, *67* (3–4), 317–322.

158. V.N. Chebotin. Coupled Chemical Diffusion of Ions and Electrons in Non-stoichiometric Crystals. *Russ. Chem. Rev.* **1986**, *55* (6), 495–510.

159. I. Yokota. On the Theory of Mixed Conduction with Special Reference to Conduction in Silver Sulfide Group Semiconductors. *J. Phys. Soc. Jpn.* **1961**, *16* (11), 2213–2223.

160. S.-H. Lee, H.M. Cheong, C.E. Tracy, A. Mascarenhas, J.R. Pitts, G. Jorgensen, S.K. Deb. Alternating Current Impedance and Raman Spectroscopic Study on Electrochromic a-WO_3 Films. *Appl. Phys. Lett.* **2000**, *76* (26), 3908–3910.

161. H.-S. Shim, J.W. Kim, Y.-E. Sung, W.B. Kim. Electrochromic Properties of Tungsten Oxide Nanowires Fabricated by Electrospinning Method. *Sol. Energy Mater. Sol. Cells* **2009**, *93* (12), 2062–2068.

162. C.A.C. Sequeira, D.M.F. Santos. Tungsten Oxide Electrochromic Windows with Lithium Polymer Electrolytes. *J. Electrochem. Soc.* **2010**, *157* (6), J202–J207.

163. V.V. Kondalkar, S.S. Mali, R.R. Kharade, R.M. Mane, P.S. Patil, C.K. Hong, J.H. Kim, S. Choudhury, P.N. Bhosale. Langmuir–Blodgett Self Organized Nanocrystalline Tungsten Oxide Thin Films for Electrochromic Performance. *RSC Adv.* **2015**, *5* (34), 26923–26931.

164. S.J. Yoo, J.W. Lim, Y.-E. Sung, Y.H. Jung, H.G. Choi, D.K. Kim. Fast Switchable Electrochromic Properties of Tungsten Oxide Nanowire Bundles. *Appl. Phys. Lett.* **2007**, *90* (17), 173126.

165.   M.S. Mattson. Li Insertion into WO_3 : Introduction of a New Electrochemical Analysis Method and Comparison with Impedance Spectroscopy and the Galvanostatic Intermittent Titration Technique. *Solid State Ionics* **2000**, *131* (3–4), 261–273.

166.   P. Córdoba-Torres, T.J. Mesquita, R.P. Nogueira. Relationship between the Origin of Constant-Phase Element Behavior in Electrochemical Impedance Spectroscopy and Electrode Surface Structure. *J. Phys. Chem. C* **2015**, *119* (8), 4136–4147.

167.   P. Córdoba-Torres, T.J. Mesquita, O. Devos, B. Tribollet, V. Roche, R.P. Nogueira. On the Intrinsic Coupling between Constant-Phase Element Parameters $α$ and Q in Electrochemical Impedance Spectroscopy. *Electrochim. Acta* **2012**, *72*, 172–178.

168.   L.S. Wang, B.P. Hichwa, S.P. Sapers, J.G.H. Mathew, N.A. O'Brien. Impedance Spectroscopy Study of Physical Vapor Deposited Amorphous WO_3 Electrochromic Thin Films. In *Proceedings of the Symposium on Thin Film Solid Ionic Devices and Materials,* Vol. 95; J.B. Bates, Ed.; The Electrochemical Society: Pennington, 1996; pp. 63–75.

169.   L. Wang, J. Zhao, X. He, J. Gao, J. Li, C. Wan, C. Jiang. Electrochemical Impedance Spectroscopy (EIS) Study of $LiNi_{1/3}Co_{1/3}Mn_{1/3}O_2$ for Li-ion Batteries. *Int. J. Electrochem. Sci.* **2012**, *7*, 345–353.

170.   M. Deepa, D.P. Singh, S.M. Shivaprasad, S.A. Agnihotry. A Comparison of Electrochromic Properties of Sol–Gel Derived Amorphous and Nanocrystalline Tungsten Oxide Films. *Curr. Appl. Phys.* **2007**, *7* (2), 220–229.

171.   Y. Djaoued, P.V. Ashrit, S. Badilescu, R. Brüning. Synthesis and Characterization of Macroporous Tungsten Oxide Films for Electrochromic Application. *J. Sol-Gel Sci. Technol.* **2003**, *28* (2), 235–244.

172.   A. Cremonesi, D. Bersani, P.P. Lottici, Y. Djaoued, P.V. Ashrit. WO_3 Thin Films by Sol–Gel for Electrochromic Applications. *J. Non-Cryst. Solids* **2004**, *345/346*, 500–504.

173.   Y. Fang, X. Sun, H. Cao. Influence of PEG Additive and Annealing Temperature on Structural and Electrochromic Properties of Sol–Gel Derived WO_3 Films. *J. Sol-Gel. Sci. Technol.* **2011**, *59* (1), 145–152.

174. W.-T. Wu, W.-P. Liao, L.-Y. Chen, J.-S. Chen, J.-J. Wu. Outperformed Electrochromic Behavior of Poly(ethylene Glycol)-Template Nanostructured Tungsten Oxide Films with Enhanced Charge Transfer/Transport Characteristics. *Phys. Chem. Chem. Phys.* **2009**, *11* (42), 9751–9758.

175. W. Cheng, E. Baudrin, B. Dunn, J.I. Zink. Synthesis and Electrochromic Properties of Mesoporous Tungsten Oxide. *J. Mater. Chem.* **2001**, *11* (1), 92–97.

176. K.-W. Kim, T.Y. Yun, S.-H. You, X. Tang, J. Lee, Y. Seo, Y.-T. Kim, S.H. Kim, H.C. Moon, J.K. Kim. Extremely Fast Electrochromic Supercapacitors based on Mesoporous WO_3 Prepared by an Evaporation-Induced Self-Assembly. *NPG Asia Mater.* **2020**, *12* (1), 84.

177. S. Sallard, T. Brezesinski, B.M. Smarsly. Electrochromic Stability of WO_3 Thin Films with Nanometer-Scale Periodicity and Varying Degrees of Crystallinity. *J. Phys. Chem. C* **2007**, *111* (19), 7200–7206.

178. S. Sallard, M. Schröder, C. Boissière, C. Dunkel, M. Etienne, A. Walcarius, T. Oekermann, M. Wark, B.M. Smarsly. Bimodal Mesoporous Titanium Dioxide Anatase Films Templated by a Block Polymer and an Ionic Liquid: Influence of the Porosity on the Permeability. *Nanoscale* **2013**, *5* (24), 12316–12329.

179. P. Cop, K. Hess, S. Werner, R. Meinusch, B.M. Smarsly, H. Kozuka. Comparison of In-Plane Stress Development in Sol–Gel- and Nanoparticle-Derived Mesoporous Metal Oxide Thin Films. *Langmuir* **2019**, *35* (50), 16427–16437.

180. P.-W. Chen, C.-T. Chang, T.-F. Ko, S.-C. Hsu, K.-D. Li, J.-Y. Wu. Fast Response of Complementary Electrochromic Device Based on WO_3/NiO Electrodes. *Sci. Rep.* **2020**, *10* (1), 8430.

181. X.G. Wang, Y.S. Jang, N.H. Yang, L. Yuan, S.J. Pang. XPS and XRD Study of the Electrochromic Mechanism of WO_x Films. *Surf. Coat. Technol.* **1998**, *99* (1–2), 82–86.

182. R. Ostermann, B.M. Smarsly. Does Mesoporosity Enhance Thin Film Properties? A Question of Electrode Material for Electrochromism of WO_3. *Nanoscale* **2009**, *1* (2), 266–270.

183. S. Göbel. *Anpassung der Elektrolytzusammensetzung an verschieden poröse WO_3 – Schichten hinsichtlich ihres elektrochromen Schaltverhaltens.* Master Thesis, JLU Gießen, (Work in Progress).

184. A.-T. Tran, F. Huet, K. Ngo, P. Rousseau. Artefacts in Electrochemical Impedance Measurement in Electrolytic Solutions due to the Reference Electrode. *Electrochim. Acta* **2011**, *56* (23), 8034–8039.

185. G. Hsieh, S.J. Ford, T.O. Mason, L.R. Pederson. Experimental Limitations in Impedance Spectroscopy: Part I – Simulation of Reference Electrode Artefacts in Three-Point Measurements. *Solid State Ionics* **1996**, *91* (3–4), 191–201.

186. L.H.J. Raijmakers, M.J.G. Lammers, P.H.L. Notten. A New Method to Compensate Impedance Artefacts for Li-Ion Batteries with Integrated Micro-Reference Electrodes. *Electrochim. Acta* **2018**, *259*, 517–533.

187. M. Gaberscek, J. Moskon, B. Erjavec, R. Dominko, J. Jamnik. The Importance of Interphase Contacts in Li Ion Electrodes: The Meaning of the High-Frequency Impedance Arc. *Electrochem. Solid-State Lett.* **2008**, *11* (10), A170–A174.

188. D. Chatzikyriakou, A. Maho, R. Cloots, C. Henrist. Ultrasonic Spray Pyrolysis as a Processing Route for Templated Electrochromic Tungsten Oxide Films. *Microporous Mesoporous Mater.* **2017**, *240*, 31–38.

189. A. Enesca, L. Andronic, A. Duta. The Influence of Surfactants on the Crystalline Structure, Electrical and Photocatalytic Properties of Hybrid Multi-Structured (SnO_2, TiO_2 and WO_3) Thin Films. *Appl. Surf. Sci.* **2012**, *258* (10), 4339–4346.

190. H. Kaper, I. Djerdj, S. Gross, H. Amenitsch, M. Antonietti, B.M. Smarsly. Ionic Liquid- and Surfactant-Controlled Crystallization of WO_3 Films. *Phys. Chem. Chem. Phys.* **2015**, *17* (27), 18138–18145.

191. M. Deepa, A.K. Srivastava, S.N. Sharma, Govind, S.M. Shivaprasad. Microstructural and Electrochromic Properties of Tungsten Oxide Thin Films Produced by Surfactant Mediated Electrodeposition. *Appl. Surf. Sci.* **2008**, *254* (8), 2342–2352.

192. A. Memar, C.M. Phan, M.O. Tade. Controlling Particle Size and Photoelectrochemical Properties of Nanostructured WO_3 with Surfactants. *Appl. Surf. Sci.* **2014**, *305*, 760–767.

193. D. Susanti, A.A.G.P. Diputra, L. Tananta, H. Purwaningsih, G.E. Kusuma, C. Wang, S. Shih, Y. Huang. WO_3 Nanomaterials Synthesized via a Sol-Gel Method and Calcination for Use as a CO Gas Sensor. *Front. Chem. Sci. Eng.* **2014**, *8* (2), 179–187.

194. M. Reichhardt. *Herstellung von Wolframoxid-Dünnfilmen mittels Spin-Coating unter Zugabe von TritonX als Additiv und spektroelektrochemische Untersuchung*, Report of Elective Module "Dünne Schichten und Oberflächen", JLU Gießen, 2021.

195. L. Basso. *Investigation on the Influence of Annealing Time and Concentration of Non-ionic Surfactants on the Electrochromic Properties of Spin-Coated WO$_3$ Thin Films*, Report of Consolidation Module, JLU Gießen, 2021.

196. P.F. Eiland, R. Pepinsky. X-Ray Examination of Iron Biscyclopentadienyl. *J. Am. Chem. Soc.* **1952**, *74* (19), 4971.

197. C.O. Laoire, E. Plichta, M. Hendrickson, S. Mukerjee, K.M. Abraham. Electrochemical Studies of Ferrocene in a Lithium Ion Conducting Organic Carbonate Electrolyte. *Electrochim. Acta* **2009**, *54* (26), 6560–6564.

198. J.B. Shotwell, R.A. Flowers II. Electrochemical Investigation of the Solvolytic Properties of Ethylammonium Nitrate (EAN) and Propylammonium Nitrate (PAN). *Electroanalysis* **2000**, *12* (3), 223–226.

199. E.B. Sandell, S.S. Goldich. The Rarer Metallic Constituents of Some American Igneous Rocks. II. *J. Geol.* **1943**, *51* (3), 167–189.

200. L. Fabbrizzi. The Ferrocenium/Ferrocene Couple: A Versatile Redox Switch. *ChemTexts* **2020**, *6* (4), 22.

201. J.A. Page, G. Wilkinson. The Polarographic Chemistry of Ferrocene, Ruthenocene and the Metal Hydrocarbon Ions. *J. Am. Chem. Soc.* **1952**, *74* (23), 6149–6150.

202. G. Feng, Y. Xiong, H. Wang, Y. Yang. Cyclic Voltammetry Investigation of Diffusion of Ferrocene within Propylene Carbonate Organogel Formed by Gelator. *Electrochim. Acta* **2008**, *53* (28), 8253–8257.

203. J. Reiter, J. Vondrák, Z. Mička. The Electrochemical Redox Processes in PMMA Gel Electrolytes—Behaviour of Transition Metal Complexes. *Electrochim. Acta* **2005**, *50* (22), 4469–4476.

204.   J. Janisch, A. Ruff, B. Speiser, C. Wolff, J. Zigelli, S. Benthin, V. Feldmann, H.A. Mayer. Consistent Diffusion Coefficients of Ferrocene in Some Non-aqueous Solvents: Electrochemical Simultaneous Determination Together with Electrode Sizes and Comparison to Pulse-Gradient Spin-Echo NMR Results. *J. Solid State Electrochem.* **2011**, *15* (10), 2083–2094.

205.   A.J. Zara, S.S. Machado, L.O.S. Bulhões, A.V. Benedetti, T. Rabockai. The Electrochemistry of Ferrocene in Non-aqueous Solvents. *J. Electroanal. Chem. Interfacial Electrochem.* **1987**, *221* (1–2), 165–174.

206.   S.-I. Lee, U.-H. Jung, Y.-S. Kim, M.-H. Kim, D.-J. Ahn, H.-S. Chun. A Study of Electrochemical Kinetics of Lithium Ion in Organic Electrolytes. *Korean J. Chem. Eng,* **2002**, *19* (4), 638–644.

207.   C. Lupo, F. Eberheim, D. Schlettwein. Facile Low-Temperature Synthesis of Nickel Oxide by an Internal Combustion Reaction for Applications in Electrochromic Devices. *J. Mater. Sci.* **2020**, *55* (29), 14401–14414.

208.   L. Basso. *Electrochromic Cells Based on Solution-Processed Active Electrode Materials*. Master Thesis, JLU Gießen, (Work in Progress).

209.   C.C. Chen. Characterization of Porous WO_3 Electrochromic Device by Electrochemical Impedance Spectroscopy. *J. Nanomater.* **2013**, *2013*, 785023.

210.   A.W. Snow. Phthalocyanine Aggregation. In *The Porphyrin Handbook,* Vol. 17; K.M. Kadish, K.M. Smith, R. Guilard, Eds.; Academic Press: San Diego, 2003; pp. 129–176.

211.   D. Schlettwein, D. Wöhrle, N. I. Jaeger. Reversible Reduction and Reoxidation of Thin Films of Tetrapyrazinotetraazaporphyrines. *J. Electrochem. Soc.* **1989**, *136* (10), 2882–2886.

212.   D.G. de Oteyza, E. Barrena, J.O. Ossó, S. Sellner, H. Dosch. Thickness-Dependent Structural Transitions in Fluorinated Copper-Phthalocyanine ($F_{16}CuPc$) Films. *J. Am. Chem. Soc.* **2006**, *128* (47), 15052–15053.

Acknowledgements

List of Co-supervised Lab-Projects and Thesis Modules

- S. Göbel. *Anpassung der Elektrolytzusammensetzung an verschieden poröse* WO_3 *– Schichten hinsichtlich ihres elektrochromen Schaltverhaltens*. Master Thesis, Work in Progress, JLU Gießen.

- L. Basso. *Electrochromic Cells Based on Solution-Processed Active Electrode Materials*, Master Thesis, Work in Progress, JLU Gießen.

- S. Göbel. *Reproduzierbarkeit und spektroelektrochemische Charakterisierung von verbunden-mesoporösen Wolframoxidschichten durch Zugabe von PEG600 und* PIB_{50}-*b*-PEO_{45} *als Additive*. Report of Specialization Module, JLU Gießen, 2022.

- L. Basso. *Passive and Active Inorganic Oxide Counter Electrodes for the Realization of Electrochromic Devices: Study on* NiO_{1+y}, CeO_2, *and* $Ce_yTi_{1-y}O_2$ *Sol-Gel Prepared Thin Films*. Report of Specialization Module, JLU Gießen, 2021.

- L. Basso. *Investigation on the Influence of Annealing Time and Concentration of Non-ionic Surfactants on the Electrochromic Properties of Spin-Coated* WO_3 *Thin Films*. Report of Consolidation Module, JLU Gießen, 2021.

- F. Eberheim. *Optimierung des elektrochromen Schaltverhaltens von* WO_3 *– Filmen durch Beeinflussung der inneren Struktur mittels strukturdirigierender Agenzien*. Master Thesis, JLU Gießen, 2021.

- F. Eberheim. *Herstellung von elektrochromen WOx-Schichten mit PEG als Additiv und spektroelektrochemische Charakterisierung in wässrigen Elektrolyten*. Report of Consolidation and Specialization Module, JLU Gießen, 2021.

- M. Eckert. *Spektroelektrochemische und ToF-SIMS Untersuchung von Additiveinflüssen während der Dünnfilmpräparation auf die Lithiuminterkalation von Wolframoxid*. Report of Consolidation Module, JLU Gießen, 2021.

- M. Reichhardt. *Herstellung von Wolframoxid-Dünnfilmen mittels Spin-Coating unter Zugabe von TritonX als Additiv und spektroelektrochemische Untersuchung*. Report of Elective Module "Dünne Schichten und Oberflächen", JLU Gießen, 2021.

- T.P. Schneider. *Alterung im elektrochromen Schaltverhalten von mittels Spin-Coating präparierten Wolframoxid-Filmen*. Bachelor Thesis, JLU Gießen, 2020.

- T.P. Schneider. *Elektrochemische Abscheidung und spektroelektrochemische Charakterisierung von Wolframoxid-Dünnfilmen*. Report of Study Project. JLU Gießen, 2020.

- M. Wasem. *Optische und elektrische Charakterisierung von perfluorierten Phthalocyaninen ($F_{16}PcInCl$)*, Report of Elective Module "Dünne Schichten und Oberflächen". JLU Gießen, 2020.

- S. Göbel. *Elektrochemische und spektroelektrochemische Charakterisierung methoxylierter und fluorierter Bis(bis(8-chinolinyl)amid)$_2$metall(II)-Komplexe*, Bachelor Thesis. JLU Gießen, 2019.

- S. Göbel. *Elektrochemische und spektroelektrochemische Charakterisierung von unsubstituierten Bis(bis(8-quinolinyl)amid)$_2$metall(II)-Komplexen*, Report of Study Project. JLU Gießen, 2019.

- S. Göbel, L. Gümbel. *Präparation von dünnen Wolframoxid-Filmen unter Zugabe von PEG als Additiv und deren elektrochemische Charakterisierung*, Report of Elective Module "Dünne Schichten und Oberflächen". JLU Gießen, 2018.

List of Conference Contributions

- T.H.Q. Nguyen, M. Pelmuş, C. Colomier, S.M. Gorun, D. Schlettwein, "Mixed Ionic and Electronic Conduction in Appropriately Substituted Phthalocyanine Thin Films for Reversible and Fast Electrochromic Switching", 239th ECS Meeting with the 18th International Meeting on Chemical Sensors (IMCS) 2021, Digital Meeting. **Oral presentation**.

- T.H.Q. Nguyen, F. Eberheim, S. Göbel, L. Gümbel, P. Cop, M. Eckert, T.P. Schneider, B.M. Smarsly, D. Schlettwein, "Influence of Polymer Additives During Spin-Coating of WO_3 Thin Films on their Spectroelectrochemical Performance", Bunsen-Tagung 2021, Digital Meeting. **Poster**.

- T.H.Q. Nguyen, M. Pelmuş, M. Schäfer, S.M. Gorun, D. Schlettwein, "Dependence of Electron and Ion Transport on the Intermolecular Coupling in Fluorinated Phthalocyanine Thin Films as Electrochromic Materials", Virtuelle DPG-Frühjahrstagung 2021, Digital Meeting. **Poster**.

- T.H.Q. Nguyen, D. Schlettwein, "Spectroelectrochemical Performance of Electrochromic Thin Films for the Application in Smart Windows", RTG 2204 - International Workshop 2019, Schloss Rauischholzhausen, **Oral presentation**.

- T.H.Q. Nguyen, D. Schlettwein, "Increasing the Spectroelectrochemical Performance of WO_3 Films Prepared by Spin-Coating with Additives", DPG-Frühjahrstagung 2019, Regensburg, **Oral presentation**.